DOKUZ EYLÜL UNIVERSITY
GRADUATE SCHOOL OF NATURAL AND APPLIED SCIENCES

EXPERIMENTAL AND NUMERICAL STUDY OF LOCAL SCOUR AROUND BRIDGE PIERS WITH DIFFERENT CROSS SECTIONS CAUSED BY FLOOD HYDROGRAPH SUCCEEDING STEADY FLOW

by
Aslı BOR TÜRKBEN

March, 2015
İZMİR

EXPERIMENTAL AND NUMERICAL STUDY OF LOCAL SCOUR AROUND BRIDGE PIERS WITH DIFFERENT CROSS SECTIONS CAUSED BY FLOOD HYDROGRAPH SUCCEEDING STEADY FLOW

A Thesis Submitted to the
Graduate School of Natural and Applied Sciences of Dokuz Eylül University
In Partial Fulfillment of the Requirements for the Degree of Doctor of Philosophy in Civil Engineering, Hydraulics Hydrology Water Resources Program

by
Aslı BOR TÜRKBEN

March, 2015
İZMİR

Ph.D. THESİS EXAMINATION RESULT FORM

We have read the thesis entitled **"EXPERIMENTAL AND NUMERICAL STUDY OF LOCAL SCOUR AROUND BRIDGE PIERS WITH DIFFERENT CROSS SECTIONS CAUSED BY FLOOD HYDROGRAPH SUCCEEDING STEADY FLOW"** completed by **ASLI BOR TÜRKBEN** under supervision of **PROF. DR. MEHMET ŞÜKRÜ GÜNEY** and we certify that in our opinion it is fully adequate, in scope and in quality, as a thesis for the degree of Doctor of Philosophy.

Prof. Dr. Mehmet Şükrü GÜNEY

Supervisor

Prof. Dr. Gökmen TAYFUR	Prof. Dr. Davut ÖZDAĞLAR
Thesis Committee Member	Thesis Committee Member
Prof. Dr. Yalçın ARISOY	Doç. Dr. Mete KÖKEN
Examining Committee Member	Examining Committee Member

Prof. Dr. Ayşe OKUR

Director

Graduate School of Natural and Applied Sciences

ACKNOWLEDGMENTS

I would like to thank my advisor Prof. Dr. M. Şükrü GÜNEY for making this work possible. I am very grateful for his constant guidance, support and encouragement. I also would like to special thank my committee members Prof Dr. Gökmen TAYFUR and Prof. Dr. Davut ÖZDAĞLAR for their guidance and valuable contributions.

This study would not be possible without the support of The Scientific and Technical Research Council of Turkey TUBİTAK (Project number 109M637). I would also like to thank Prof. Dr. Turhan ACATAY, for his precious advices and suggestions.

I would like to thank my colleagues at Hydraulic Laboratory for their helps. Also I am grateful to our technician İsa ÜSTÜNDAĞ who helped me along the experiments.

I would like to thank Güler POYRAZ for having good times during coffee breaks and also her continuous support. I would like to Mert TÜRKBEN for his help and support.

Special thanks to my sister Gizem BOR who have supplied inestimable and patient support and encouragement. Laboratory experiments were carried out with the prodigious help of her.

Finally, I would like to thank my mother and father for their boundless love and for all they have done for me. Finally, I wish to thank my dearest husband, Levent TÜRKBEN, for his love, encouragement and inspiration. I would like to dedicate this thesis to my family.

ASLI BOR TÜRKBEN

EXPERIMENTAL AND NUMERICAL STUDY OF LOCAL SCOUR AROUND BRIDGE PIERS WITH DIFFERENT CROSS SECTIONS CAUSED BY FLOOD HYDROGRAPH SUCCEEDING STEADY FLOW

ABSTRACT

Design of the bridges by considering structural and hydraulic problems is necessary for their safety. Local scour around bridge piers and foundations, as a result of flood flows, is one of the major causes of their failure.

In this thesis, local scour around bridge piers in both steady and unsteady flow cases were studied under clear water conditions, by using different shaped piers. The main goal of the experiments is to examine the final scour depths, the time dependent scour depths and the geometry of scour holes around five different types of piers under unsteady flow conditions which succeed a steady flow of 5 minutes. The other objective is the comparison of the experimental findings with those available in the relevant literature and also with the results obtained from the numerical simulations in order to make some practical suggestions.

The final and the temporal evaluations of the scour depths were measured for circular, square, rectangular, rectangular with circular nose and rectangular with trapezoidal nose piers. The scour hole lengths, widths and areas were recorded by means of two cameras. The equilibrium scour depths were determined after translating the time varied scour depth curves to analytical expressions. Regression analyses were performed in order to derive empirical relations about temporal variation of the scour depths for both steady and unsteady cases. The shape factor values were investigated based on the experimental findings and the obtained values were compared with those obtained previously by different researchers.

The numerical solution was realized by using the software ANSYS FLUENT with RNG k-ε turbulence model for circular and square piers. The numerical and experimental values are compared and interpreted.

The high values of determination coefficients revealed that the suggested empirical relations are significant statically. An acceptable accordance was observed between numerical and experimental results.

Keywords: Pier scour, unsteady flows**,** local scour, ANSYS FLUENT, numerical solution.

KARARLI AKIM İZLEYEN TAŞKIN HİDROGRAFI NEDENİYLE FARKLI ENKESİTLİ KÖPRÜ AYAKLARI ETRAFINDA OLUŞAN YEREL OYULMALARIN DENEYSEL VE SAYISAL ARAŞTIRILMASI

ÖZ

Yapısal ve hidrolik problemleri dikkate almak köprü tasarımının güvenliği için gereklidir. Taşkın akımlarının neden olduğu, köprü ayakları çevresindeki yerel oyulmalar köprü yıkılmalarının en önemli nedenidir.

Bu tez de, köprü ayakları etrafındaki yersel oyulmalar hem kararlı hem de kararsız akım şartları altında ve temiz su oyulması şartlarında farklı tip hidrograflar kullanılarak ölçülmüştür. Bu tezin genel amacı nihai oyulma derinlikleri, zamana göre gelişen oyulma derinlikleri ve oyulma çukurunun boyutlarını beş farklı ayak şekli için ilk 5 dakikası kararlı rejimde olan 5 farklı hidrograf altında ölçmektir. Diğer bir amaç ise, deneysel bulguları mevcut yaklaşımlar çerçevesinde karşılaştırmak ve numerik simülasyonlar gerçekleştirerek bazı Pratik yaklaşımlar sunabilmektir.

Nihai ve zamana göre gelişen oyulma derinlikleri, dairesel, kare, dikdörtgen, dairesel uçlu dikdörtgen ve trapez uçlu dikdörtgen ayak kullanılarak ölçülmüştür. Oyulma genişliği ve oyulma boyu 2 farklı kamera ile kaydedilmiştir. Denge oyulma derinlikleri, zaman göre değişen oyulma derinliği eğrilerinin analitik çözümü sonucu elde edilmiştir. Yeni analitik yaklaşımlar geliştirebilmek için kararlı ve kararsız akım şartları altındaki deney verilerine regresyon analizi yapılmıştır. Deney verileri kullanılarak bu çalışma için şekil katsayıları elde edilmiştir ve literatürdeki diğer araştırmacıların sunduğu katsayılarla karşılaştırılmıştır.

Nümerik çözüm ANSYS FLUENT programı kullanılarak RNG *k-ε* türbülans modeli ile dairesel ve kare ayak için gerçekleştirilmiştir. Nümerik çözümden elde edilen sonuçlar deneysel verilerle karşılaştırılmış ve yorumlanmıştır.

Determinasyon katsayılarının yüksek olduğu ampirik ilişkiler, istatistiksel olarak anlamlı olduğunu ortaya koymuştur.

Anahtar kelimeler: Köprü ayağı oyulması, kararsız akımlar**,** yerel oyulma, ANSYS FLUENT, nümerik çözüm.

CONTENTS

Pages

LIST OF FIGURES

Pages

LIST OF TABLES

Pages

CHAPTER ONE
INTRODUCTION

1.1 General

Bridges are an important part of transportation system which carry people and vehicles across. They are subjected to dynamic loads (wind, earthquake, flood …etc.) more than other transportation structures. Designing of the bridges for both structural and hydraulic considerations is necessary for safety. If not properly designed, constructed and maintained, bridges can be damaged. Statistical studies (Richardson and Davis, 2001) showed that, the most common cause of bridge failures is from floods scouring bed material from around bridge piers (60% of 1000), the others being collision, overloading and deficiencies in the design. Hoffmans and Verheji (1997) have noted that local scour around bridge piers and foundations, as a result of flood flows, is considered to be the major cause of bridge failure. It brings economic problems nationwide and has also caused tragic results.

The study of the Federal Highway Administration (FHWA) for 383 bridges collapsed in 1973 showed that 25% through the pier and 75% through abutment damage. In 1985, 73 bridges were destroyed by floods in Pennsylvania, Virginia, and West Virginia. In 1987, scour was found to be the main cause of the Scholarie Creek Bridge failure in New York in which 10 people were died (Ting et al., 2001; Wardhana and Hadipriono, 2003). Eight people were died in the Hatchie River in Tennessee, as the result of the collapse of the bridge in 1989. Briaud's study in 1999 showed that 60% of failures are due to scour in the USA for the last 30 years. The study in USA shows that 53% of the 503 failure bridge was related to hydraulic factors, only 3% being related to earthquakes. There are many bridge failed due to the floods in Turkey; in 1990 Trabzon, in 1991 Malatya, in 1998 Bartin, in 2001 Hatay, in 2007 Antalya (Alara Bridge), in 2012 Çaycuma and in 2013 Şırnak…etc. The Alara Bridge collapsed because of scouring around the bridge piers. According to the İstanbul Technical University's 2012 Caycuma report, the cause of the collapse of the bridge is scouring around the piers in the middle of the river and so the bridge was not able to carry its own loads.

The relevant studies show that governments spend millions of dollars for scour related to bridge damages. New bridge foundations should be designed to withstand the effects of scour from extreme floods. An accurate estimation of the maximum depth of scour and the local scour hole geometry are essential to a safe and economical design of the bridges. Underestimation of maximum scour depth causes shallow foundation design which is not safe. On the other hand overestimation of maximum scour depth results in deep foundations which are not economical. The existing structures should be inspected periodically following estimation of the scour hole and protective projects for increasing the safety, if necessary.

The main objective of this study is to analyze the scour depth and the geometry the scour hole due to various hydrographs for five different types of piers. The approach is based on the image processing with a video camera during the unsteady conditions. The dimensions of the scour hole were determined by using the experimental values of scour contours. The experimental findings are evaluated by using the empirical expressions available in the literature. Besides, the numerical simulations were conducted to investigate the time dependent dimension of scour hole, the maximum scour depths, the effect of turbulence flow in the scour hole area. The software FLUENT was used to predict the 3D flow patterns around five different types of piers. The experimental findings were compared with those obtained from the ANSYS FLUENT software.

This thesis includes seven chapters.

Chapter 1 contains the Introduction part.

Fundamentals of the phenomenon of scouring and previous relevant experimental and mathematical studies are summarized in Chapter 2.

The experimental setup and details of the experimental procedures were described in Chapter 3. Chapter 4 involves the experimental results. Analysis of the experimental findings is supplied in Chapter 5.

Chapter 6 contains a brief presentation of the package ANSYS FLUENT and the comparison of the experimental results with those obtained from the software package.

Conclusions of the study and the recommendations are given in Chapter 7.

CHAPTER TWO
SCOUR MECHANISM AND LITERATURE REVIEW

2.1 General

The scour mechanism is one of the most favorite environmental topics of the modern world. Many researchers have an interest in the investigation of the scour phenomenon around bridge piers and abutments for about sixty years. There are different approaches to solve engineering problems; however they still need to be developed. In general, there are two types of scour according to the sediment transport mode; clear water scour and live bed scour. When sediment is removed from the scour hole, but not transport on the other parts of the bed by the flow, the clear water scour occurs. In the live bed scour, sediment particles are transported in the other parts of bed by the flow. The basic mechanism creating the scour around a bridge pier has been identified as the system of vortices which develops around the pier. The system of vortices depends on various factors such as properties of flow, the bed material in the stream and pier geometry (Figure 2.1). Because of these vortices, both the flow and the sediment transport processes during the scour hole development are highly complex.

As there are many uncertainties involved in this phenomenon, scour prediction is complex and difficult. However, it is necessary to do so for the protection of bridges and other infrastructure, especially during design planning stages. Scour prediction requires expertise and experience in several fields of engineering, as well as an understanding of the behavior of flowing water and its interactions with structures and soils. In the literature, investigations concerning the local scour estimation are based on dimensional analysis and correlation of small-scale laboratory experiments data because of the complexity of site conditions. The available equations and methods for estimating local scour at bridges are based primarily on laboratory research. These researches are mainly about the maximum depth and the dimensions of the scour hole. Only limited success is achieved by the attempts to model scour computationally. The studies are based mostly on equilibrium conditions under very long flow durations in clear water conditions. The selection of the countermeasure type and the geometry of the scour hole is essential for a safe and economical design of bridges under different flow hydrographs. In fact, the empirical relationships can only predict the scour depths well under similar conditions. Besides, site investigations are needed to increase knowledge of the subject.

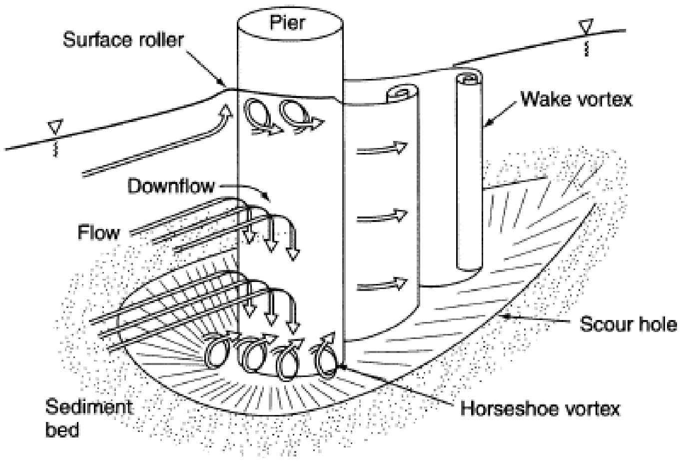

Figure 2.1 Vortex systems around a bridge pier (Raudkivi and Sutherland,1981)

In addition to experiments, numerical methods based on computational fluid dynamics (CFD) were delivered for understanding scour mechanism by researchers. Recent developments in CFD allow numerical simulations of local scour around a bridge pier (Olsen and Melaaen, 1993; Richardson and Panchang, 1998; Wang and Jia, 1999; Li and Lin, 2000; Tseng et al., 2000). Numerical simulations are currently complex because of the turbulence effects in practical engineering problems.

The experimental findings are evaluated by using common statistical methods. Nonlinear Multiple Regression (NLMR) model, used in this thesis, is described as a nonlinear equation. The scour mechanism has nonlinear behavior, so in this thesis NLMR model was selected. Nonlinear Multiple regression equation can be expressed as follows;

$$y = b_0 + b_1 x_1 + b_2 x_2 + b_{11} x_1^2 + b_{22} x_2^2 + ... \tag{2.1}$$

The performance of NLMR model configurations is based on the root mean square error (RMSE), mean absolute error (MAE) and determination coefficient of R^2 of nonlinear regression line between the predicted and observed values. These parameters are expressed as follows;

$$RMSE = \sqrt{\frac{\sum_{i=1}^{n} (X_{obs,i} - X_{model,i})^2}{n}} \tag{2.2}$$

$$MAE = \frac{1}{n}\sum_{i=1}^{n} \left| X_{obs,i} - X_{model,i} \right| \tag{2.3}$$

$$R^2 = 1 - \frac{\sum_{i=1}^{n} \left(X_{obs,i} - X_{model,i} \right)^2}{\sum_{i=1}^{n} \left(X_{obs,i} - \overline{X_{model,i}} \right)^2} \tag{2.4}$$

where;

$X_{obs,i}$ and $X_{model,i}$ = observed and modelled i values (at time t)

$\overline{X}_{model,i}$ = average of model values

n = number of data

2.2 Local Scour Mechanism at Bridge Piers

Local scour defined as sudden removal of the material around the piers, abutments, spurs, and embankments is caused by an acceleration of the flow, the increased velocities and associated vortices around the obstruction. The basic mechanism creating the local scour around a bridge pier has been identified as the system of vortices developed around the pier. The strength and size of the vortex system depend on the properties of flow, sediment type and river bed and pier shapes. The vortices reported by Raudkivi (1991) are separated into components identified as in Figure 2.1; horseshoe vortex, downflow in front of the pier, wake vortex and trailing vortex. It can be seen that the horseshoe vortex results from the piling up of the water on the upstream surface of the pier subsequent the acceleration of the flow around the pier. The horseshoe vortex causes the removal of the bed material from the base of pier and it is more effective once the scour hole occurs. The scour hole develops around the pier because the transport rate of sediment away from the pier region is greater than the transport rate into the pier region. The wake vortices that are generated from flow separation at the sides of the pier are vertical vortices. The wake vortex effects decrease very quickly as going to the downstream of the pier. The wake vortices are weaker than the horseshoe vortex. It means that maximum scour depth occurs at the upstream face of the pier. The bridge pier makes the river bed narrow so average velocity increases. The sediment transport rate increases in this narrow area. The flow velocity decreases suddenly and flow depth increases and there is a stagnation point at the piers upstream face as flow reaches the pier. In that point there is a pressure difference between stagnation point and the upstream. The turbulent boundary layer separates around the pier because of the pressure difference. As the flow velocity decreases gradually from water surface to the bed level, the pressure also decreases. Therefore, downflow occurs from high pressure to low pressure in front of the pier. In fact, both the downflow on the bed and the horseshoe vortex are the principal factors leading to the creation of a scour hole. The trailing vortex occurs only if the pier is completely submerged in water. The trailing vortex has an influence on horseshoe vortex. As long as the flow depth decreases, the trailing vortex effects on horseshoe vortex become weaker and local scour depth is reduced for shallow flow (Yanmaz, 2002).

There are two different scour types whether there is (or isn't) sediment load transport from upstream in alluvial rivers: clear water scour and live bed scour. Maximum scour depth and scour hole diameter depend on conditions of transport varying in time.

2.2.1 Clear Water Scour Mechanism

Clear water scour occurs when the flow conditions do not satisfy or exceed the criteria for incipient motion, and the sediment particles at the upstream of the bridge structure in the alluvial bed do not start to move. It means that the flow inertia is relatively low and, the bed shear stress is smaller than the threshold value defined for the given bed material. However, scour occurs around the bridge structure due to the local acceleration of the flow and continues until the scour hole becomes stable. The typical examples for clear water scour can be regarded as armored streambeds, coarse bed material streams, vegetated channels, in the downstream of a dam due to the impinging effect of the jet or flat gradient streams. In early stages, sediment particles erode rapidly around the bridge foundation, however scour hole development reaches maximum and equilibrium over a longer period of time than live bed scour equilibrium (Figure 2.2). Flow conditions are quieter than live bed scour flow conditions, so the scour depth varies more slowly in time. In equilibrium stage there is no sediment load transport from hole. This situation can be quite dangerous for the structure because flow uses power only scouring in the stream.

2.2.2 Live Bed Water Scour Mechanism

If there is sediment transport in the upstream reach into the bridge section, live bed scour occurs. When flow intensity increases, shear stress in the upstream exceeds the critical shear stress and acts together with vortex in the scour hole. Therefore, the scour hole evolution does not depend only on the flow properties in the scour hole but also on properties in the upstream flow conditions. The scour depth is developed more slowly initially, and then increases rapidly (Yanmaz, 2002). Bed forms cause resistance changes in the upstream, so sediment load in the scour hole depends on shear stress in the upstream. For live bed scour, the scour depth reaches maximum in a short time. Afterwards, according to the changes of shear stress in the upstream bed, the sediment rate increases or decreases. It causes detachment or deposition on the riverbed. When the rate of sediment load becomes stable in the scour hole, the equilibrium conditions are reached. In this case oscillations are not observed. Scour depth observations with mean approach velocity for clear water and live bed conditions are illustrated in Figure 2.2.

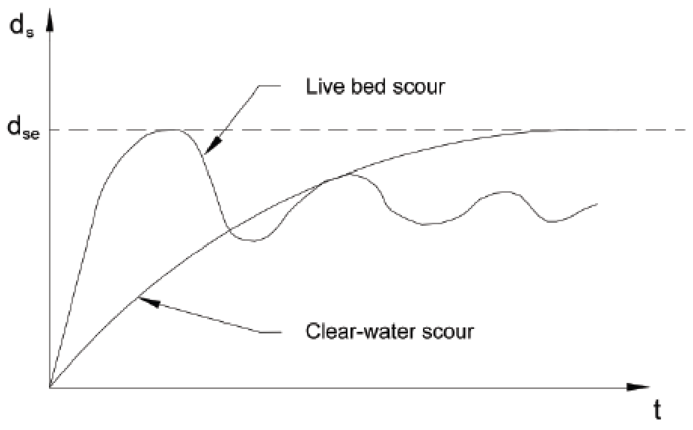

Figure 2.2 Scour depth as a function of time for clear water and live bed conditions (Yanmaz, 2002) (d_s is scour depth and d_{se} is equilibrium scour depth)

2.3 Parameters Affecting the Scour Mechanism

Predicting the maximum scour depth is very important for well constriction of the bridge piers. Although many researchers have been interested in the phenomenon of scour around bridge piers and abutments for about sixty years, a general statement has not been developed yet. The three dimensional turbulent flow, vortices around the piers and the sediment transport processes during the scour hole development are highly complex. The scour depth d_s is influenced by pier width b, the mean approach of velocity u, water and sediment densities ρ, ρ_s, mean approach critical velocity u_c, approach water depth h, kinematic viscosity of water υ, gravitational acceleration g, mean sediment size D_{50}, geometric standard deviation of particle size distribution σ_g, pier shape and alignment of the pier Sh, Al and time t. The dimensionless parameters can be generated using Buckingum's- π theorem and the dimensionless parameters can be written as (Melville and Chiew, 1999);

$$d_s = f_1 \text{ [Flow Parameters } (\rho, \upsilon, u, h, g)\text{, Sediment Parameters } (D_{50}, \sigma_g, \rho_s, u_c)\text{, Pier and Channel Geometry } (b, Sh, Al)\text{, Flow Time } (t)\text{]} \quad (2.1)$$

Many effects of parameters can be negligible for simplicity, both sediment and water density is constant, the absence of the viscous effects and channel has smooth sidewalls, there is no group effect and the effect of Reynolds number is ignored (R_e numbers range from 8900 to 57500). Hence, Eq. 2.1 can be rewritten as;

$$\frac{d_s}{b} = f_2\left(F_r, \frac{u}{u_c}, \frac{h}{b}, \frac{b}{D_{50}}, K_s, \frac{ut}{b}, \sigma_g\right) \tag{2.2}$$

where;

F_d = Froude number

Ettema et al. (1998) suggested that Froude number is not adequately accounted for maximum scour depth formulations unless there was complete geometric similitude of pier, sediment and flow.

If the flow intensity is $1 \geq u/u_c$, it means that the scour is clear water scour, otherwise live bed scour. Scour depth is in minimum value as $u/u_c \approx 1.5 \sim 2.0$ because bed forms are more efficient. As flow velocity increases, the scour depth reaches maximum value again. That mechanism is very complex to explain in experimental conditions. So, most of researchers have used Froude number instead of flow intensity in situations.

In shallow flows, the interference of the surface roller ahead of the bridge with the downflow and horseshoe vortex reduced the scour depth. However as the flow depth increases, that interference decreases, it means that scour depth is independent from the flow depth in intermediate or deep flows.

The effect of sediment coarseness term b/D_{50} can be neglected for $b/D_{50}>50$ because its effect decreases in such situation (Raudkivi, 1986). The local scour pattern depends on the local flow structure as well as the type and properties of the erodible bed. In this thesis, $b/D_{50}>50$ and thus its effects are negligible. However, the effect of b/D_{50} was discussed in the literature (Yanmaz, 2002). Also if the bed material properties do not change, the standard deviation of particle size distribution can be neglected.

Although most of the experimental studies are carried out in equilibrium conditions, many researchers have studied time effect. Equilibrium scour occurs when scour depth does not change with time. As seen in Figure 2.2, the scour depth is developed asymptotically under clear water conditions. On the other hand, under live bed conditions, the equilibrium depth is reached more quickly thereafter the scour depth oscillates due to the passage of the bed material. In fact, it is very difficult to find the most appropriate formula due to the turbulent effects, scale effects, sediment transport mechanism or time variation effects. Besides, experimental studies should be supported by field observations and numerical model simulations.

As can be seen from Figure 2.3, the scour depth development is higher initially. There is no doubt that natural rivers are mostly in non-equilibrium state. Because the real river systems behave as unsteady flow in non-equilibrium state, treating the system with steady flow in equilibrium state is a simplification. Studying steady flow is easier than unsteady flows in governing mathematical models although the real world situation corresponds to the unsteady flow. Such a transformation is possible only if the wave shape does not change as the wave propagates.

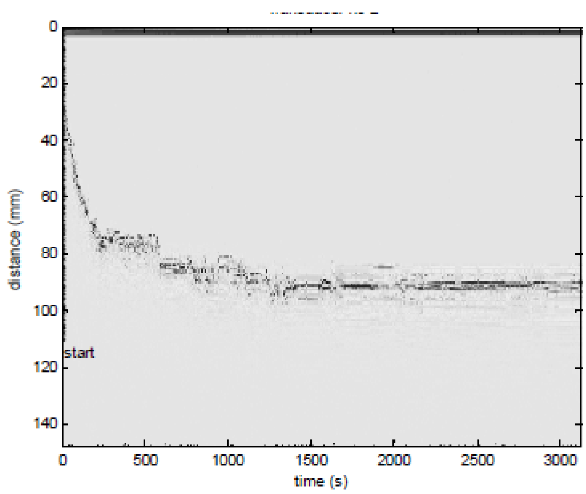

Figure 2.3 Temporal development of clear water scours around a circular pier (Gümgüm, 2012)

There exist a lot of empirical formulas in the literature given for steady and unsteady conditions. Some of them are used to compare the experimental findings of this thesis. These equations are provided in Chapter 5.

2.4 Literature Review

It is known that floods cause disasters and damage throughout the world every year. Hence, the researchers study bridge pier scouring to reduce the damages of the disasters and to maximize the benefits of the water resources structures. The studies of the bridge pier scouring can be performed in three ways; physical studies, field observation and numerical simulations. Physical studies are related to experimental studies to estimate the depth of local scour around bridge piers. Results from the laboratory experiments should be supported by field measurements. However it is very difficult to take real time data in the field and sometimes it is even impossible. Mathematical studies are related to theoretical and numerical methods. Development in CFD enables the hydraulic engineers to study the local scour around the bridge pier based on hydrodynamics principles.

2.4.1 Physical Studies

Physical studies were done by doing experiments in laboratory channels. It is difficult to represent a river by a laboratory channels; so many assumptions are usually incorporated in laboratory studies. The laboratory studies are still important for understanding of basic concepts of river flow and sediment transport for scouring mechanism. Many investigators have developed empirical methods to represent sediment scouring phenomena using data obtained in laboratory. By the laboratory studies maximum scouring depth equations can be improved and scour countermeasures can be developed. In literature, most of the laboratory data are about the scour around cylindrical piers.

One of the first studies in laboratory was performed by Yarnell and Nagler (1931). They wanted the show that the maximum scour depth depends on the shape and the location and the geometry of the pier. They found that the maximum depth of scour occurred at upstream face of the pier for large blunt shaped piers and at the downstream face of the pier for sharp nosed shaped piers.

Chabert and Engeldinger (1956) studied time and velocity effects on clear water and live bed local scouring at bridge piers. They showed that the maximum scour depth oscillated around the average depth.

Laursen (1963) derived the relationship for both clear water and live bed scour as a function of pier geometry, sediment and flow properties. He suggested an equation for the equilibrium depth of scour for pier. The equation based on the limit of clear water scour occurred when the bed shear stress on the approach section was equal to the critical shear stress for initiation of bed motion.

Shen et al. (1966, 1969) studied time dependent variation both in clear water and live bed scouring by using 21 circular diameters. The tests were conducted to show effects of the different pier geometry, sediment and flow properties on the scour time. They allowed scour to occur around a six-inch circular pier for desired depth and measured velocity distributions with a small Pitot tube in uniform bed materials. They found three types of vortex systems as trailing, horseshoe, and wake and explained them in detail. They showed that the geometry of the structure is important in determining the strength of the vortex system. In addition, they developed an empirical equation involving the diameter, averaged velocity and upstream water depth. Cunha (1975) indicated that Shen et al. (1969) study was based on narrow range of flow and sediment conditions, so that study was not suitable for practical applications. The study of Shen et al. (1969) had a single time scale, however scour time histories indicate generally multiple time scales.

Nicollet and Ramette (1971) studied the oscillations of the scour depth. Hancu (1971) conducted a series of scour experiments and developed an equation depending on Froude number for the maximum scour depth in the case of the clear water scour around circular pier.

Breusers et al. (1977) conducted a series of live bed scour experiments with different diameter of pipes. They developed a method depending on the pier size for estimating maximum scour depth as a function of time. They observed that stagnation pressure causes shear layers generated at the surface near the sediment bed. Because of this shear layers the pier becomes unstable and detachment accelerates from both sides of the pier. There were wake vortices behind the pier that are dissipated as they move downstream. The wake vortices are usually recognized from the small scale eddies.

Ettema (1980) performed an experimental study on temporal variation of scour around piers in uniform, non-uniform and layered bed sediments. Raudkivi and Etterna (1983) conducted a serial of experiments around cylindrical piers using non uniform sediments and developed a chart. They analyzed the effect of pier diameters and grain sizes on maximum scour depth. They commented that the local scour pattern depends on the local flow structure as well as the type and properties of the erodible bed.

Günyaktı (1988) derived formulas for determining clear water scour for abutments, circular and non-circular piers by using experimental data. Yanmaz and Altinbilek (1991) derived a semi empirical model using dimensional analysis and they studied the effects of these parameters. They conducted experiments by using cylindrical and square piers in clear water scour conditions with uniform bed material. The model gives time dependent scour variation based on sediment continuity equation around the piers.

Kothyari et al. (1992) derived a model of scour evolution around cylindrical piers in uniform sediment under live bed and unsteady flow conditions. They used 1 m wide rectangular flume and pier diameters between 0.065 and 0.17 m. They conducted both steady and unsteady experiments. Their studies have brought out the effect of flow conditions, pier diameter and its shape, sediment size and its non-uniformity and nature of flow (clear water or live bed) on scour. Kothyari and Ranga Raju (2001) derived a semi empirical formulation using previous data. Kothyari et al.

(2007) performed studies with Oliveto and Hager's model for calculating the equilibrium scour depth.

Chatterjee et al. (1994) measured the time variation of scour depth downstream of an apron due to a submerged jet. Richardson and Davis's (1995) approach known as the California State University Equation (CSU) (or HEC 18) is widely used in USA. Their equation contains all scour parameters for general scour.

Melville (1975) conducted detailed experiments and measured mean flow directions, mean flow magnitude and turbulent flow fluctuations around a circular pile in equilibrium sediment conditions. Melville et al. (1977) presented their results about the flow field, turbulence intensity distributions and boundary shear stresses in the scour zone of a circular pier under clear water conditions. They used a hydrogen bubble technique to trace the flow patterns in the scour hole. They observed that the scour hole was extended when a strong vertical downward flow developed. The horseshoe vortex system due to the downflow increased rapidly and the velocity near the bottom of the hole decreased as the scour hole was aggrandized. Mean bed shear stress was estimated by Newton's equation for viscosity at 2 mm from the bottom. Melville and Raudkivi (1996) made detailed laboratory study of local scour at a non-uniform circular pier (cylinder pier with foundation). They stated that maximum shear stress occurs at the sides of the pier, which also coincides with the location where the scour commences.

Chiew and Melville (1996) and Melville and Chiew (1999) presented many laboratory data that describe the temporal development of the local scour around narrow circular bridge piers of diameter D, under clear water conditions. They developed an equation for equilibrium scour depth. Melville and Chiew (1999) demonstrated also that time scale and maximum scour depth are subjected to similar influences of flow and sediment properties, as might be expected because they are inherently interdependent. They developed an equation for equilibrium scour depth at a bridge pier as a function of time in clear water scour. Their equations can be used for both maximum scour and scour hole estimations.

Totapally et al. (1999) examined the temporal variations of local scour. They used stepped hydrographs and concluded that a logarithmic equation represented the variation of the scour with time.

Graf and Istiarto (2002) investigated the flow patterns at upstream and downstream of the circular pier and measured turbulent Reynolds stresses using an Acoustic Doppler Velocity Profiler (ADVP). They concluded that there was a lot of turbulent kinetic energy in the scour hole as compared to the approach flow but that the turbulent kinetic energy was very strong at the foot of the circular pier on the upstream side.

Ballio and Orsi (2001) studied time variation of the scour depth at bridge abutments. They gave an expression for abutment scour depth as a function of time. Cardoso and Bettess (1999) tested the effect of the abutment length on the temporal variation of the scour depth.

Diab (2011) studied different shape of piers with different angle under steady flow conditions. He obtained predictions of scour depth, scour radius and scour hole volume equations.

Oliveto and Hager (2002) conducted extensive laboratory tests with non-uniform sediments. Coleman et al. (2003) derived an empirical equation for time dependent variation in scour depth around abutments in uniform sediment. Their estimation was based on equilibrium scour parameters. Mia and Nago (2003) derived an equation for temporal variation of scour depth around circular pier based on Yalin's (1977) study.

Dey and Barbhuiya (2005) studied scour depth around short abutments of vertical wall in uniform and non-uniform sediments. Oliveto and Hager (2005) carried out similar experiments in 2005 with cylindrical piers in equilibrium conditions. They extended their scour formula to spur dikes and studied the effect of unsteady flow. Chang et al. (2004) carried out experiments under both steady and unsteady with uniform and non-uniform sediments.

Oliveto and Hager (2005) carried out similar experiments with cylindrical piers in equilibrium conditions. They extended their scour formula to spur dikes and studied the effect of unsteady flow.

Link (2006) conducted experiments for studying time variation of three dimensional scour hole geometry for a circular pier. He measured time dependent scour hole geometry by high resolution non-intrusive method. Alabi (2006) used collars in his experiments for reducing the effects of local scour at bridge piers. His aim was to study the temporal development of the scour for a pier with and without a collar.

Yanmaz (2006) modified his previous study (Yanmaz and Atinbilek (1991)) using a recent sediment pickup function for cylindrical piers. He conducted extensive experiment to investigate time dependent characteristics for scour holes around cylindrical and square piers and vertical wall abutments under clear water conditions with uniform bed materials. He measured temporal variations and scour contours in scour hole. He investigated time dependent characteristics of scour holes around cylindrical and square piers and vertical wall abutments under clear water conditions with uniform bed materials. He measured temporal variations in scour depth and scour contours. He developed semi empirical formulation to calculate the scour hole volume.

Kose (2007) carried out an experimental study to observe temporal variation of scour depth and contours around vertical wall and wing wall abutments. In his study, experiments were stopped at the end of different test durations to determine the contours of scour hole around abutments by using point gages. He developed a semi empirical model for determining time dependent variation of clear scour water depth around vertical wall abutments.

Kothyari et al. (2007) derived a relation for temporal scour evolution of single pier by relating the scour depth to the difference between the actual and the entrainment densimetric particle Froude numbers.

Hager and Unger (2010) developed formula previously proposed by Oliveto and Hager (2002,2005) and generalized temporal sour depth due to a single peaked flood wave. They combined Olivetto and Hager (2002) formulas.

Guney et al. (2011) measured local scour hole contours around bridge piers under unsteady flow conditions. Ultrasonic Velocity Profiler (UVP) was used to measure temporal variation of scour depth indirectly.

Lu et al. (2011) studied the temporal development of scour depth around cylindrical piers with unexposed foundations. They proposed a semi empirical model and also tested against experimental data.

Elsebaie (2013) studied the maximum scour depth and its pattern along longitudinal as well as in transverse directions. He realized a much longer duration of tests. He found that the maximum scour depth was depending both on time and flow rate.

Lanca et al. (2013) conducted experiments for long duration clear water scour to investigate the effect of sediment coarseness. Experiments were carried out for the flow intensity close to the threshold condition of initiation of sediment motion. They characterized the scour depth with time evolution.

Lopez et al. (2014) studied experimentally the final scour depth around cylindrical piers under flood waves. An approach to estimate the final scour depth under a flood wave is proposed, based on the local scour depth calculated with steady flow equations under peak flow conditions. Also, they tested performance of existing expressions with new experimental data.

Experimental studies have the limitations due to the complexity of representing a real life river conditions. However, it helps us to understand basic concepts of river flow and it provides a detailed analysis for parameters related to physics of the problem. Laboratory studies should be supported by numerical models because of the scale effects.

2.4.2 Field Observations

The geomorphologic data of river can be obtained by a topographic survey, including a land survey and underwater surveying, or by repetitive surveying on pre-determined ranges. Also, surveying of rivers are required to determine sedimentation rates and to assess detachment and scouring of the bed. For surveying, manual sounding poles, sounding weights and echo sounders are commonly used. For reasons of economy, accuracy and expediency, sedimentation surveys were carried out in cross small river reaches. More advanced instruments have been adopted as electronic distance measuring systems for large rivers. Sedimentation surveys are best reliable for the accurate positioning of measuring points where no deposition or erosion takes place, the elevation of the bed surface should coincide with that measured in a previous survey (Bor et al, 2008). This is a good check of the accuracy and reliability of the sedimentation surveys. In addition to this detailed bathymetry map, thickness and long-term average accumulation rates of the lake or river can be determined by using echo sounder systems (Odhiambo and Boss 2004). Other studies in literature about surveying using acoustic methods include the technical details of scanning (Urick 1983), techniques used for sediment mapping (Higginbottom et al. 1995), and the comparison of different echoes on sediment type (Collins and Gregory 1996). Also, in hydrometric stations for sediment measurement, suspended sediment discharge and sediment concentration, size gradation of suspended sediment and bed material or scouring bridges can be measured the whole year around.

The Federal Highway Administration (FHWA) in the United States and the U.S, Geological Survey (USGS) initiated a co-operative National Scour Study in 1987 to collect field measurements of bridge scour at bridge sites throughout the U.S. This program generated a U.S. national bridge scour database of 470 field measurements of local scour depth at bridge piers. The data were selected carefully and doubtful measurements were omitted (Melville and Coleman, 2002).

Coleman and Melville (2001) presented evaluation on failure of three bridges in New Zeeland. Gao et al. (1993) developed an equation from Chinese data of local scour at bridge piers, including 212 live-bed data and 40 clear water data. The equation was tested using field data given by Froehlich (1989) and 184 filed data from U.S.S.R.

Ansari and Qadar (1994) derived equations fitting more than 100 field measurements of pier scour depth including 40 measurements from India. Also, they compared the field data with Neill (1973), Melville and Sutherland (1988) equations for scour depth calculations.

Ghorbani (2008) studied the hydraulic effects of flow depth and velocity, sediment characteristics such as specific gravity, internal friction angle, particle size, and particle size distribution and bridge pier geometry on scouring. He collected field data of 6 bridges and 3 rivers in Fars Province, Iran. He used the statistical and physic mathematical methods analyzing the data to provide a very rough estimate of risk.

Gulbahar (2009) used the field data of the Gediz Bridge, Manisa Turkey. His research was about understanding the performance of several pier scour equations. Theoretical pier scour was calculated using several equations with field data and solutions were compared.

Khassaf and Shakir (2013) used Hydrologic Engineering Center River Analysis System (HEC-RAS) program to evaluate local scour around group piers of Babil Bridge in the middle of Iraq. Also the solutions were compared with the observed field data. The local scour depth at group piers of Babil Bridge was calculated and they found that the piers of the bridge were safe against scouring in the present time, because the depth of the maximum local scour was less than the depth of foundation of the bridge. The field work consisted of collecting bed material samples and geometric data.

Beg (2013) tested fourteen commonly used and cited bridge pier scour predictors against published laboratory and field data obtained from literature experimental data in order to ascertain which of the predictors produce a reasonable estimate of the bridge pier local scour depth. The study showed that the predictors of Laursen and Toch and Jain & Fischer were good estimators.

Collecting field real time observations can explain the real life systems better than flume experiments but it is very difficult to collect real time data in the field even sometimes it is impossible.

2.4.3 Numerical Simulations

Sedimentation is the consequence of a complex natural process involving soil detachment, entrainment, transport and deposition. Not only three dimensional flow and sediment transport equations are nonlinear but also unknowns are more than equations available. It causes closure problem needed in turbulence modeling. On the other hand, developing the solution is very hard for generalized three dimensional cases with unsteady and non-uniform conditions both for sediment and fluid flow. In recent years, CFD has been widely used by researchers.

Olsen and Melaaen (1993) and Olsen and Kjellesvig (1998) predicted local scour simulating three dimensional flow and sediment transport model. They solved Reynolds Averaged Navier-Stokes (RANS) equations with the k-ε model for turbulence closure using the finite volume method (FVM). Also they tested results with experimental data which revealed to be close to each other's. They ignored the transient terms in RANS equations in the simulations, so the calculated flow field did not capture the complexities observed in experimental flow field around a model pier. The flow assumed steady and the transient terms were omitted. The fluctuations at downstream were therefore not reproduced, and thus, the erosion downstream of the pier may not be modeled correctly. Moreover, they solved the bed sediment conservation equation by iterating the procedure until the scour hole at an equilibrium state was obtained for both suspended and bed load.

Olsen (2003) simulated water and sediment flows with SSIIM model (Sediment Simulation In Intakes with Multiblock). The SSIIM model is numerical software to simulate sediment and flow equations. The ability of the SSIIM model is to analyze complex geometries of the river beds. SSIIM model solves three dimensional Navier Stokes differential equations based on Unsteady Reynolds Average Navier-Stokes (URANS) equations with k-ε model. Esmaeili (2009) employed the SSIIM model to calculate maximum scour depth using flow hydrograph. Nekoufar and Kouhpari (2013) modeled upstream of the cylindrical pier using software SSIIM. They expressed the pier as non-submerged plate's perpendicular to the water flow.

Salaheldin (2004) used three dimensional numerical model FLUENT to simulate the separated turbulent flow around vertical circular piers in clear water. The studies were performed by using different turbulence models. The results were compared with several sets of experimental data. The Reynolds stress model performed quite well in simulating velocity distribution on flat bed and scour hole as well as shear stress distribution on flat bed around circular piers.

Nagata et al. (2005) conducted the local scouring simulation applying three dimensional RANS model. They used a nonlinear k-ε model including quadratic terms. The sediment transport and flow momentum equations of k and ε were discretized by the finite-volume method. They solved both velocity and pressure terms with the highly simplified mark and cell HSMAC method (Hirt and Cook 1972) and compared with the mark and cell (MAC) method (Harlow and Welch 1965).

Liu and García (2008) developed model called FOAMSCOUR which can simulate three dimension local scour around bridge piers. FOAMSCOUR model solves the URANS equations with k-ε closure using Volume of Fluid (VOF) method. Indeed, while the model solves the flow equations in three dimensional, the sediment equations are solved in two dimensions.

Constantinescu and Squires (2004) and Kirkil et al. (2009) gave brief information about DES code in their study in 2004. Constantinescu and Squires (2004) developed DES model by using an unsteady fully developed inlet boundary condition. The unsteady conditions were obtained by a separate precursor simulation. Kirkil et al. (2009) studied with the large scale eddies around a circular pier with an equilibrium scour hole using Detached Eddy Simulation (DES) model.

Köken and Göğüş (2010) investigated effect of abutment length on the bed shear stress and the horseshoe vortex system, by using DES model. Köken and Constantinescu (2011) studied the flow and turbulence feature in a scour hole around spike dikes and discussed the scour hole development mechanism.

Many researchers have studied bridge scouring mechanism developing two phase model techniques. The interactions of fluid – particle or particle – particle can be set by Eulerian and Lagrangian frames. The set of Eulerian-Eulerian frame was introduced by Zhao and Fernando, 2007; Liu and Shen, 2010; Azhari et al., 2010; Yeganeh-Bakhtiary et al., 2011 to examine erosion of the sedimentation. Lagrangian frame was proposed by Pasiok and Stilger-Szydlo, 2010; Escauriaza and Sotiropoulos (2011b) for sediment transportation. Pasiok and Stilger-Szydlo (2010) developed Large Eddy Simulation (LES) model using Open FOAM CFD toolbox and FVM discretization. They investigated turbulence flow around bridge piers and studied scouring around piers. Escauriaza and Sotiropoulos (2011b) developed DES model with Lagrangian frame and FVM discretization. Recent studies show that CFD models can be developed for sediment bed load and suspended load in unsteady and non-equilibrium conditions.

Asano (1990) studied a partial two phase flow model. He examined the vertical velocity of particles both by empirical formulations and equations. The solutions of the empirical equations gave more accurate solutions than governing equations. His study was extended to formulate a complete set of two-phase flow equations by Li and Sawamoto (1995). Ali et al. (1997) showed that the renormalization group (RNG) k-ε model gives a good estimation of the velocity field and bed shear stress.

Dou (1997), Jia et al. (2001) and Wu and Wang (1999) analyzed the mechanism of local scour at bridge piers using a numerical model in three dimensional flow conditions. They used empirical formulations for calibrating sediment transport within the scour hole. Wang and Jia (1999) simulated the evolution of the scour hole around the bridge pier by using CCHE3D. The comparisons were quite compatible.

Chang et al. (1999) used a Large Eddy simulation (LES) model to solve the flow equations around a bridge pier with a fixed bed and no scour. They used Van Rijn (1984) bed load formula to calculate the sediment transport. The results were tested against the time series data of Ettema (1980). The scour hole development with time results were adjusted with experimental data.

Richardson et al. (1998) researched the scouring around piers and simulated equations using FLOW3D package program with the RNG k-ε model. The scouring phenomenon was simulated by solving the 3D Navier-Stokes equations. Without modeling sediment transport, they estimated the depth of equilibrium scour simply by means of the Lagrangian particle-tracking analysis. They compared the results with experimental data and comparisons were good.

Karim and Ali (2000) developed a model using FLUENT based on conditions presented by Ali and Lim (1986) and Wu and Rajaratnam (1995). They compared the results with the investigators previously mentioned. The bottom shear stress results were adjusted by experimental data. In 2002, Ali and Karim (2002) used FLUENT to predict the three dimensional flow field around a circular pier for rigid beds. They also predicted bed shear stress. They performed various simulations with different time steps. They compared the results with Yanmaz and Altinbilek (1991)'s experimental data. There was satisfactory agreement between the bed shear stresses predicted by FLUENT and those calculated from the experimental velocities near the bed due to the solutions that reported at a distance of 8 mm above the bed by Yanmaz and Altınbilek (1991).

Sümer et al. (2003) studied three dimensional flow around piers using a finite volume hydrodynamic module with k-ε turbulence model. They showed that the movement of sediment particles under the influence of forces entraining the particles is more than the average amount. They also studied the effects of turbulence intensity on the fluctuations of bed shear stress as well as movement of sediment material.

Salaheldin et al. (2004) used three dimensional numerical model FLUENT to simulate the separated turbulent flow around vertical circular piers in clear water. The study was performed by using different turbulence models. The results were compared with several sets of experimental data. The Reynolds stress model performed quite well in simulating velocity distribution on flat bed and scour hole as well as shear stress distribution on flat bed around circular piers.

Yüksel (2007) determined the submerged circular jet velocity distribution around a cylindrical pile experimentally and numerically in her thesis. Acoustic Doppler Velocimeter (ADV) was used to determine the velocity distributions for different jet cases. In the numerical solution, Yüksel (2007) used FLUENT with RNG $k - \varepsilon$ turbulence model and turbulence intensity was taken I=%10. It was found that there is a good agreement between the experimental results and the literature. The numerical results were used to obtain the variation of bed shear stress around the pile at the rigid bottom and the scour hole.

Zhao and Fernando (2007) performed CFD simulation using FLUENT to evaluate the scour around pipes using Eulerian-Eulerian coupled two phase model for fluid and solid phases. They investigated the effect of different sediment transport modes on the development of scour.

Huang et al. (2008) simulated three dimensional scour model using FLUENT. They presented scale effects on turbulent flow and sediment scour. Their study was based on the Froude similarity law for the large scale model. Effects of scale on turbulence flow and sediment scour were investigated by comparing different results obtained from a full scale numerical model to those derived from the Froude similarity method.

Many researchers have studied bridge scouring mechanism developing two phase model techniques. The study with Eulerian model was introduced by Zhao and Fernando, 2007; Liu and Shen, 2010; Azhari et al., 2010; Yeganeh-Bakhtiary et al., 2011 to examine erosion of the sedimentation.

Kayser and Gabr (2013) developed a numerical model for North Carolina Outer Banks site damaged by Hurricane Irene in 2011 by fluid dynamics (CFD) software, FLOW-3D. The model is used to assess the scour depth at a bridge pier and the results are compared against values that are based on ISEEP. They obtained that the scour depths estimated using ISEEP parameters agree relatively well with values obtained from the 3D numerical analyses.

CHAPTER THREE
EXPERIMENTAL SET UP, INSTRUMENTATION AND PROCEDURE

3.1 Aim of the Experiments

The transport of bed material under steady and unsteady flow conditions was previously investigated in Hydraulics Laboratory of Civil Engineering Department of Dokuz Eylül University. For this purpose, the experiments were supported by TÜBİTAK via the project no: 106M274 (Final Report, 2009). The experiments were carried out in the rectangular flume 18.6 m long, 0.80 m wide and 0.75 m deep. The slope can be adjusted in horizontal (Figure 3.1). In 2009, a series of local scour around bridge pier experiments were started in the scope of the project TÜBİTAK 109M637 (Final Report, 2012). Local scour around bridge piers in both steady and unsteady flow conditions were measured by using plexiglass pier models with different sizes and different shapes.

The main goal of this thesis experiments is to examine the final scour depth, the time dependent scour depth and the geometry of scour hole around five different types of piers under unsteady flow conditions which maintained a steady flow of 5 minutes. The other objective is the comparison of the experimental findings with those available in the relevant literature and with the results obtained from the numerical simulations in order to make some practical suggestions.

3.2 Experiment Setup

The scheme of the experimental system is shown in Figure 3.2. The rectangular flume has transparent side walls made from plexiglass. Water is pumped from main tank having a volume of 27 m^3. The flume has a platform which is 1 m wide and 1.8 m height with ladder. The main tank and rectangular basin are at the downstream end of the flume. The water levels can be adjusted by tail gate shown in Figure 3.3. The first three meters of the flume is a rigid part of 26 cm height. The test section is between 11 m and 12 m in the flume. Drive Link-C software is used to control pump which has a maximum capacity of 100 l/s and generating hydrographs by increasing and decreasing the pump speed (Figure 3.4). The pump has 18.5 kW power and 1450 rpm rotational speed.

Figure 3.1 General view of the experimental setup. a) From the upstream end b) From the downstream end

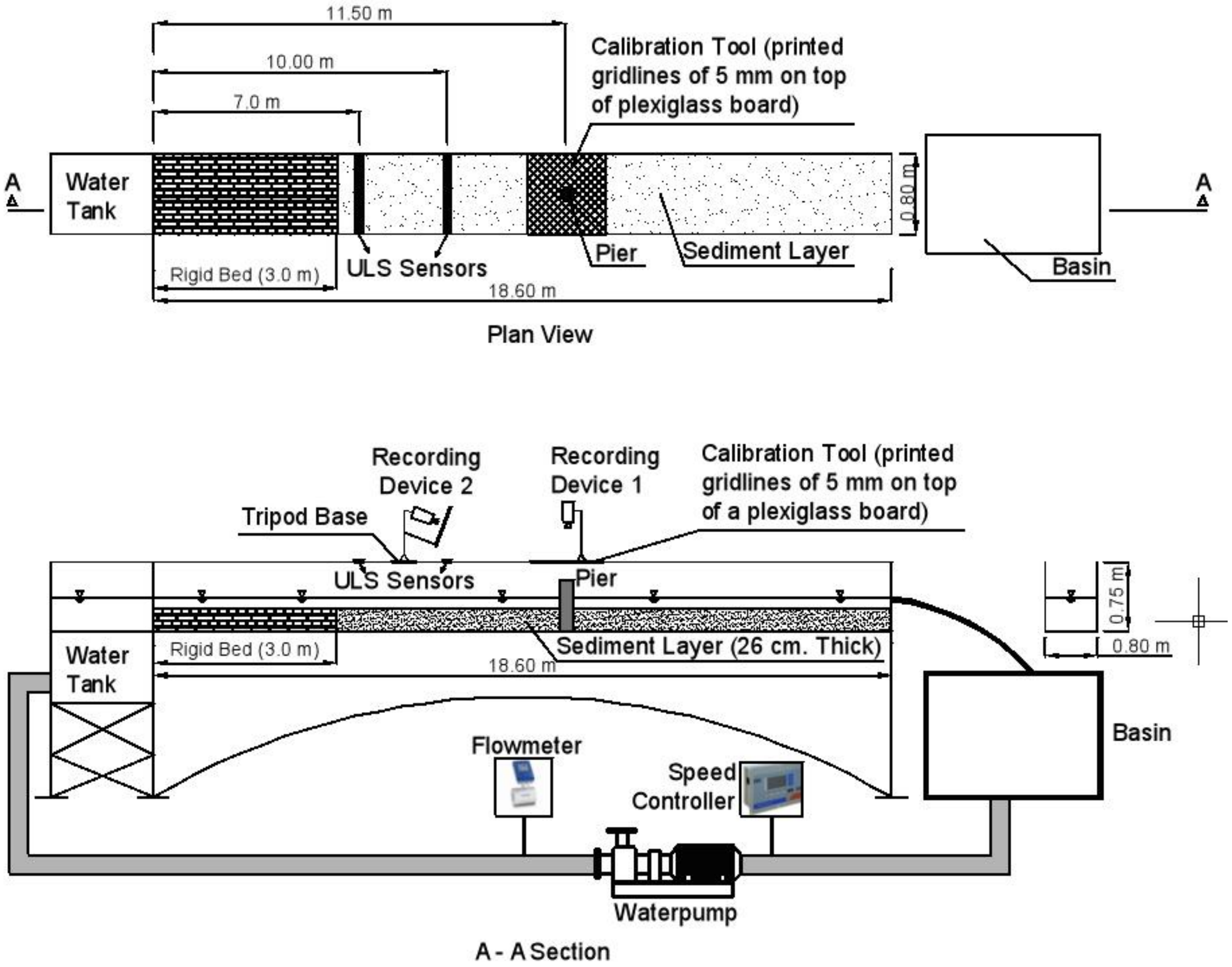

Figure 3.2 Scheme of the experimental system

Figure 3.3 a) Adjustable tail gate b) Adjustable downstream support of the flume

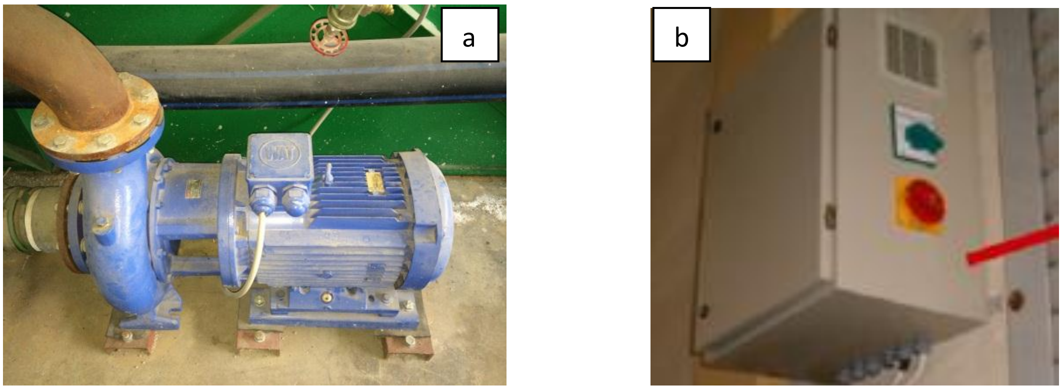

Figure 3.4 a) Pump b) Pump rotational speed control unit

3.2.1 Bed Material Characteristics

The uniform graded material with $D_{50}=1.68$ mm was used. The geometric standard deviation was $\sigma_g=1.83$ which implies that the sediment can be assumed as uniform and its specific gravity was 2.65. The bed material is shown in Figure 3.5a.

Sieve analysis was performed with 4 different samples and grain distribution was obtained as given Table 3.1. The samples were taken from the different locations of the flume. The grain distribution curve is given in Figure 3.5b.

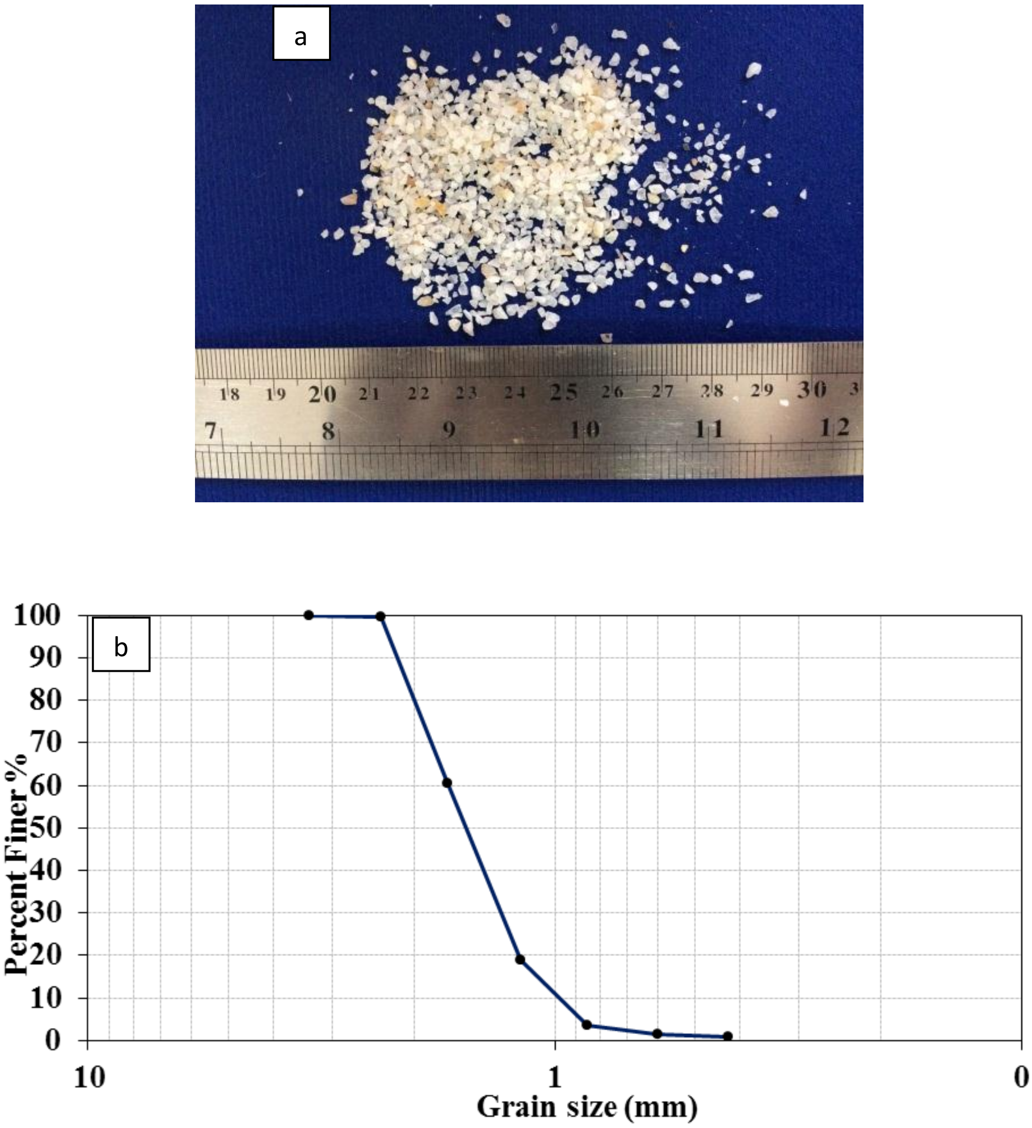

Figure 3.5 a) Sediment sample used in this study b) The grain distribution curve

Table 3.1 Summary of the sieve analysis

Grain size (mm)	**Sample 1**	**Sample 2**	**Sample 3**	**Sample 4**	**Mean**
3.35	0.27	0.28	0.04	0.44	0.26
2.36	2.16	2.62	1.39	1.97	2.04
1.7	277.62	338.81	175.16	707.55	374.79
1.18	293.67	381.62	201.50	627.43	376.06
0.85	109.98	145.67	81.43	211.90	137.25
0.6	14.05	27.77	10.37	37.93	22.53
0.425	4.37	12.89	2.45	16.11	8.96
sieve under	5.92	9.02	4.81	9.92	7.42
D_{50}	1.69	1.66	1.67	1.71	1.68
D_{95}	2.27	2.32	2.40	2.41	2.35
$D_{84.1}$	2.17	2.15	2.19	2.21	2.18
$D_{15.9}$	1.20	1.12	1.21	1.24	1.19
σ_g	1.34	1.39	1.35	1.34	1.35

3.2.2 Pier Types

Circular, square, rectangular, rectangular width circular nose and rectangular width trapezoidal nose piers were used in the experiments. The pier sizes and geometry were chosen for easy comparison. The piers are made of plexiglass and fixed to the sediment layer. Pier shapes and their dimensions are given in Figure 3.6.

3.2.3 Instrumentation

3.2.3.1 Visualization of Scouring

The development of the scour hole was recorded by two video cameras, one located between 11 m and 12 m of the flume and the other was located at 10 m of the flume with an angle of 45°in order to obtain the plan view of the scour hole. The first camera was mounted 41.5 cm above 80×100 cm plexiglass plate on which 5.0×5.0 mm squares were drawn just like milimetric paper. This plate was 54 cm far from the bed. The second camera was mounted 27 cm above 210×297 cm plexiglass plate with meshes of 5.0×5.0 mm. This plate was 120 cm far from the piers. The records were analyzed by processing the images and the time dependent scour depth and scour hole area were determined. The details of this procedure are given in Figure 3.7.

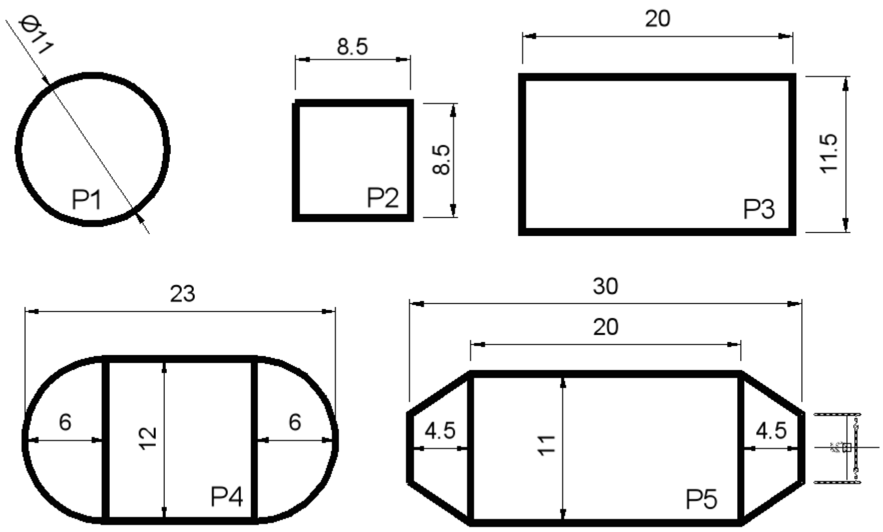

Figure 3.6 Pier types for Testing (all dimensions are in cm)

Figure 3.7 Picture illustrating the measurement equipment and sketch related to the measurement procedure by using two cameras

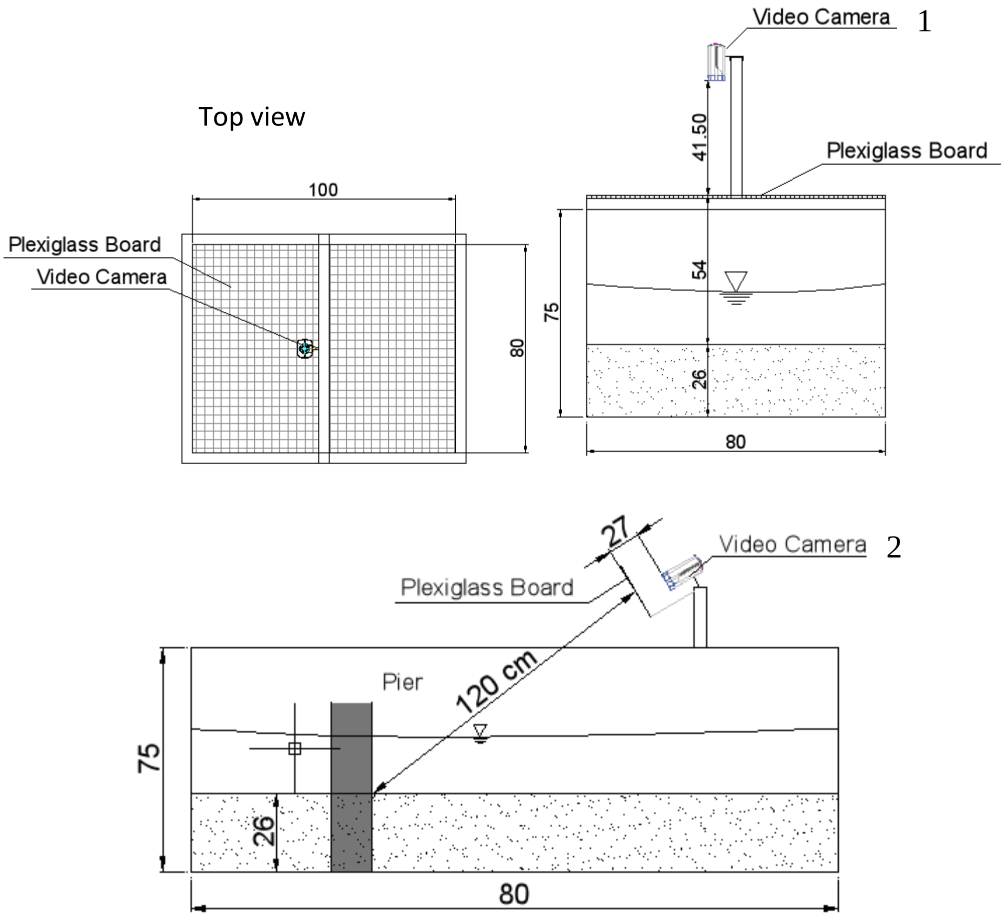

Figure 3.7 Picture illustrating the measurement equipment and sketch related to the measurement procedure by using two cameras (continued)

3.2.3.2 Measurement of the Flow Rate

The discharge was determined by OPTIFLUX 1000 (manufactured by Krohne) that is an electromagnetic flow sensor (Figure 3.8). It works according to Faraday Law and it was mounted on the pipe and before the upstream of the flume. It gives good results with a precision of 0.01 l/s. It can be combined with a data recorder allowing a convenient usage.

Figure 3.8 Flow meter

3.2.3.3 Measurement of the Flow Depths

ULS (Ultrasonic Level Sensor) shown in Figure 3.9 was used to measure the flow depth. Two different sensors were used in this thesis. First sensor was located in 7 m of the flume and second sensor was located in 10 m from the upstream end of the flume (shown in Figure 3.1). Degree of precision of the ULS is $\pm 0.1mm$.

Figure 3.9 Ultrasonic Level Sensor ULS

3.3 Experimental Procedure

In this thesis, 25 experiments were conducted with five different types of piers. All experiments were performed in clear water conditions. Five types of hydrographs were generated by the adjustment of the pump rotational speed. During the first 5 minutes of the experiments the discharge $Q_{st}(L/s)$ was keep constant and then it was increased to $Q_p(L/s)$ peak values under unsteady condition.

Table 3.2 shows the parameters of the triangular hydrographs where $h_{st}(cm)$ is the water depth for steady condition and $h_p(cm)$ is the water depth for peak conditions. Also $t_{st}(min)$ means time at the end of the steady conditions, $t_p(min)$ means peak time and $t_{end}(min)$ means total time of the hydrograph. The hydrographs are shown in Figure 3.10. Discharge values were recorded during the experiments. Flow depths were measured by ULS at 7 m and 10 m of the flume.

Table 3.2 Parameters of the Hydrographs

Hid No	Q_{st} (lt/s)	Q_p (lt/s)	h_{st} (cm)	h_p (cm)	t_{st} (min)	t_p (min)	t_{end} (min)
Hid 1	8	45	6	20.39	5	5	15
Hid 2	8	63	6	22.61	5	5	15
Hid 3	8	73	6	23.52	5	5	15
Hid 4	8	63	6	22.61	5	10	25
Hid 5	8	63	6	22.61	5	20	45

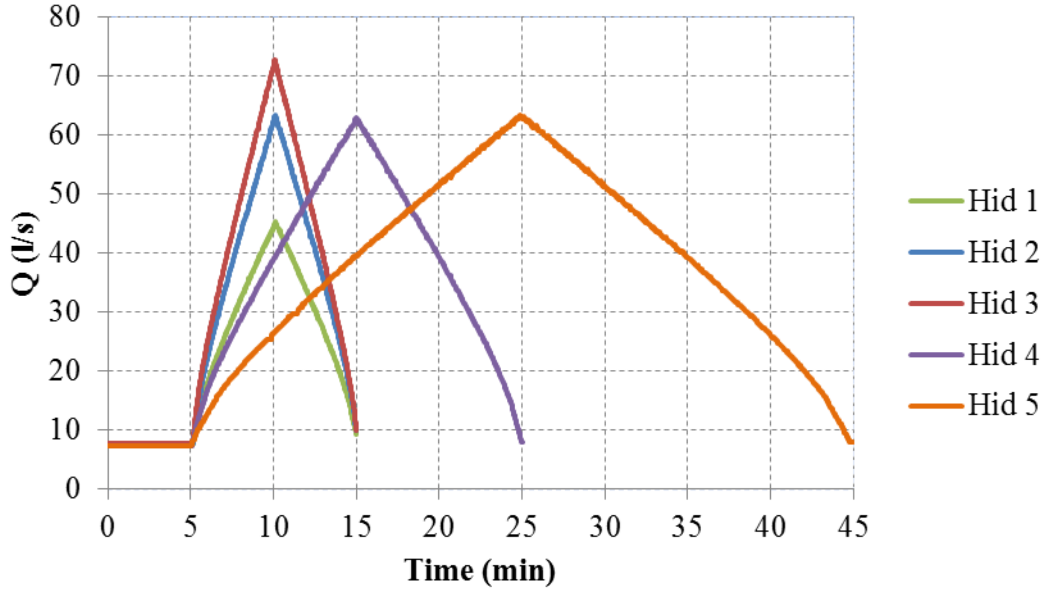

Figure 3.10 Hydrographs used in the study

3.3.1 Scour Depth Measurements

Temporal variations of scour depth at the upstream face of the piers, maximum scour depths at the downstream face and at the lateral face of the piers were examined. It was observed that, while maximum scour depths occurred at the upstream face of the piers for rounded piers, maximum scour depths occurred at the upstream corners for squared piers. Measurement points are shown in Figure 3.11. Summary of the experiments are presented in the Chapter 4 where $d_{s1}(cm)$ (Point A) is scour depth at the upstream face of the pier, $d_{s2}(cm)$ (Point B) is maximum scour depth at the lateral face of the pier, $d_{s3}(cm)$ (Point C) is maximum scour depth at the downstream face of the pier. The sediment bed was flattened before each experiment test and water is supplied gently withouth causing any disturbance to the bed material. Before the tests, bed levels were determined and scour depths d_s were specified according to these measured values. During the experiments, the cameras recorded the bed elevations allowing the determination of the scour depth at point A and a configuration of the scour hole. After the experiments, water was removed gently, the bed topology was measured with laser meter and illustrated in Golden software Surfer programme. In Point B and Point C, maximum scour depths were measured by laser meter.

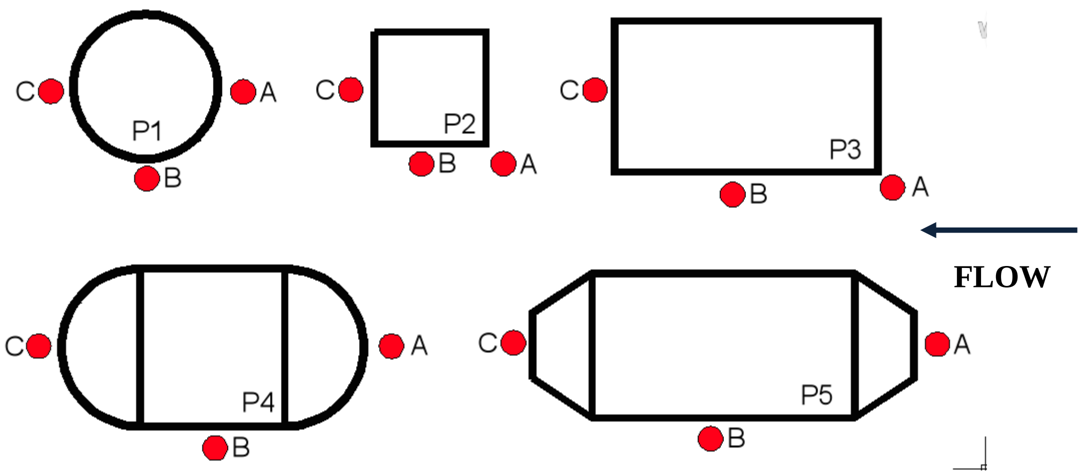

Figure 3.11 Location of the measurement points

3.3.2 Scour Contour Measurements

Length and width of the scour holes were measured in the course of experiments. The flume bed was flattened at the beginning of each test run. As mentioned before, measurements were performed with two methods, with a laser meter and with a video camera. Laser meter is used only at the end of each hydrograph when the water was removed from the flume. At the end of the tests, water was removed gently from the flume and the bed topography was not disturbed. A grid system (1.0×1.0 cm square) was built around the pier and the scour hole contours were identified by surveying with laser meter and results were plotted as contour lines of scour holes with the Golden software Surfer programme and converted to Autocad drawings.

During hydrographs, a video camera is used to determine scour area at different time steps. The camera records were analyzed by processing the images and all were converted to Autocad drawings. Many difficulties were encountered during the measurements. While water was rising during the hydrograph, the images of scour holes became overestimated due to optical diffraction. At each time step, water level above the layer of sediment was different. Therefore, a calibration was required in order to correctly determine the scour area. To do so, a centimeter grid was printed on a transparent plexiglass. In Autocad, scour hole dimensions were plotted for corresponding times. That scale ratio which was used for the calibration was used for each time step of the related experience. Also, final state processed images were compared with Surfer topology maps. An acceptable accordance was observed. The overlapping state of measured and image drawings are detailed in Chapter 4.

To overcome some visual observational difficulties, the measurements were repeated until appropriate measurements were obtained.

3.3.3 Determination of the Calibration Curve

A ruler was placed in the flume bottom. When there is no water in the flume, A length of 1 cm on the millimeter plate corresponds to a length of 1 cm on the ruler.

The calibration curve was generated by reading ruler measurements while the flow depth was rising in the flume. Table 3.3 shows the first camera calibration parameters. The ruler and milimetric plate values were same up to water level of 12 cm in the flume. When the peak flow depth was reached the difference was only 1 mm. If the water level is too high, large errors in the measurement camera is likely high. Figure 3.12 and Table 3.4 show the second camera values. These values are used to derive analytical expressions.

Table 3.3 Calibration parameters of Camera 1

water depth h (cm)	**read value d_{read} (cm)**	**real value d_{real} (cm)**	**$c=d_{read}/d_{real}$**
2	1	1	1
4	1	1	1
6	1	1	1
8	1	1	1
10	1	1	1
12	1	1	1
14	1.1	1	1.1
16	1.1	1	1.1
18	1.1	1	1.1
20	1.1	1	1.1
22	1.1	1	1.1
24	1.1	1	1.1

Table 3.4 Calibration parameters of Video Camera 2

water depth h (cm)	read value d_{read} (cm)	real value d_{real} (cm)	$c=d_{read}/d_{real}$
2	1	3.8	0.26
4	1	4	0.25
6	1	4	0.25
8	1	4.2	0.24
10	1	4.3	0.23
12	1	4.5	0.22
14	1	4.6	0.22
16	1	4.7	0.21
18	1	4.8	0.21
20	1	4.9	0.20
22	1	5	0.20
24	1	5.1	0.20

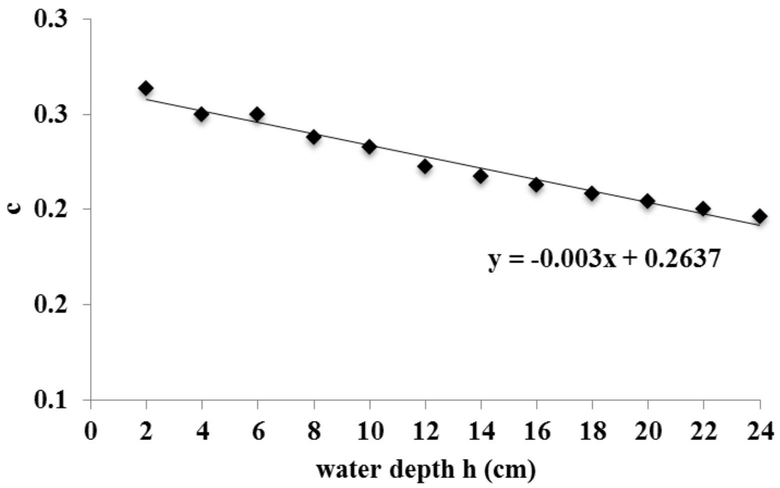

Figure 3.12 Analytical expression for Video Camera 2

CHAPTER FOUR
EXPERIMENTAL FINDINGS

4.1 Flow Parameters

In this chapter, the results obtained from the experiments are presented. 25 experiments were carried out with five different types of piers. All the pier shapes are presented separately. The rating curve which describes the water depth *h (cm)* versus flow rate *Q (L/s)* is given in Figure 4.1.

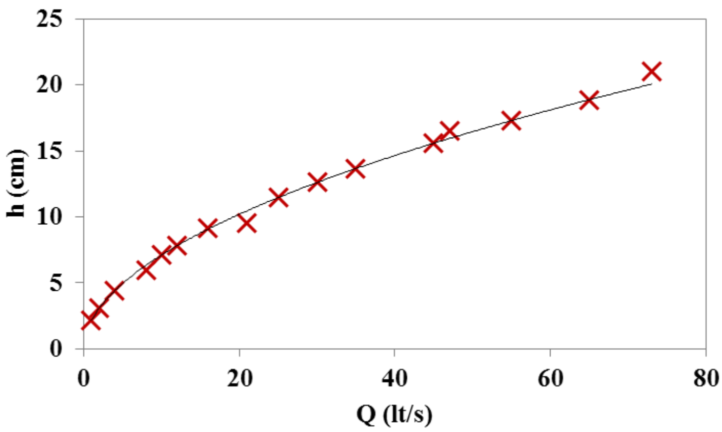

Figure 4.1 Rating curve of the flume

The characteristics of the hydrographs used in this study are given in Table 3.2. The hydrographs given in Figure 3.10 are represented in Figure 4.2 together with corresponding flow depth.

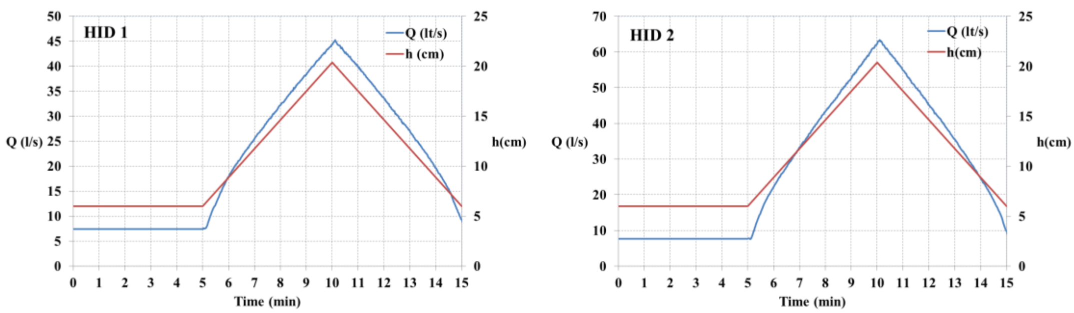

Figure 4.2 Hydrographs and corresponding water depths

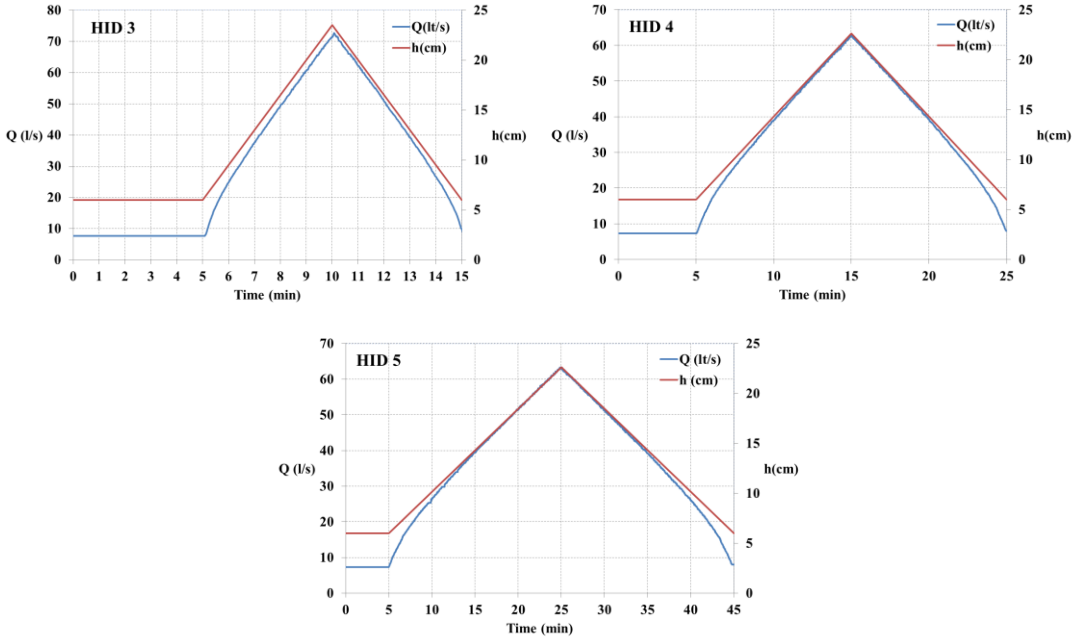

Figure 4.2 Hydrographs and corresponding water depths (continued)

In all hydrographs first 5 min duration corresponds to steady conditions. The base flow rate is 8 L/s and calculated flow parameters are h/b= 0.55, u/u_c =0.35, F_r =0.22 and $F_{d=}$ 1.03.

The flow parameters related to unsteady conditions are given in Tables 4.1, 4.3, 4.5, 4.7 and 4.9. Where; *b(cm)*= the pier diameter for circular piers or the pier width for other piers, I= u/u_c (flow intensity).

The mean critical velocities u_c are calculated using the logarithmic average velocity equation (Yanmaz, 2002).

$$\frac{u_c}{u_{*c}} = 5.75 \log 5.53 \frac{h}{D_{50}} \tag{4.2}$$

Critical shear velocity u_{*c} is found by using the following equation given by Melville and Coleman (2000), D_{50} being in *mm.*

$$u_{*c} = 0.0305\sqrt{D_{50}} - \frac{0.0065}{D_{50}} \qquad \text{for } 1\ mm \leq D_{50} \leq 100\ mm \tag{4.1}$$

F_r (flow Froude number) and F_d (densimetric Froude number) are expressed as follows (Oliveto and Hager (2002)):

$$F_r = \frac{u}{\sqrt{gh}} \tag{4.3}$$

$$F_d = \frac{u}{\sqrt{g' D_{50}}} \tag{4.4}$$

where; g'= reduced gravitational acceleration $g' = ((\rho_s - \rho)/\rho)g$

Scour depths (d_{s1}) were calculated with calibration equation in Figure 3.12.

4.2 Local Scour around Circular Pier (P1)

5 series of the experiments were conducted with circular pier $D=11\ cm$. The flow parameters and the final scour depths at points A,B and C are summarized in Table 4.1 for unsteady conditions. The time dependent scour depths at point A (d_{s1}) for whole experiments are given in Figure 4.3.

Table 4.1 Flow parameters and measured scour depths

Exp. No:	t_p	t_{end}	Q_{st} - Q_p	h_{st} - h_p	h_p/b	b/D_{50}	I_p	$F_{r(peak)}$	$F_{d(peak)}$	d_{s1}	d_{s2}	d_{s3}
	min	min	lt/s	cm						cm	cm	cm
1	10	15	8 - 45	6 - 20.39	1.85	65.48	0.48	0.20	1.67	3.8	3.4	0.8d
2	10	15	8 - 63	6 - 22.61	2.06	65.48	0.59	0.23	2.11	6.0	5.0	0.6d
3	10	15	8 - 73	6 - 23.52	2.14	65.48	0.65	0.26	2.35	6.0	4.5	0.5
4	15	25	8 - 63	6 - 22.61	2.06	65.48	0.59	0.23	2.11	6.0	3.6	0.0
5	25	45	8 - 63	6 - 22.61	2.06	65.48	0.59	0.23	2.11	6.5	5.5	1.7

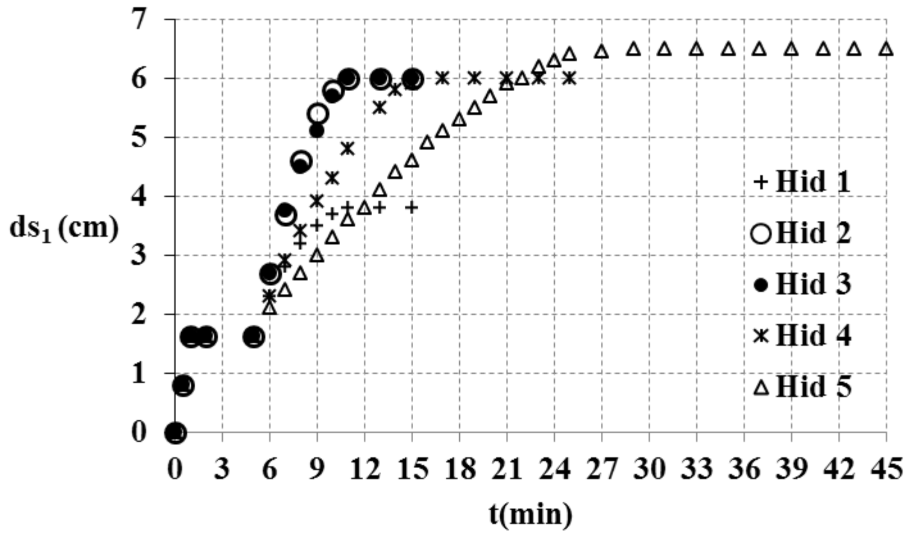

Figure 4.3 Temporal variations of the scour depth at point A

At the end of the each experiment, the dimensions of the scour hole are also measured. The pictures corresponding to different scour holes related to various hydrographs are given in Figure 4.4.

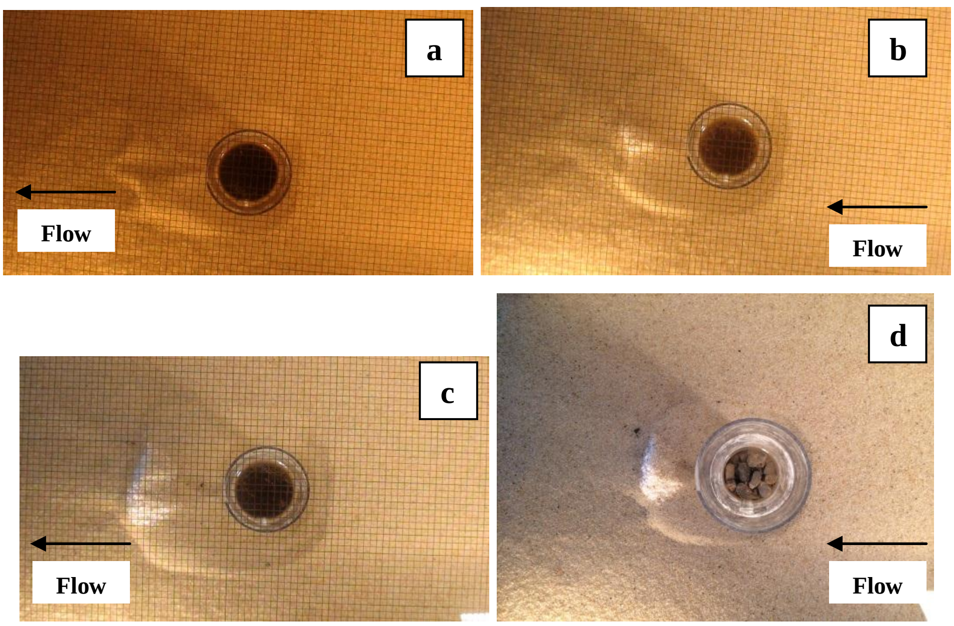

Figure 4.4 Scour hole configurations at the end of each tests for a) Hid 1 b) Hid 2 c) Hid 3 d)Hid 4 and e)Hid 5

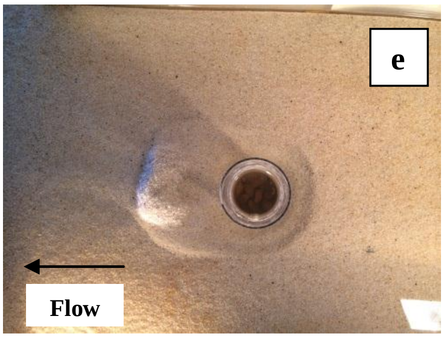

Figure 4.4 Scour hole configurations at the end of each tests for a) Hid 1 b) Hid 2 c) Hid 3 d)Hid 4 and e)Hid 5 (continued)

The bed elevations along the centerline obtained from the laser meter are depicted in Figure 4.5, the initial bed elevation being the datum. It can be seen in Figure 4.4 Hid 5 gives more deposition downstream face of the pier. Maximum scour and deposition measurements along the centerline are presented in Table 4.2.

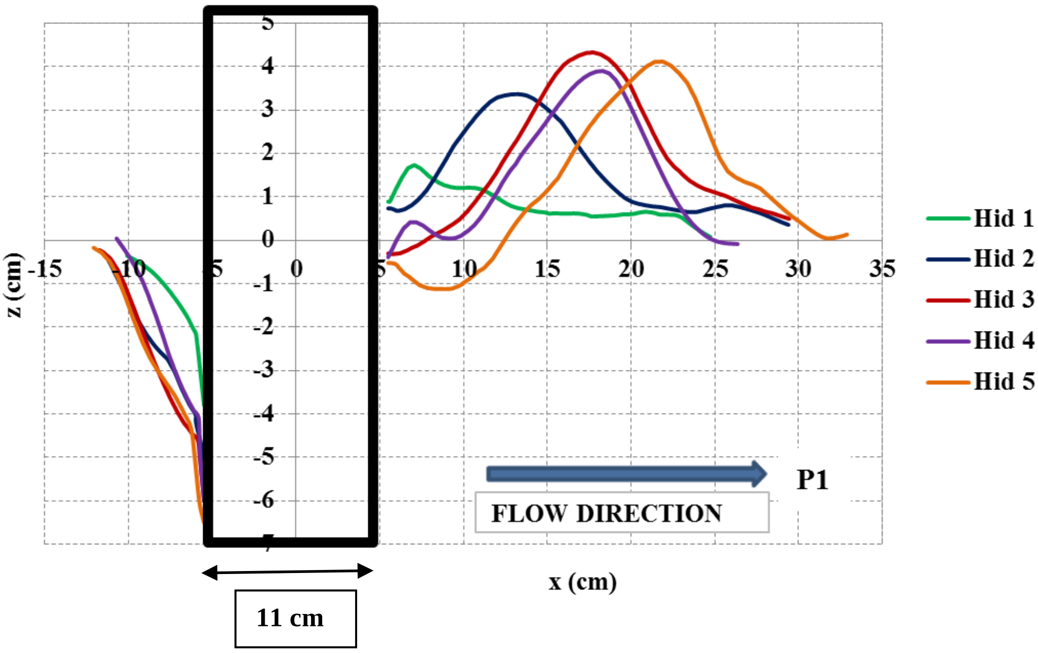

Figure 4.5 Bed elevations along the centerline at the end of tests

Table 4.2 Maximum scour and deposition depths along the centerline at the end of tests

Hydrograph	Q_p	t_p	maximum scour depth	x_p	maximum deposition height	x_p
	L/s	min	cm	cm	cm	cm
Hid 1	45	10	-3.80	-5.5	1.73	7.05
Hid 2	63	10	-6.01	-5.5	3.36	13.29
Hid 3	73	10	-6.05	-5.5	4.32	17.76
Hid 4	63	15	-6.00	-5.5	3.90	18.33
Hid 5	63	25	-6.52	-5.5	4.11	21.91

4.3 Local Scour around Square Pier (P2)

5 series of the experiments were conducted with square pier *b=8.5 cm*. The flow parameters are summarized in Table 4.3 for unsteady conditions. The time dependent scour depths at point A for different hydrographs are given in Figure 4.6.

Table 4.3 Flow parameters and measured scour depth

Exp. No:	t_p	t_{end}	Q_{st} - Q_p	h_{st} - h_p	h_p/b	b/D_{50}	I_p	$F_{r(peak)}$	$F_{d(peak)}$	d_{s1}	d_{s2}	d_{s3}
	min	min	lt/s	cm						cm	cm	cm
6	10	15	8 - 45	6 - 20.39	2.40	50.60	0.48	0.20	1.67	4.0	2.9	0.8d
7	10	15	8 - 63	6 - 22.61	2.66	50.60	0.59	0.23	2.11	6.5	4.5	0.5
8	10	15	8 - 73	6 - 23.52	2.76	50.60	0.65	0.26	2.35	7.5	7.0	1.5
9	15	25	8 - 63	6 - 22.61	2.66	50.60	0.59	0.23	2.11	6.5	2.9	0.5
10	25	45	8 - 63	6 - 22.61	2.66	50.60	0.59	0.23	2.11	7.5	4.5	1.5

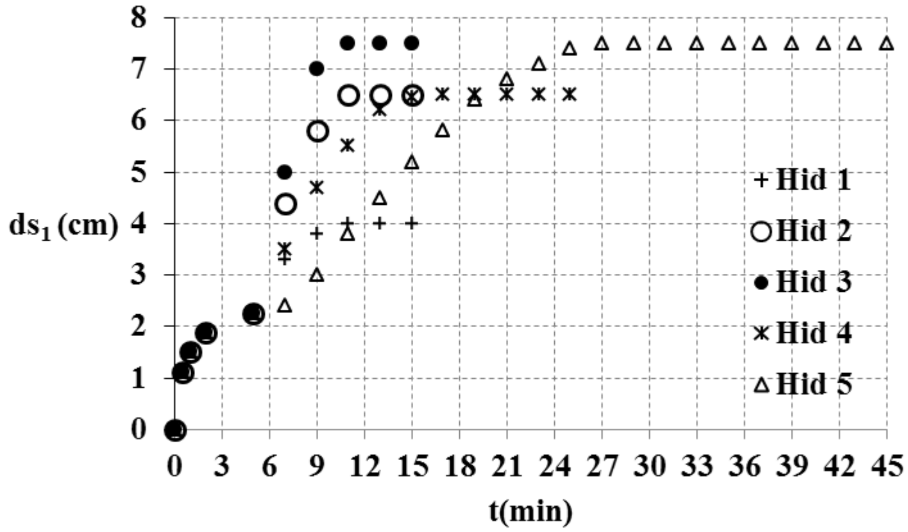

Figure 4.6 Temporal variations of the scour depth at point A

The final scour hole pattern around square pier at the end of the experiments are shown in Figure 4.7. It can be seen that the scours are symmetric according to the pier axis.

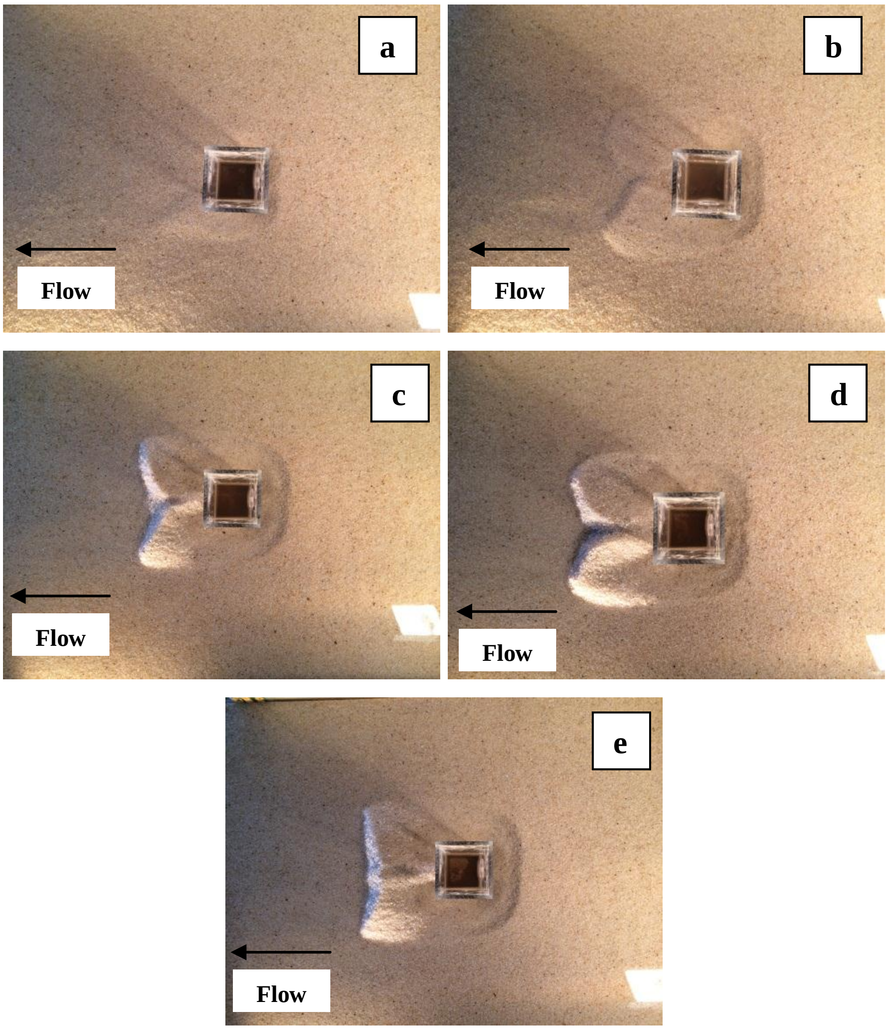

Figure 4.7 Scour hole configurations at the end of tests for experiment set up for a) Hid 1 b) Hid 2 c) Hid 3 d)Hid 4 and e)Hid 5

The bed elevations along the centerline obtained from the laser meter are presented in Figure 4.8. Maximum deposition was occurred downstream of the pier by Hid 5. All the centerline maximum scour and deposition measurements are presented in Table 4.4.

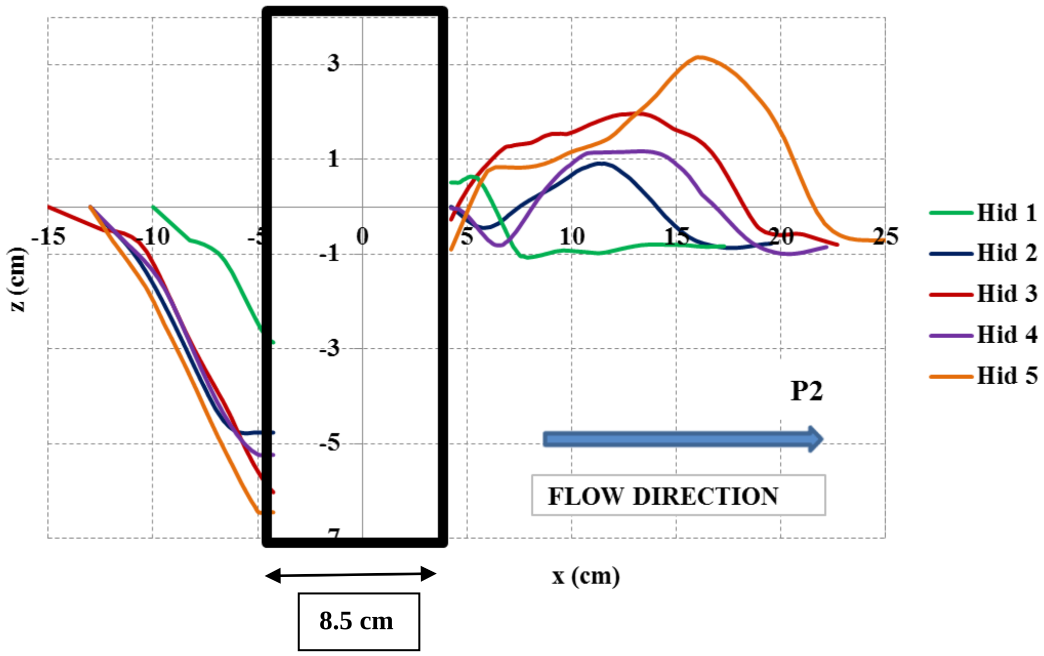

Figure 4.8 Bed elevations along the centerline at the end of tests

Table 4.4 Maximum scour and deposition depths along the centerline at the end of tests

Hydrograph	**Q_p**	**t_p**	**maximum scour depth**	**x_p**	**maximum deposition height**	**x_p**
	L/s	**min**	**cm**	**cm**	**cm**	**cm**
Hid 1	45	10	-2.86	-4.25	0.64	5.16
Hid 2	63	10	-4.78	-4.25	0.92	11.59
Hid 3	73	10	-6.03	-4.25	1.97	13.09
Hid 4	63	15	-5.24	-4.25	1.17	13.22
Hid 5	63	25	-6.45	-4.25	3.16	15.97

4.3 Local Scour around Rectangular Pier (P3)

5 series of the experiments were conducted with circular pier $b=11.5$ cm. The flow parameters are summarized in Table 4.5 for unsteady conditions. The time dependent scour depths at point A for different hydrographs are given in Figure 4.9.

Table 4.5 Flow parameters and measured scour depth

Exp. No:	t_p min	t_{end} min	Q_{st} - Q_p lt/s	h_{st} - h_p cm	h_p/b	b/D_{50}	I_p	$F_{r(peak)}$	$F_{d(peak)}$	d_{s1} cm	d_{s2} cm	d_{s3} cm
11	10	15	8 - 45	6 - 20.39	1.77	68.45	0.48	0.20	1.67	4.5	0.5	0.17d
12	10	15	8 - 63	6 - 22.61	1.97	68.45	0.59	0.23	2.11	7.5	0.8	0.92d
13	10	15	8 - 73	6 - 23.52	2.05	68.45	0.65	0.26	2.35	8.5	2.0	0.71d
14	15	25	8 - 63	6 - 22.61	1.97	68.45	0.59	0.23	2.11	8.0	0.0	0.91d
15	25	45	8 - 63	6 - 22.61	1.97	68.45	0.59	0.23	2.11	8.0	1.5	0.51d

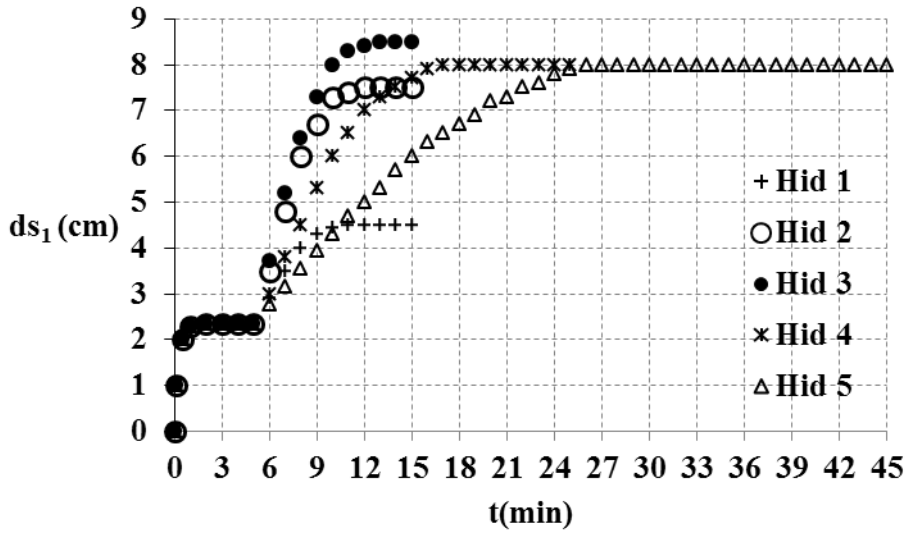

Figure 4.9 Temporal variations of the scour depth at point A

The final scour hole pictures around rectangular pier at the end of the experiments are shown in Figure 4.10. All the pictures show that scour is symmetric.

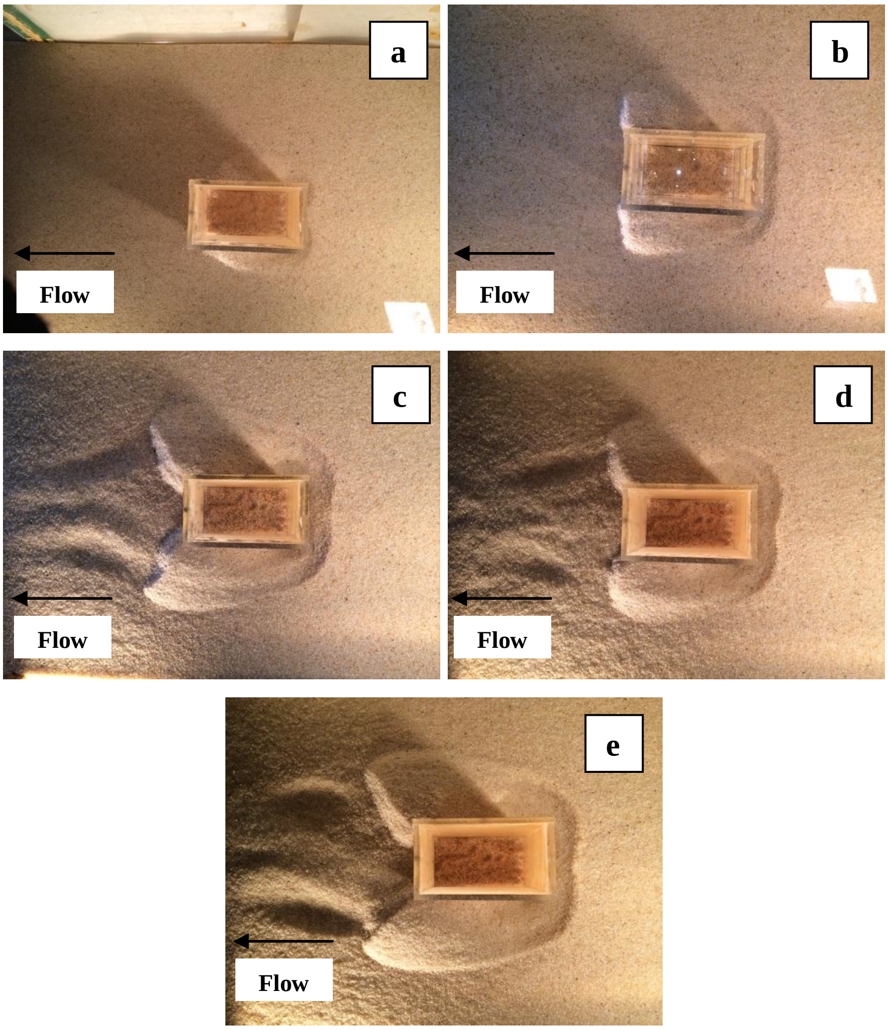

Figure 4.10 Scour hole configurations at the end of tests for experiment set up for a) Hid 1 b) Hid 2 c) Hid 3 d)Hid 4 and e)Hid 5 (continued)

The bed elevations along the centerline obtained from the laser meter are depicted in Figure 4.11. Maximum deposition was occurred downstream of the pier by Hid 5. As it can be seen in Figure 4.11, there is not a significant deposition at the downstream face of the pier as square or cylinder pier. On the other hand deposition occurs sides of the rectangular pier. All the centerline maximum scour and deposition measurements are presented in Table 4.6.

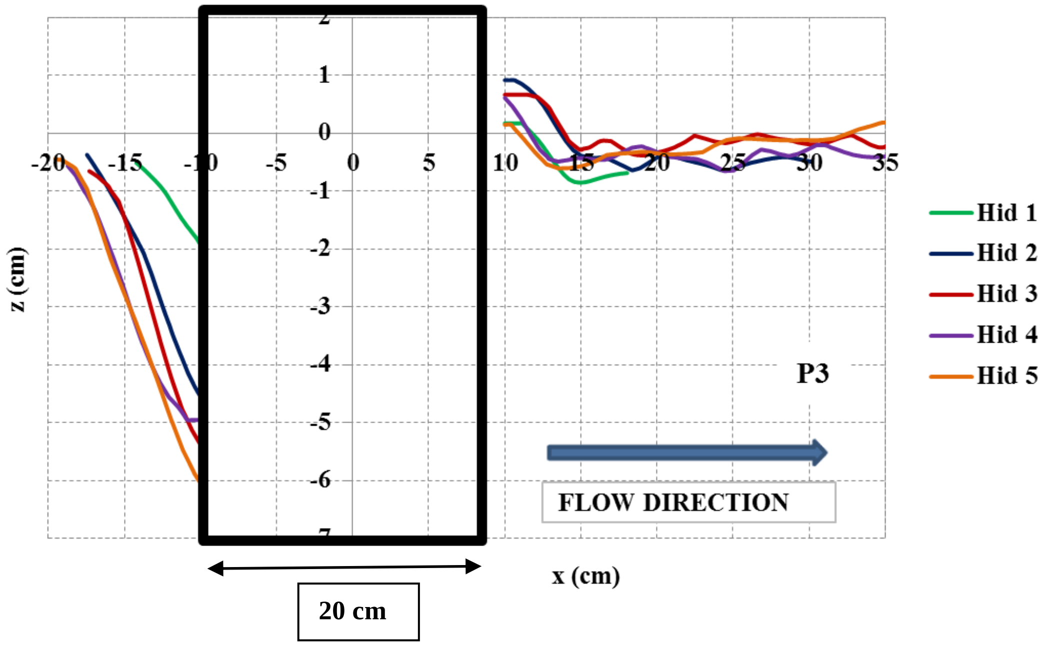

Figure 4.11 Bed elevations along the centerline at the end of tests

Table 4.6 Maximum scour and deposition depths along the centerline at the end of tests

Hydrograph	Q_p	t_p	maximum scour depth	x_p	maximum deposition height	x_p
	L/s	min	cm	cm	cm	cm
Hid 1	45	10	-1.93	-10	0.17	10.00
Hid 2	63	10	-4.55	-10	0.92	10.63
Hid 3	73	10	-5.38	-10	0.67	11.49
Hid 4	63	15	-4.95	-10	0.62	10.00
Hid 5	63	25	-6.05	-10	0.51	42.69

4.4 Local Scour around Rectangular with Circular Nose Pier (P4)

5 series of the experiments were conducted with rectangular with circular nose pier with $b=12$ *cm*. The flow parameters are summarized in Table 4.7 for unsteady conditions. The time dependent scour depths at point A for different hydrographs are given in Figure 4.12.

Table 4.7 Flow parameters and measured scour depth

Exp. No:	t_p min	t_{end} min	Q_{st} - Q_p lt/s	h_{st} - h_p cm	h_p/b	b/D_{50}	I_p	$F_{r(peak)}$	$F_{d(peak)}$	d_{s1} cm	d_{s2} cm	d_{s3} cm
16	10	15	8 - 45	6 - 20.39	1.70	71.43	0.48	0.20	1.67	4.2	0.5	0.1d
17	10	15	8 - 63	6 - 22.61	1.88	71.43	0.59	0.23	2.11	4.4	0.6	0.1d
18	10	15	8 - 73	6 - 23.52	1.96	71.43	0.65	0.26	2.35	6.0	1.5	0.05d
19	15	25	8 - 63	6 - 22.61	1.88	71.43	0.59	0.23	2.11	4.4	0.4	0.1d
20	25	45	8 - 63	6 - 22.61	1.88	71.43	0.59	0.23	2.11	5.5	2.5	0.8d

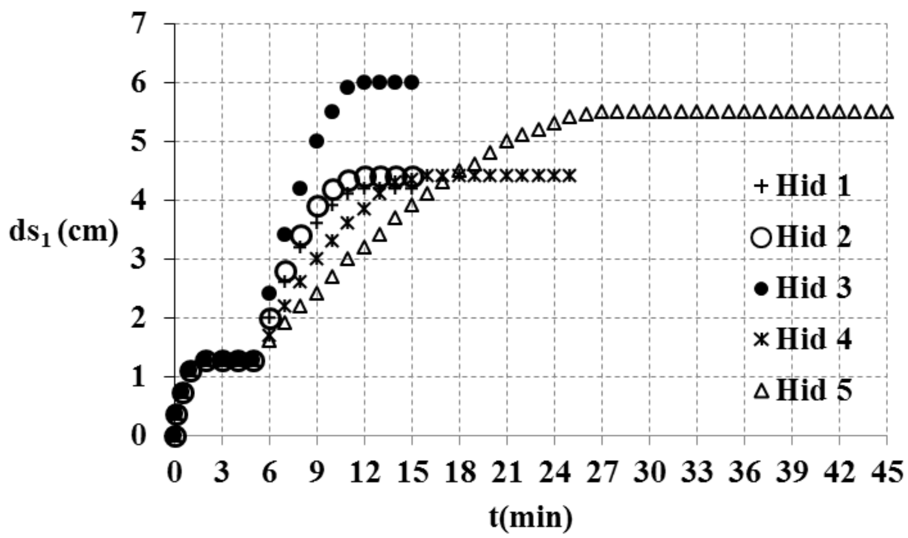

Figure 4.12 Temporal variations of the scour depth at point A

The final scour hole photographs for rectangular with circular nose at the end of the experiments are presented in Figure 4.13.

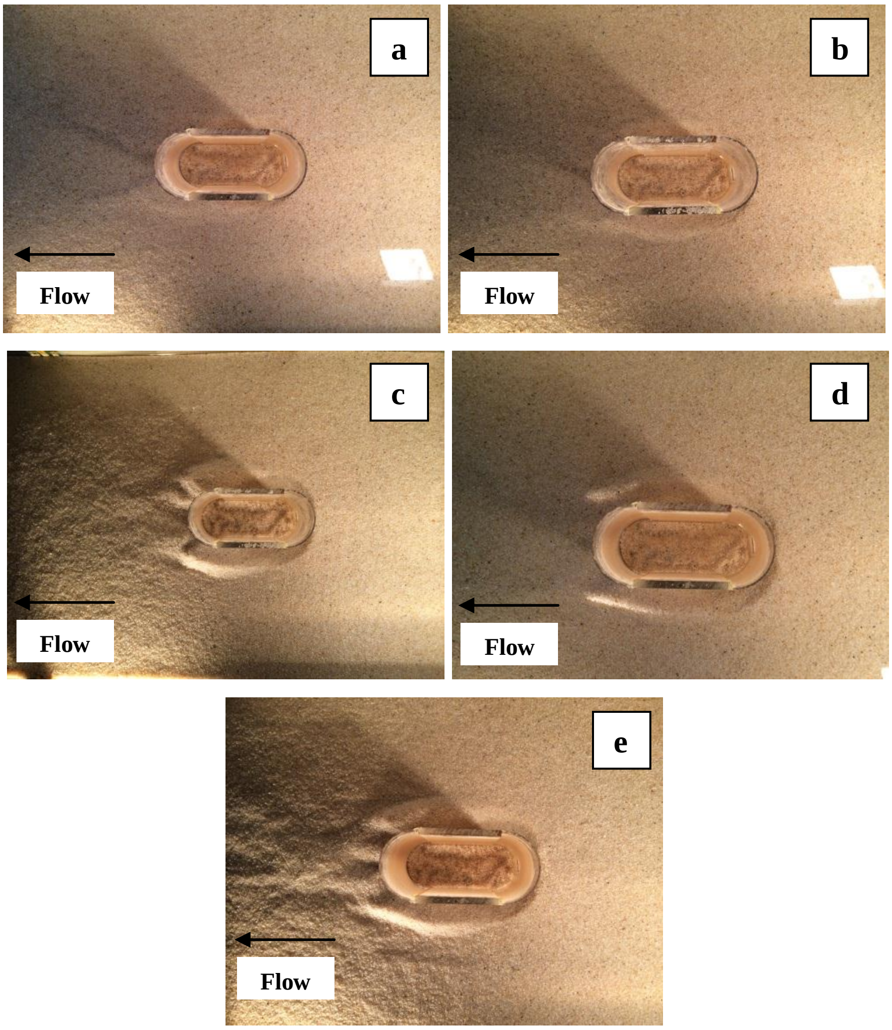

Figure 4.13 Scour hole configurations at the end of tests for experiment set up for a) Hid 1 b) Hid 2 c) Hid 3 d)Hid 4 and e)Hid 5 (continued)

The bed elevations along the centerline obtained from the laser meter are showed in Figure 4.14. Maximum deposition was occurred downstream of the pier by Hid 5. As it can be seen in Figure 4.14, there is not a significant deposition at the downstream face of the pier as rectangular pier. All the centerline maximum scour and deposition measurements are presented in Table 4.8.

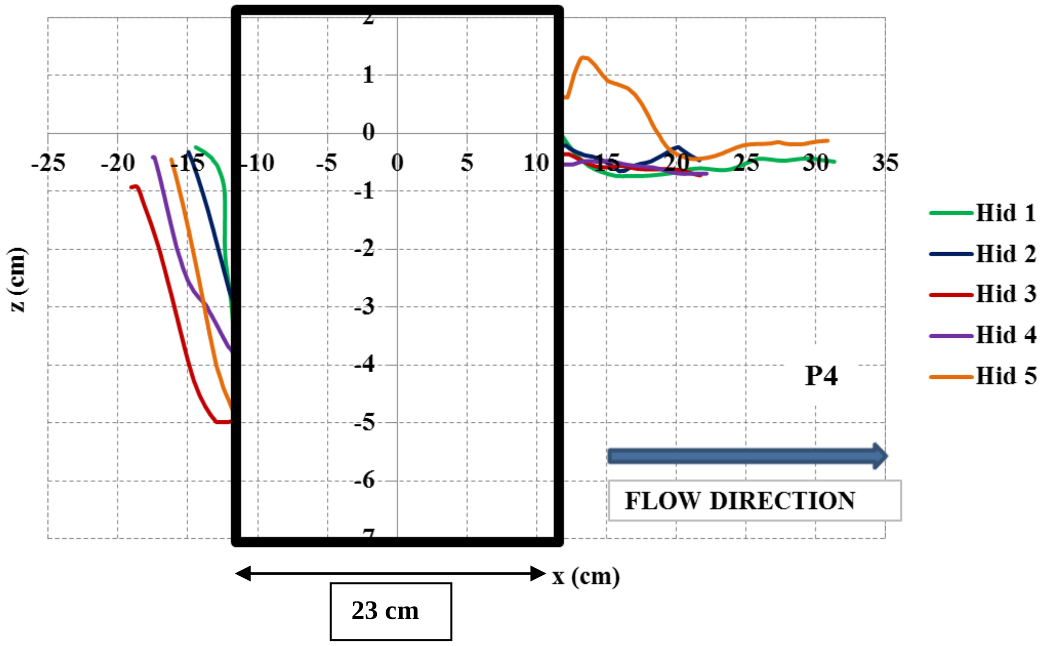

Figure 4.14 Bed elevations along the centerline at the end of tests

Table 4.8 Maximum scour and deposition depths along the centerline at the end of tests

Hydrograph	Q_p	t_p	maximum scour depth	x_p	maximum deposition height	x_p
	L/s	min	cm	cm	cm	cm
Hid 1	45	10	-4.20	-11.50	0.10	11.50
Hid 2	63	10	-4.40	-11.50	0.10	11.50
Hid 3	73	10	-6.00	-11.50	0.05	11.50
Hid 4	63	15	-4.43	-11.50	0.10	11.50
Hid 5	63	25	-5.50	-11.50	1.30	13.67

4.5 Local Scour around Rectangular with Trapezoidal Nose Pier (P5)

5 series of the experiments were conducted with rectangular with trapezoidal nose pier with *b=11 cm*. The flow parameters are summarized in Table 4.9 for unsteady conditions. The time dependent scour depths at point A for different hydrographs are given in Figure 4.15.

Table 4.9 Flow parameters and measured scour depth

Exp. No:	t_p	t_{end}	Q_{st} - Q_p	h_{st} - h_p	h_p/b	b/D_{50}	I_p	$F_{r(peak)}$	$F_{d(peak)}$	d_{s1}	d_{s2}	d_{s3}
	min	min	lt/s	cm						cm	cm	cm
21	10	15	8 - 45	6 - 20.39	1.85	65.48	0.48	0.20	1.67	2.2	0.0	1.3d
22	10	15	8 - 63	6 - 22.61	2.06	65.48	0.59	0.23	2.11	4.0	0.3d	1.4d
23	10	15	8 - 73	6 - 23.52	2.14	65.48	0.65	0.26	2.35	5.0	0.0	1.6d
24	15	25	8 - 63	6 - 22.61	1.85	65.48	0.59	0.23	2.11	4.5	0.0	2.2d
25	25	45	8 - 63	6 - 22.61	1.85	65.48	0.59	0.23	2.11	5.5	1.0	1.2d

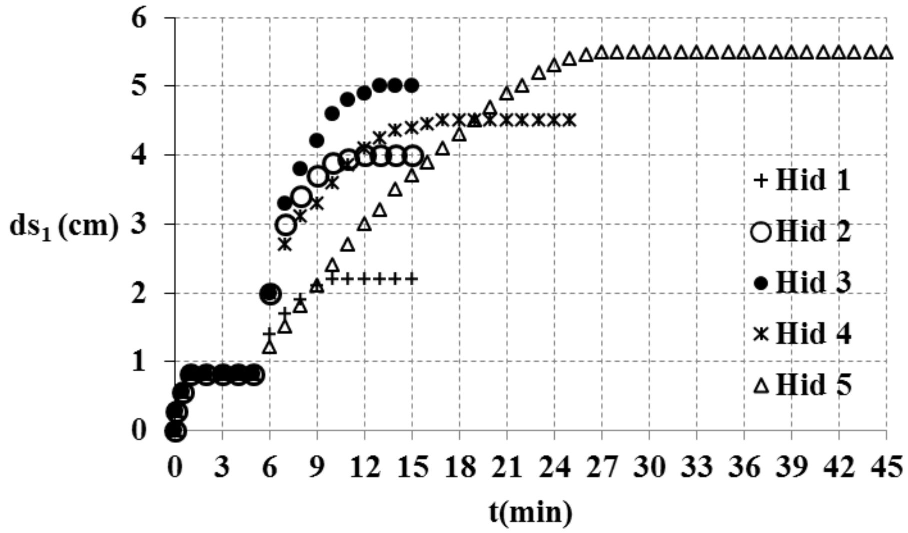

Figure 4.15 Temporal variations of the scour depth at point A

The final scour hole photographs for rectangular with trapezoiadl nose at the end of the experiments are shown in Figure 4.16.

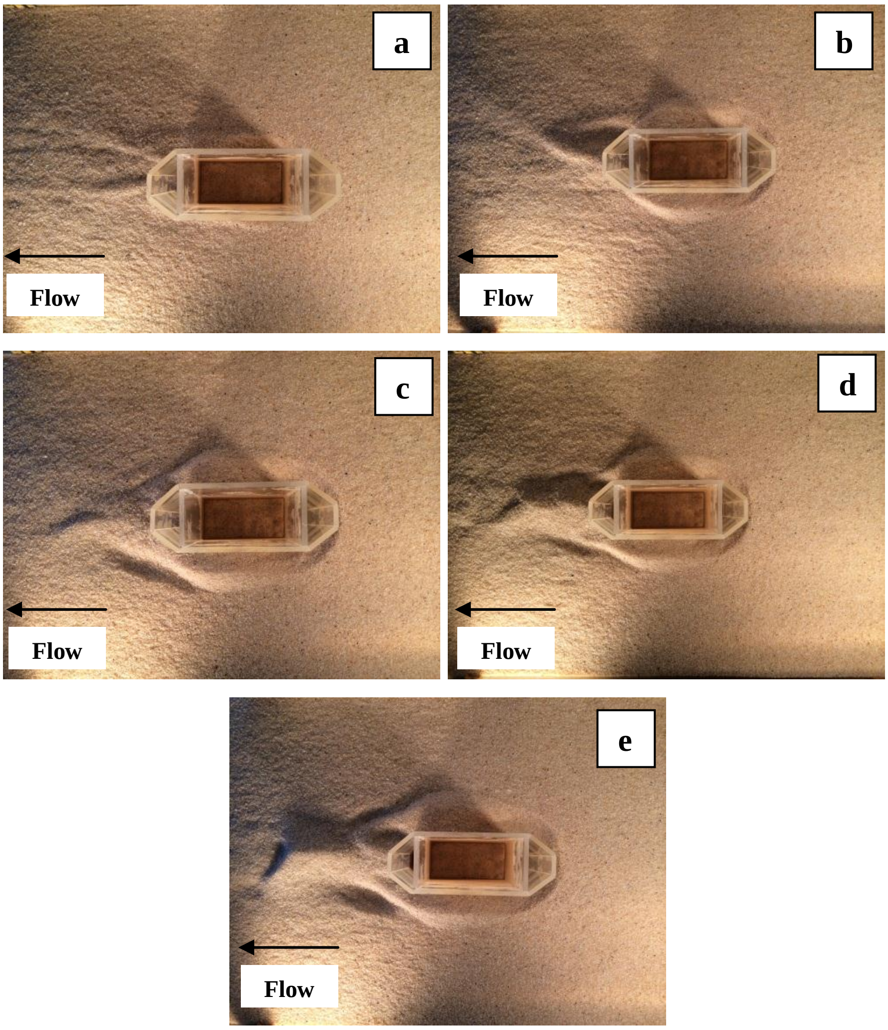

Figure 4.16 Scour hole configurations at the end of tests for experiment set up for a) Hid 1 b) Hid 2 c) Hid 3 d)Hid 4 and e)Hid 5 (continued)

The bed elevations along the centerline obtained from the laser meter are presented in Figure 4.17. Maximum deposition was occurred downstream of the pier by Hid 5. All the centerline maximum scour and deposition measurements are presented in Table 4.10.

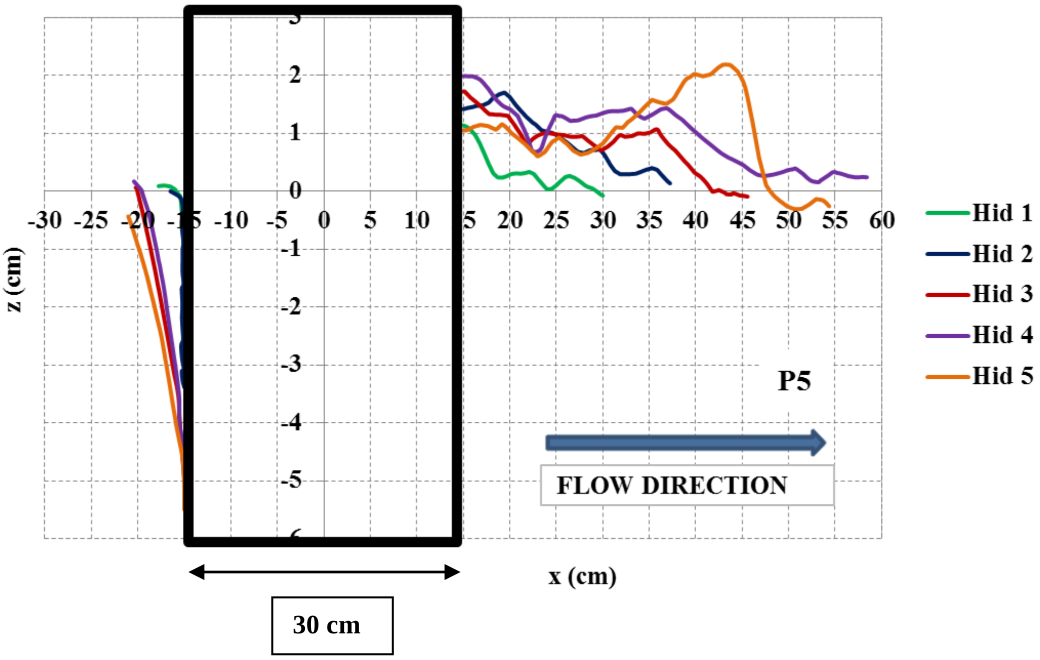

Figure 4.17 Bed elevations along the centerline at the end of tests

Table 4.10 Maximum scour and deposition depths along the centerline at the end of tests

Hydrograph	**Q_p**	**t_p**	**maximum scour depth**	**x_p**	**maximum deposition height**	**x_p**
	L/s	**min**	**cm**	**cm**	**cm**	**cm**
Hid 1	45	10	-2.20	-15	1.14	15.00
Hid 2	63	10	-4.00	-15	1.71	19.43
Hid 3	73	10	-5.00	-15	1.72	15.15
Hid 4	63	15	-4.50	-15	2.00	15.00
Hid 5	63	25	-5.50	-15	2.19	43.42

CHAPTER FIVE
ANALYSIS OF THE RESULTS

5.1 Analyses in Steady Flow Conditions

The steady flow results in which base flow rate is 8 L/s are analyzed in three different sections: time dependent scour depth $d_s(t)$, equilibrium scour depth d_{se} and relative scour depth d_s/b. The influence of the pier shape is also analyzed and the specifically determined pier shape factor values K_s are proposed on the basis of the experimental results. The scour hole dimensions at the end of the experiments are analyzed. Also, some equations in literature are tested with experimental findings and results are compared.

The temporal scour depth was expressed by mathematical function suggested in Sheppard et. al. (2004).

$$d_s(t) = a\left[1-\exp\left(-bt\right)\right]+c\left[1-\exp\left(-dt\right)\right] \tag{5.1}$$

The values of the coefficients *a, b, c* and *d* were obtained by the nonlinear regression analysis, and they are presented in Table 5.1. The equilibrium scour depths were obtained by setting the time to infinity $(t=\infty)$. The final and equilibrium scour depths are presented in Table 5.2. The equilibrium scour depths are lightly higher than the measured final scour depths in the case of piers P1, P2 and P5. The difference is large for the rectangular with circular nose pier. The measured final scour depths $(d_s(t))$corresponding to each pier are presented in Figure 5.1, together with the calculated equilibrium scour depths.

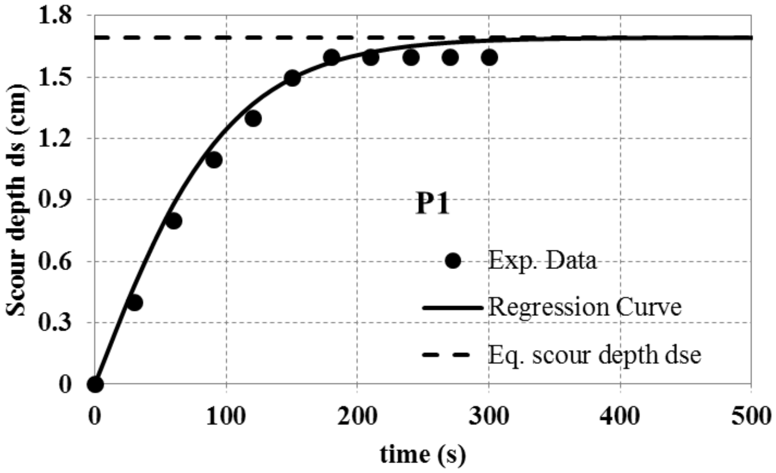

$$d_s(t) = -8.905[1-\exp(-0.022t)] + 10.598[1-\exp(-0.02t)]$$

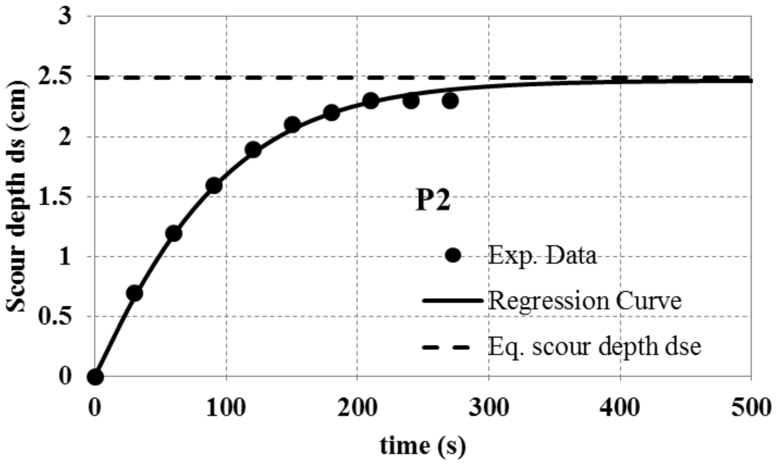

$$d_s(t) = -7.949[1-\exp(-0.018t)] + 10.417[1-\exp(-0.016t)]$$

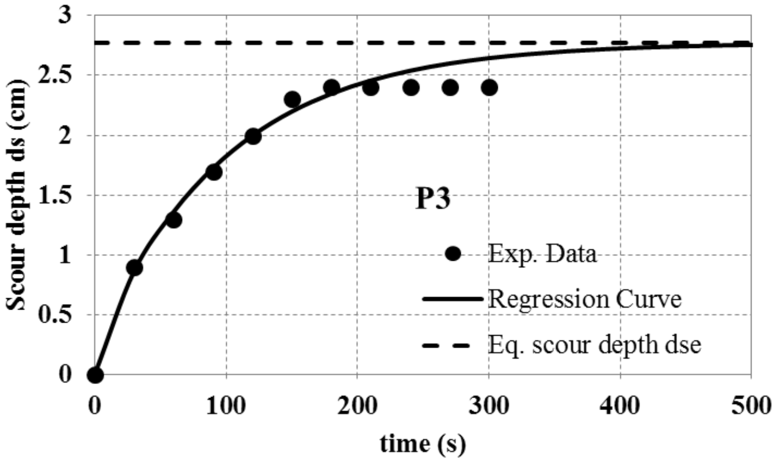

$$d_s(t) = 0.197[1-\exp(0.775t)] + 2.576[1-\exp(-0.01t)]$$

Figure 5.1 Time dependent scour depths; experimental data, curve fitting and predicted equilibrium scour depth

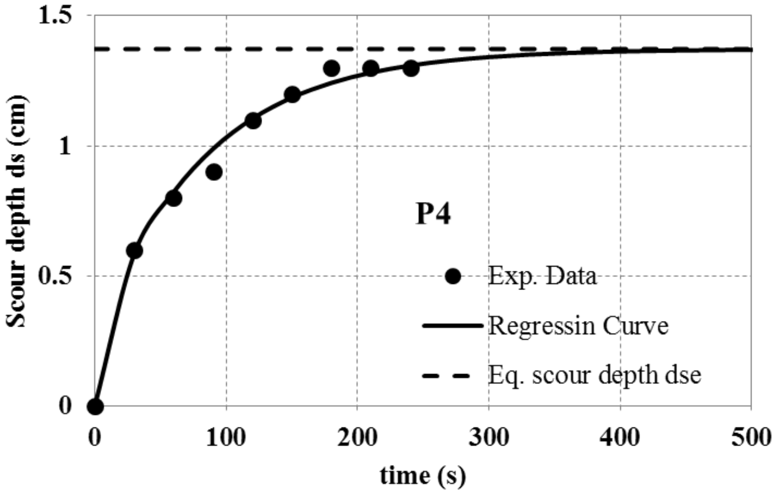

$$d_s(t) = 0.243[1 - \exp(0.748t)] + 1.129[1 - \exp(-0.012t)]$$

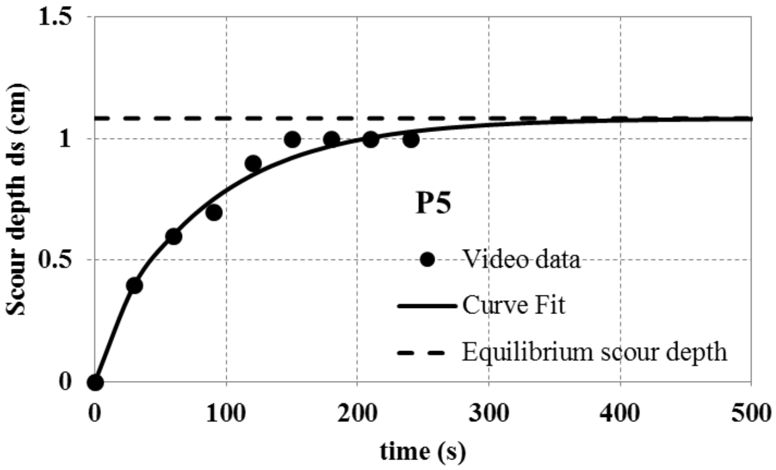

$$d_s(t) = 0.101[1 - \exp(1.037t)] + 0.983[1 - \exp(-0.012t)]$$

Figure 5.1 Time dependent scour depths; experimental data, curve fitting and predicted equilibrium scour depth (continued)

Table 5.1 Coefficients of Eq. 5.1 for each pier

PIER	a	b	c	d
P1	-8.905	0.022	10.598	0.020
P2	-7.949	0.018	10.417	0.016
P3	0.197	0.775	2.576	0.010
P4	0.243	0.748	1.129	0.012
P5	0.101	1.037	0.983	0.012

Table 5.2 Measured final depths and predicted equilibrium scour depths

PIER	Final scour depth d_s *(cm)*	Equilibrium scour depth d_{se} *(cm)*
P1	1.6	1.7
P2	2.3	2.5
P3	2.4	2.9
P4	1.3	1.4
P5	1.0	1.1

The calculated equilibrium scour depths are used in the subsequent regression analyses to obtain the evolution of the scour depth in the following form:

$$\frac{d_s(t)}{d_{se}} = \left[1 - \exp\left(-A\frac{t}{t_e}\right)\right] \tag{5.2}$$

where;

A = coefficient

t_e = time to developed equilibrium scour depth

It was observed that, the time to reach 90% of the equilibrium scour depth was provided at the end of the experiments. So, equilibrium time values *(t_e)* were equal to nearly 600 s for P1, 1000 s for P2, 700 s for P3, 1000 s for P4 and 600 s for P5. The obtained equations are given in each relevant figure. The measured values versus predicted ones are also depicted in separate figures together with determination coefficients, root mean square errors and mean absolute errors.

The results related to the circular pier (P1) are given Figures 5.2 and 5.3.

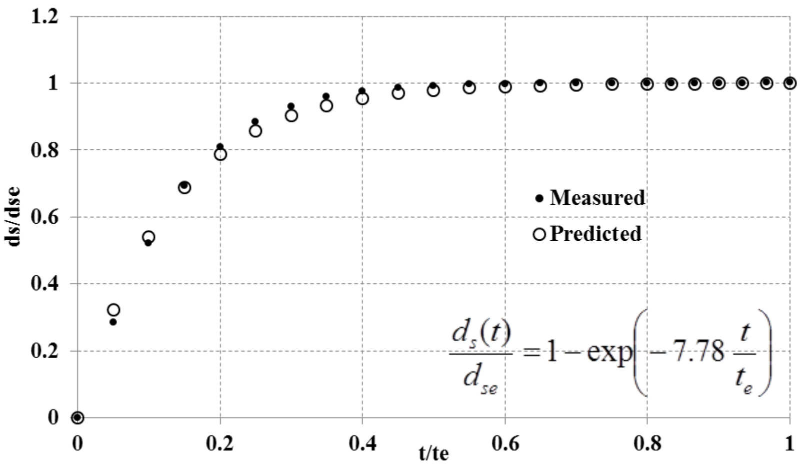

Figure 5.2 Measured and predicted d_s/d_{se} values

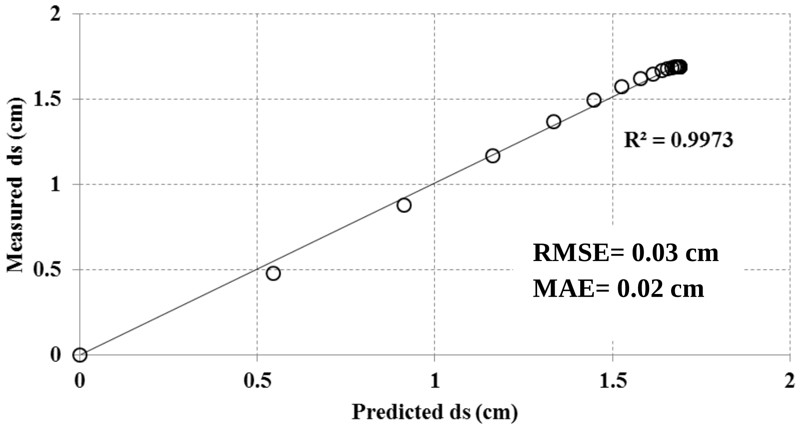

Figure 5.3 Measured scour depths versus predicted scour depths

Figure 5.4 and 5.5 represent the results corresponding to the square pier (P2)

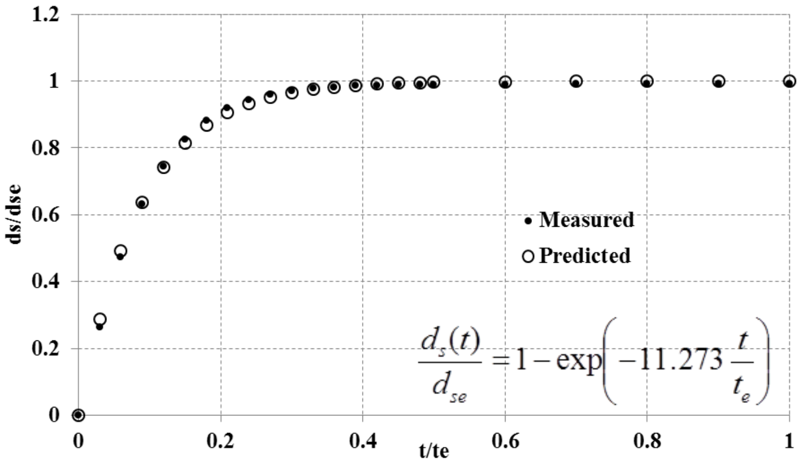

Figure 5.4 Measured and predicted d_s/d_{se} values

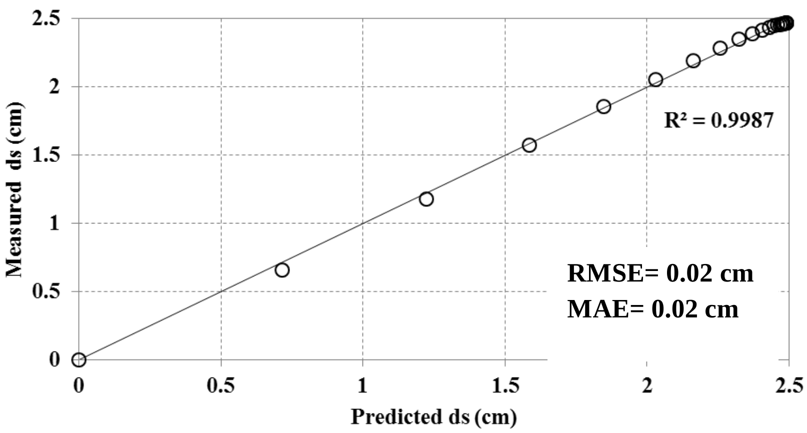

Figure 5.5 Measured scour depths versus predicted scour depths

The results related to the rectangular pier (P3) are given Figures 5.6 and 5.7.

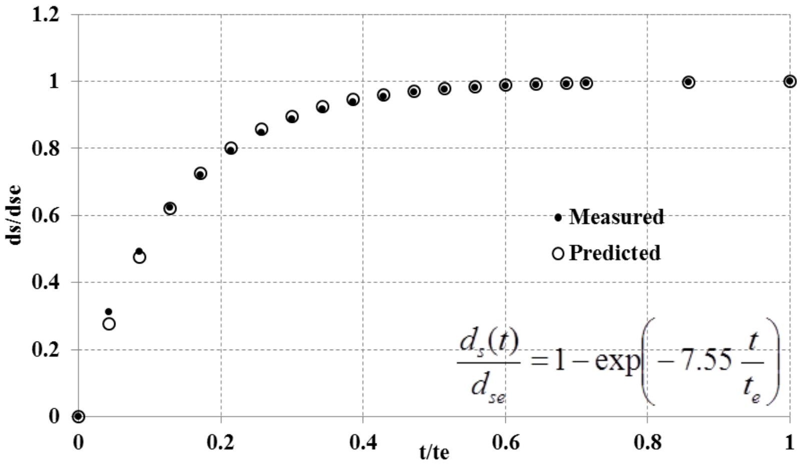

Figure 5.6 Measured and predicted d_s/d_{se} values

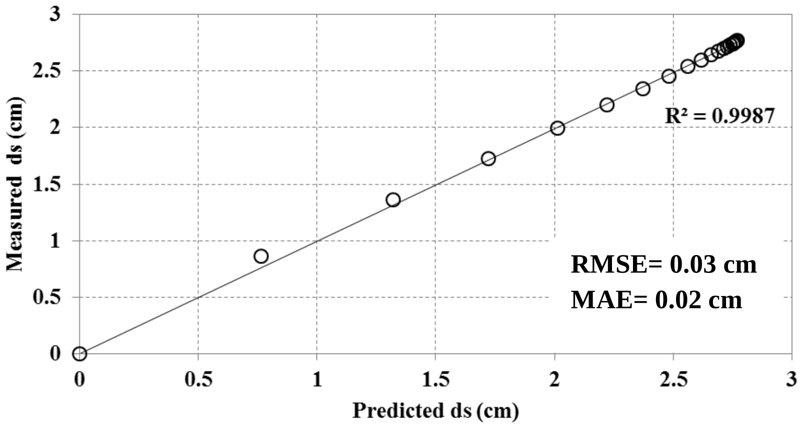

Figure 5.7 Measured scour depths versus predicted scour depths

Figures 5.8 and 5.9 show the results related to the rectangular with circular nose pier (P4).

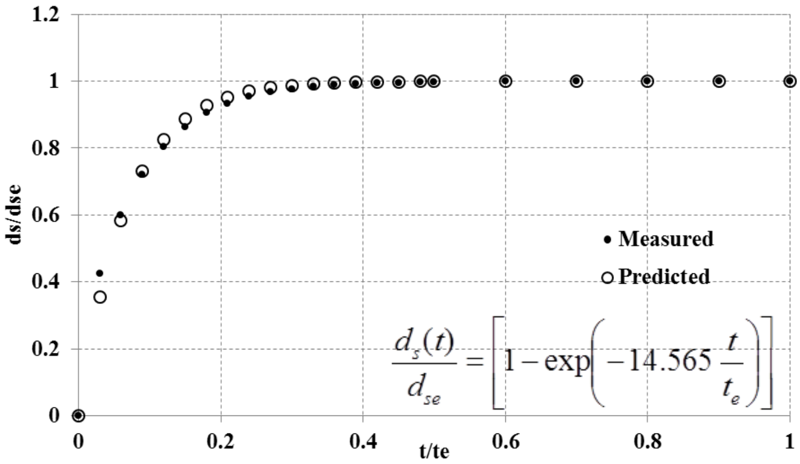

Figure 5.8 Measured and predicted d_s/d_{se} values

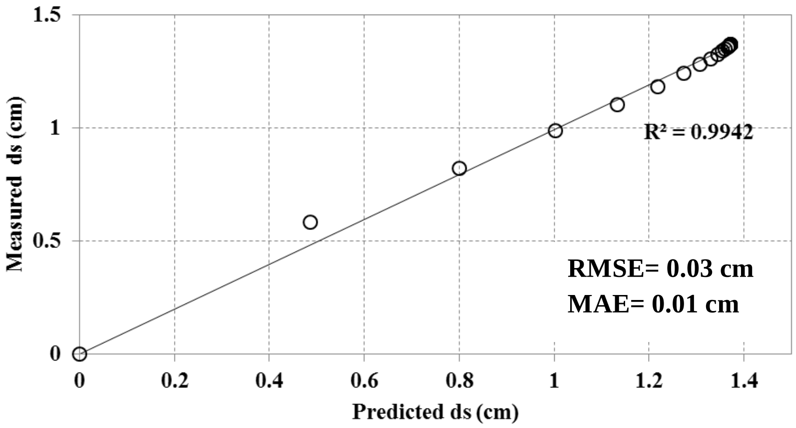

Figure 5.9 Measured scour depths versus predicted scour depths

Figure 5.10 and 5.11 represent the results corresponding to the rectangular with trapezoidal nose pier (P5)

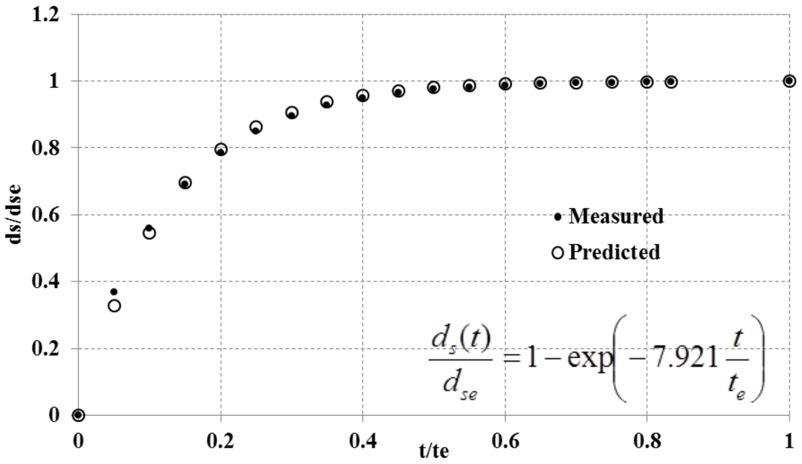

Figure 5.10 Measured and predicted d_s/d_{se} values

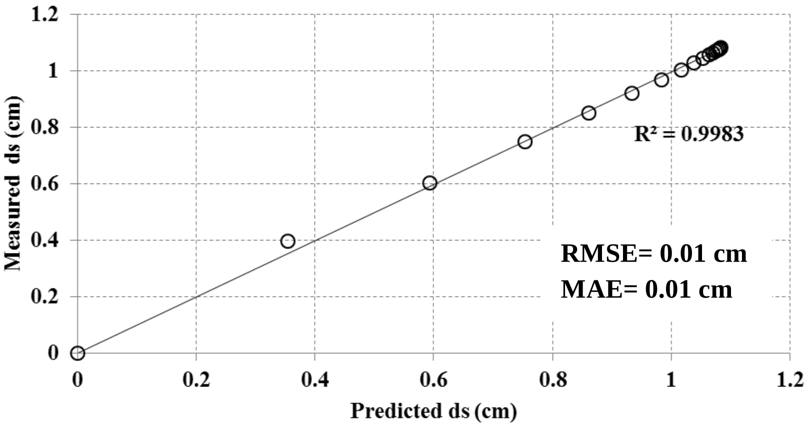

Figure 5.11 Measured scour depths versus predicted scour depths

Similar analysis is performed to obtain empirical relations for the time evolution of the dimensionless scour depth by using an equation as Eq. 5.3. The so obtained relations are given for each pier shape separately.

$$\frac{d_s(t)}{b} = A\left[1 - \exp\left(-B\frac{ut}{b}\right)\right] \tag{5.3}$$

where;

A = coefficient

The results of this study are compared with those obtained by Oliveto and Hager (2002), because of the similarity in the experimental conditions.

Oliveto and Hager (2002) presented a study referred to the temporal evolution of scour depth as a function of approach flow depth and approach velocity with extensive laboratory data. Their equation was based on densimetric Froude number and effects of sediment granulometry.

$$Z = z/z_R = 0.068 N \sigma_g^{-0.5} F_d^{1.5} \log\left(\frac{\sigma_g^{\frac{1}{3}} \sqrt{g' D_{50}}}{b^{2/3} h^{1/3}} \times t \right) \tag{5.4}$$

where,

Z = non-dimensional scour depth

z = scour depth

z_R = reference length $z_R = \left(hb^2\right)^{1/3}$

F_d = densimetric particle Froude number

N = shape factor equal to 1 for circular pier and 1.25 for square and rectangular piers (rectangular with circular nose and rectangular with trapezoidal nose piers cases are excluded, because of the absence of related data in literature).

In Oliveto and Hager (2002) study D_{50}=5.3, 1.2 and 3.1 mm with σ_g=1.43, 1.8 and 2.15, respectively, h is between 0.02 – 0.20 cm and F_d is between1.48 – 3.86.

In this study σ_g=1.83, h=6.00 cm, F_d=1.67 and D_{50}=1.68 mm.

5.1.1 Circular Pier

The regression analysis is performed by using 25 experimental values and the following expressions are obtained. Figure 5.12 illustrates the numerical results and measured values. The *z/z_r* values calculated from Eq. 5.4 are transformed to *d_s/b* for the sake of comparison.

$$\frac{d_s(t)}{b} = 0.16\left[1 - \exp\left(-0.008\frac{ut}{b}\right)\right] \qquad (5.5)$$

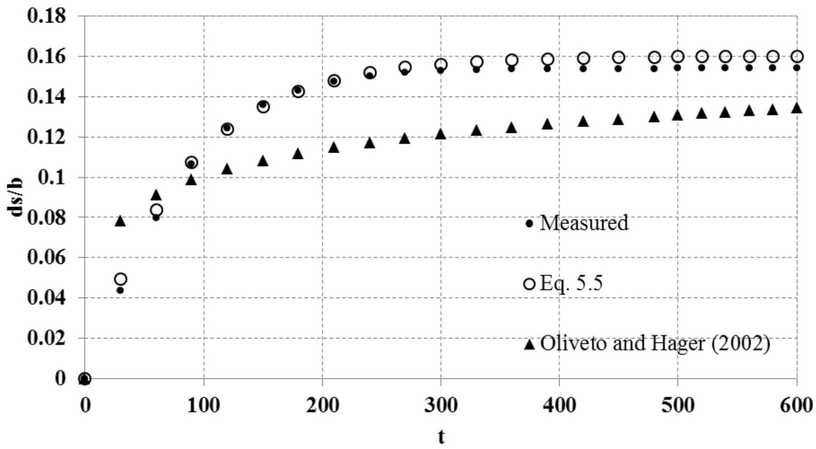

Figure 5.12 Comparison of numerical results and measured values (*t* in s)

The *RMSE*, *MAE* and R^2 values are summarized in Table 5.3. Figure 5.13 shows a comparison between observed and predicted scour depths.

Table 5.3 Computed *RMSE*, *MAE* and R^2 values

Expressions	RMSE	MAE	R^2
	cm	cm	
Equation 5.5	0.05	0.04	1.00
Oliveto and Hager	0.28	0.26	0.87

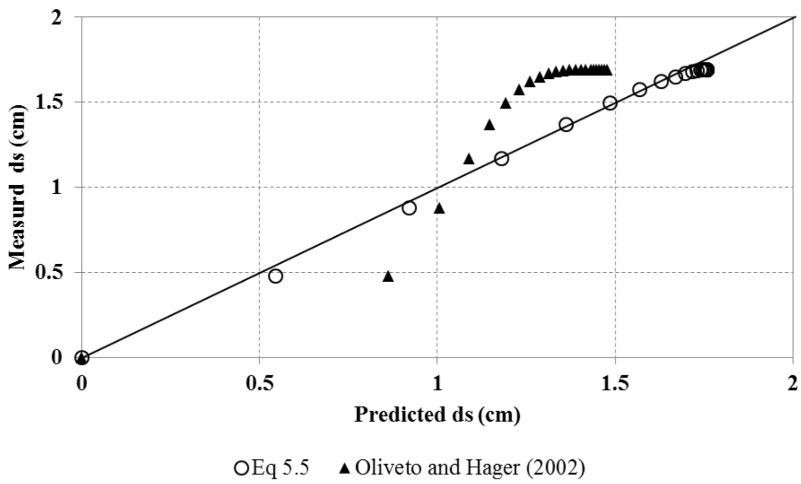

Figure 5.13 Measured scour depths versus predicted scour depths

5.1.2 Square Pier

The constants of the Eq. 5.3 is obtained through nonlinear regression analysis and the best fit line time scale of relative scour depth d_s/b is presented with the obtained constants below:

$$\frac{d_s(t)}{b} = 0.292\left[1 - \exp\left(-0.006\frac{ut}{b}\right)\right] \tag{5.6}$$

The measured experimental data are compared with Eq. 5.6 and Eq. 5.4 developed by Oliveto and Hager (2002) in Figure 5.14. The z/z_r values calculated from Eq. 5.4 are transformed to d_s/b for the sake of comparison.

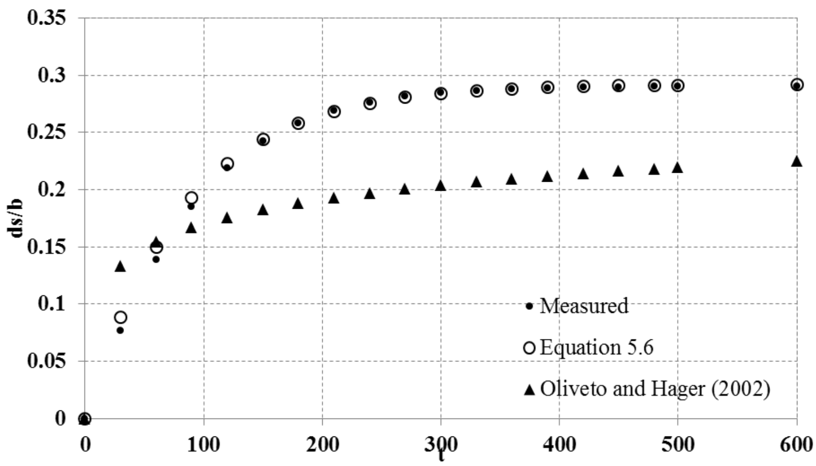

Figure 5.14 Comparison of numerical results and measured values (t in s)

The $RMSE$, MAE and R^2 values are summarized in Table 5.4. Figure 5.15 shows a comparison between observed and predicted data.

Table 5.4 Computed $RMSE$, MAE and R^2 values

Expressions	**RMSE**	**MAE**	**R^2**
	cm	**cm**	
Equation 5.6	0.03	0.02	1.00
Oliveto and Hager	0.81	0.76	0.87

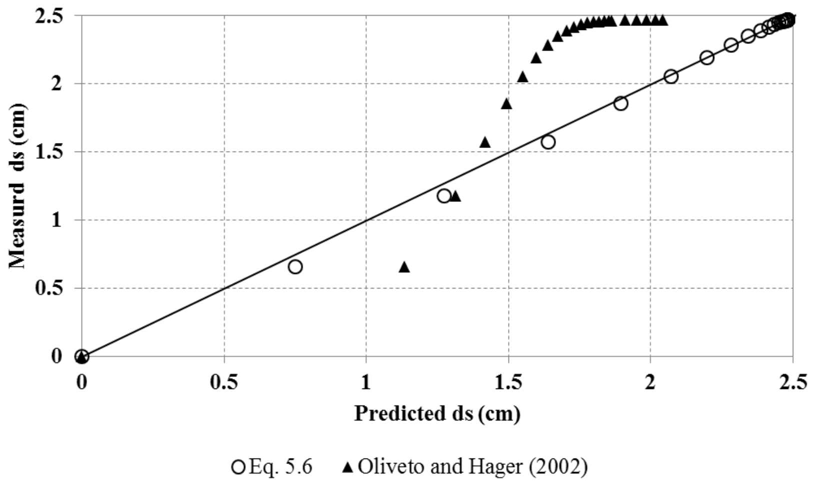

Figure 5.15 Measured scour depths versus predicted scour depths

5.1.3 Rectangular Pier

The regression analysis is performed and the constants of Eq. 5.3 are computed and the following expression is obtained. Figure 5.16 illustrates the numerical results and measured values. The z/z_r values calculated from Eq. 5.4 are transformed to d_s/b for the sake of comparison.

$$\frac{d_s(t)}{b} = 0.24\left[1 - \exp\left(-0.007\frac{ut}{b}\right)\right] \tag{5.7}$$

Figure 5.16 shows the measured experimental data are compared with Eq. 5.7 and Eq. 5.4 developed by Oliveto and Hager (2002).

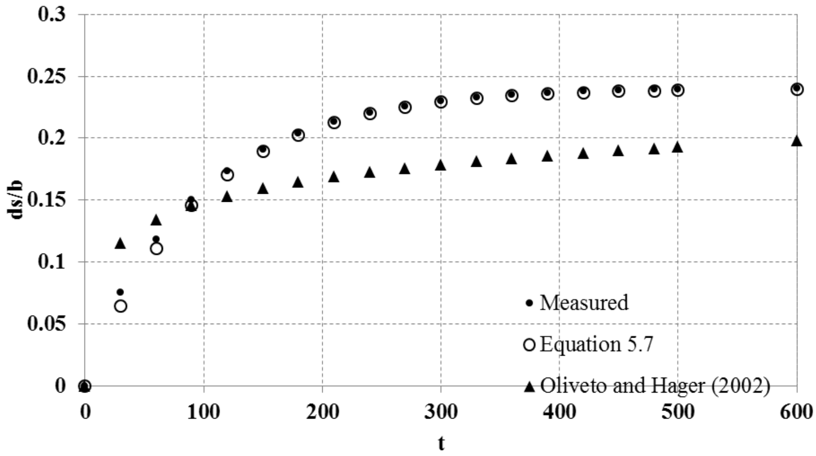

Figure 5.16 Comparison of numerical results and measured values (t in s)

The $RMSE$, MAE and R^2 values are summarized in Table 5.5. Figure 5.17 shows a comparison between observed and predicted data.

Table 5.5 Computed $RMSE$, MAE and R^2 values

Expressions	RMSE	MAE	R^2
	cm	cm	
Equation 5.7	0.04	0.02	0.99
Oliveto and Hager	0.48	0.45	0.91

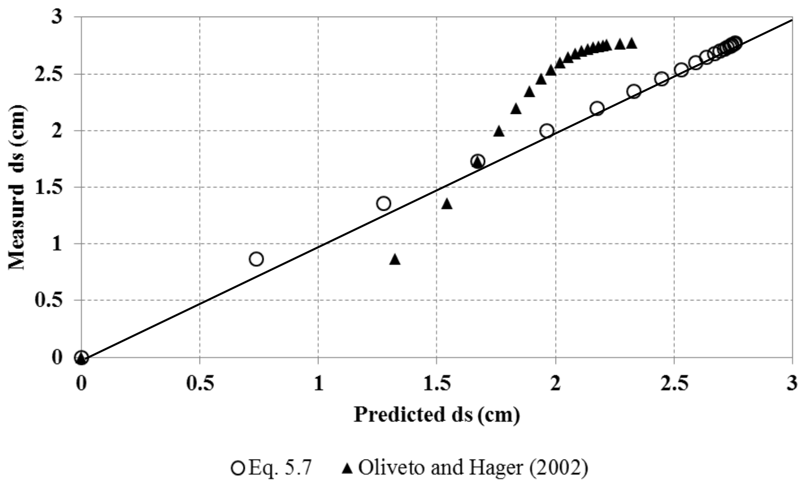

Figure 5.17 Measured scour depths versus predicted scour depths

5.1.4 Rectangular with Circular Nose Pier

The comparison with Eq. 5.4 proposed by Olivetto and Hager (2002) is not realized, because of the absence of related data in literature.

The constants of the Eq. 5.3 is obtained through nonlinear regression analysis and the best fit line time scale of relative scour depth d_s/b is presented with the obtained constants below:

$$\frac{d_s(t)}{b} = 0.113\left[1 - \exp\left(-0.011\frac{ut}{b}\right)\right] \tag{5.8}$$

Figure 5.18 shows the measured experimental data are compared with Eq. 5.8.

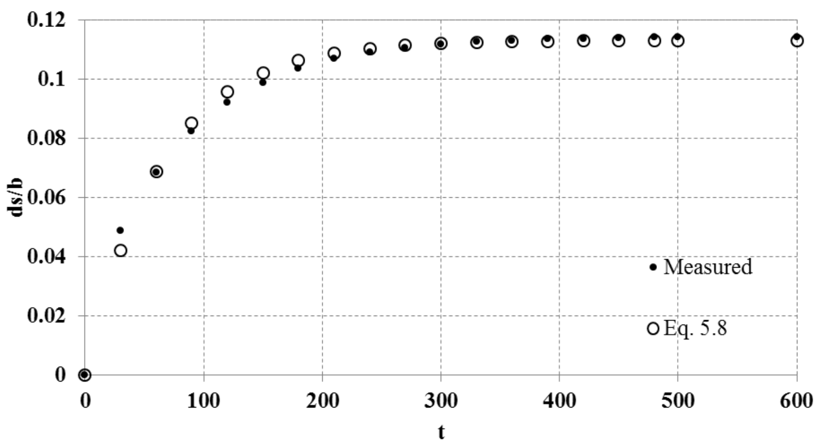

Figure 5.18 Comparison of numerical results and measured values (t in s)

The measured values versus predicted ones are depicted in Figure 5.19 together with determination coefficients, root mean square errors and mean absolute errors.

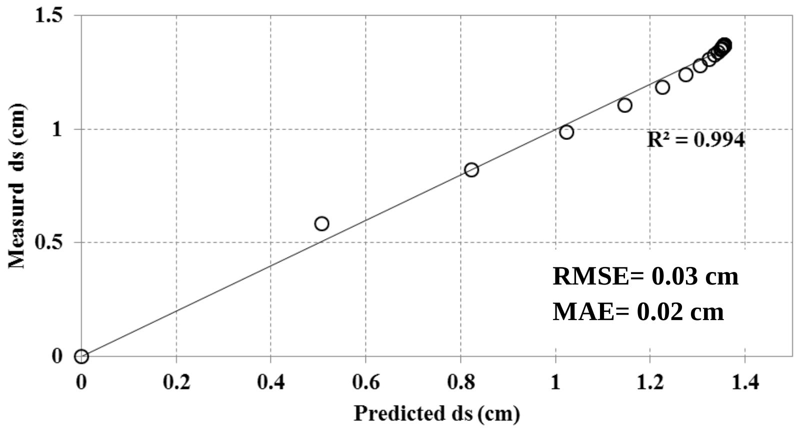

Figure 5.19 Measured scour depths versus predicted scour depths

5.1.5 Rectangular with Trapezoidal Nose Pier

The comparison with Eq. 5.4 proposed by Olivetto and Hager (2002) is not realized, because of the absence of related data in literature.

The regression analysis is performed and the following expression is obtained. Figure 5.20 illustrates the numerical results and measured values.

$$\frac{d_s(t)}{b} = 0.098\left[1 - \exp\left(-0.009\frac{ut}{b}\right)\right] \tag{5.9}$$

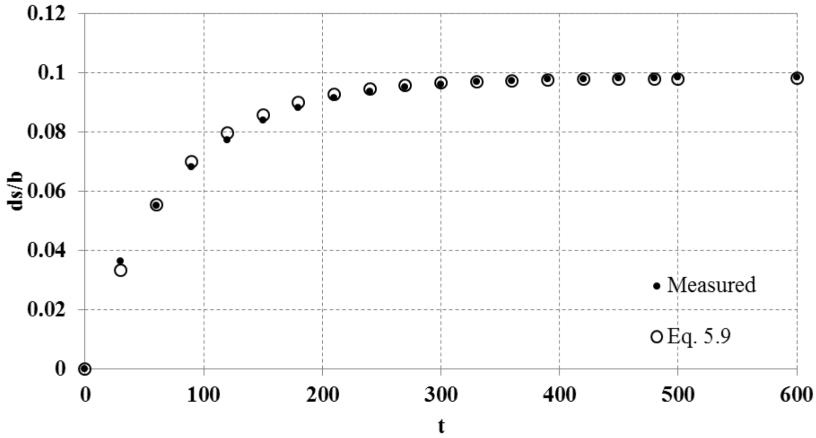

Figure 5.20 Comparison of numerical results and measured values (*t* in s)

The measured values versus predicted ones are depicted in Figure 5.21 together with determination coefficients, root mean square errors and mean absolute errors.

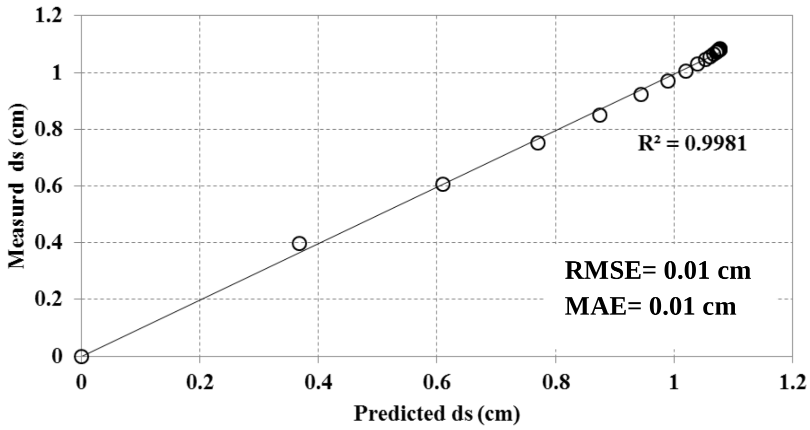

Figure 5.21 Measured scour depths versus predicted scour depths

5.1.6 Effect of Pier Shape on Scouring

Most of the experiments were carried out by using circular piers and the results are generalized for other shaped piers by taken into consideration the shape factor. These shape factors usually differ from each other. The shape factors suggested by different researchers are summarized in Table 5.6, together with those obtained from the experimental findings in this thesis.

Figure 5.22 shows time dependent scour depth $d_s(t)$ for all pier shapes in order to visualize the effect of the pier shapes. Final scour depths are very close to each other for square and rectangular piers. The smallest scour depths were observed in the case of rectangular with trapezoidal nose pier.

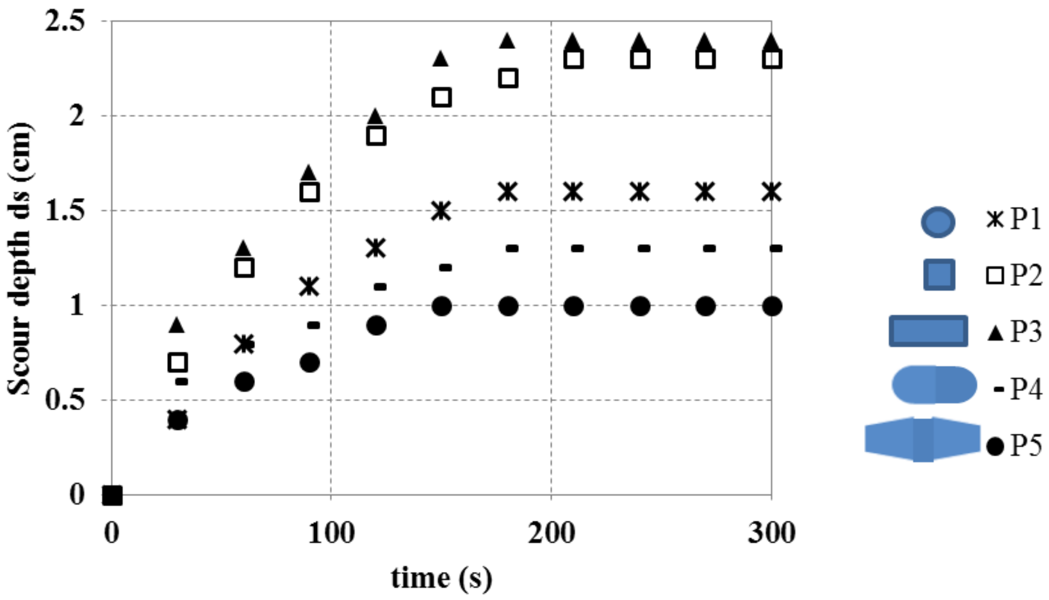

Figure 5.22 Comparison the scour depths between pier shapes under steady flow conditions

The pier shape factor values K_s tended to vary with flow shallowness *(h/b)* and the ratio *L/b* (L=pier length). The higher flow shallowness cause higher shape factor values, otherwise the higher *L/b* causes lower pier shape factor values. For design purposes a conservative approach entails utilizing the largest pier shape factor values.

Table 5.6 Pier shape factor values K_s proposed by Researchers

Pier Type	Tison (1940)	Laursen and Toch (1956)	Chabert and Engeldinger (1956)	Dietz (1972)	Breusers et.al. (1977)	Mostafa (1994)	Melville (1997)	Hoffmans and Verheij (1997)	Richardson and Davis (2001)	Oliveto and Hager (2002)	Bennett (2002)	**Ks(Calc.)**
Circular	1	0.9	1	1	1	1	1	1	1	1	1	1
Square	-	-	-	-	1.2	-	1.1	-	-	1.3	-	1.4
Rectangular	1.4	1	1.1	1.1	1.3	1.3	1	1-1.2	1.1	1.2	1.1	1.5
Rounded nosed	-	0.9	-	0.9	-	1.1	1	0.9	1	-	0.9	0.81
Trapezoidal Nose	-	-	-	-	-	-	-	-	-	-	-	0.63
Stream lined pier	0.67-0.41	0.7-0.8	0.7	-	0.8	-	-	0.7-0.8	-	-	-	-
Sharped nosed pier	-	-	-	0.65	-	-	0.9	0.65-0.76	0.9	-	-	-
Elliptic	-	0.75-0.8	-	-	-	-	-	0.6-0.8	-	-	0.8	-

5.1.7 Estimation of Scour Hole Shape under Steady Flow Conditions

The scour hole measurements were performed with the aid of data from the camera and laser meter combined with Autocad drawings at the end of the experiments. Figure 5.23 illustrates the notation used in description of the scour hole All the results in the pictures are in cm. Scour length *(L)* and scour width *(W)* are function of pier shape factor. Figure 5.24 illustrates the bed configurations for different pier shapes. In this figure, the blue line represents the boundary of scour area and red line shows the deposition area.

The calibration Tables 3.3 and 3.4 are taken in to account in generating these drawings.

The summary of the scour hole dimensions are given in Table 5.7.

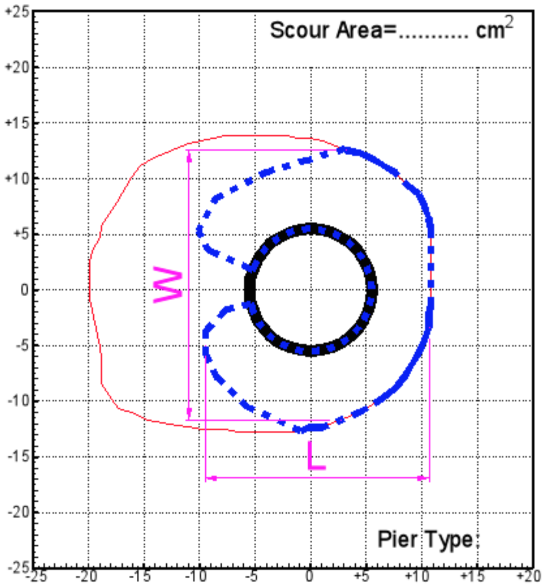

Figure 5.23 Definition sketch for scour around pier

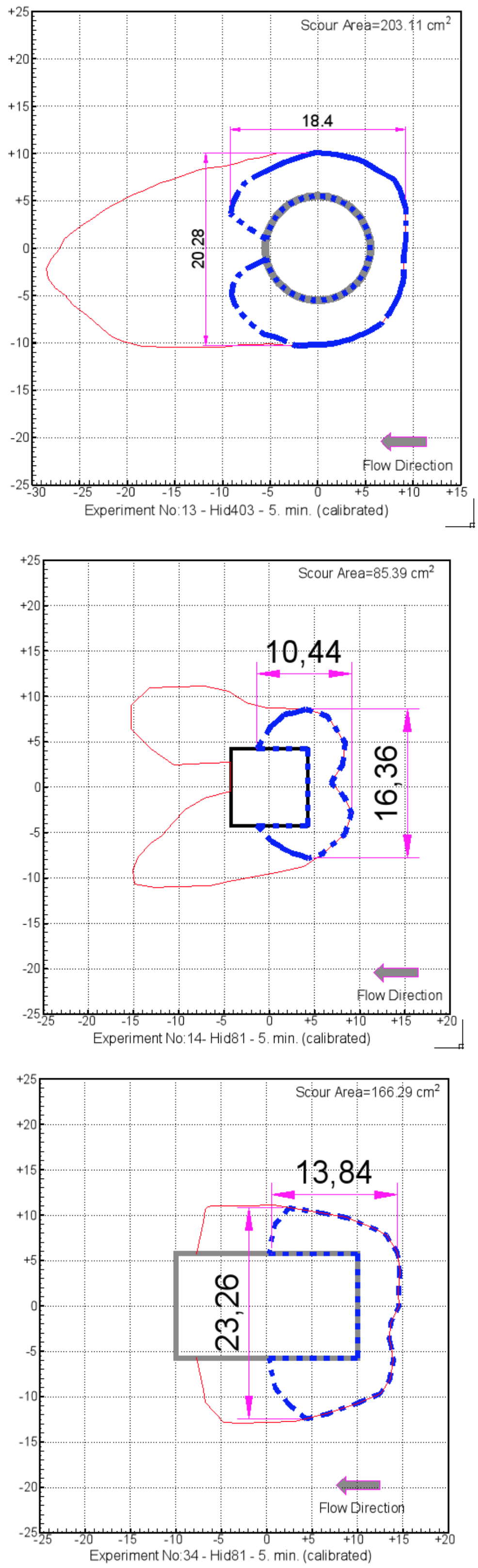

Figure 5.24 Bed configuration at t=5 min at the end of the steady flow

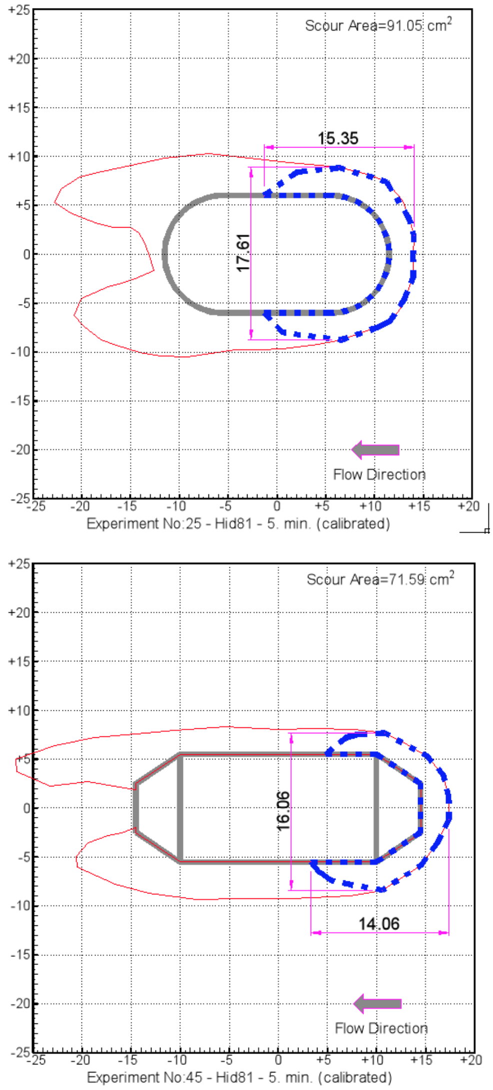

Figure 5.24 Bed configuration at t=5 min at the end of the steady flow (continued)

Table 5.7 Measurement scour hole dimensions after 5 min steady flow

Pier Shape	**Dimensions**		**Area (cm^2) A**
	L(cm)	**W(cm)**	
P1	18.35	19.08	156.89
P2	10.44	16.36	85.39
P3	13.84	23.26	166.29
P4	15.35	17.61	91.05
P5	14.06	16.06	71.59

The scour parameters concerning steady conditions are given in Table 5.8. Where; $b_c = bK_s$: characteristic pier width *(L)* and $a_c = \pi b_c^2$: characteristic cross sectional area of the pier *(L^2)*

Table 5.8 Dimensionless parameters corresponding to steady flow experiments

Pier Shape	**h/b_c**	**d_{se}/b_c**	**L/b_c**	**W/b_c**	**A/a_c**
P1	0.55	0.15	1.67	1.73	0.41
P2	0.50	0.18	0.88	1.37	0.19
P3	0.35	0.17	0.80	1.35	0.18
P4	0.62	0.14	1.58	1.81	0.31
P5	0.87	0.16	2.03	2.32	0.47

Das et. al. (2014) performed experiments by using circular, square, equilateral triangular and flat plate piers. They measured geometrical scour parameters under clear water conditions. They observed that the equilibrium scour parameters, namely scour depth, length, width and area were depended on the characteristic pier width. After the dimensional analysis, they proposed the following relation;

$$\frac{d_{se}}{b_c} = f_1\left(\frac{h}{b_c}\right) \tag{5.10}$$

The dimensionless scour length *(L/b_c)*, the dimensionless scour width *(W/b_c)* and the dimensionless scour area *(A/a_c)* can be expressed in terms of flow shallowness *(h/b_c)* and relative scour depth *(d_{se}/b_c)*.

$$\frac{L}{b_c} = f_2\left(\frac{h}{b_c}, \frac{d_{se}}{b_c}\right) \tag{5.11}$$

$$\frac{W}{b_c} = f_3\left(\frac{h}{b_c}, \frac{d_{se}}{b_c}\right) \tag{5.12}$$

$$\frac{A}{a_c} = f_4\left(\frac{h}{b_c}, \frac{d_{se}}{b_c}\right) \tag{5.13}$$

In this study, it is showed that the pier shape factor varies nonlinearly with flow shallowness *(h/b_c).* Accordingly, after the regression analysis, the following empirical relation was obtained for the pier shape coefficient.

$$K_s = 2.87e^{-1.80\left(\frac{h}{b_c}\right)} \tag{5.14}$$

Figure 5.25 shows the graph of the curve related to Eq. 5.14 together with experimental shape factor values. The observed shape factor values versus predicted ones are plotted in Figure 5.26. The deflection between the predicted and observed data is between -20% and +20%.

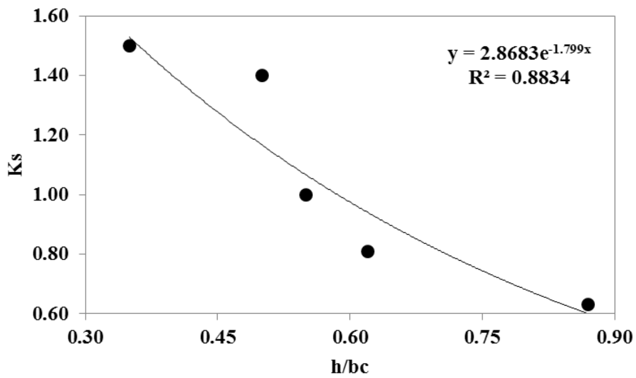

Figure 5.25 Pier shape factor values versus flow shallowness

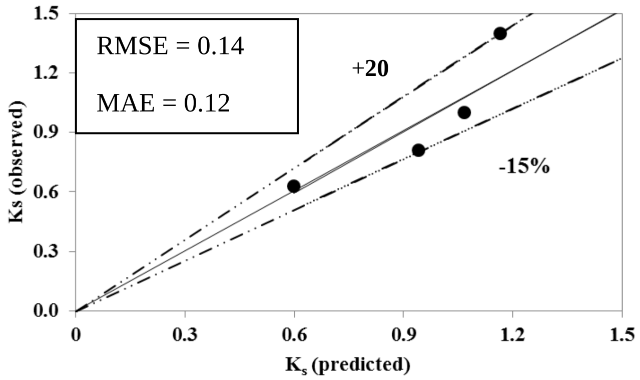

Figure 5.26 Observed and predicted pier shape factor values

Following Das et al. (2014), the empirical relation Eq. 5.15 for the relative scour depth was obtained;

$$\frac{d_{se}}{b_c} = -0.44\left(\frac{h}{b_c}\right)^2 + 0.55\left(\frac{h}{b_c}\right) \tag{5.15}$$

Figure 5.27 illustrates relative scour depth values calculated from Eq. 5.15 and measured ones. The deflection between the predicted and observed data is between -20% and +20%.

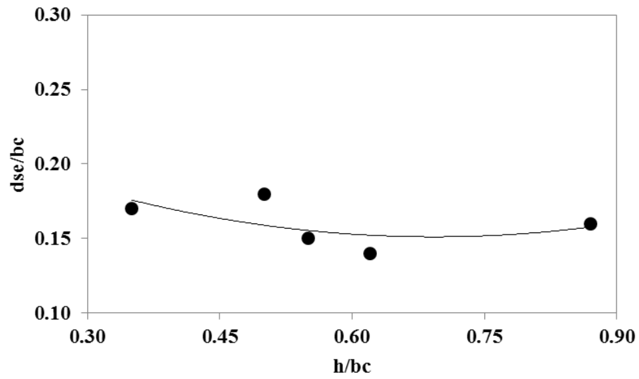

Figure 5.27 Relative equilibrium scour depths versus flow shallowness

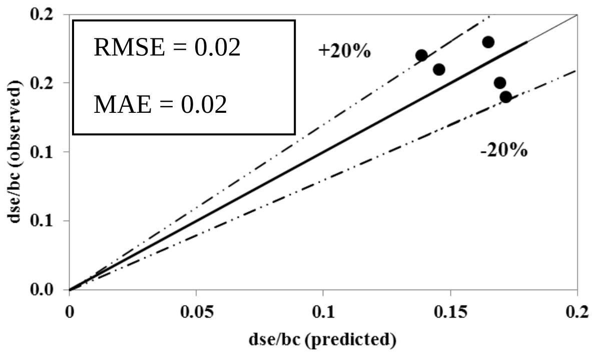

Figure 5.28 Observed and predicted relative equilibrium scour depths

The following empirical relations were obtained by taken into consideration the forms existing in the literature (such as Das et. al. (2014)).

The expression of the dimensionless scour length L/b_c was found as follows:

$$\frac{L}{b_c} = \left[\left(\frac{h}{b_c}\right) - 14.14\right]\frac{d_{se}}{b_c} + \left[1.9\left(\frac{h}{b_c}\right) + 2.47\right] \tag{5.16}$$

Observed and predicted values of dimensionless scour length are plotted in Figure 5.29. The deflection between the predicted and observed data is between -10% and +10%.

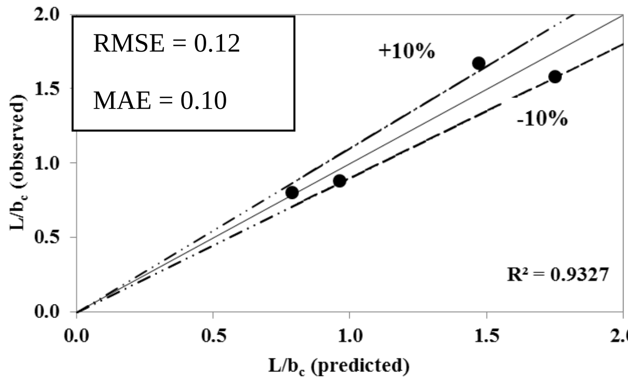

Figure 5.29 Observed and predicted dimensionless scour length L/b_c

The expression of the dimensionless scour width W/b_c was found as follows:

$$\frac{W}{b_c} = \left[\left(\frac{h}{b_c}\right) - 4.983\right]\frac{d_{se}}{b_c} + \left[1.693\left(\frac{h}{b_c}\right) + 1.443\right] \tag{5.17}$$

Observed and predicted values of dimensionless scour width are plotted in Figure 5.30. The deflection between the predicted and observed data is between -10% and +10%.

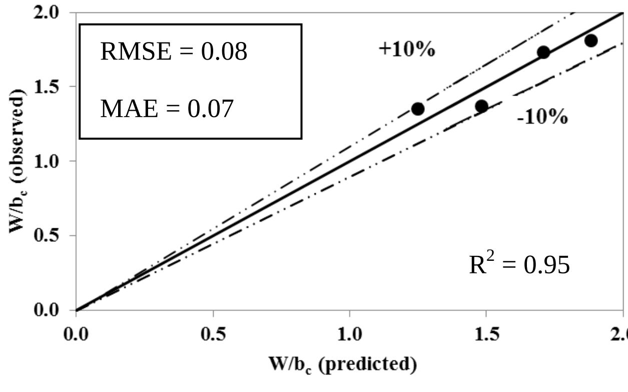

Figure 5.30 Observed and predicted dimensionless scour width W/b_c values

The expression of the dimensionless scour area A/a_c was found as follows:

$$\frac{A}{a_c}=\left[-1.059\left(\frac{h}{b_c}\right)+1.571\right]e^{\left[17.23\left(\frac{h}{b_c}\right)-17.085\right]\frac{d_{se}}{b_c}} \tag{5.18}$$

Observed and predicted values of dimensionless scour area are plotted in Figure 5.31. The deflection between the predicted and observed data is between -20% and +20%.

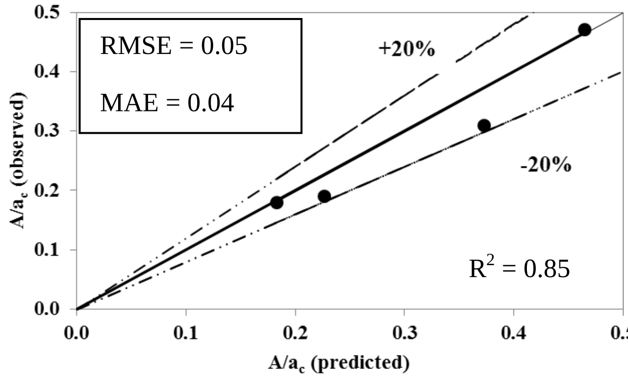

Figure 5.31 Observed and predicted dimensionless scour area A/a_c values

5.2 Analyses in Unsteady Flow Conditions

The unsteady flow results were analyzed in two sections: time dependent scour depth $d_s(t)$ and relative scour depth d_s/b. The pier shape factor values K_s were analyzed under unsteady flow conditions. The time variation of scour hole dimensions were analyzed. Also the equations in literature were tested with experimental findings and results were compared.

Chang et. al. (2004), Oliveto and Hager (2002, 2005), Lai et. al. (2009) and Lopez et. al. (2014) studied temporal variation of scour depths under unsteady flow conditions and showed that the recession period of hydrograph plays a minor role in scouring process. This fact is also observed in Figure 5.18 in which the final scour depths are reached at about 60% of the hydrograph duration.

The temporal variation of scour depth with increasing time can be expressed as mathematical function to fit scour time history data.

$$d_s(t) = a[1-\exp(-bt)] + c[1-\exp(-bt)] \tag{5.19}$$

5.2.1 The Computational Scour Depth Methods for Piers Under Unsteady Flow Conditions in Literature

Oliveto and Hager (2005) researched effect of unsteady flow on scour development. They presented the following for computing the time dependent scour variables under unsteady flow conditions. The general time dependent scour equation was presented in Eq. 5.4. The step of calculation method is presented below (Oliveto and Hager (2005)).

1. At time $t=t_0$ sediment movement starts when $F_d = u/(g' d_{50})^{1/2} \geq \Phi_\beta F_{di}$ where;

$$\Phi_\beta = 1-(2/3)\beta^{(1/4)} \tag{5.20}$$

$$\beta = D/B \tag{5.21}$$

$$F_{di} = 1.08 D_*^{1/12} (R_h / d_{50})^{1/6} \tag{5.22}$$

where;

$D_* = \left(g'/\upsilon^2\right)^{1/3} d_{50}$ dimensionless sediment size *(*υ=kinematic viscosity*)* (Oliveto and Hager (2002). In this study D_* = 42.5.

R_h = hydraulic radius

2. Suitable subdivision of total scour time t_e-t_0=$n\Delta t$ until the end of flood hydrograph at t_e. Typically Δt was equal to $t_e/10$.

3. At time $t=t_0$, $Z=0$ whereas at time $t=t_1$, $T_1 = \left[\sigma_g^{1/3}(g' d_{50})^{1/2} / (h_{0,1} D^2)^{1/3}\right]\Delta t$, where $h_{0,1}$ is the average approach depth

for $n=1$. Non-dimensional scour depth at T_1 is $Z_1 = 0.068\sigma_g^{-1/2} F_{d0,1}^{1.5} \log T_1$ and thus $z_1 = (h_{0,1} D^2)^{1/3} Z_1$. So the initial conditions at time $t=t_1$ are $z(t_1)=z_1$ and $Q=Q_1, h_0=h_1$.

4. At time $t=t_1$ (in the interval t_1, t_2) the relative scour depth is $Z_1 = z_1/(h_{1,2} D^2)^{1/3}$ where $h_{1,2}$ is the average approach depth. The corresponding time is $T_1=10^E$ where $Z_1 = z_1/(h_{1,2} D^2)^{1/3}$ and dimensional time is $t_1' = \left[(h_{1,2} D^2)^{1/3} / \sigma_g^{1/3} (g' d_{50})^{1/2}\right] T_1$ and $t_2' = t_1' + \Delta t$ so the results $T_1 = \left[\sigma_g^{1/3} (g' d_{50})^{1/2} / (h_{1,2} D^2)^{1/3}\right] t_2'$ with $Z_2 = 0.068\sigma_g^{-1/2} F_{d1,2}^{1.5} \log T_2$ and scour depth $z_1 = (h_{1,2} D^2)^{1/3} Z_2$. It is important that whereas t_1 and t_2 times are real times, t_1' and t_2' times are fictitious times. They are correspond to times $z=z_1$ and $z=z_2$ with approach flow depth $h_{1.2}$ and $F_d=F_{d1,2}$. In constant z_1 and z_2 are the scour depths at the real times t_1 and t_2.

5. This processes is repeated up to time $t_e=n\Delta t$, resulting in $z(t_e)=z_e$.

Hager and Unger (2010) researched the effect of peak flow rate on pier scour. They developed the formula previously proposed by Oliveto and Hager (2002,2005) and generalized temporal sour depth due to a single peaked flood wave. They combined Olivetto and Hager (2002) formula with Manning and Strickler equation $(q = KS_o^{1/2} h_0^{5/3})$. Oliveto and Hager (2002) formula becomes;

$$Z_M(T_M) = \left[Q_M(T_M)\right]^{0.8n} \log(\gamma T_M) \tag{5.23}$$

where,

$Z_M = z/z_M$ relative scour depth in flood peak

$T_M = t/t_M$ normalized time

Q_M = flood discharge (M subscript means peak flow)

n = hydrograph shape parameter (in this thesis n=5 found by trial and error method)

The computation of scour progress involves time step method $\Delta T_{M.}$ They offered optimum step length ΔT_M =0.01. First of all at $T_{M1} = \Delta T_M$, discharge Q_M is computed from Eq. 5.23 and it is substituted in Eq. 5.24 to obtain Z_{M1}.

$$Q_M = \left[T_M \exp(1 - T_M)\right]^n \tag{5.24}$$

The corresponding time is $T_{M1} = \gamma^{-1} x\ 10^E$ with the exponent $E = Z_M / Q_M^{0.8n}$. For step $T_{M2} = 2\Delta T_M$ discharge is $Q_{M2} = Q_{M1} + \Delta Q$ and result scour depth increase $Z_{M2} = Z_{M1} + \Delta Z_M$. This routine is applied until the entire flood wave has passed, resulting in the end (subscript e) scour depth Z_{Me}.

$$\frac{Z}{Z_{Me}} = 0.5\left(1 + \tanh\left\{(1.1 + 0.98n)\left[T_M - \left(0.92 - 0.66 \times 0.7^n\right)\right]\right\}\right) \tag{5.25}$$

where; $Z = z/z_R$ relative scour depth

5.2.2 Analyses of Time Scale of d_s/b for Circular Pier

Time dependent scour depths $d_s(t)$ are illustrated in Figure 5.32 together with hydrograph.

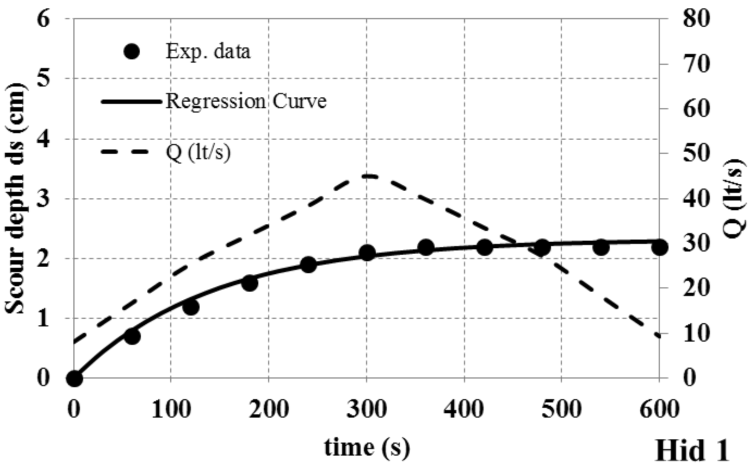

Figure 5.32 Time dependent scour depths $d_s(t)$for each hydrographs

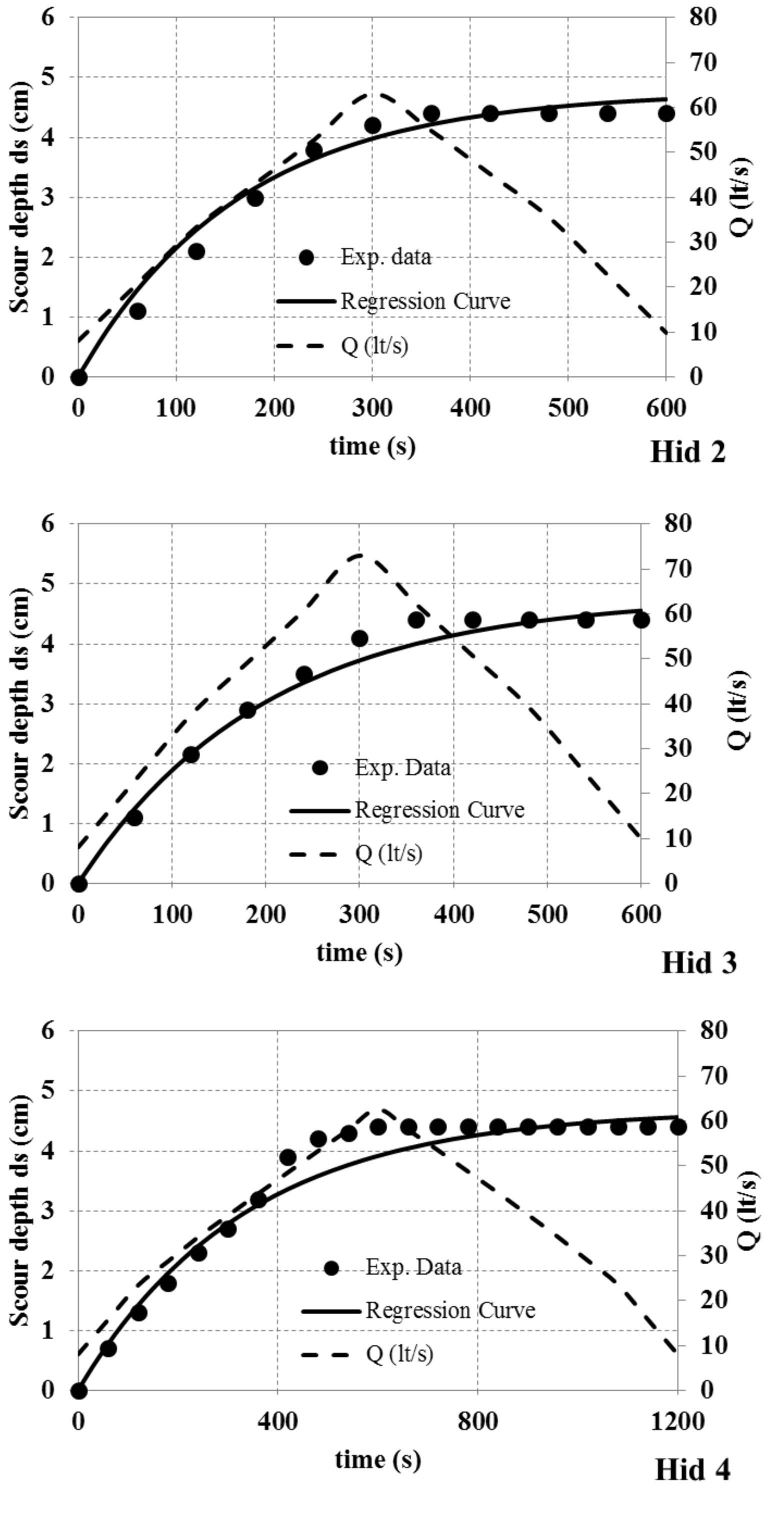

Figure 5.32 Time dependent scour depths $d_s(t)$for each hydrographs (continued)

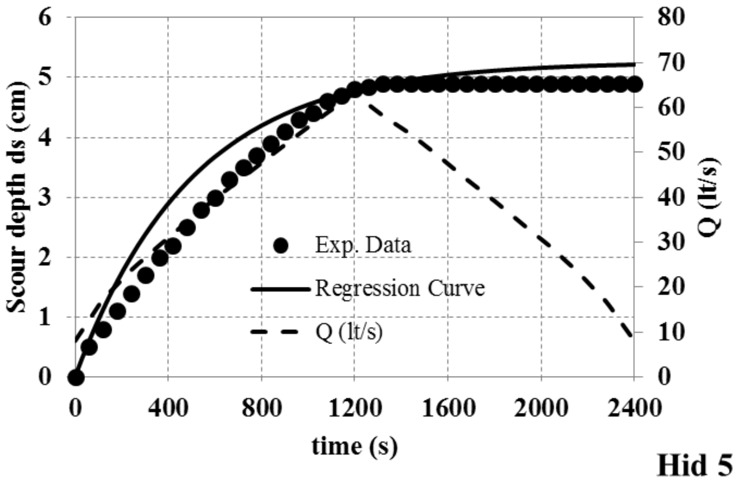

Figure 5.32 Time dependent scour depths $d_s(t)$for each hydrographs (continued)

Overall, the values of the *a*, *b*, *c* and *d* were observed by nonlinear regression analysis and presented in Table 5.9.

Table 5.9 Coefficients of Eq. 5.19 for each hydrographs

Hydrograph	a	b	c
Hid 1	0.590	0.007	1.729
Hid 2	1.968	0.006	2.799
Hid 3	1.906	0.005	2.888
Hid 4	2.191	0.003	2.500
Hid 5	2.786	0.002	2.473

Figure 5.33 gives the measured values and the calculated ones by using Oliveto and Hager (2005) and Hager and Unger (2010). The computed d_s values for Hid 1 are presented in Table 5.10 understanding computational scheme of the Oliveto and Hager (2005) method.

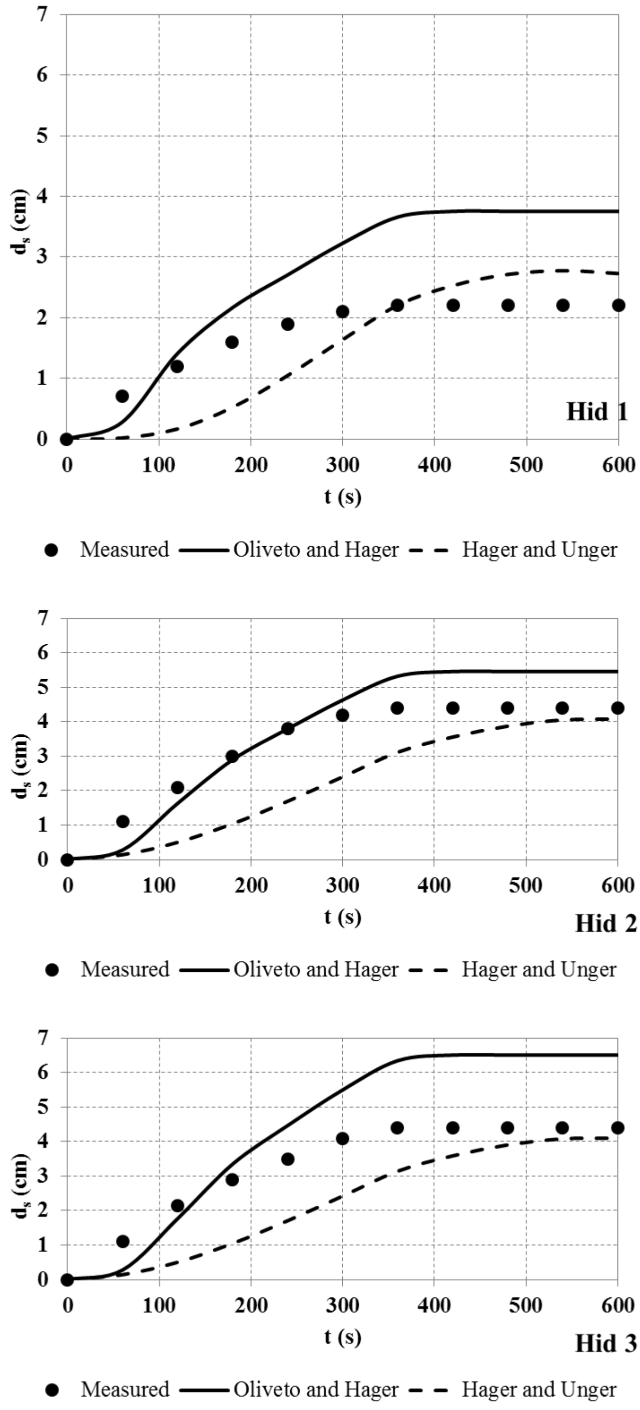

Figure 5.33 Comparison of measured and calculated scour depth values with Oliveto and Hager (2005) and Hager and Unger (2010)

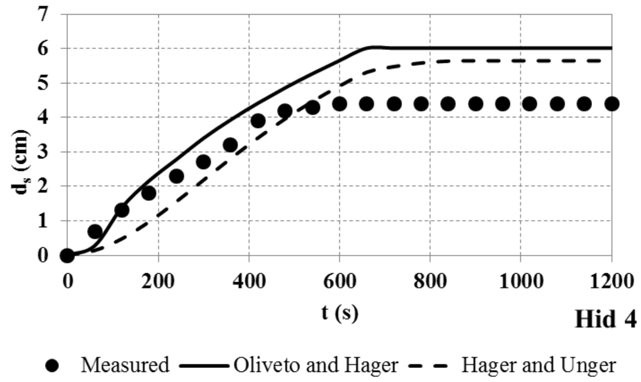

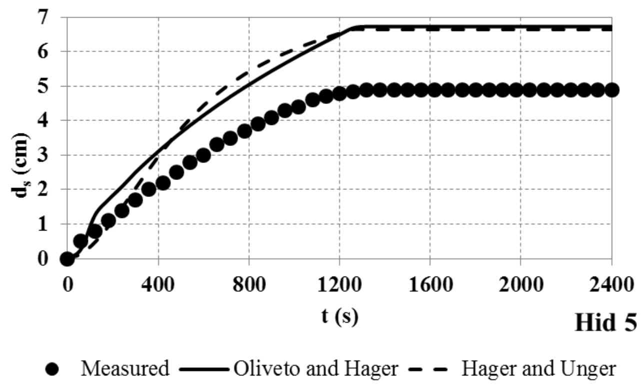

Figure 5.33 Comparison of measured and calculated scour depth values with Oliveto and Hager (2005) and Hager and Unger (2010) (continued)

The computed error measures of $RMSE$, MAE and R^2 are summarized in Table 5.10. The sediment entrainment is predicted well under Hid 1 hydrograph with Oliveto and Hager (2005) suggestion. As flow increases, the estimates are away from the measured values.

Table 5.10 Computed $RMSE$, MAE and R^2 values

	Hid 1	Hid 2	Hid 3	Hid 4	Hid 5	Hid 1	Hid 2	Hid 3	Hid 4	Hid 5
Root Mean Square Error, RMSE (cm)	1.14	0.76	1.52	1.21	1.51	0.65	1.27	1.20	0.91	1.52
Mean Absolute Error, MAE (cm)	0.98	0.64	1.31	1.07	1.43	0.55	1.07	1.01	0.82	1.42
R^2	0.90	0.91	0.91	0.98	0.98	0.21	0.53	0.57	0.87	0.98
	Oliveto and Hager (2005)					Hager and Unger (2010)				

5.2.3 Analyses of Time Scale of d_s/b for Square Pier

Figure 5.34 shows that time dependent scour depth $d_s(t)$ values together with hydrograph.

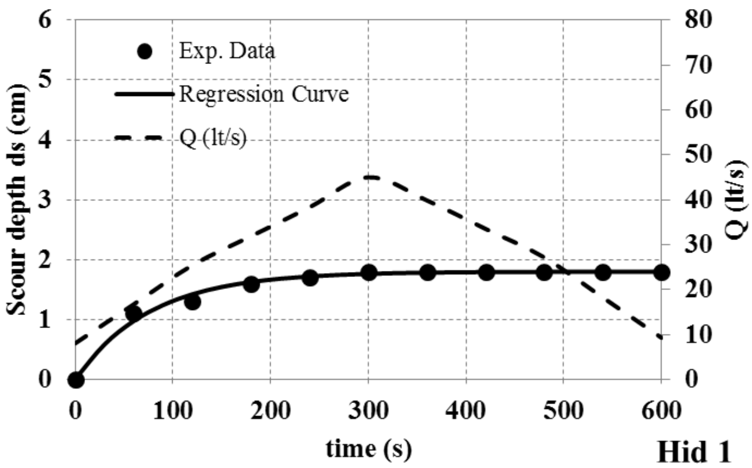

Figure 5.34 Time dependent scour depths $d_s(t)$for each hydrographs

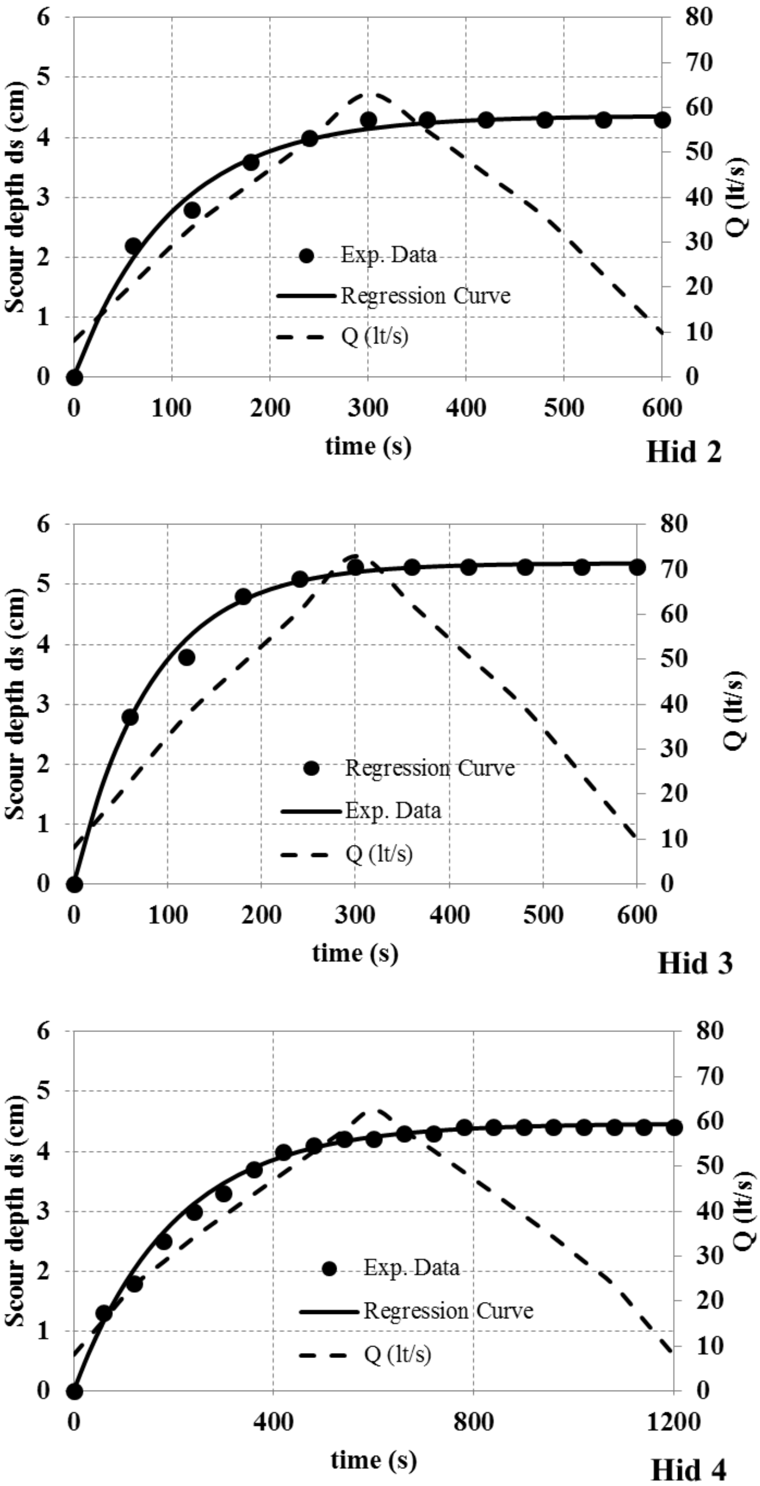

Figure 5.34 Time dependent scour depths $d_s(t)$for each hydrographs (continued)

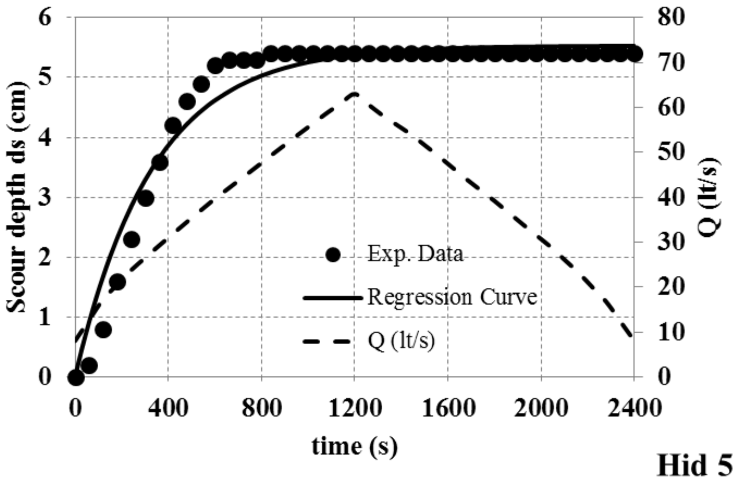

Figure 5.34 Time dependent scour depths $d_s(t)$for each hydrographs (continued)

The increase in time dependent scour depth with increasing time behavior was expressed as before with Eq. 5.19. Overall, the values of the *a*, *b*, *c* and *d* were observed by nonlinear regression analysis and presented in Table 5.11.

Table 5.11 Coefficients of Eq. 5.19 for each hydrographs

Hydrograph	a	b	c
Hid 1	-2.829	0.013	4.628
Hid 2	-0.898	0.010	5.258
Hid 3	0.791	0.012	4.564
Hid 4	4.764	0.005	-0.299
Hid 5	-5.852	0.003	11.384

5.2.4 Analyses of Time Scale of d_s/b for Rectangular Pier

Time dependent scour depths $d_s(t)$ are illustrated in Figure 5.35 together with hydrograph.

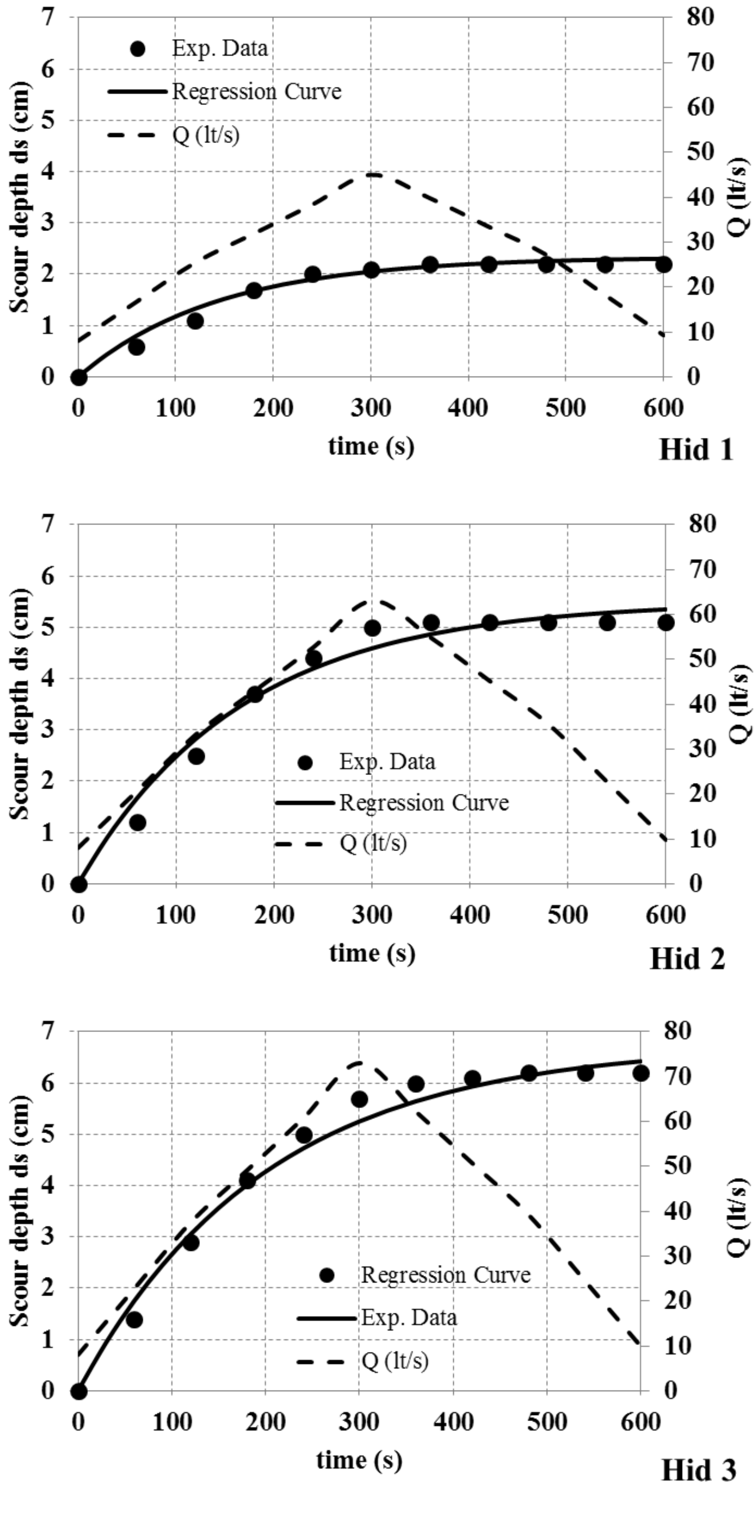

Figure 5.35 Time dependent scour depths $d_s(t)$for each hydrographs

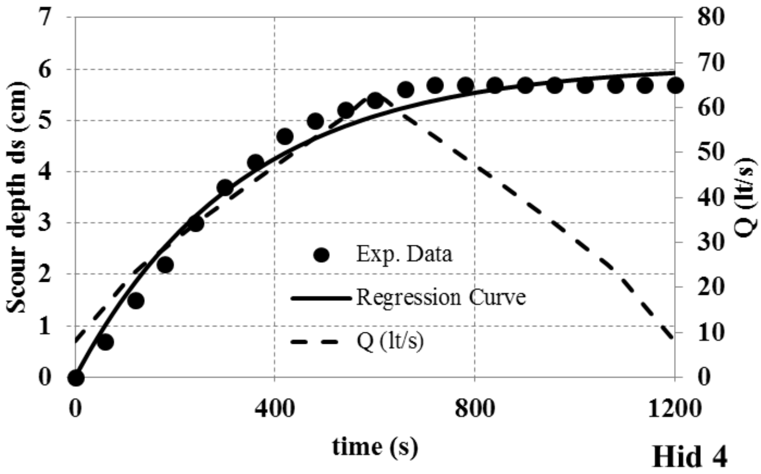

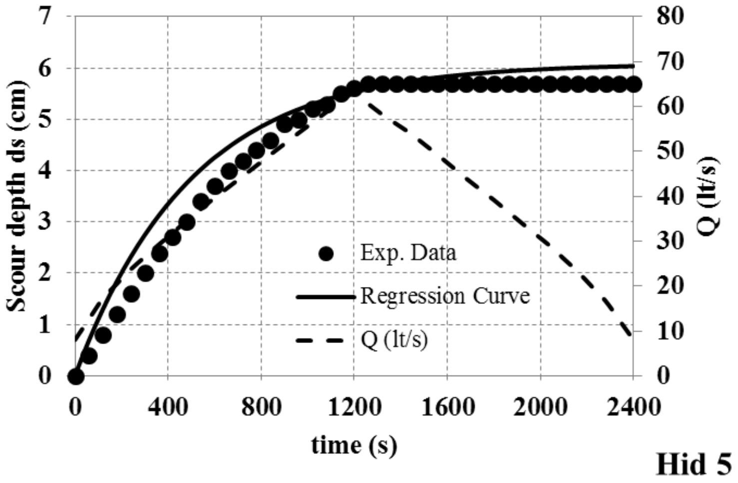

Figure 5.35 Time dependent scour depths $d_s(t)$for each hydrographs (continued)

The increase in time dependent scour depth with increasing time behavior was expressed as before with Eq. 5.19. Overall, the values of the *a*, *b*, *c* and *d* were obtained by nonlinear regression analysis and presented in Table 5.12.

Table 5.12 Coefficients of Eq. 5.18 for each hydrographs

Hydrograph	a	b	c
Hid 1	3.635	0.007	-1.298
Hid 2	9.918	0.006	-4.419
Hid 3	16.007	0.005	-9.247
Hid 4	-33.912	0.003	40.003
Hid 5	21.027	0.002	-14.941

5.2.5 Analyses of Time Scale of d_s/b for Rectangular with Circular Nose Pier

Figure 5.36 shows that time dependent scour depth $d_s(t)$ values together with hydrograph.

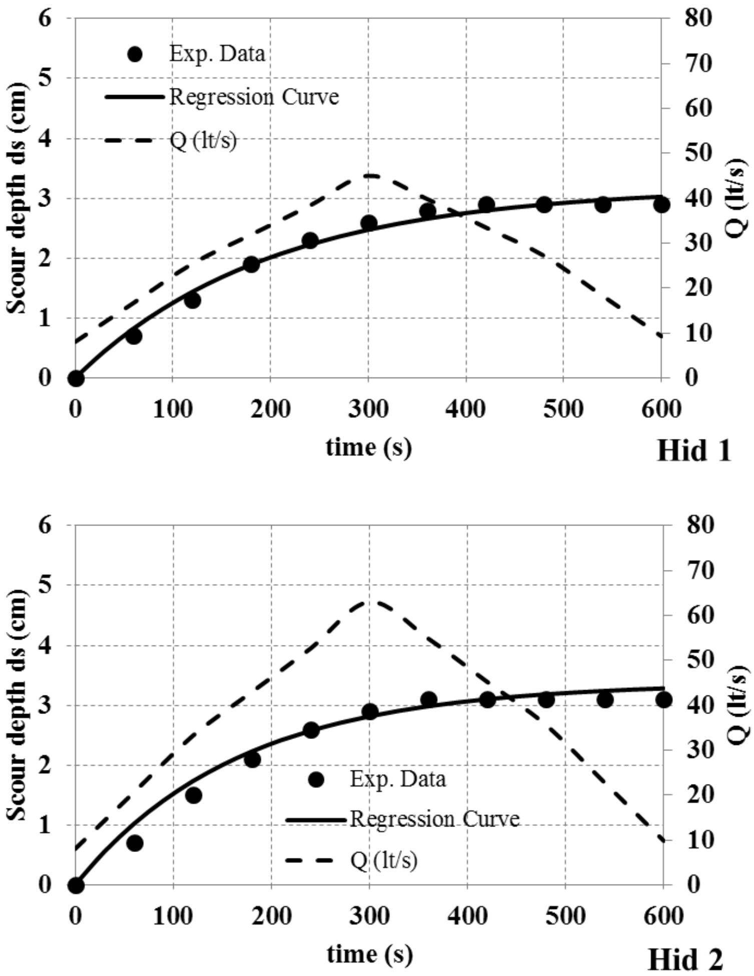

Figure 5.36 Time dependent scour depths $d_s(t)$for each hydrographs

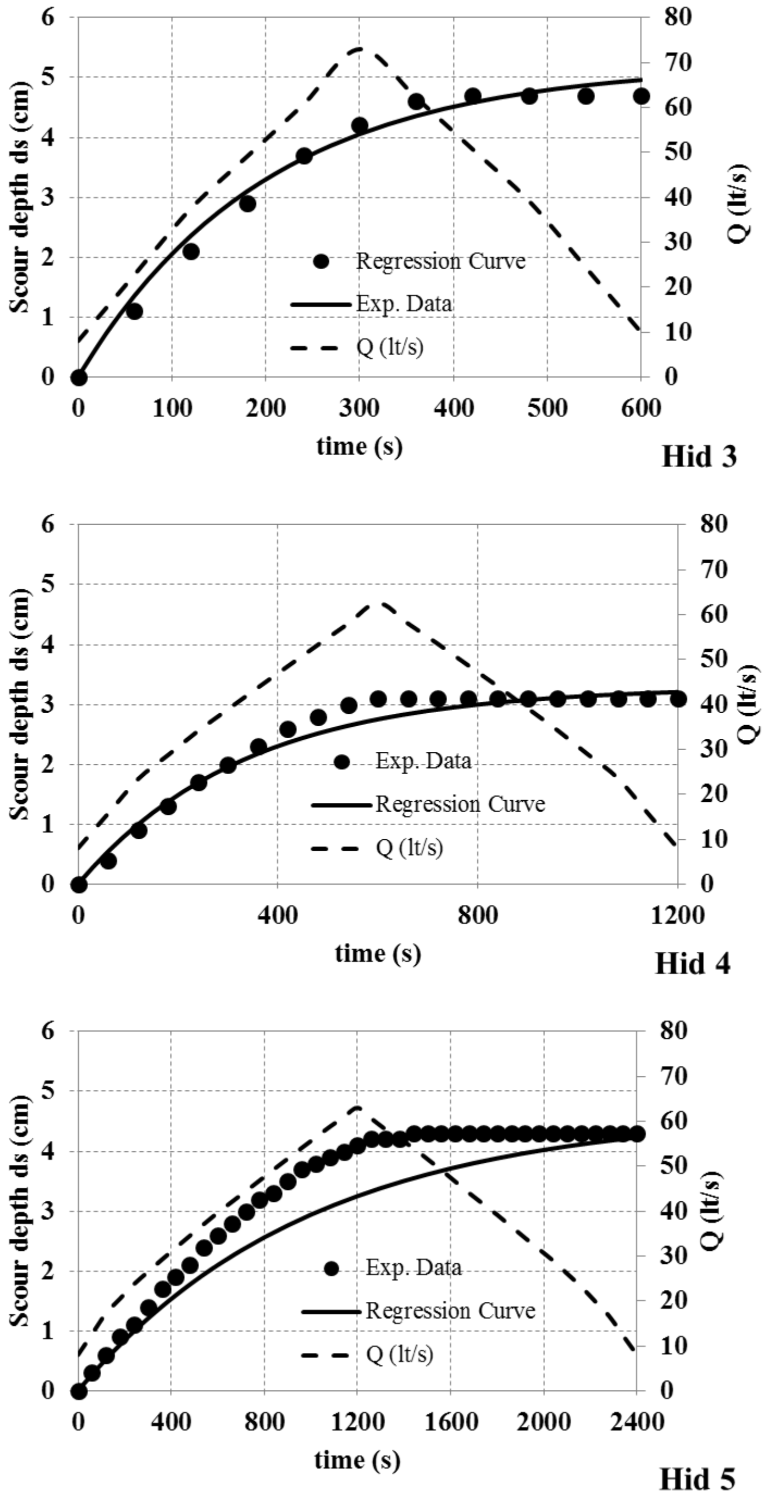

Figure 5.36 Time dependent scour depths $d_s(t)$for each hydrographs (continued)

The increase in time dependent scour depth with increasing time behavior was expressed as before with Eq. 5.19. Overall, the values of the *a, b, c* and *d* were obtained by nonlinear regression analysis and presented in Table 5.13.

Table 5.13 Coefficients of Eq. 5.18 for each hydrographs

Hydrograph	a	b	c
Hid 1	0.775	0.005	2.410
Hid 2	7.464	0.006	-4.091
Hid 3	0.525	0.005	4.696
Hid 4	-4.429	0.003	7.727
Hid 5	-5.010	0.001	9.662

5.2.6 Analyses of Time Scale of d_s/b for Rectangular with Trapezoidal Nose Pier

Figure 5.37 depicted that time dependent scour depth $d_s(t)$ values together with hydrograph.

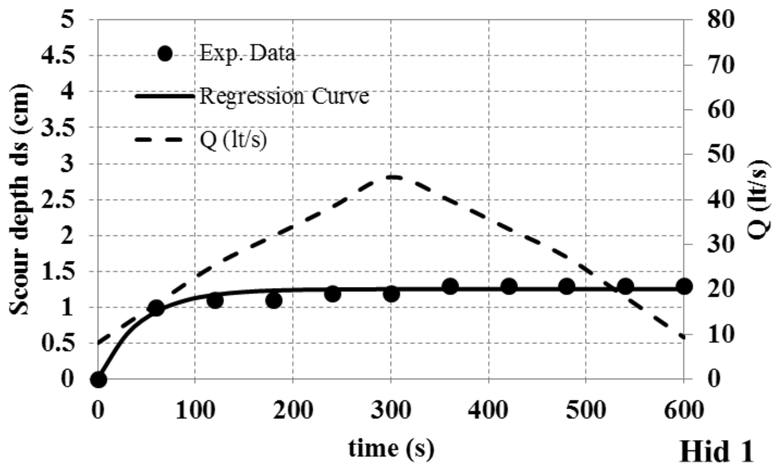

Figure 5.37 Time dependent scour depths $d_s(t)$for each hydrographs

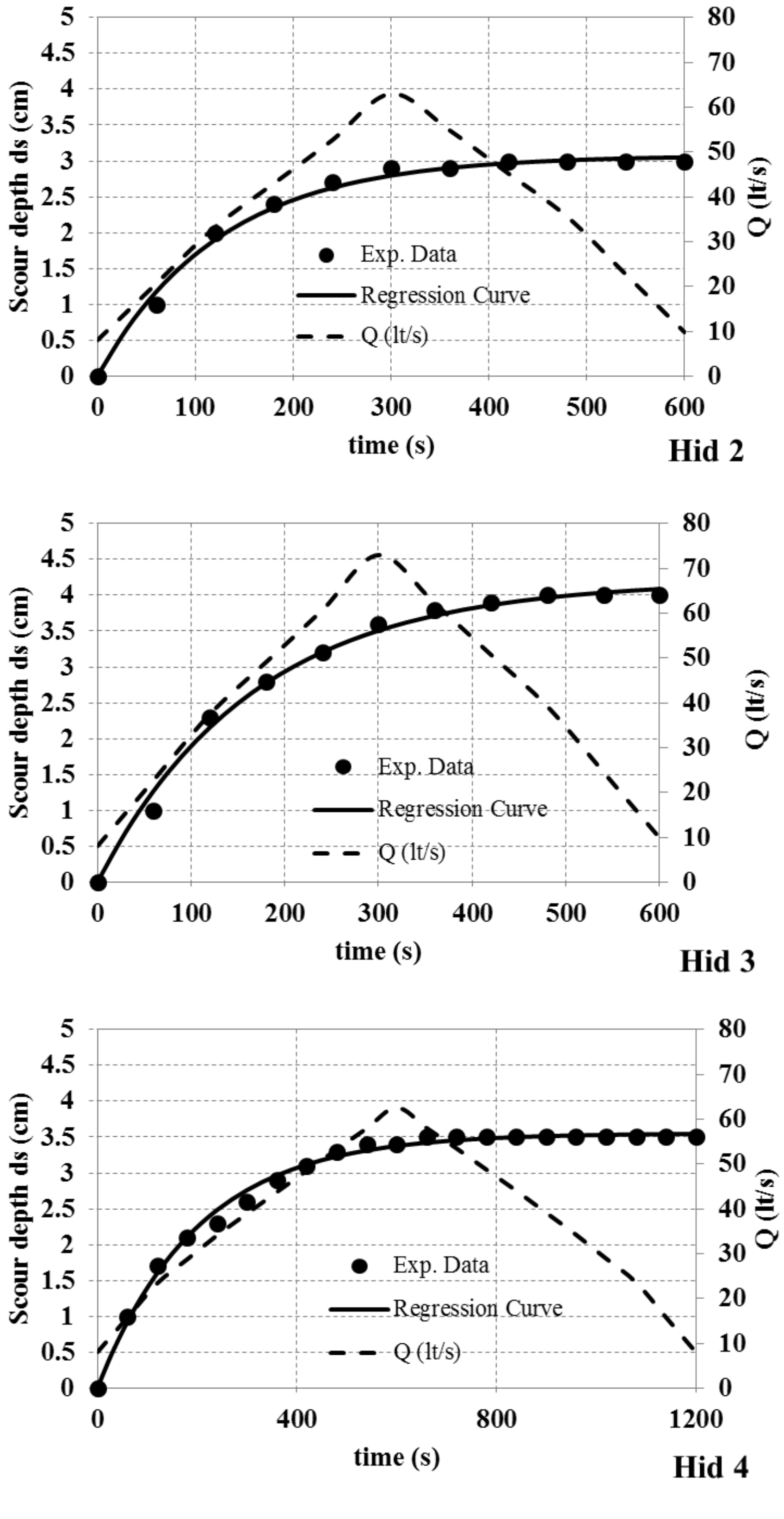

Figure 5.37 Time dependent scour depths $d_s(t)$for each hydrographs (continued)

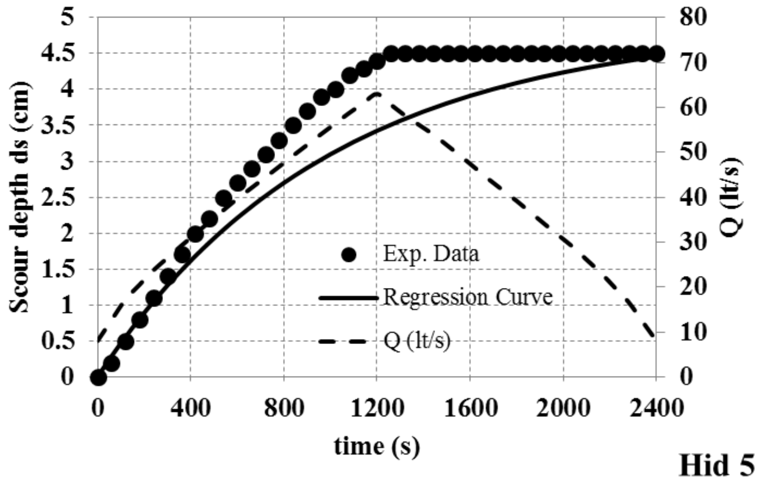

Figure 5.37 Time dependent scour depths $d_s(t)$for each hydrographs (continued)

The increase in time dependent scour depth with increasing time behavior was expressed as before with Eq. 5.19. Overall, the values of the *a*, *b*, *c* and *d* were obtained by nonlinear regression analysis and presented in Table 5.14.

Table 5.14 Coefficients of Eq. 5.18 for each hydrographs

Hydrograph	a	b	c
Hid 1	3.126	0.023	-1.874
Hid 2	2.677	0.008	0.400
Hid 3	3.274	0.006	0.929
Hid 4	1.171	0.005	2.383
Hid 5	24.908	0.001	-20.006

5.2.7 Effect of Pier Shape on Scouring under Unsteady Flow Conditions

The temporal variations of the scour depth under different hydrographs are plotted in Figure 5.38 for various pier shapes.

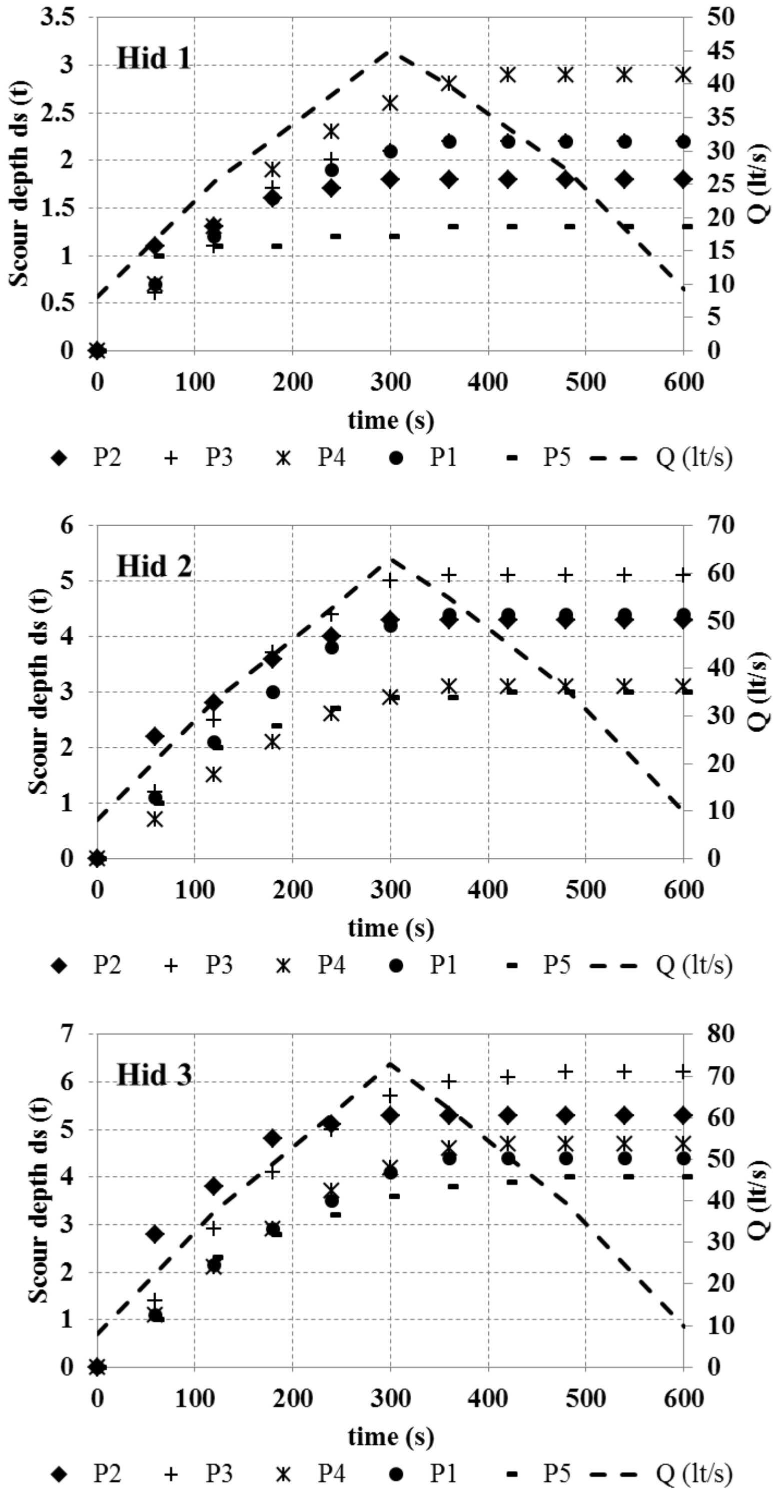

Figure 5.38 Scour depths versus time under unsteady flow conditions

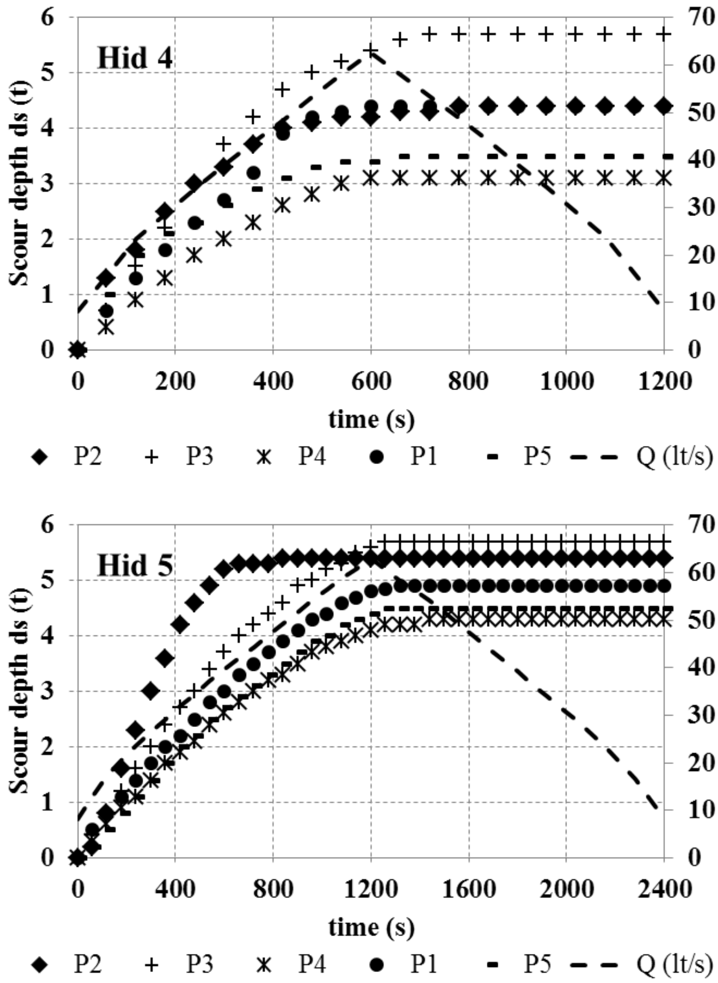

Figure 5.38 Scour depths versus time under unsteady flow conditions (continued)

The observed pier shape factor values are presented in Table 5.15 in terms of hydrographs peak flow rates and hydrograph duration.

Table 5.15 Observed pier shape factor values K_s according to Hydrographs peak flow rates

Pier Shape	**b (mm)**	**L (mm)**	**L/b**	**t_p (min)**	**Q_p (m^3/s)**	**h/b**	**K_s (calc.)**
P1	110	110	1.00	5	0.045	1.85	1.00
P1	110	110	1.00	5	0.063	2.06	1.00
P1	110	110	1.00	5	0.073	2.14	1.00
P1	110	110	1.00	10	0.063	2.06	1.00
P1	110	110	1.00	20	0.063	2.06	1.08
P2	850	850	1.00	5	0.045	2.40	1.05
P2	850	850	1.00	5	0.063	2.66	1.08
P2	850	850	1.00	5	0.073	2.77	1.25
P2	850	850	1.00	10	0.063	2.66	1.08
P2	850	850	1.00	20	0.063	2.66	1.25
P3	115	200	1.74	5	0.045	1.87	1.18
P3	115	200	1.74	5	0.063	2.10	1.25
P3	115	200	1.74	5	0.073	2.19	1.42
P3	115	200	1.74	10	0.063	2.10	1.33
P3	115	200	1.74	20	0.063	2.10	1.33
P4	120	230	1.92	5	0.045	1.70	1.11
P4	120	230	1.92	5	0.063	1.88	0.73
P4	120	230	1.92	5	0.073	1.96	1.00
P4	120	230	1.92	10	0.063	1.88	0.73
P4	120	230	1.92	20	0.063	1.88	0.92
P5	110	300	2.73	5	0.045	1.85	0.58
P5	110	300	2.73	5	0.063	2.06	0.67
P5	110	300	2.73	5	0.073	2.14	0.83
P5	110	300	2.73	10	0.063	2.06	0.75
P5	110	300	2.73	20	0.063	2.06	0.92

5.2.8 Estimation of Scour Hole Shape under Unsteady Flow Conditions

The scour hole measurements were performed with the aid of data from the camera and laser meter combined with Surfer software program at the end of each experiment.

5.2.8.1 Scour Hole Measurements for Circular Pier

Figure 5.39 shows the video camera picture before the image processing for different hydrographs.

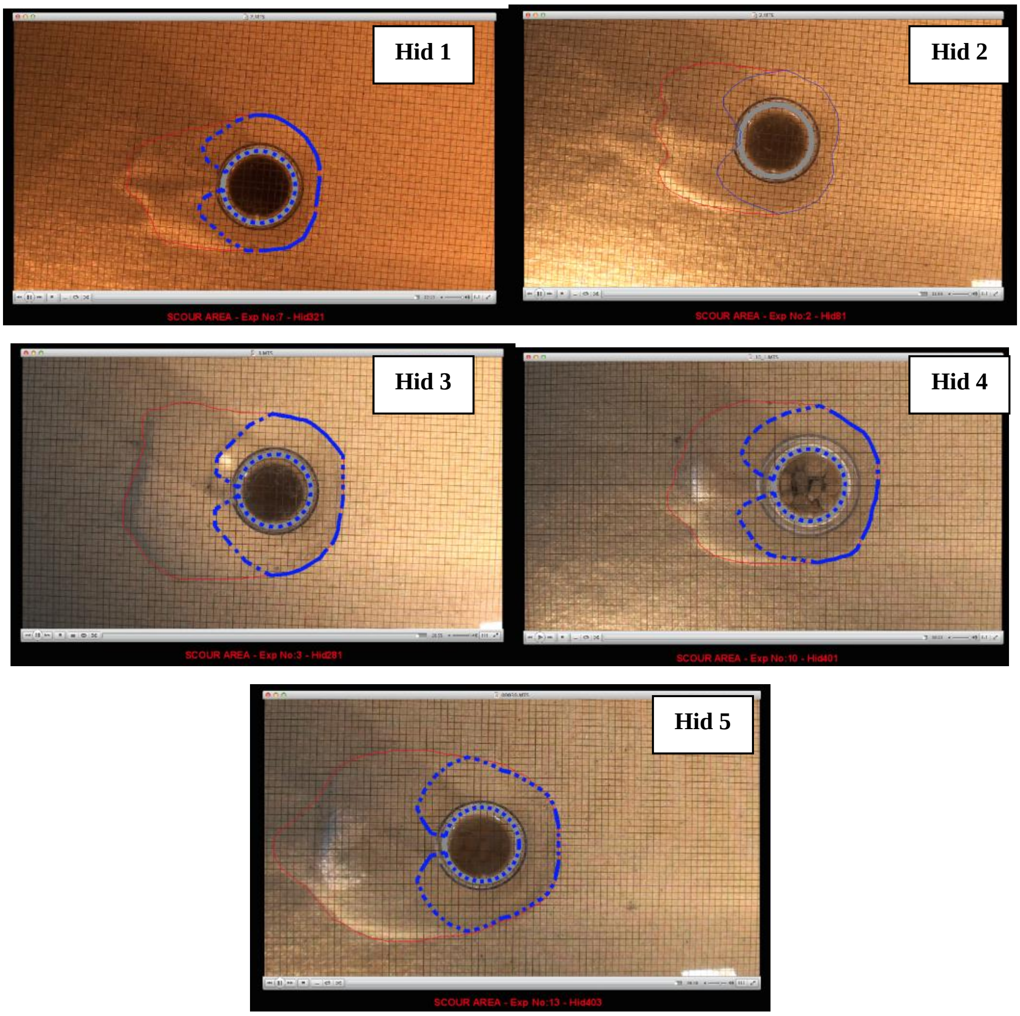

Figure 5.39 Video Camera 1 data before image processing

Figure 5.40, 5.41, 5.42, 5.43 and 5.44 illustrate the development of scour hole around the circular pier, respectively under Hid 1, Hid 2, Hid 3, Hid 4 and Hid 5. Surfer map from the laser meter readings at the end of the experiments formed by image processing. Pink pants correspond to laser meter readings, camera measures illustrated with blue pants.

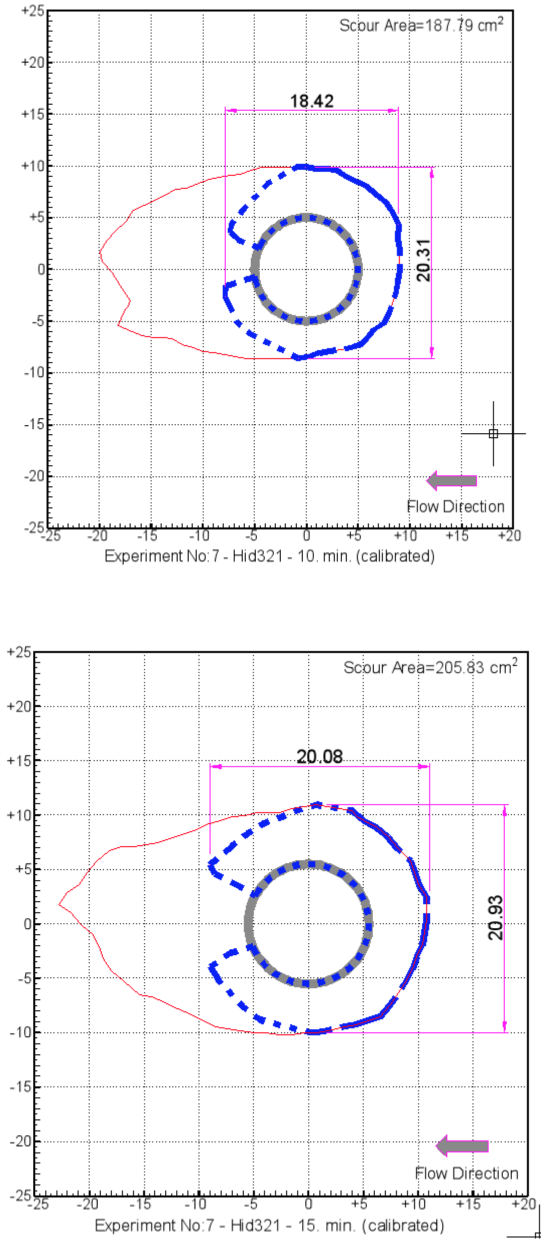

Figure 5.40 Bed configuration at t=5 min and t=10 min for Hid 1

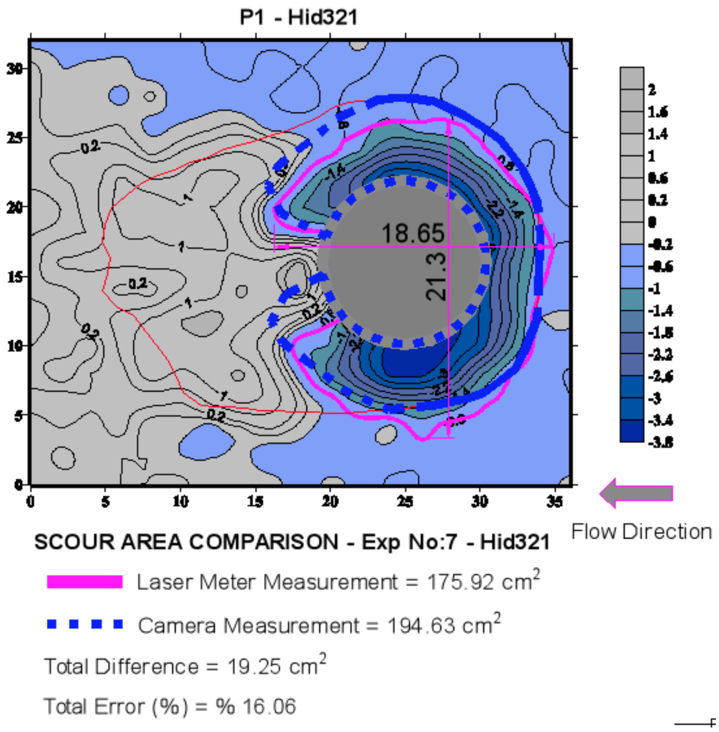

Figure 5.40 Bed configuration at t=5 min and t=10 min for Hid 1 (continued)

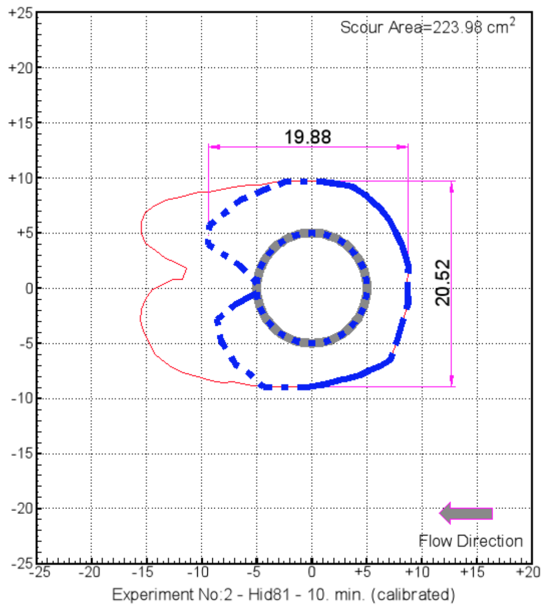

Figure 5.41 Bed configuration at t=5 min and t=10 min for Hid 2

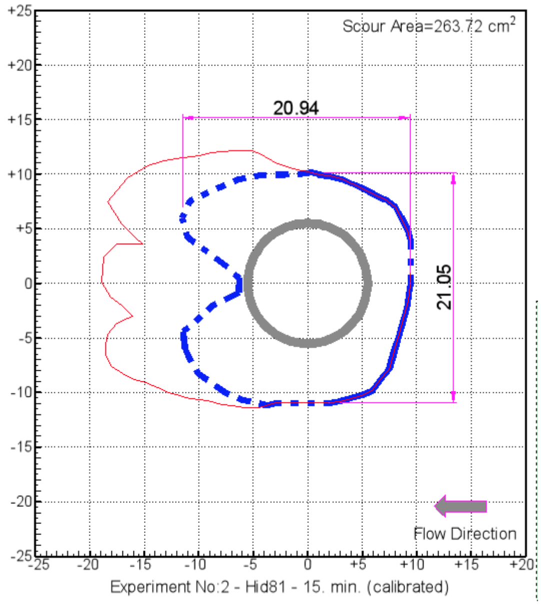

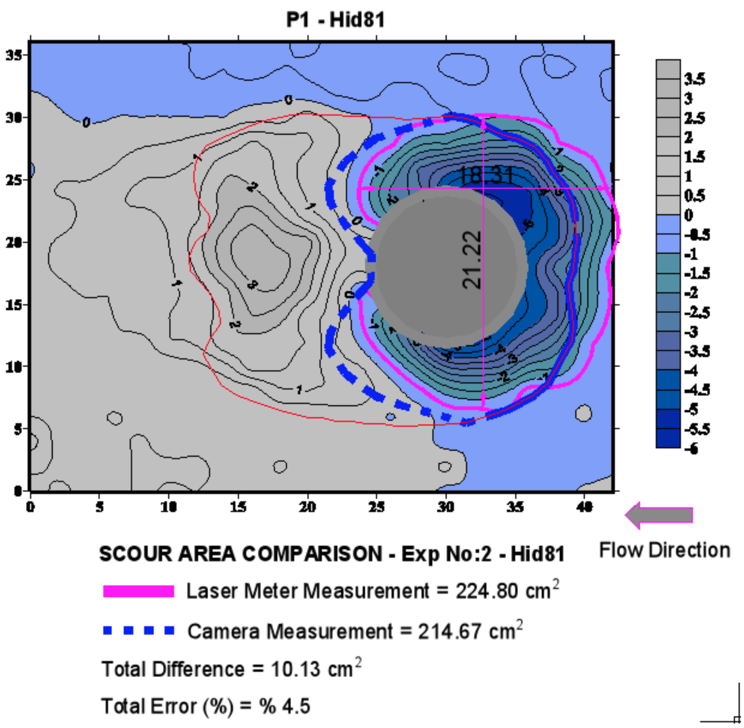

Figure 5.41 Bed configuration at t=5 min and t=10 min for Hid 2 (continued)

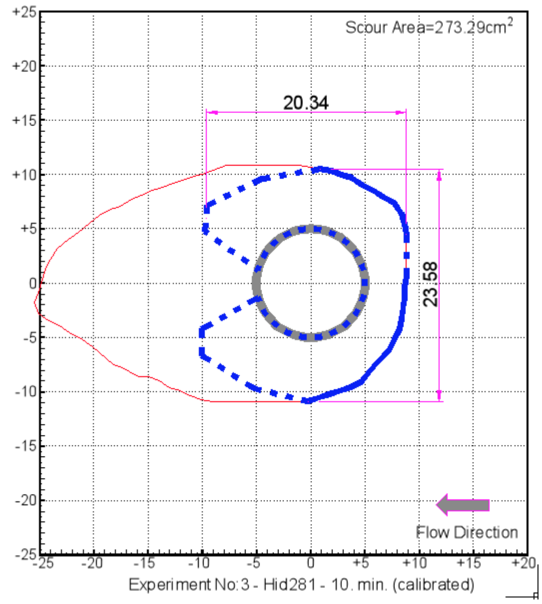

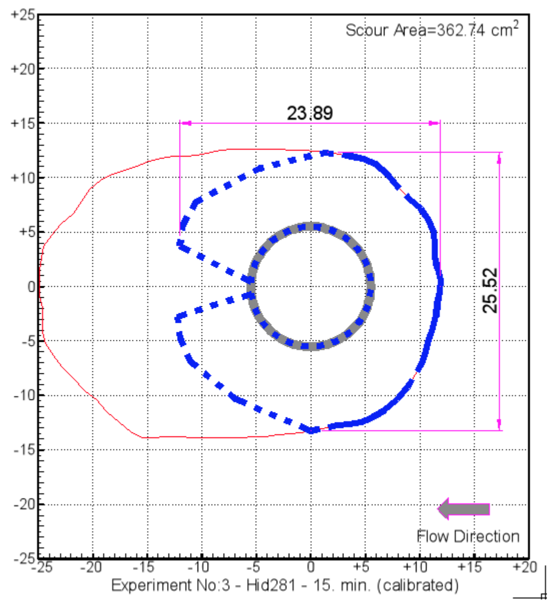

Figure 5.42 Bed configuration at t=5 min and t=10 min for Hid 3

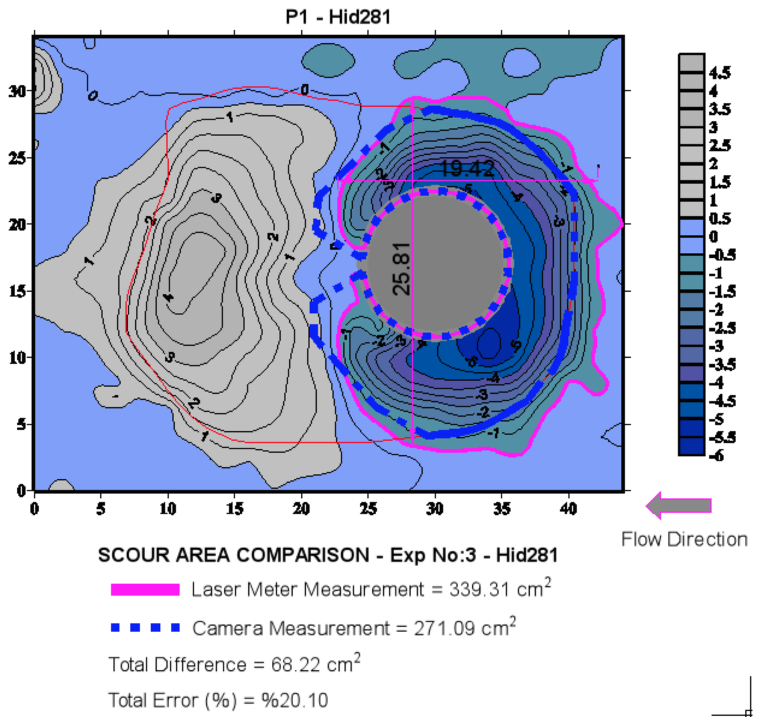

Figure 5.42 Bed configuration at t=5 min and t=10 min for Hid 3 (continued)

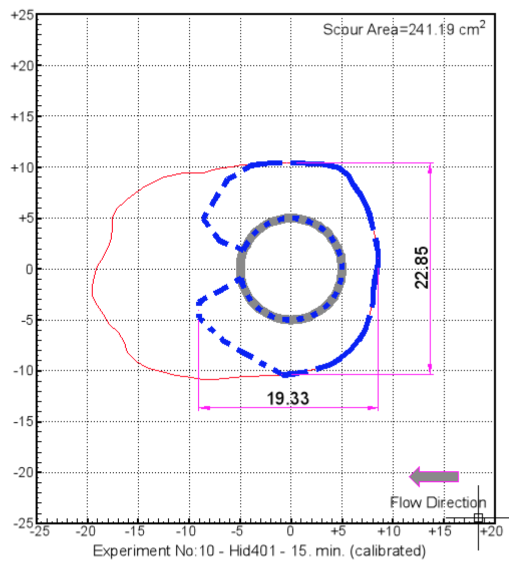

Figure 5.43 Bed configuration at t=10 min and t=20 min for Hid 4

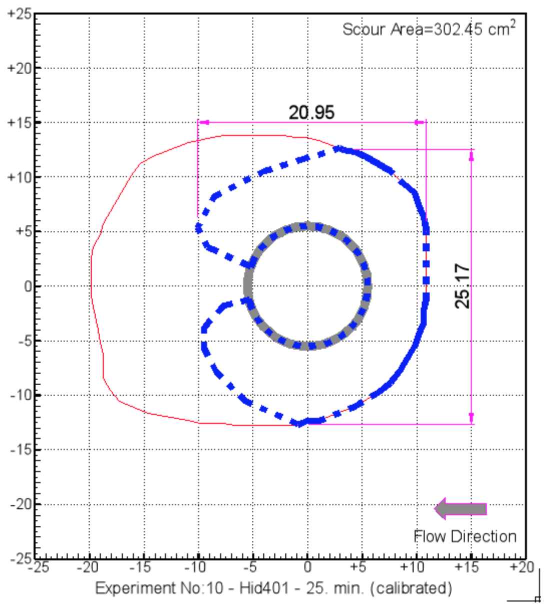

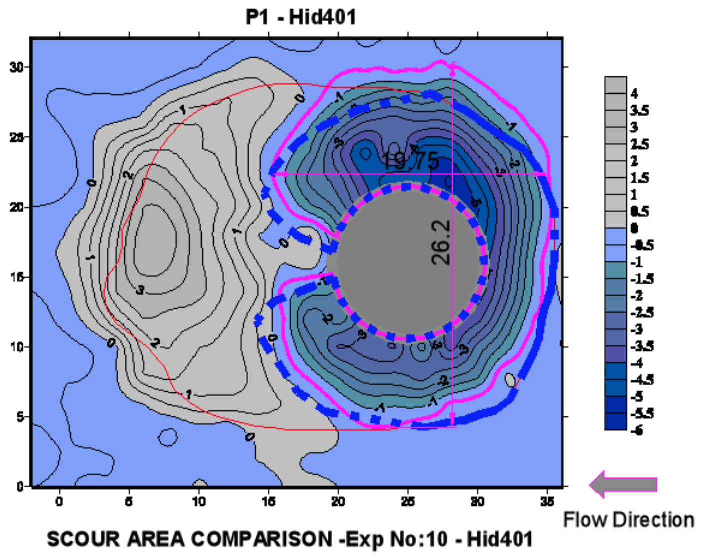

Figure 5.43 Bed configuration at t=10 min and t=20 min for Hid 4 (continued)

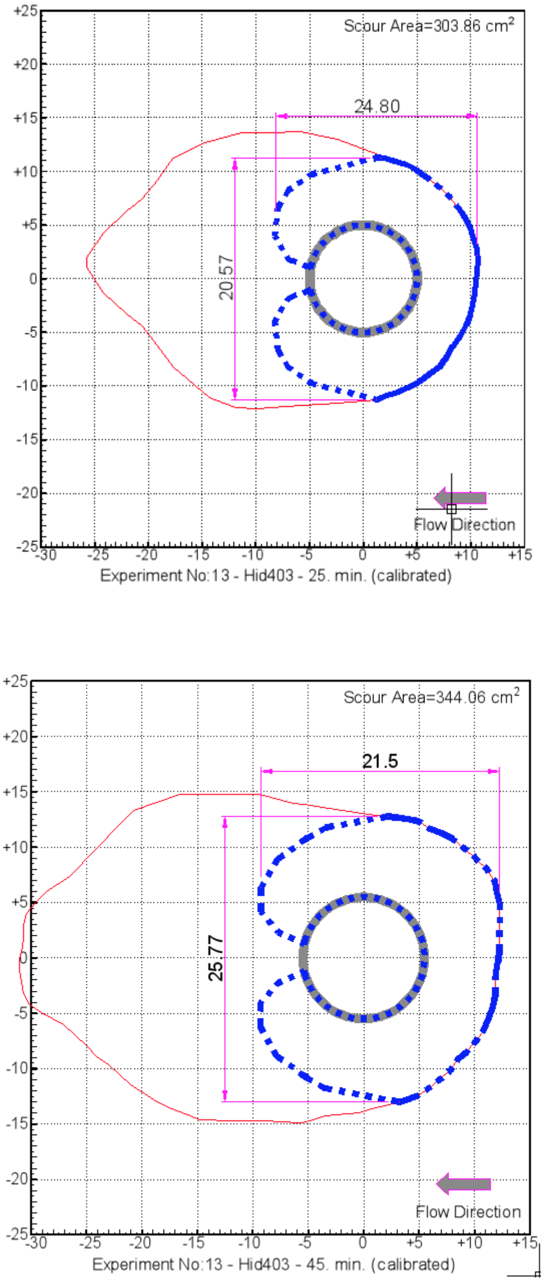

Figure 5.44 Bed configuration at t=20 min and t=40 min for Hid 5

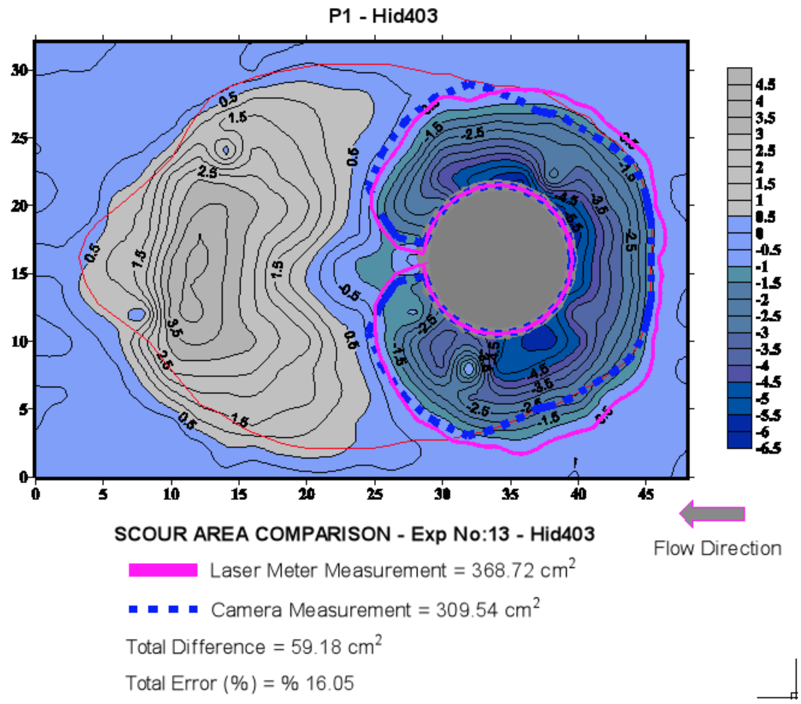

Figure 5.44 Bed configuration at t=20 min and t=40 min for Hid 5 (continued)

The observed scour hole dimensions are summarized for circular pier in Table 5.16.

Table 5.16 Scour hole measurements for circular pier

Hyd. ID	b (cm)	Time (min.)	Water Depth (cm)	Dimensions			Area (cm^2)
				d_{s1} (cm)	L(cm)	W(cm)	
Hid 1	11	5	20.39	3.8	18.42	20.31	187.79
Hid 1	11	10	6.00	3.9	20.08	20.93	205.83
Hid 2	11	5	22.61	5.8	19.88	20.52	223.98
Hid 2	11	10	6.00	6.1	20.94	21.05	263.62
Hid 3	11	5	23.52	5.8	20.34	23.58	273.29
Hid 3	11	10	6.00	6.1	23.89	25.52	362.74
Hid 4	11	10	22.61	6.1	19.33	22.85	241.19
Hid 4	11	20	6.00	6.1	20.95	25.17	302.45
Hid 5	11	20	22.61	6.5	20.57	24.80	303.86
Hid 5	11	40	6.00	6.6	21.50	25.77	344.06

5.2.8.2 Scour Hole Measurements for Square Pier

Figure 5.45 shows the video camera picture before the image processing for different hydrographs.

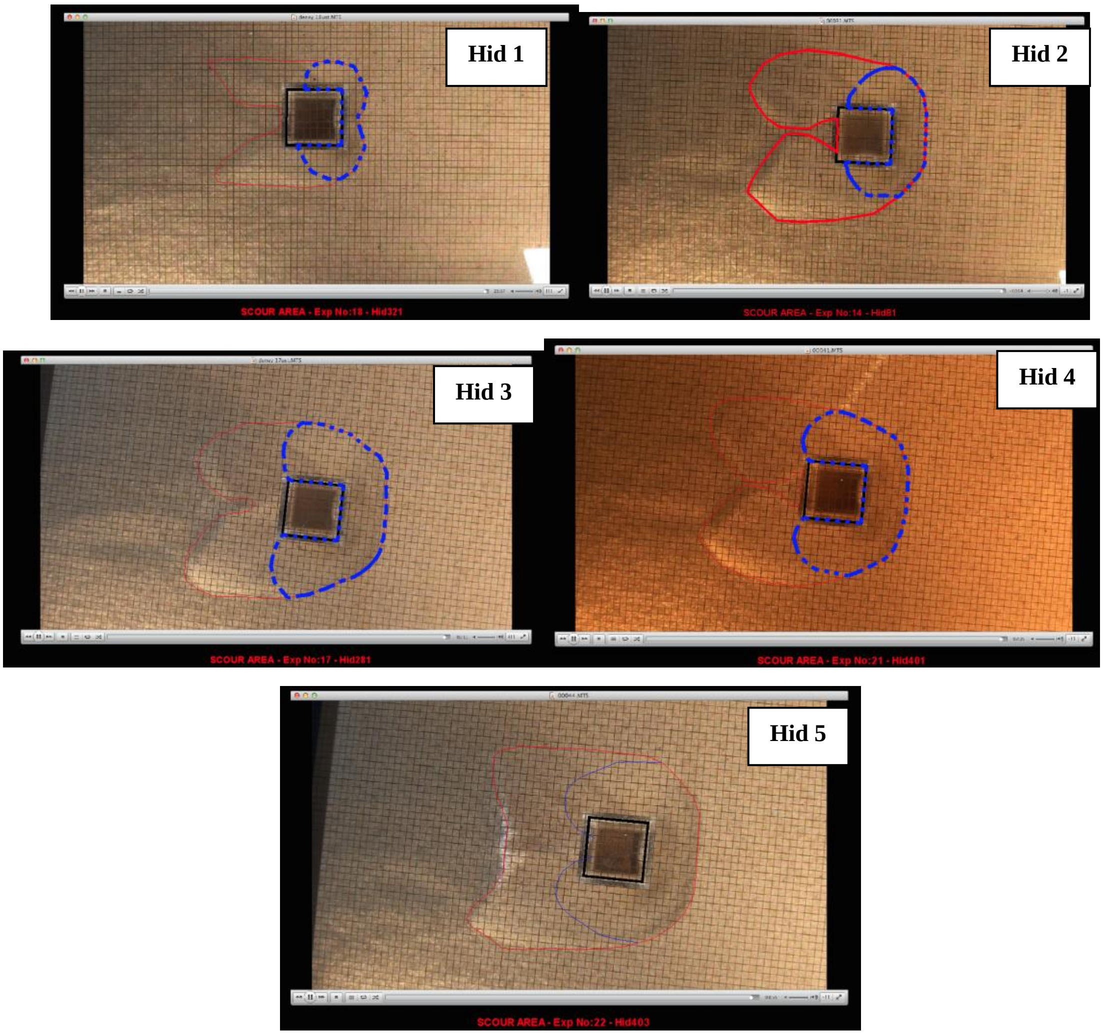

Figure 5.45 Video Camera 1 data before image processing

Figure 5.46, 5.47, 5.48, 5.49 and 5.50 present the development of scour hole around the square pier, respectively under Hid 1, Hid 2, Hid 3, Hid 4 and Hid 5.

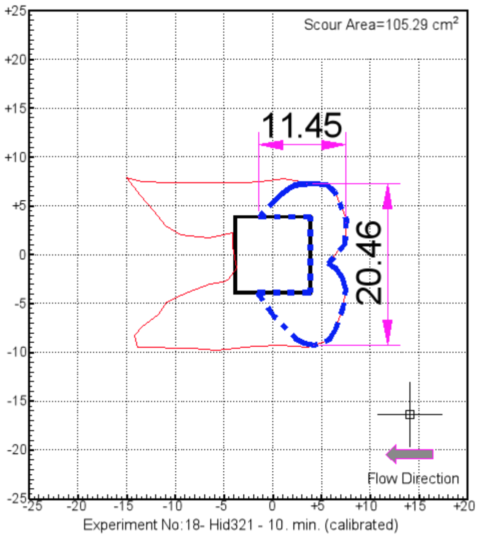

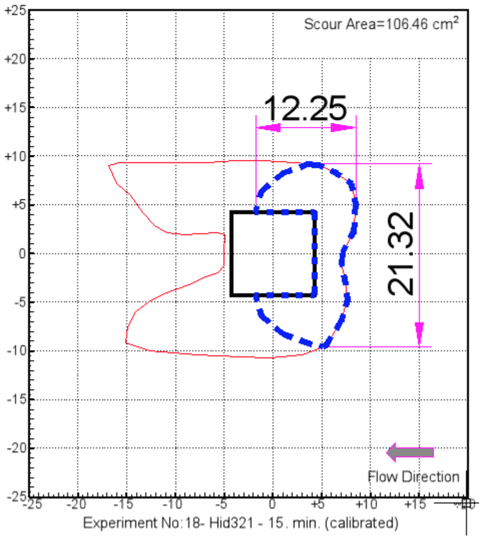

Figure 5.46 Bed configuration at t=5 min and t=10 min for Hid 1

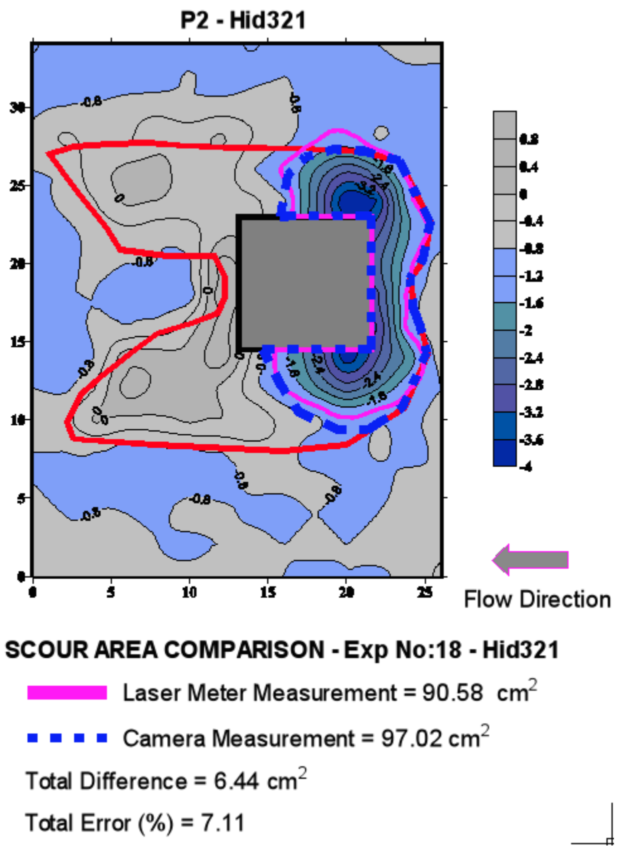

Figure 5.46 Bed configuration at t=5 min and t=10 min for Hid 1 (continued)

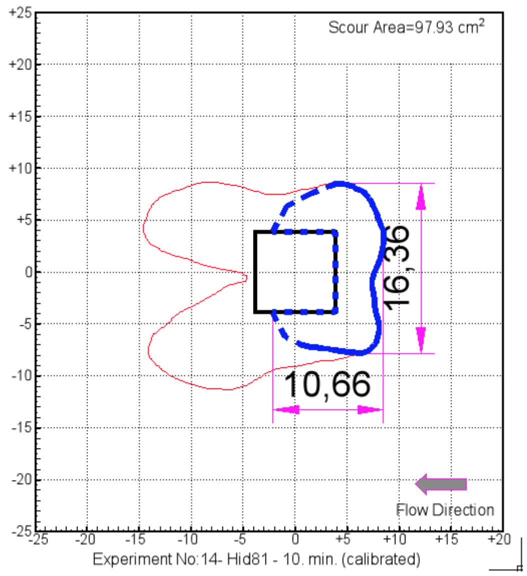

Figure 5.47 Bed configuration at t=5 min and t=10 min for Hid 2

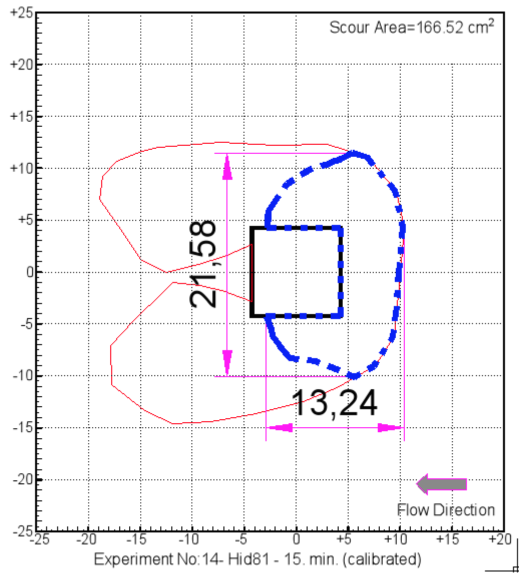

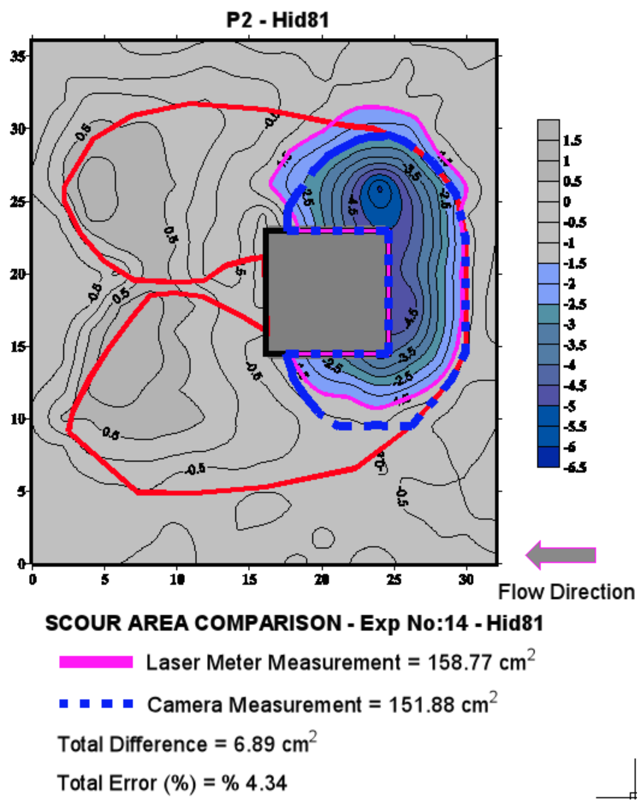

Figure 5.47 Bed configuration at t=5 min and t=10 min for Hid 2 (continued)

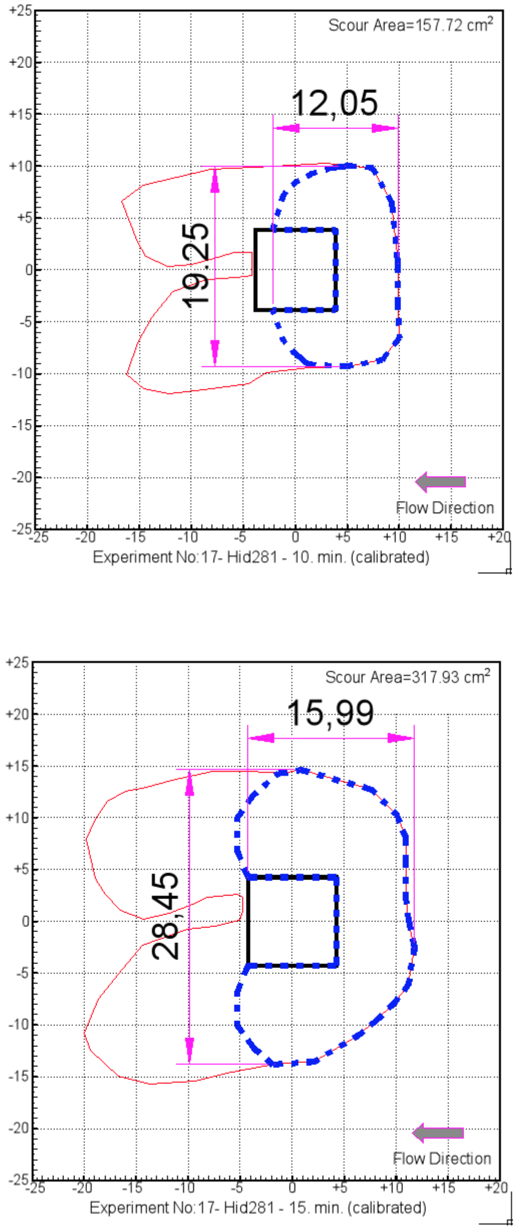

Figure 5.48 Bed configuration at t=5 min and t=10 min for Hid 3

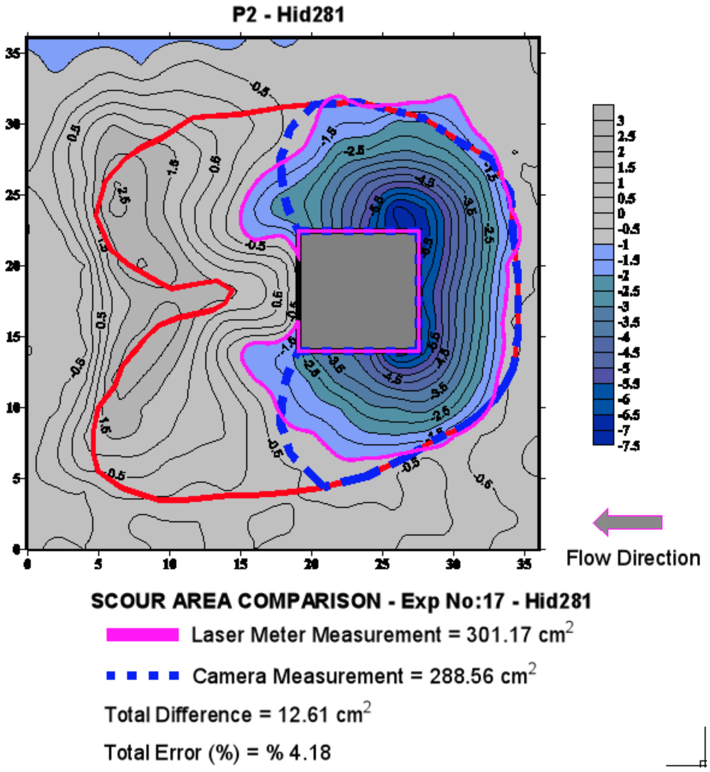

Figure 5.48 Bed configuration at t=5 min and t=10 min for Hid 3 (continued)

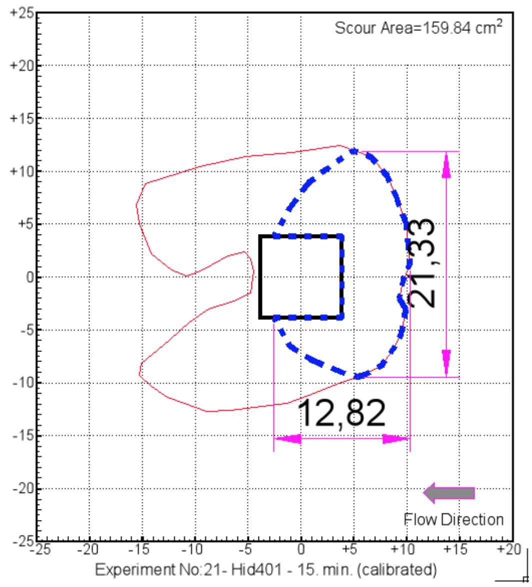

Figure 5.49 Bed configuration at t=10 min and t=20 min for Hid 4

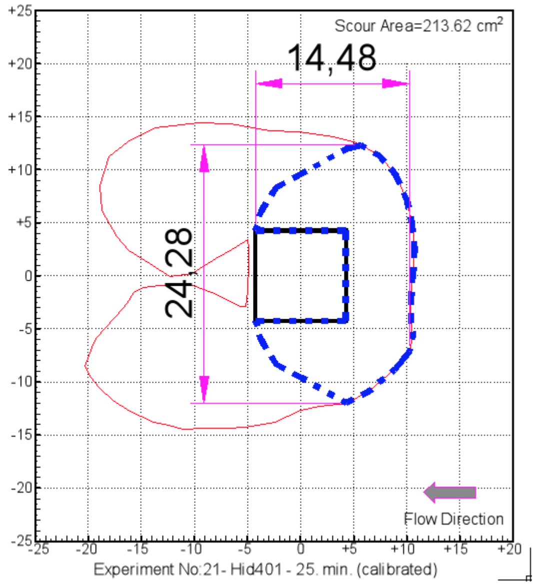

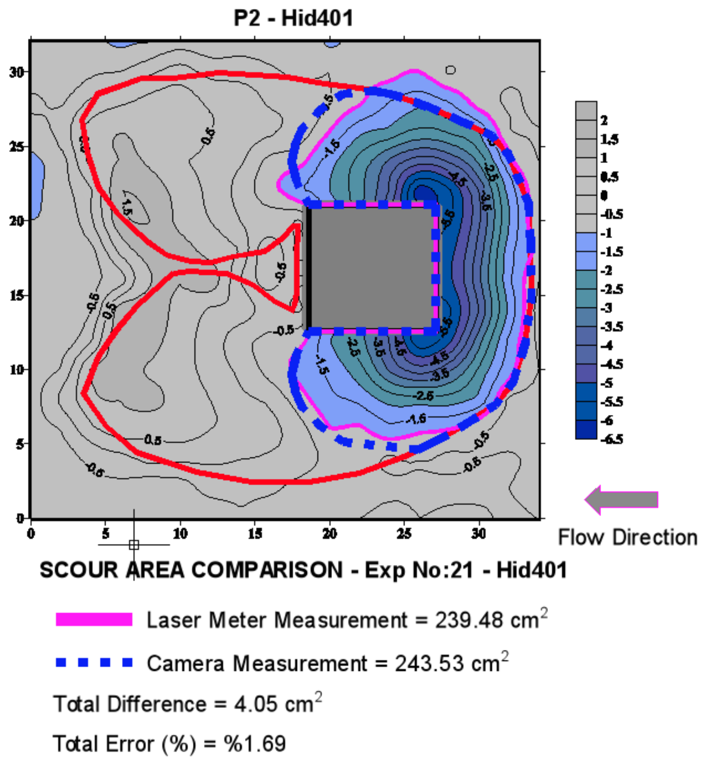

Figure 5.49 Bed configuration at t=10 min and t=20 min for Hid 4 (continued)

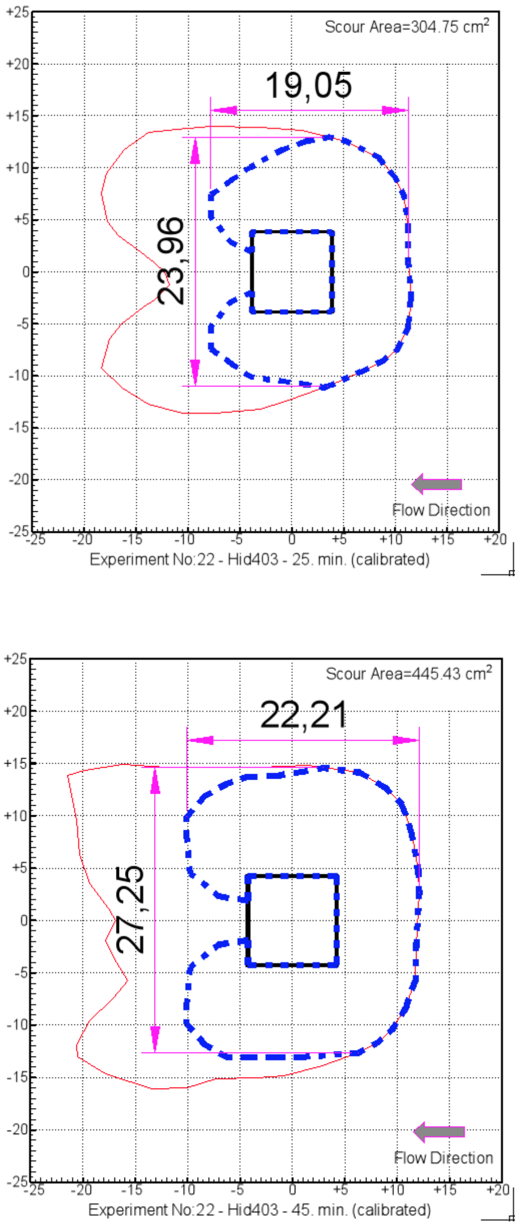

Figure 5.50 Bed configuration at t=20 min and t=40 min for Hid 5

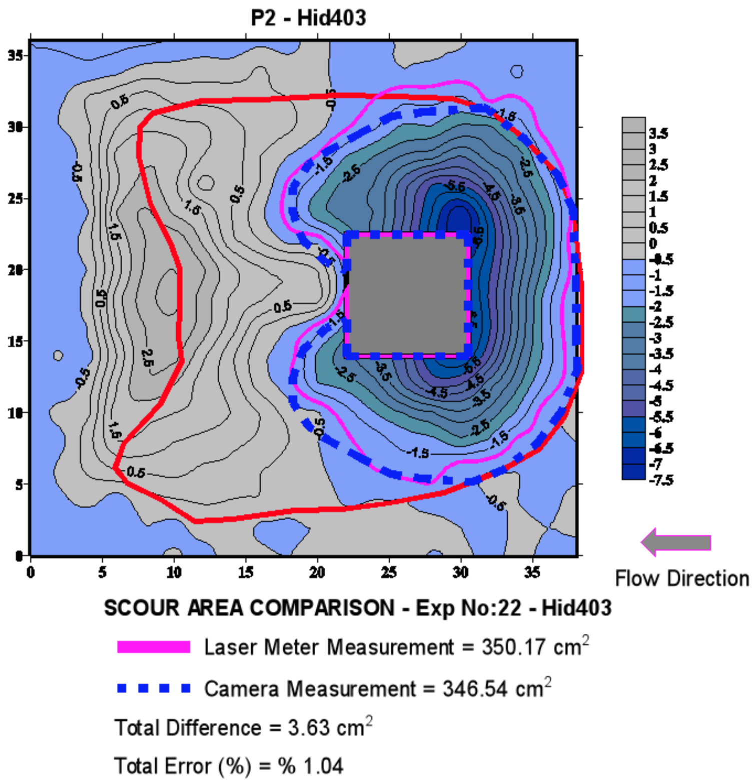

Figure 5.50 Bed configuration at t=20 min and t=40 min for Hid 5 (continued)

The observed scour hole dimensions are summarized for square pier in Table 5.17.

Table 5.17 Scour hole measurements for square pier

Hyd. ID	b (cm)	Time (min.)	Water Depth (cm)	Dimensions			Area (cm^2)
				d_{s1} (cm)	L(cm)	W(cm)	
Hid 1	8.5	5	20.39	4.1	11.45	20.46	105.29
Hid 1	8.5	10	6.00	4.1	12.25	21.32	106.46
Hid 2	8.5	5	22.61	6.6	10.66	16.36	97.93
Hid 2	8.5	10	6.00	6.6	13.24	21.58	166.52
Hid 3	8.5	5	23.52	7.6	12.05	19.25	157.72
Hid 3	8.5	10	6.00	7.6	15.99	28.45	317.93
Hid 4	8.5	10	22.61	6.5	12.82	21.33	159.84
Hid 4	8.5	20	6.00	6.7	14.48	24.28	213.62
Hid 5	8.5	20	22.61	7.7	19.05	23.96	304.75
Hid 5	8.5	40	6.00	7.7	22.21	27.25	445.43

5.2.8.3 Scour Hole Measurements for Rectangular Pier

Figure 5.51 indicates the video camera picture before the image processing for different hydrographs.

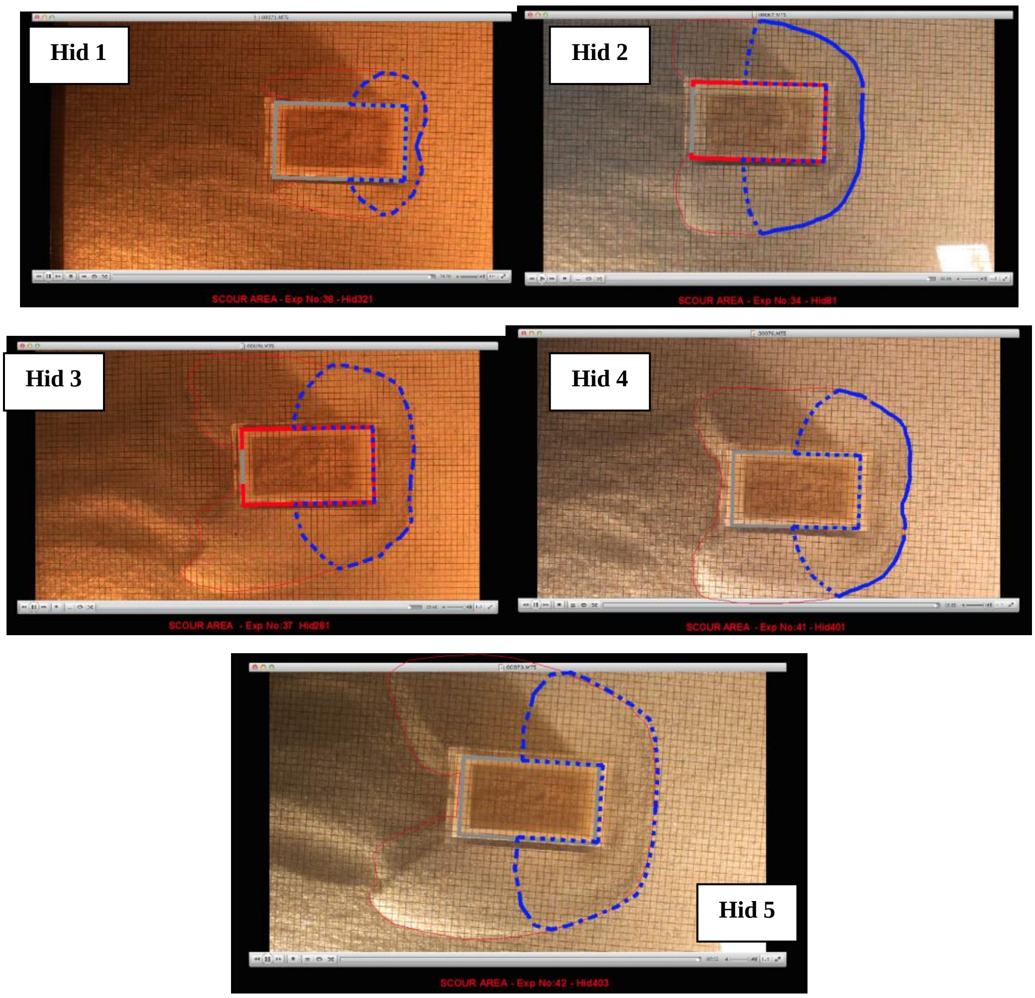

Figure 5.51 Video Camera 1 data before image processing

Figure 5.52, 5.53, 5.54, 5.55 and 5.56 present the development of scour hole around the square pier, respectively under Hid 1, Hid 2, Hid 3, Hid 4 and Hid 5.

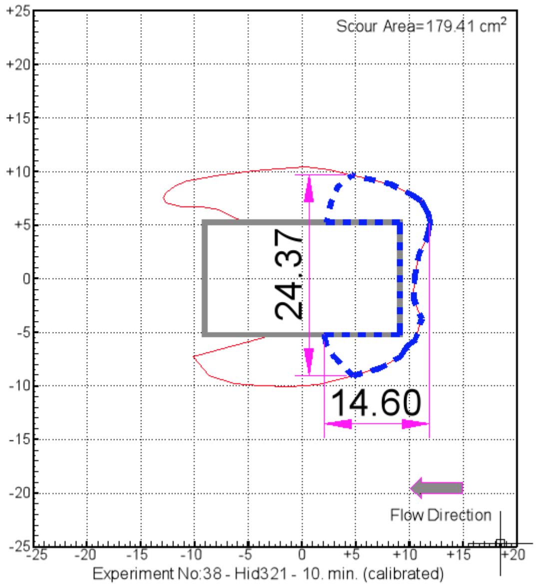

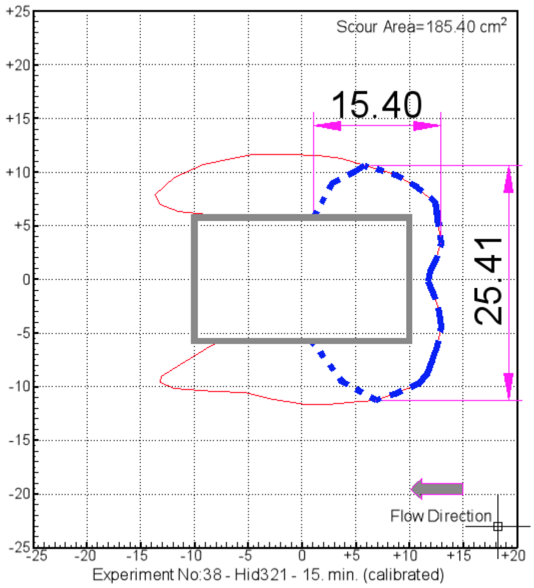

Figure 5.52 Bed configuration at t=5 min and t=10 min for Hid 1

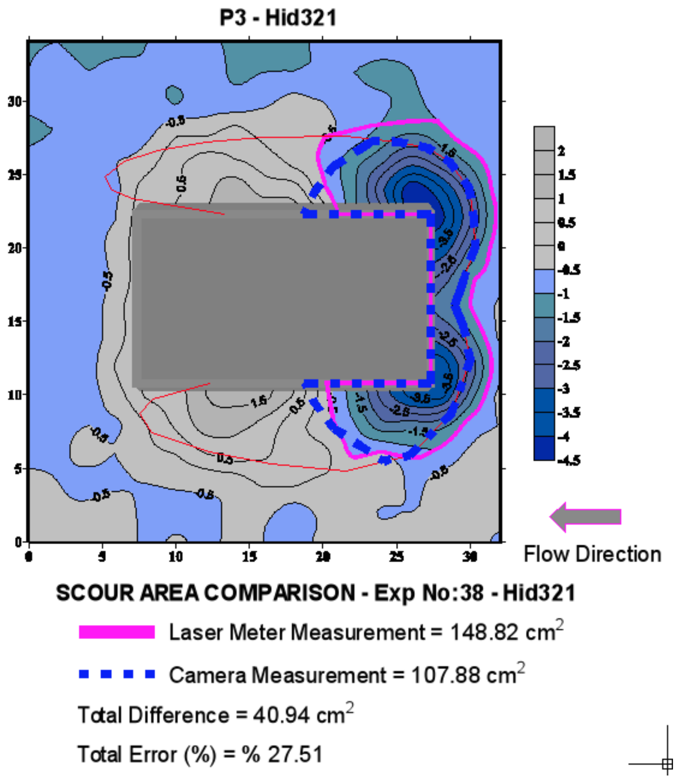

Figure 5.52 Bed configuration at t=5 min and t=10 min for Hid 1 (continued)

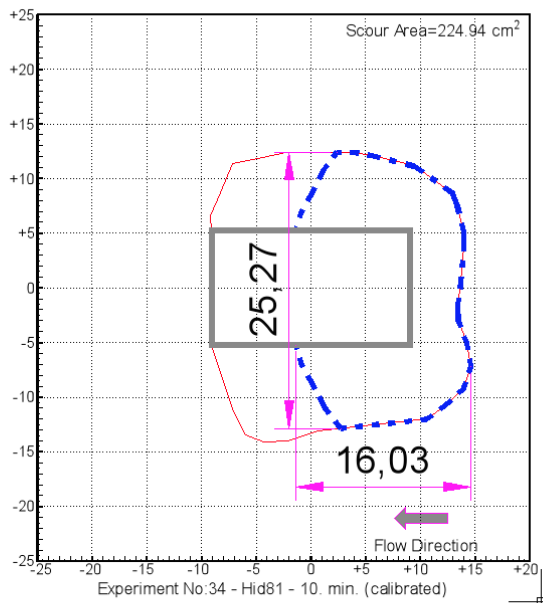

Figure 5.53 Bed configuration at t=5 min and t=10 min for Hid 2

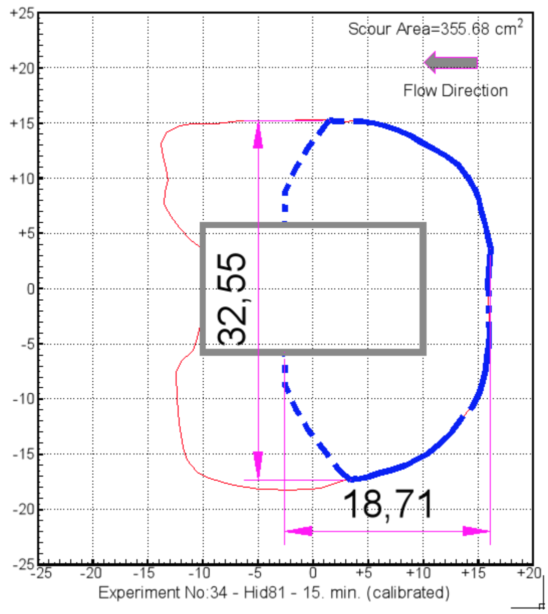

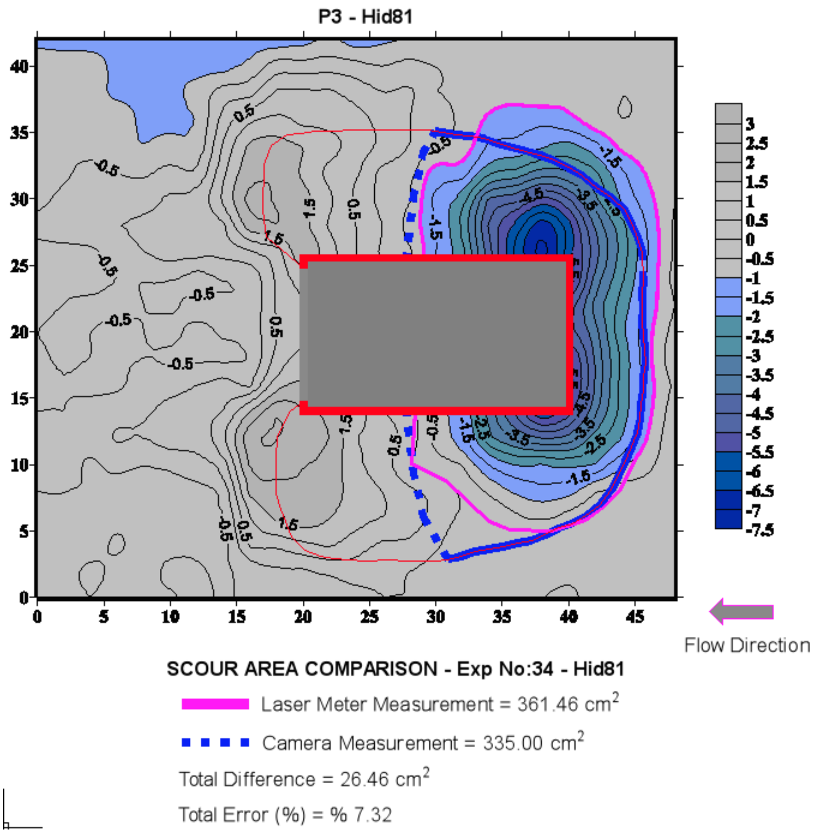

Figure 5.53 Bed configuration at t=5 min and t=10 min for Hid 2 (continued)

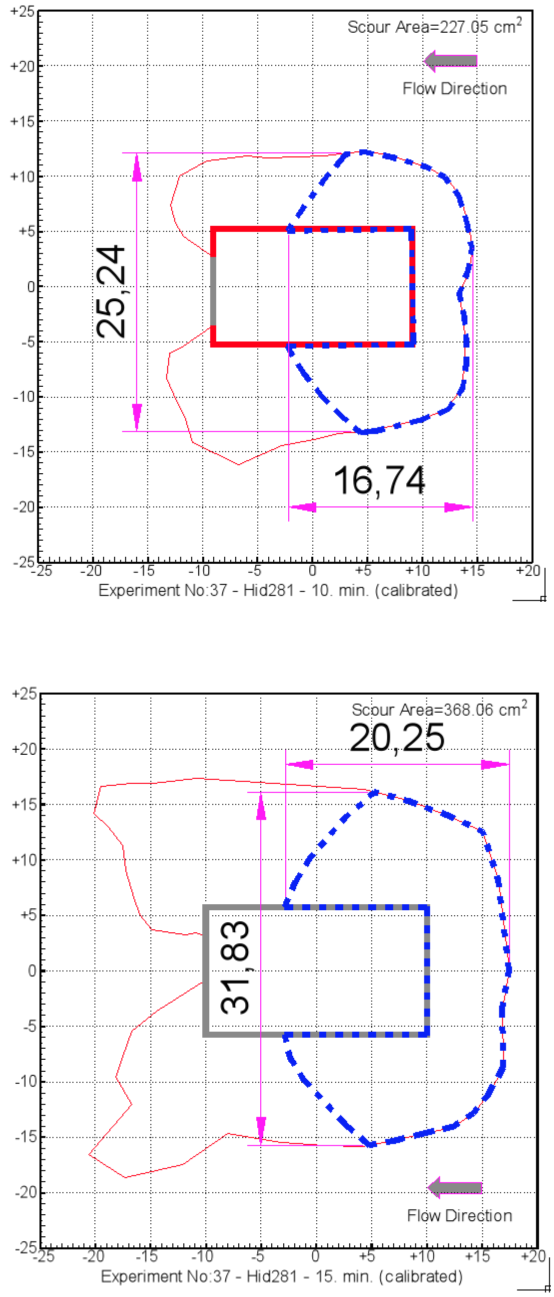

Figure 5.54 Bed configuration at t=5 min and t=10 min for Hid 3

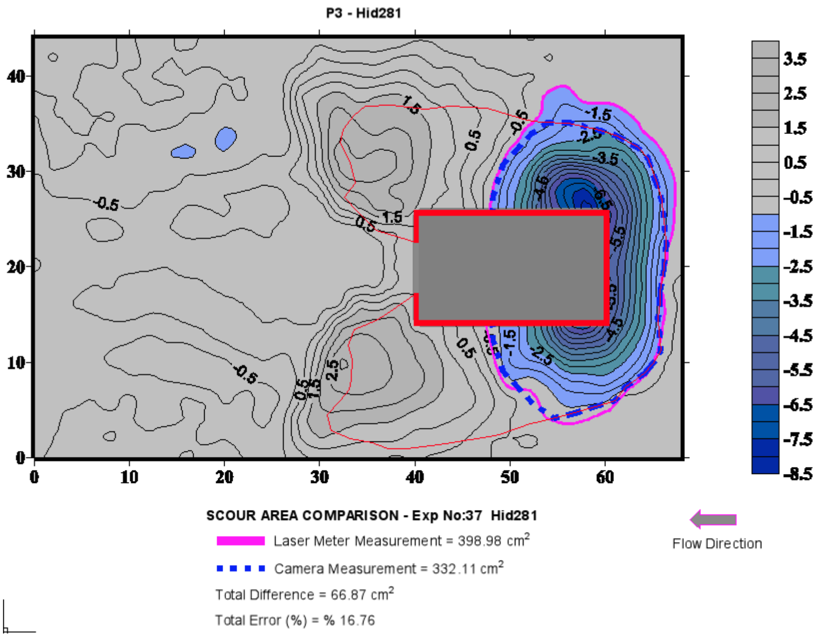

Figure 5.54 Bed configuration at t=5 min and t=10 min for Hid 3 (continued)

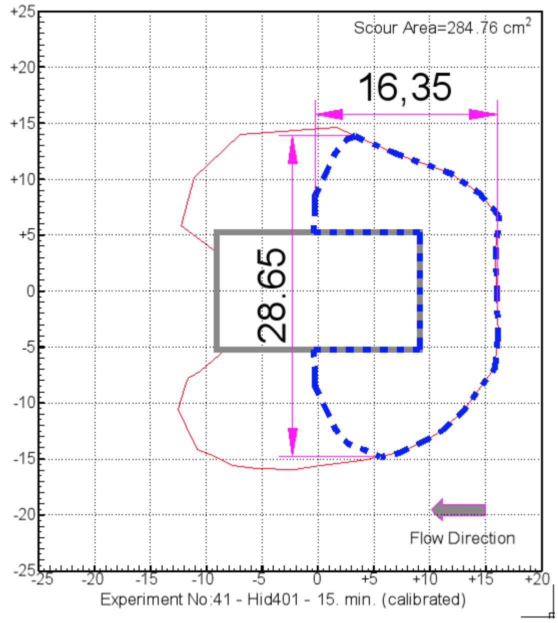

Figure 5.55 Bed configuration at t=15 min and t=25 min for Hid 4

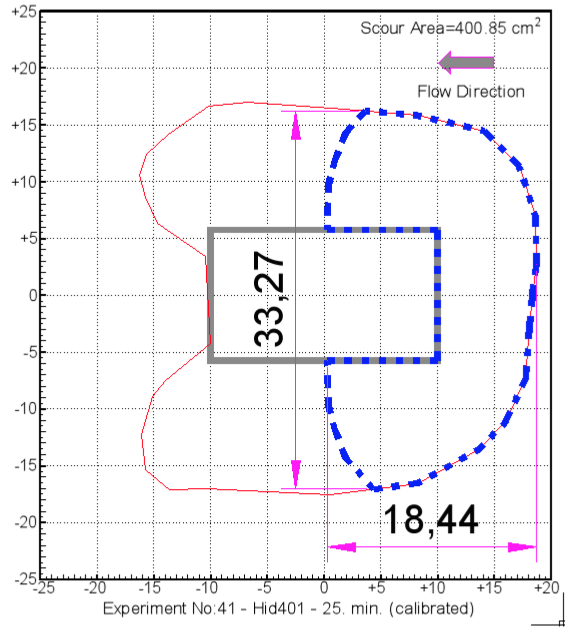

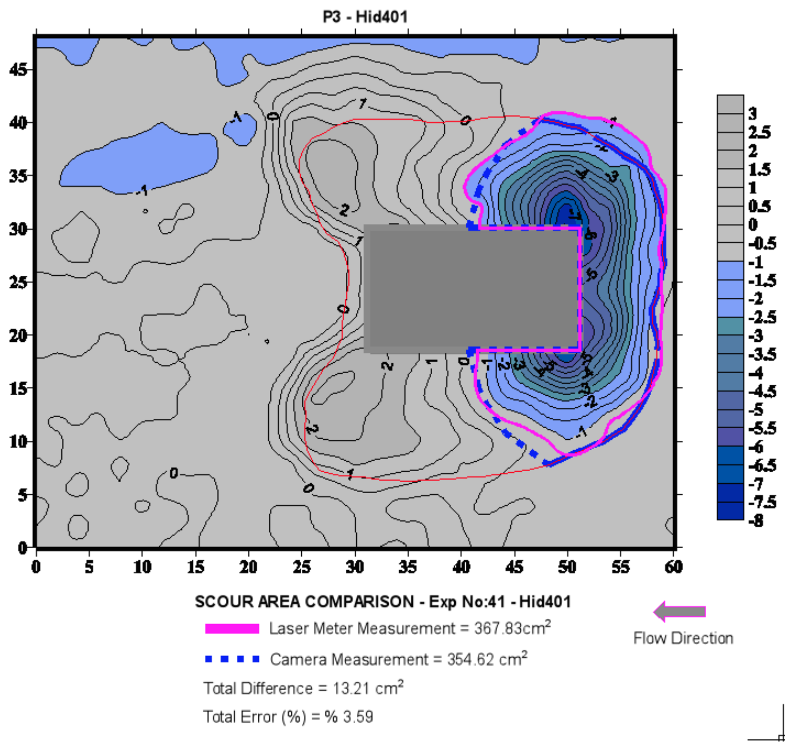

Figure 5.55 Bed configuration at t=15 min and t=25 min for Hid 4 (continued)

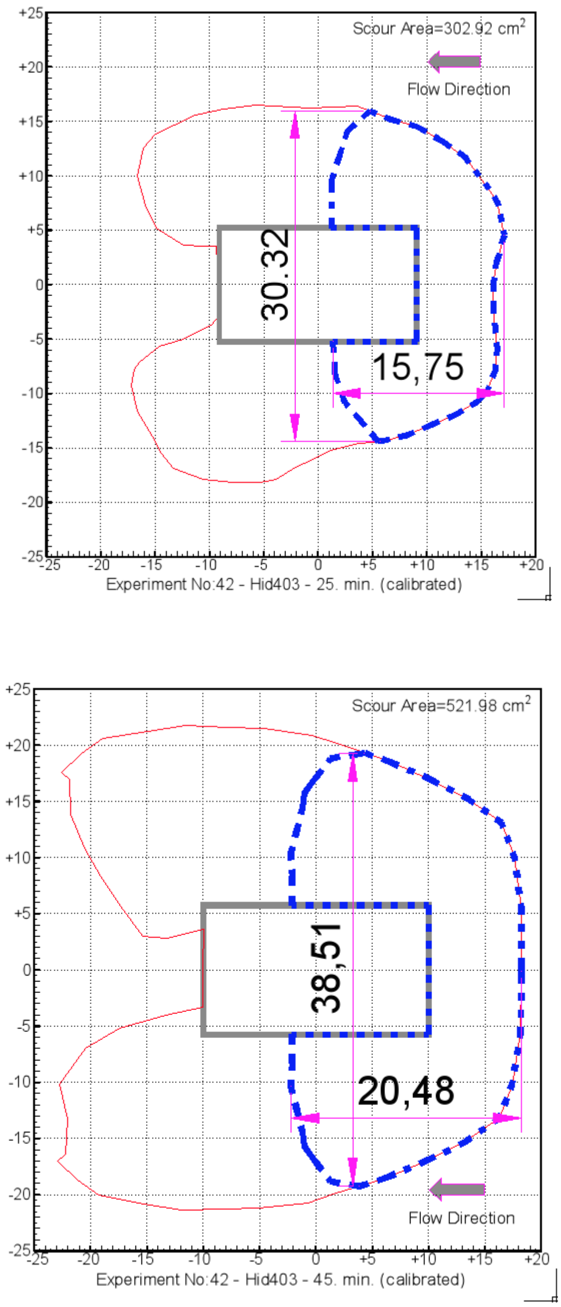

Figure 5.56 Bed configuration at t=25 min and t=45 min for Hid 5

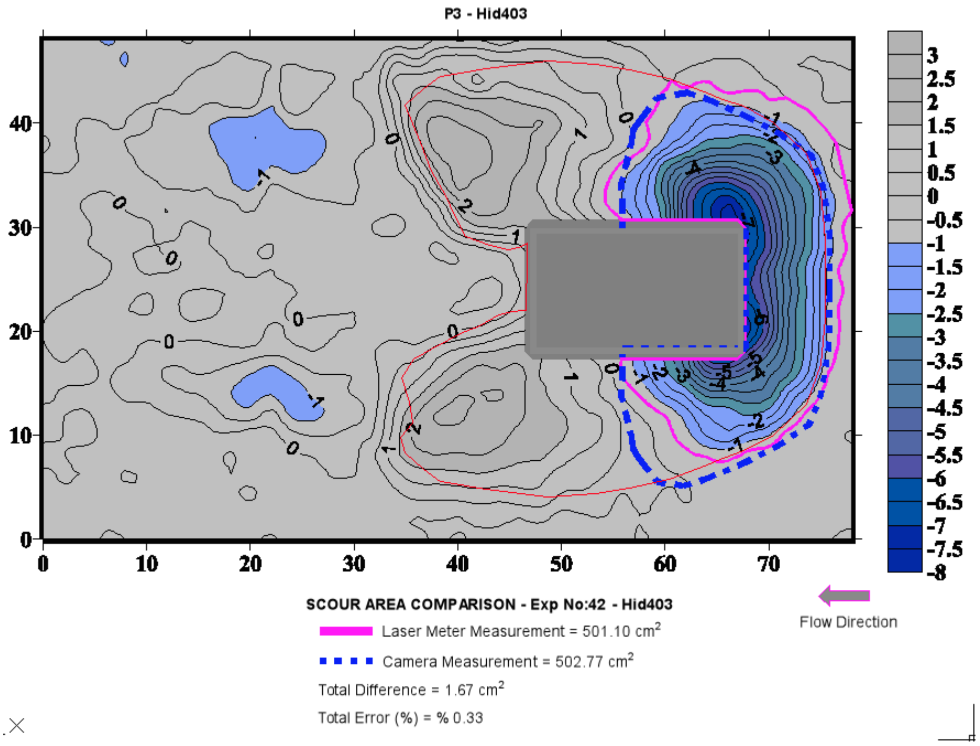

Figure 5.56 Bed configuration at t=25 min and t=45 min for Hid 5 (continued)

The observed scour hole dimensions are summarized for rectangular pier in Table 5.18.

Table 5.18 Scour hole measurements for rectangular pier

Hyd. ID	b (cm)	Time (min.)	Water Depth (cm)	Dimensions			Area (cm^2)
				d_{s1} (cm)	L(cm)	W(cm)	
Hid 1	11.5	5	20.39	4.5	14.60	24.37	179.41
Hid 1	11.5	10	6.00	4.6	15.40	25.41	185.40
Hid 2	11.5	5	22.61	7.4	16.03	25.26	224.94
Hid 2	11.5	10	6.00	7.5	18.71	32.55	355.68
Hid 3	11.5	5	23.52	8.1	16.74	25.23	227.05
Hid 3	11.5	10	6.00	8.6	20.25	31.83	368.06
Hid 4	11.5	10	22.61	7.8	16.35	28.65	284.76
Hid 4	11.5	20	6.00	8.1	18.44	33.27	400.85
Hid 5	11.5	20	22.61	8.0	15.75	30.32	302.92
Hid 5	11.5	40	6.00	8.1	20.48	38.51	521.98

5.2.8.4 Scour Hole Measurements for Rectangular With Circular Nose Pier

Figure 5.57 reveals the video camera picture before the image processing for different hydrographs.

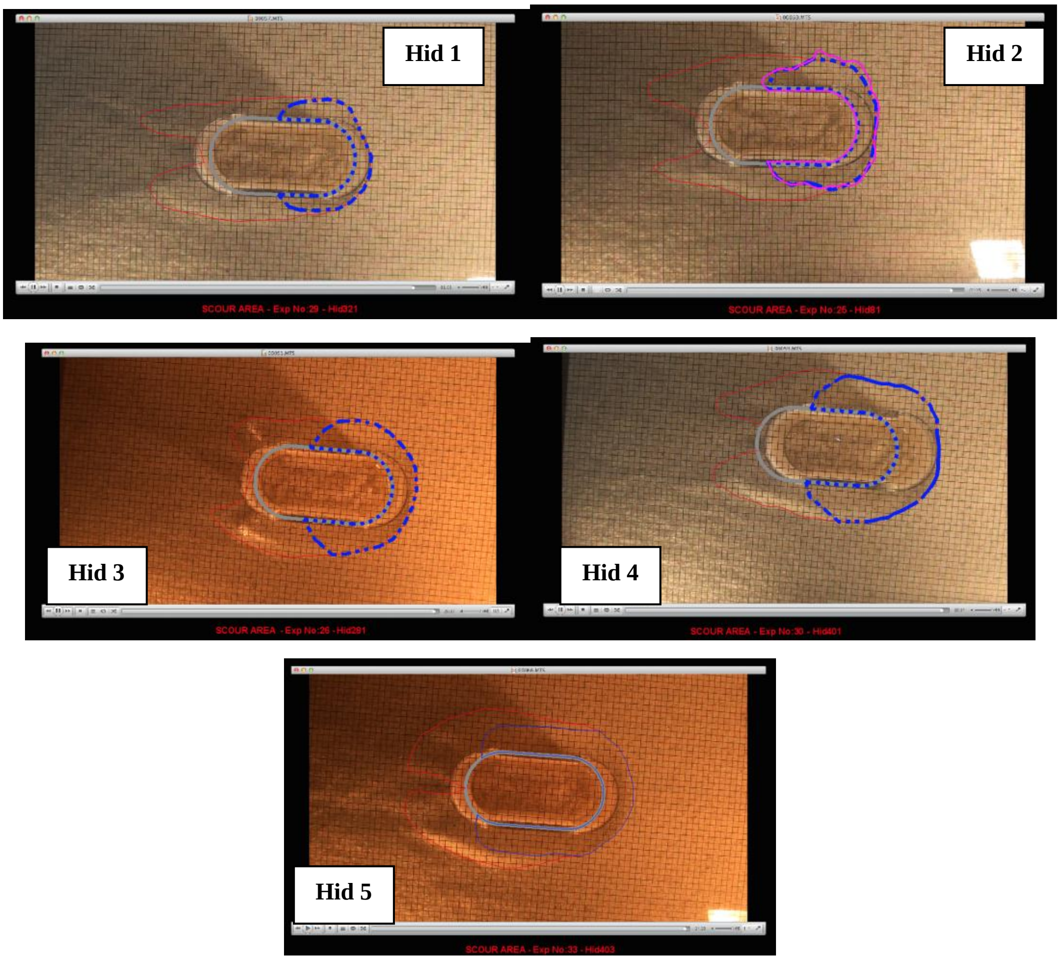

Figure 5.57 Video Camera 1 data before image processing

Figure 5.58, 5.59, 5.60, 5.61 and 5.62 show the development of scour hole around the square pier, respectively under Hid 1, Hid 2, Hid 3, Hid 4 and Hid 5.

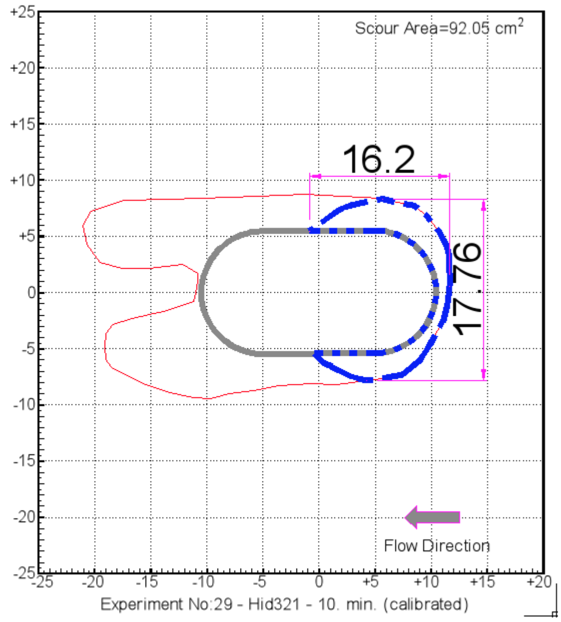

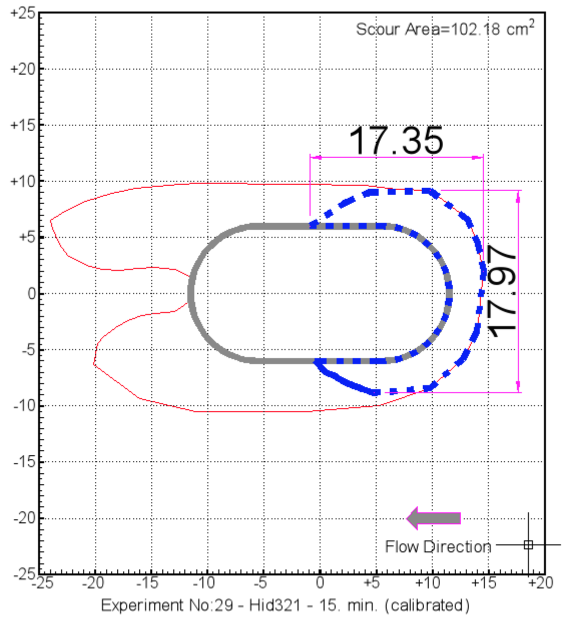

Figure 5.58 Bed configuration at t=5 min and t=10 min for Hid 1

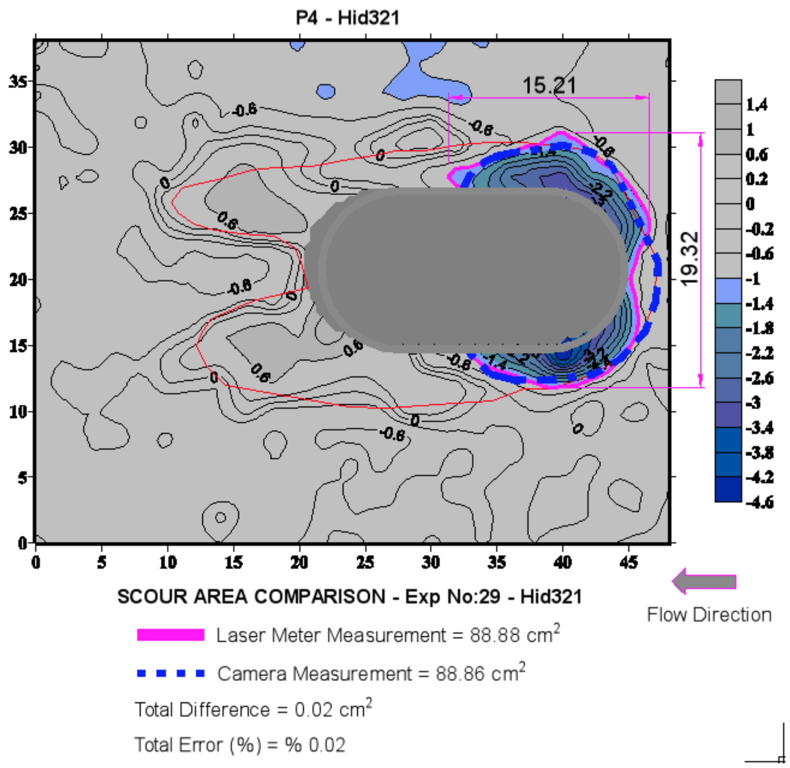

Figure 5.58 Bed configuration at t=5 min and t=10 min for Hid 1 (continued)

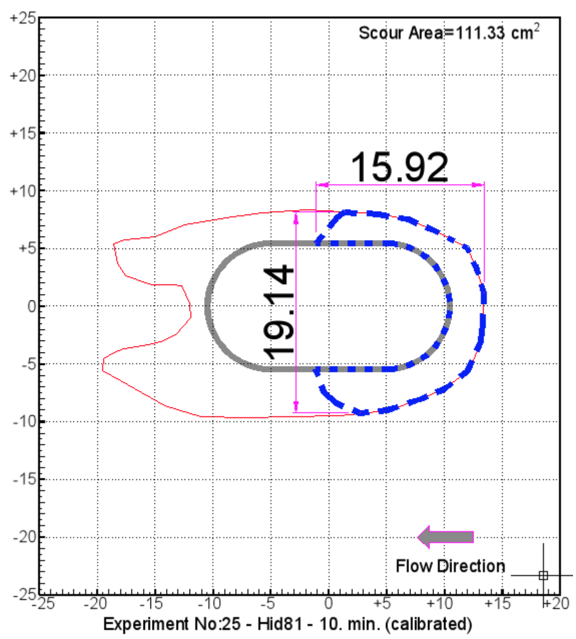

Figure 5.59 Bed configuration at t=5 min and t=10 min for Hid 2

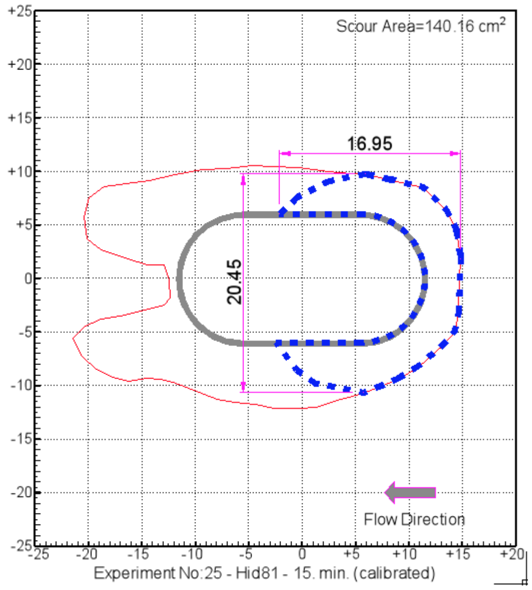

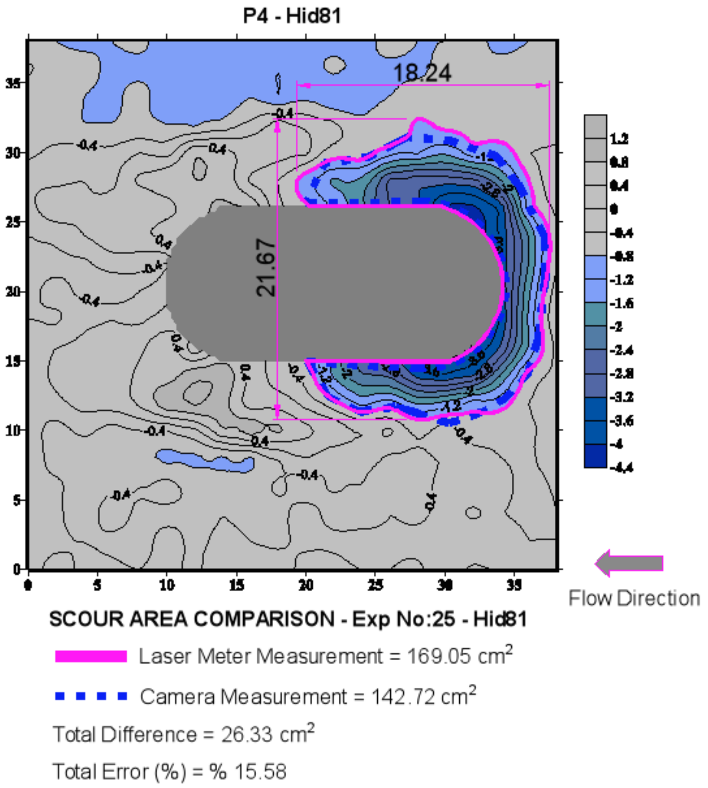

Figure 5.59 Bed configuration at t=5 min and t=10 min for Hid 2 (continued)

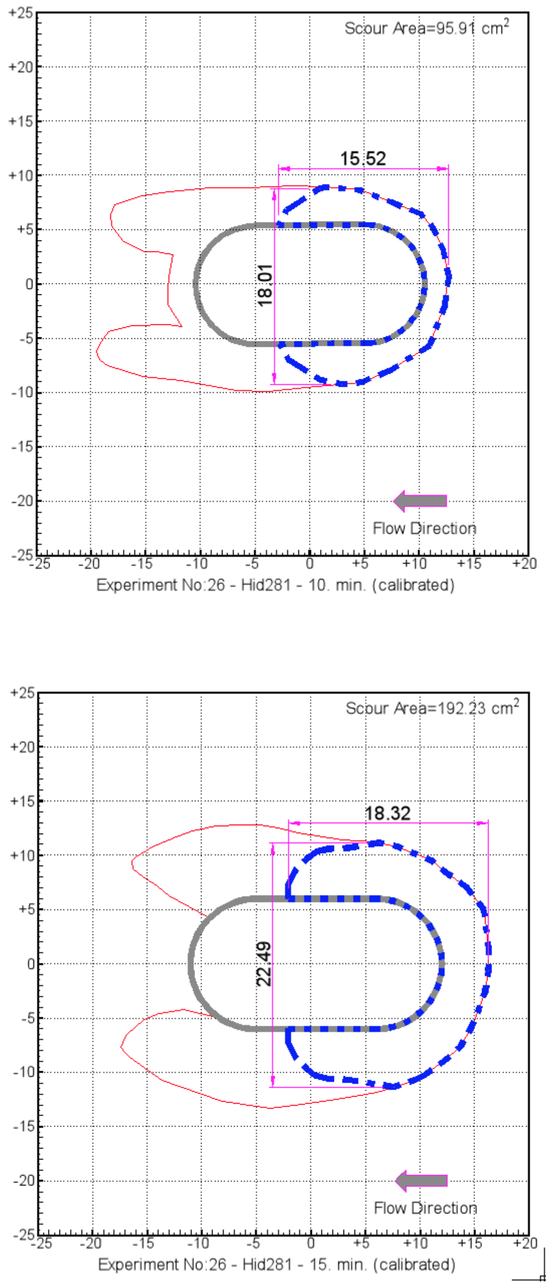

Figure 5.60 Bed configuration at t=5 min and t=10 min for Hid 3

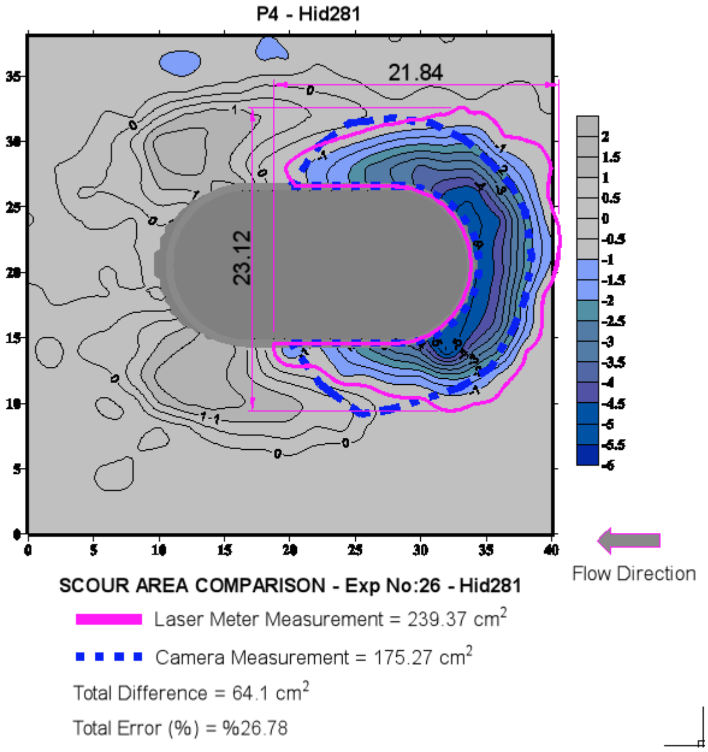

Figure 5.60 Bed configuration at t=5 min and t=10 min for Hid 3 (continued)

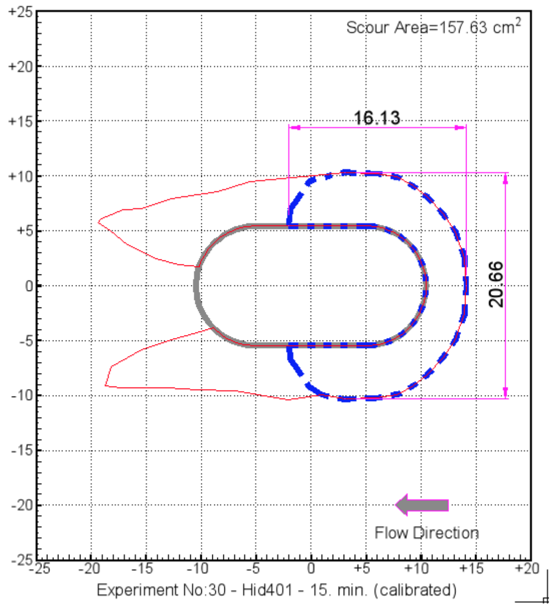

Figure 5.61 Bed configuration at t=15 min and t=25 min for Hid 4

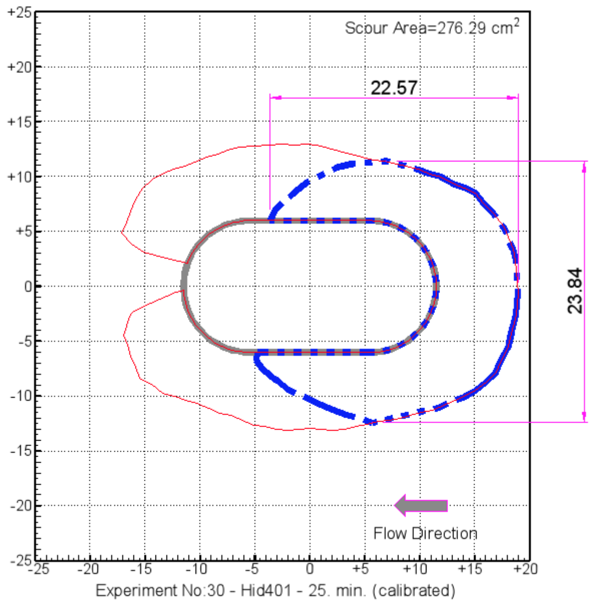

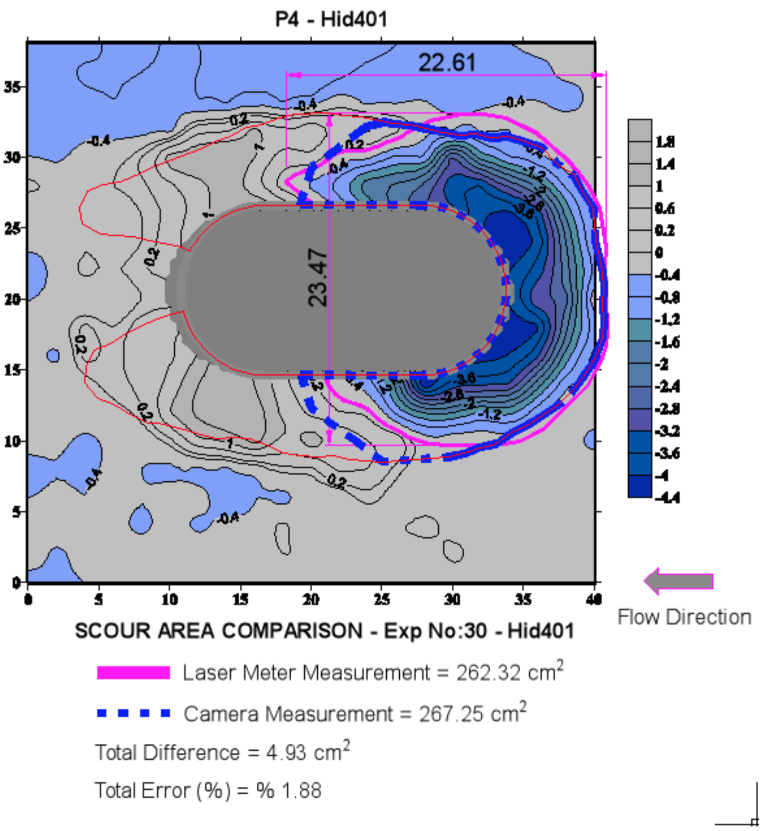

Figure 5.61 Bed configuration at t=15 min and t=25 min for Hid 4 (continued)

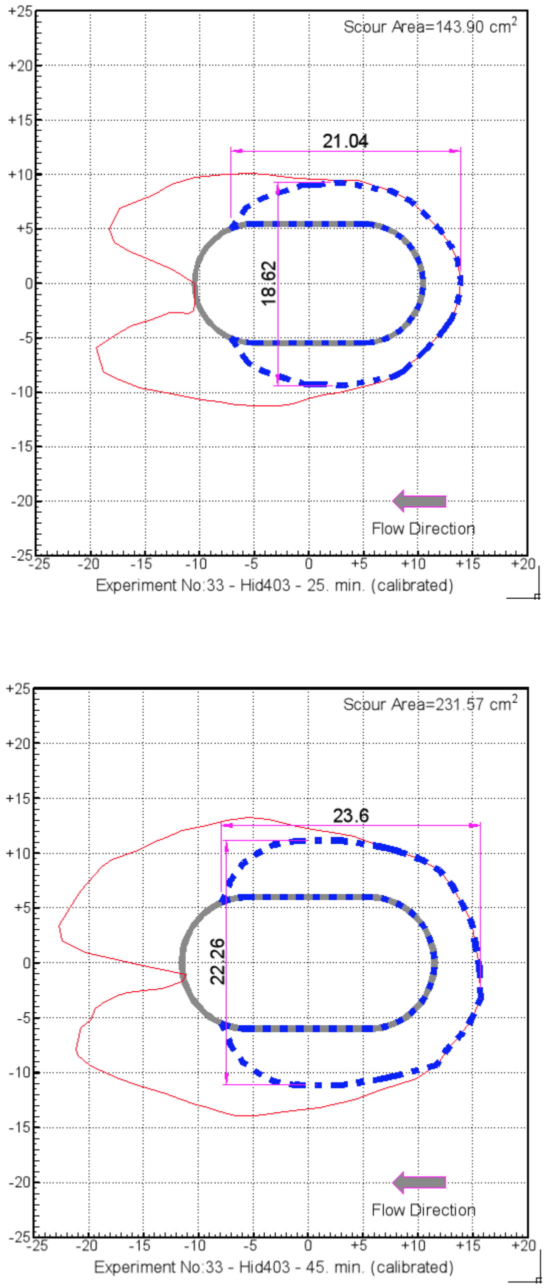

Figure 5.62 Bed configuration at t=25 min and t=45 min for Hid 5

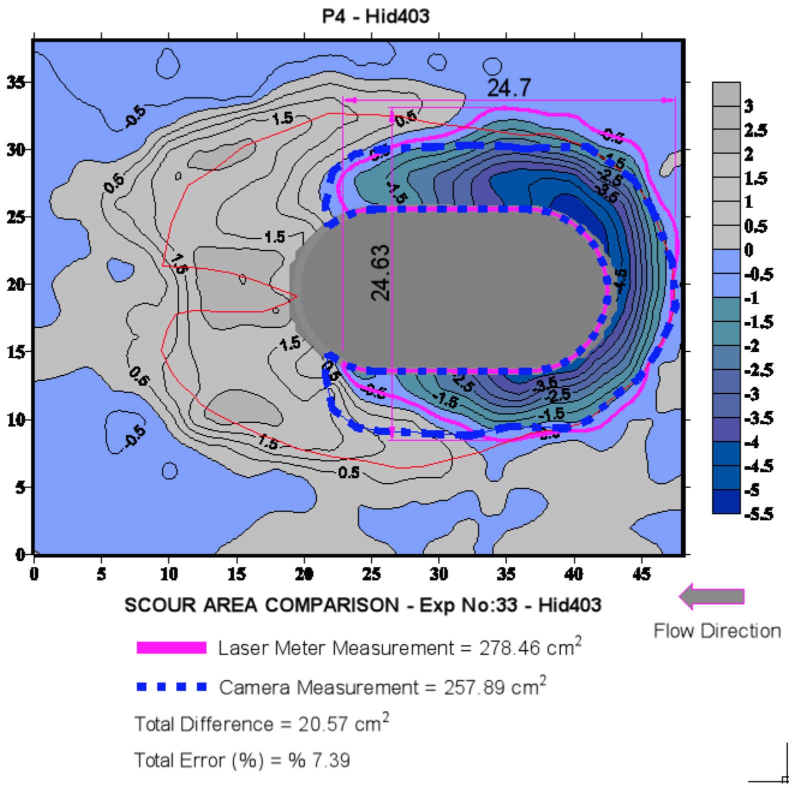

Figure 5.62 Bed configuration at t=25 min and t=45 min for Hid 5 (continued)

The observed scour hole dimensions are summarized for rectangular with circular nose pier in Table 5.19.

Table 5.19 Scour hole measurements for rectangular with circular nose pier

Hyd. ID	b (cm)	Time (min.)	Water Depth (cm)	Dimensions			Area (cm^2)
				d_{s1} (cm)	L(cm)	W(cm)	
Hid 1	12	5	20.39	3.9	16.20	17.76	92.05
Hid 1	12	10	6.00	4.2	17.35	17.97	102.18
Hid 2	12	5	22.61	4.2	15.92	19.14	111.33
Hid 2	12	10	6.00	4.4	16.95	20.45	140.16
Hid 3	12	5	23.52	5.5	15.52	18.01	95.91
Hid 3	12	10	6.00	6.0	18.32	22.49	192.23
Hid 4	12	10	22.61	4.4	16.13	20.66	157.63
Hid 4	12	20	6.00	4.4	22.57	23.84	276.29
Hid 5	12	20	22.61	5.4	21.04	18.62	143.90
Hid 5	12	40	6.00	5.6	23.60	22.26	231.57

5.2.8.5 Scour Hole Measurements for Rectangular With Trapezoidal Nose Pier

Figure 5.63 reveals the video camera picture before the image processing for different hydrographs.

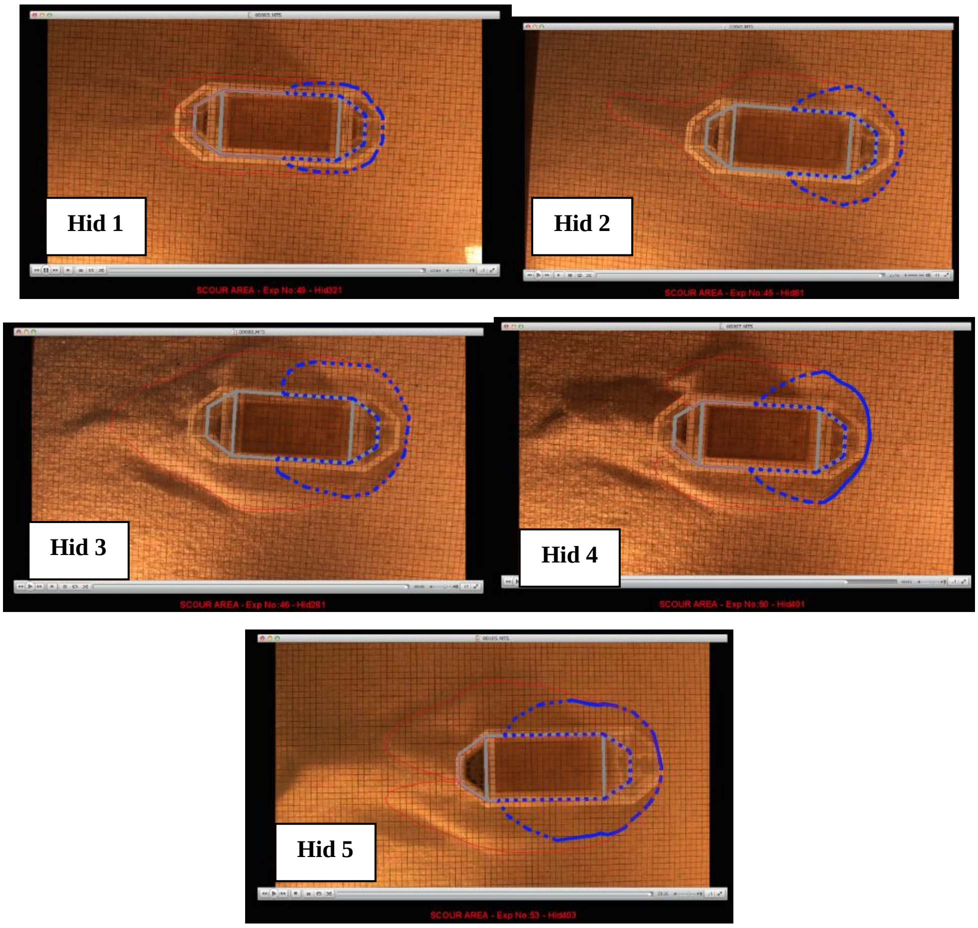

Figure 5.63 Video Camera 1 data before image processing

Figure 5.64, 5.65, 5.66, 5.67 and 5.68 display the development of scour hole around the square pier, respectively under Hid 1, Hid 2, Hid 3, Hid 4 and Hid 5.

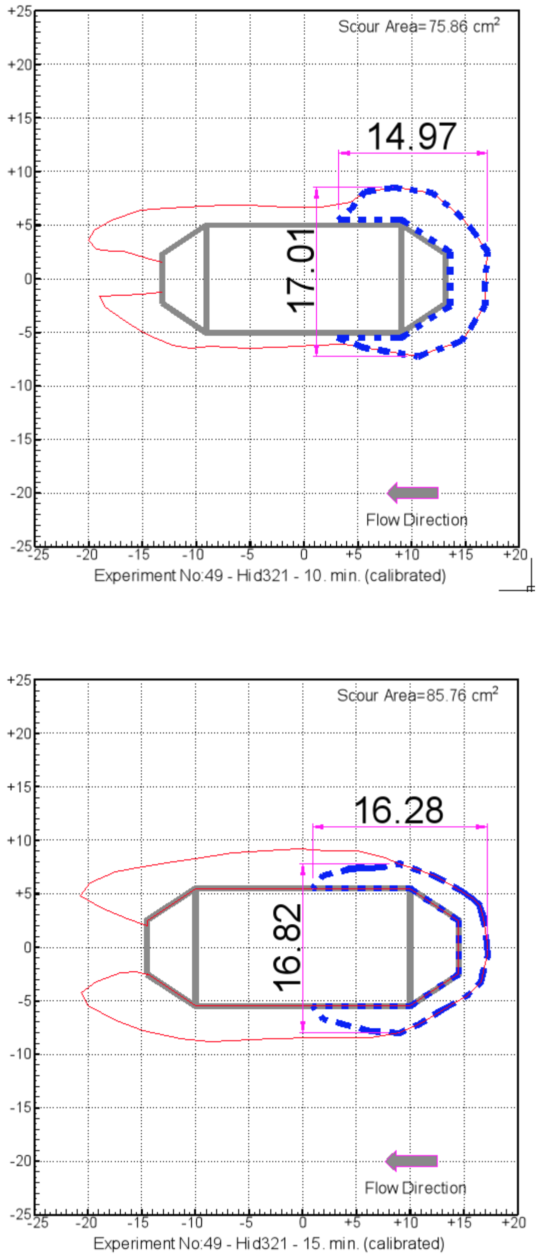

Figure 5.64 Bed configuration at t=5 min and t=10 min for Hid 1

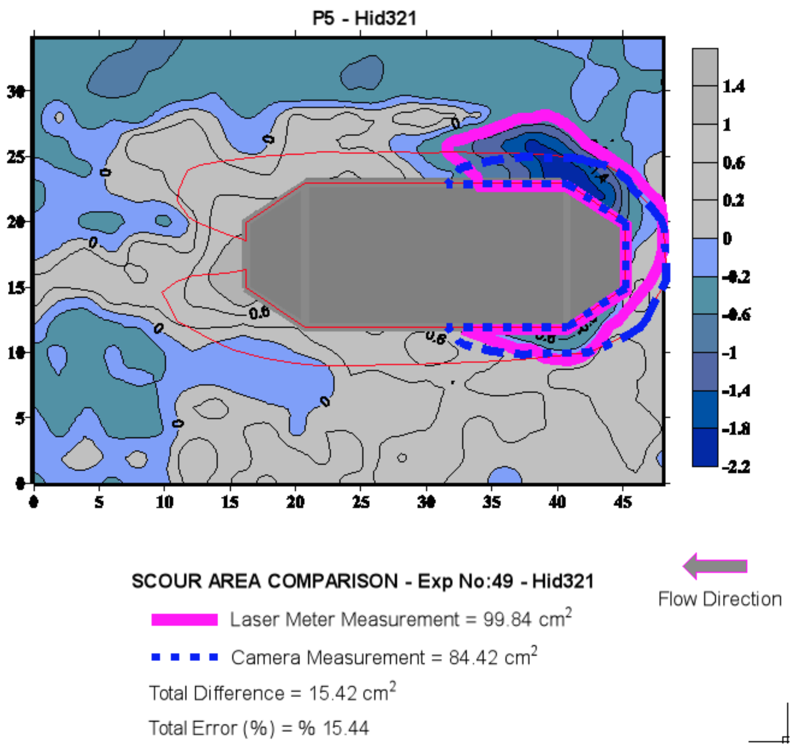

Figure 5.64 Bed configuration at t=5 min and t=10 min for Hid 1 (continued)

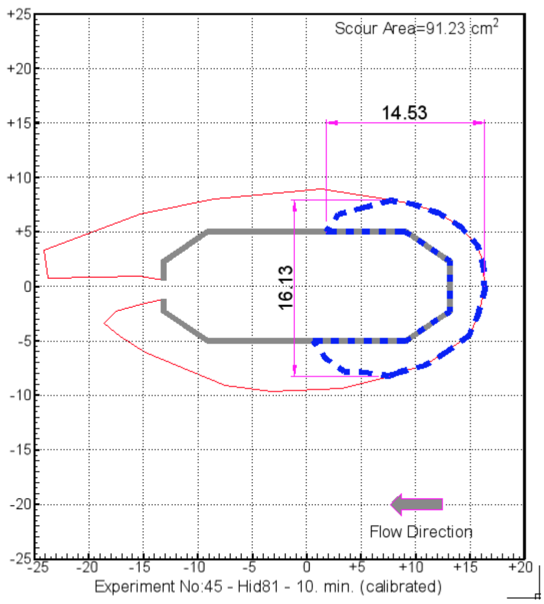

Figure 5.65 The bed configuration at t=5 min and t=10 min for Hid 2

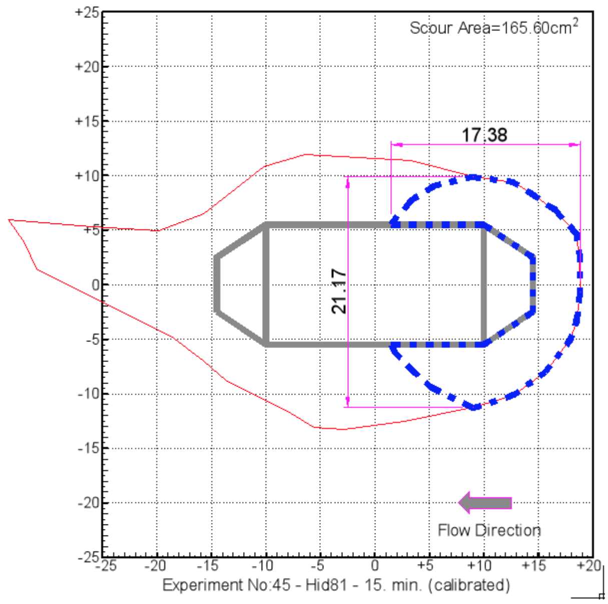

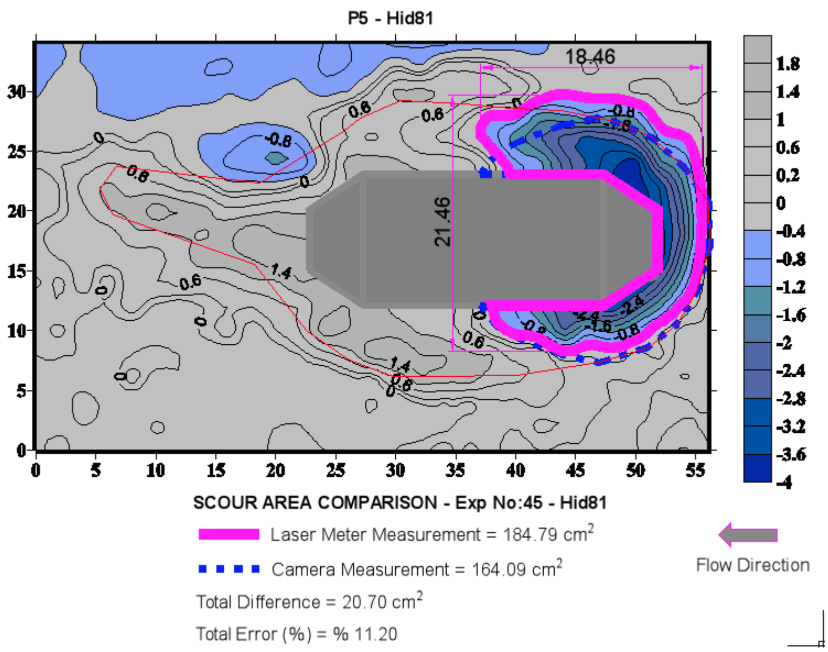

Figure 5.65 The bed configuration at t=5 min and t=10 min for Hid 2 (continued)

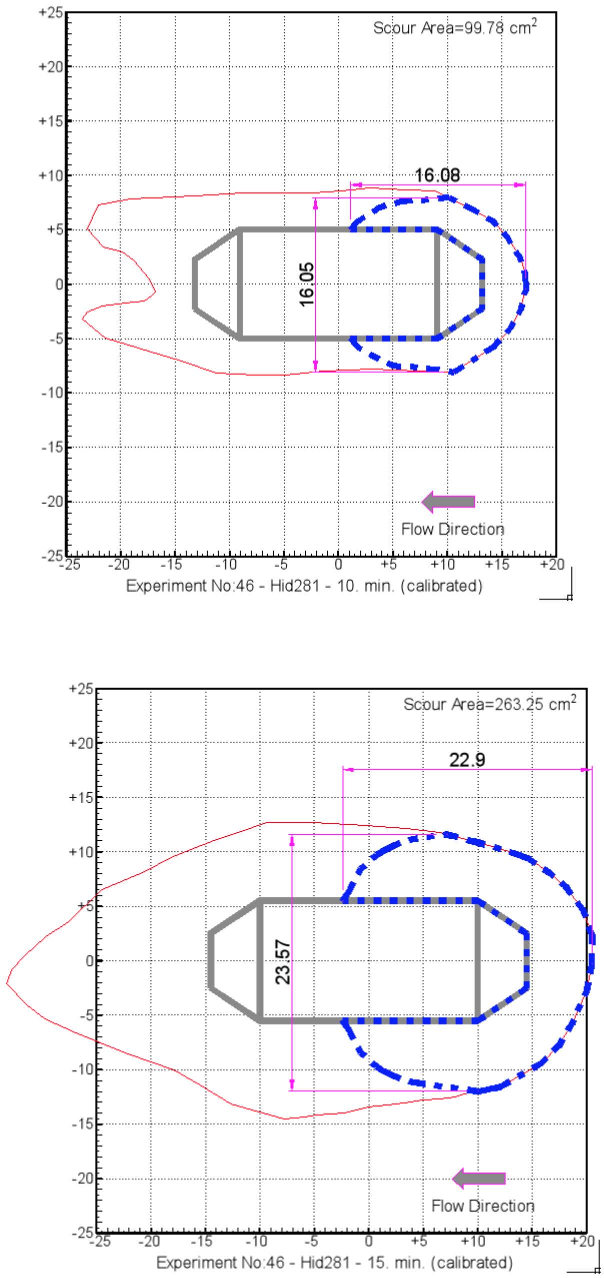

Figure 5.66 Bed configuration at t=5 min and t=10 min for Hid 3

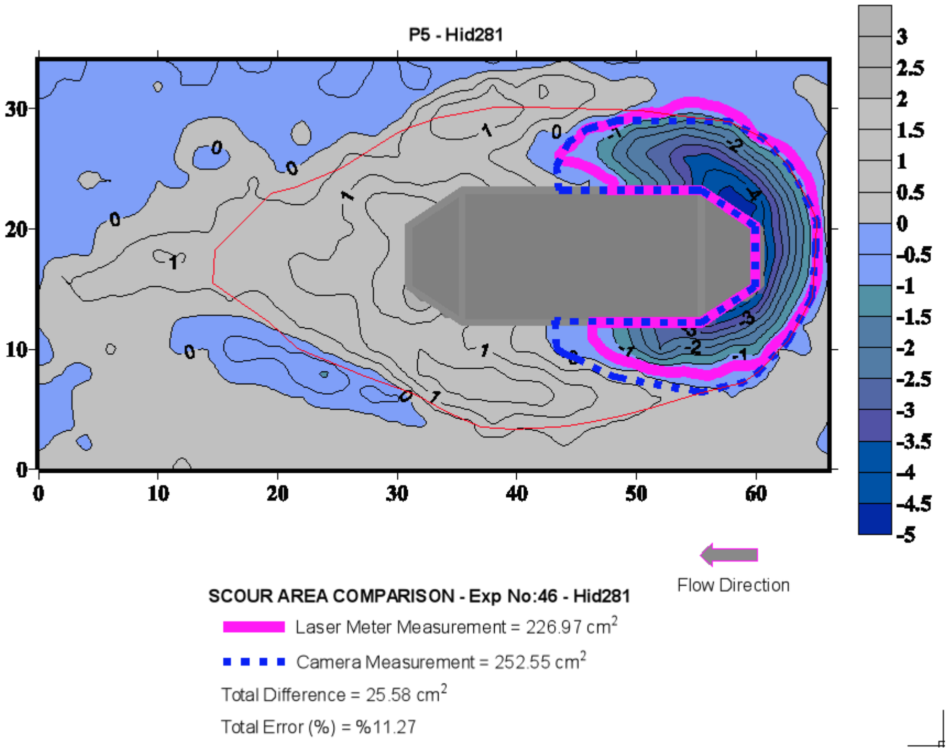

Figure 5.66 Bed configuration at t=5 min and t=10 min for Hid 3 (continued)

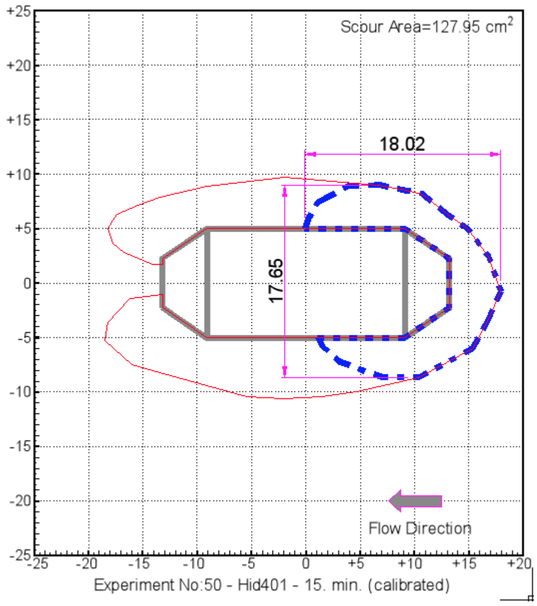

Figure 5.67 Bed configuration at t=15 min and t=25 min for Hid 4

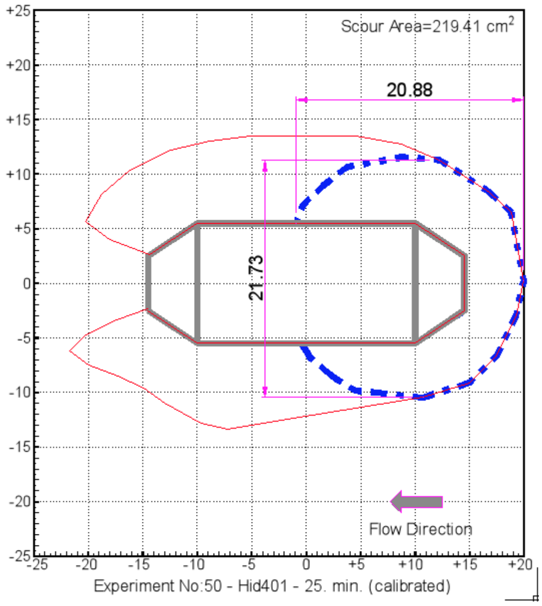

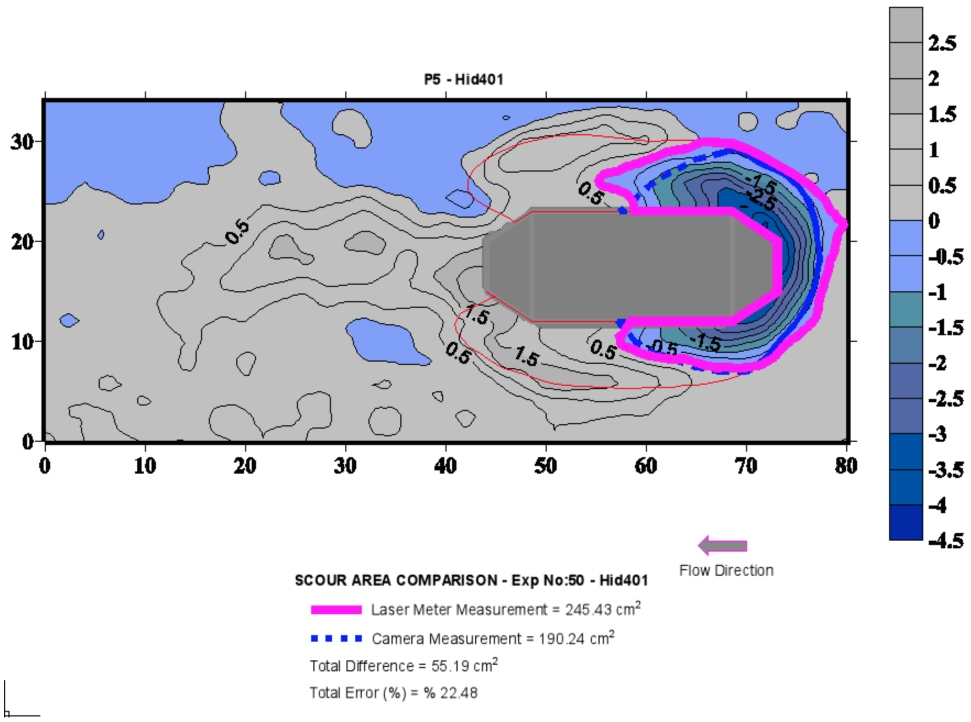

Figure 5.67 Bed configuration at t=15 min and t=25 min for Hid 4 (continued)

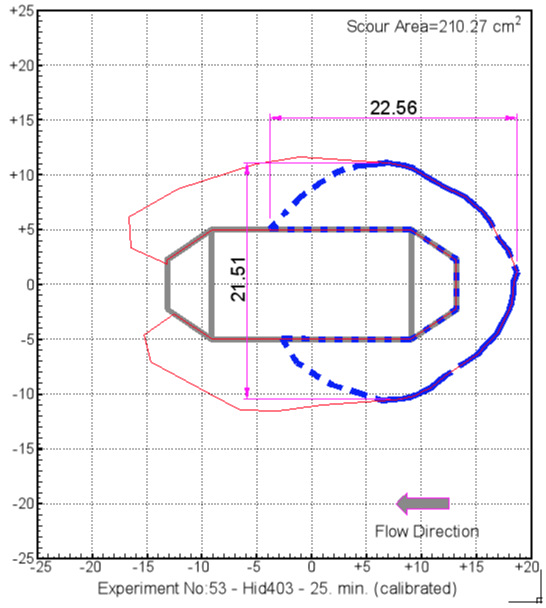

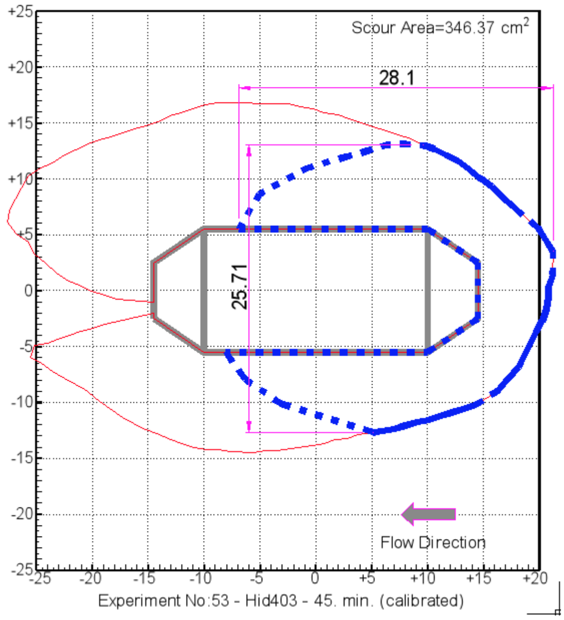

Figure 5.68 Bed configuration at t=25 min and t=45 min for Hid 5

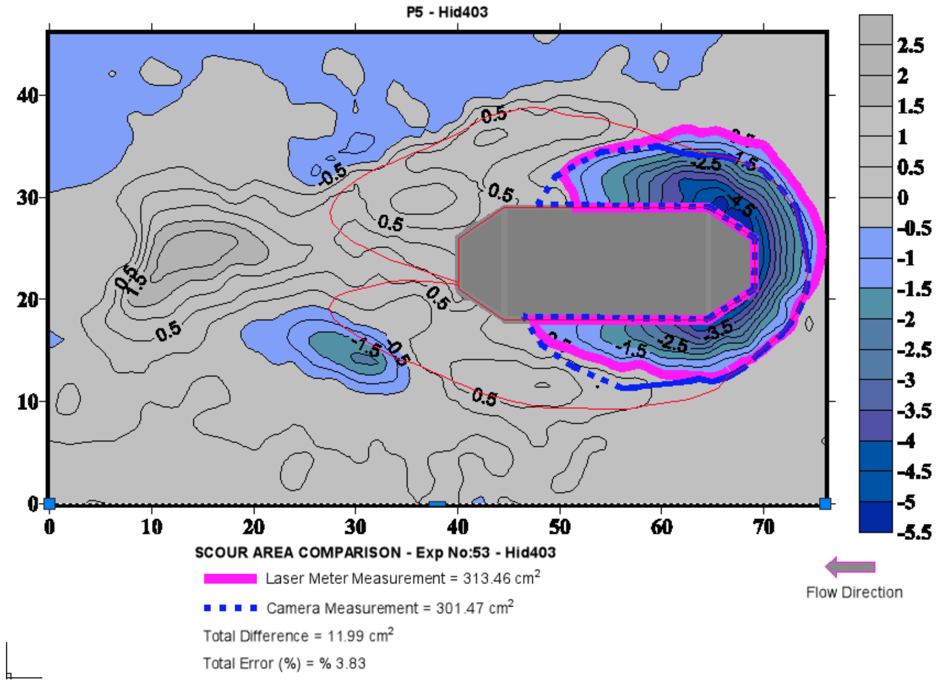

Figure 5.68 Bed configuration at t=25 min and t=45 min for Hid 5 (continued)

The observed scour hole dimensions are summarized for rectangular with trapezoidal nose pier in Table 5.20.

Table 5.20 Scour hole measurements for rectangular with trapezoidal nose pier

Hyd. ID	b (cm)	Time (min.)	Water Depth (cm)	Dimensions			Area (cm^2)
				d_{s1} (cm)	L(cm)	W(cm)	
Hid 1	11	5	20.39	2.0	14.97	17.01	75.86
Hid 1	11	10	6.00	2.1	16.28	16.82	85.76
Hid 2	11	5	22.61	3.7	14.53	16.13	91.23
Hid 2	11	10	6.00	3.8	17.38	21.17	165.60
Hid 3	11	5	23.52	4.4	16.08	16.05	99.78
Hid 3	11	10	6.00	4.8	22.90	23.67	263.25
Hid 4	11	10	22.61	4.2	18.02	17.65	127.95
Hid 4	11	20	6.00	4.3	20.88	21.73	219.41
Hid 5	11	20	22.61	5.2	22.56	21.52	210.27
Hid 5	11	40	6.00	5.3	28.01	25.71	346.37

CHAPTER SIX
NUMERICAL MODELING PIER SCOUR USING ANSYS FLUENT

6.1 Introduction

Taking real time observations are better to understand the complex real life river systems. However it is very difficult to take real time data in the field and sometimes it is even impossible. On the other hand against all flume experiment advantages, the scale effects occurred in laboratory flume experiments that were discussed briefly by Ettema et. al. (1998) can cause problems. Due to the all limitations of traditional design methods and models, CFD (computational fluid dynamics) have been widely used to study the turbulent flow and sediment transport around a pier. CFD offers an alternative way to evaluate solutions of the fluid mechanics more quickly. In this thesis, the pier scour simulation was conducted using the CFD software ANSYS FLUENT which allows application of momentum equations for both fluid and sediment phases individually with coupling Euler-Euler two phase model. The aim is to evaluate the model efficiency comparing experimental findings and numerical results.

ANSYS FLUENT has flexible and easy deforming meshes solving flow problems with unstructured meshes that allow generating geometries. However, due to the complexities of both the flow field and the scour mechanism, numerical modeling of the scour process around bridge piers remains a difficult research topic. CFD process consists of two stages; discretization stage and numerical solution. ANSYS FLUENT uses finite volume method (http://www.ansys.com).

Advances in computational fluid mechanics have provided the basis for further insight into the dynamics of multiphase flows. Currently, there are two approaches for the numerical calculation of multiphase flows: the Euler-Lagrange approach and the Euler-Euler approach. Fundamentally, in the Euler-Lagrange approach, the fluid phase is treated as a continuum by solving the time-averaged Navier-Stokes equations, while the dispersed phase is solved by tracking a large number of particles, bubbles, or droplets through the calculated flow field. The dispersed phase can exchange momentum, mass, and energy with the fluid phase. This makes the model inappropriate for modeling of any application where the volume fraction of the second phase is not negligible.

In the Eulerian multiphase models, fluid and sediment phases are treated mathematically as interpenetrating continua. The phases can be liquids, gases, solids or any used defined matters and their combinations. The momentum and continuity equations are solved for each phase and a single pressure is shared by all phases. The parameters which obtained from kinetic theory are available such as shear and bulk velocities, frictional viscosity or granular temperature …etc. In this study, the Eulerian multiphase is used to simulate scouring around piers. There are two interacting phases: water and sediment (ANSYS FLUENT 14.0 Theory Guide, 2011).

6.2 Fundamental Equations

The Eulerian two phase model mathematical formulations and components are presented below for better understanding of the scour model.

- Continuity Equation
- Momentum equation
    - Interphase Exchange Coefficients (Drag model)
    - Pressure Field
        - for Fluid Phase (SIMPLE Method)
        - for Solid Phase
            - Solid Pressure
            - Granular Temperature
    - Stress Sensor
        - Solid Stress Tensor
            - Shear Viscosity
                - Collisional Viscosity

- Kinetic Viscosity
- Frictional Viscosity
- Bulk Viscosity
- Turbulence Effects
- for Fluid Phase (turbulence models)
- for Solid Phase (Tchen Theory)
- Gravity Force

6.2.1 Governing Continuity Equation

ANSYS FLUENT solves conservation equations for each phase. In the case of granular flows, these equations can be obtained by the application of kinetic theory. According to the law of conservation of mass, both the difference of the rate of mass inflow and the rate of mass outflow must be equal to changing of volume. The continuity equation for phase *q* is (ANSYS FLUENT 14.0 Theory Guide, 2011).

$$\frac{\partial}{\partial t}\left(\alpha_q \rho_q\right) + \nabla\left(\alpha_q \rho_q \overrightarrow{V_q}\right) = 0 \tag{6.1}$$

where,

q = fluid and sediment respectively (f and s)

α_f and α_s = water volume fraction and sediment volume fraction ($\alpha_f + \alpha_s = 1$)

ρ_f and ρ_s = mass density of water and sediment respectively

$\overrightarrow{V_q}$ = the velocity of phase q

The two phase model includes fluid and solid (water and sediment) phases which denoted by *f* and *s* respectively in this research.

6.2.2 Governing Momentum Equation

The concept of incipient motion of sediment particles from the bed is important to understand the aggradation and degradation forces acting on a spherical sediment particle. One of the important forces is drag force that responsible from momentum exchange. In particle and particle interactions drag coefficient gains importance when single particle moves in a dispersed two phase mixture. Other important forces are static pressure gradient and solid pressure gradient, viscous forces and body forces. The component lift force can be neglected which is important for larger particles and virtual mass force which is appropriate when sediment density is much smaller than water density. The momentum equation states that the rate of change of momentum is equal to the resultant force acting on the control volume. The momentum balance for phase *q* by all assuming; (ANSYS FLUENT 14.0 Theory Guide, 2011).

$$\frac{\partial}{\partial t}\left(\alpha_f \rho_f \overrightarrow{V_f}\right)+\nabla\left(\alpha_f \rho_f \overrightarrow{V_f}\overrightarrow{V_f}\right)=-\alpha_f \nabla P+\nabla\overline{\overline{\tau_f}}+\alpha_f \rho_f g+K_{sf}\left(\overrightarrow{V_s}-\overrightarrow{V_f}\right) \qquad (6.2)$$

$$\frac{\partial}{\partial t}\left(\alpha_s \rho_s \overrightarrow{V_s}\right)+\nabla\left(\alpha_s \rho_s \overrightarrow{V_s}\overrightarrow{V_s}\right)=-\alpha_s \nabla P-\nabla P_s+\nabla\overline{\overline{\tau_s}}+\alpha_s \rho_s g+K_{fs}\left(\overrightarrow{V_f}-\overrightarrow{V_s}\right) \qquad (6.3)$$

where;

$\overrightarrow{V_f}$ = the velocity for fluid phase *f*

$\overrightarrow{V_s}$ = the velocity for solid phase *s*

P_s = solid pressure for granular flows in compressible flows

P = pressure for shared by both phases

$K_{sf}\left(\overrightarrow{V_s}-\overrightarrow{V_f}\right)$ and $K_{fs}\left(\overrightarrow{V_f}-\overrightarrow{V_s}\right)$ = the interaction forces between two phases

K_{sf} and K_{fs} = the interphase exchange coefficients

$\overline{\overline{\tau_s}}$ = stress tensor of solid phase

$\overline{\overline{\tau_f}}$ = Reynolds stress tensor for fluid phase

α_f and α_s= fluid and solid volume fractions respectively

The momentum interphase exchange is based on the value of interphase exchange coefficients K_{sf} and K_{fs} between two phases. For calculate the drag coefficient, Gidaspow model (Gidaspow et. al. 1992) is used as following:

$$K_{sf} = \frac{3}{4} C_D \frac{\alpha_s \alpha_f \rho_f \left| \vec{V_s} - \vec{V_f} \right|}{d_s} \alpha_f^{-2.65} \qquad \text{if} \quad \alpha_f > 0.8 \tag{6.4}$$

$$K_{sf} = 150 \frac{\alpha_s (1 - \alpha_f) \mu_f}{\alpha_f d_s^2} + 1.75 \frac{\alpha_f \alpha_s \left(\vec{V_s} - \vec{V_f} \right)}{d_s} \quad \text{if} \quad \alpha_f \leq 0.8 \tag{6.5}$$

$$C_D = \frac{24}{\alpha_f \operatorname{Re}_s} \left[1 + 0.15 (\alpha_f \operatorname{Re}_s)^{0.687} \right] \tag{6.6}$$

where,

d_s = sediment diameter

R_e = Reynolds number

For granular flows a solid pressure P_s is calculated independently and it is used for the pressure gradient term in the compressible regime (where the solids volume fraction is less than its maximum allowed value). A granular temperature is used into the model, because Maxwellian velocity distribution is indicated for particles. The solids pressure that related to granular temperature Θ_s is composed of a kinetic term and a second term due to particle collisions:

$$P_s = \alpha_s \rho_s \Theta_s + 2 \rho_s (1 + e_{ss}) \alpha_s^2 g_{0,ss} \Theta_s \tag{6.7}$$

where;

e_{ss} = the coefficient of restitution for particle collisions = 0.9 (default value)

$g_{0,ss}$ = the radial distribution function and can be expressed for one solid phase as;

$$g_{0,ss} = \left(1 - \left(\frac{\alpha_s}{\alpha_{s,\max}} \right)^{1/3} \right)^{-1} \tag{6.8}$$

The radial distribution function $g_{0,ss}$ is a distribution function that governs the transition from compressible condition with $\alpha<\alpha_{s,max}$, where the spacing between the solid particles can continue to decrease, to the incompressible condition with $\alpha=\alpha_{s,max}$, where no further decrease in the spacing can occur. The default $\alpha_{s,max}$ value is 0.63 can be taken for sand particles. The granular temperature is the proportional to the kinetic energy of the random motion of the particles. If transport equation derived from kinetic theory, it takes the form;

$$\frac{3}{2}\left[\frac{\partial}{\partial t}(\rho_s\alpha_s\Theta_s)+\nabla\left(\rho_s\alpha_s\overrightarrow{V_s}\Theta_s\right)\right]=\left(-P_s\overline{\overline{I}}+\overline{\overline{\tau_s}}\right):\nabla\overrightarrow{V_s}+ \nabla\left(k_{\Theta_s}\nabla\Theta_s\right)-\gamma\Theta_s+\phi_{fs} \tag{6.9}$$

where;

$\left(-P_s\overline{\overline{I}}+\overline{\overline{\tau_s}}\right):\nabla\overrightarrow{V_s}$ = the generation of energy by the solid stress tensor

$k_{\Theta_s}\nabla\Theta_s$ = the diffusive flux of granular energy

$\gamma\Theta_s$ = the collisional dissipation of energy

ϕ_{fs} = the kinetic energy exchange of random fluctuations in particle velocity from the solid phase to the fluid phase and can be defined as;

$$\phi_{fs}=-3K_{fs}\Theta_s \tag{6.10}$$

ANSYS FLUENT uses default Syamlal and O'Brien (1989) model for the diffusion coefficient for granular energy k_{Θ_s} is given by Eq. 6.11 below:

$$k_{\Theta_s}=\frac{15d_s\rho_s\alpha_s\sqrt{\Theta_s\pi}}{4(41-33\eta)}\left[1+\frac{12}{5}\eta^2(4\eta-3)\alpha_s g_{0,ss}+\frac{16}{15\pi}(41-33\eta)\eta\alpha_s g_{0,ss}\right] \tag{6.11}$$

where,

$$\eta=\frac{1}{2}(1+e_{ss}) \tag{6.12}$$

The collisional dissipation of energy $\gamma\Theta_s$, represents energy dissipation rate within the solid phase due to the collisions between particles and it can be defined as;

$$\gamma\Theta_s = \frac{12\left(1-e_{ss}^2\right)g_{0,ss}}{d_s\sqrt{\pi}}\rho_s\alpha_s^2\Theta_s^{3/2} \tag{6.13}$$

Viscous forces are other required component for closure of the momentum equation. Stress tensor of solid phase $\overline{\overline{\tau_s}}$ in Eq. 6.3 given as:

$$\overline{\overline{\tau_s}} = \alpha_s\mu_s\left(\nabla\overrightarrow{V_s} + \nabla\overrightarrow{V_s^T}\right) + \alpha_s\left(\lambda_s - \frac{2}{3}\mu_s\right)\nabla\overrightarrow{V_s}\overline{\overline{I}} \tag{6.14}$$

where;

μ_s = the shear viscosity of sediment phase

λ_s = the bulk viscosity of the sediment phase

Shear and bulk viscosities arise from particle momentum exchange due to translation and collision. Shear viscosity of sediment phase includes three viscosities: collisional, kinetic and optional frictional viscosity. When concentration of flow is low, solid particles move randomly by fluctuating and viscous dissipation and stress is called kinetic. In higher concentrations, solid particles move higher and it referred to as collisional. When sediment concentration in the flow is very high (more than 50% in volume), the particle motion can be as rolling, sliding or jumping along the bed is called frictional (Duarte and Murata et al., 2008). The shear viscosity of sediment phase can be defines as:

$$\mu_s = \mu_{s,kin} + \mu_{s,col} + \mu_{s,fr} \tag{6.15}$$

ANSYS FLUENT uses Syamlal and O’Brien (1989) equation for calculating kinetic viscosity is default;

$$\mu_{s,kin} = \frac{\alpha_s d_s \rho_s \sqrt{\Theta_s \pi}}{6(3-e_{ss})}\left[1+\frac{2}{5}(1+e_{ss})(3e_{ss}-1)\alpha_s g_{0,ss}\right] \tag{6.16}$$

$$\mu_{s,col} = \frac{4}{5}\alpha_s \rho_s d_s g_{0,ss}(1+e_{ss})\left(\frac{\Theta_s}{\pi}\right)^{1/2} \tag{6.17}$$

$$\mu_{s,fr} = \frac{P_s \sin\phi}{2\sqrt{I_{2D}}} \tag{6.18}$$

where;

ϕ = the angle of internal friction

I_{2D}= the second invariant of the deviatoric stress tensor

Granular kinetic theory based on that solids are in continuous and chaotic motion in the fluid. That chaotic motion can be in low concentrations or high concentrations due to the frictions between fluid and solid. The bulk viscosity of the sediment λ_s accounts for the resistance of the granular particle to compression and expansion. The following equation from Lun et. al. (1984) gives λ_s as;

$$\lambda_s = \frac{4}{3}\alpha_s \rho_s d_s g_{0,ss}(1+e_{ss})\left(\frac{\Theta_s}{\pi}\right)^{1/2} \tag{6.19}$$

Default value of the bulk viscosity of the sediment is zero but it can be change with possible expression of Lun et. al. (1984).

Only the full 3D model is suitable for a realistic simulation of local scour processes. However 3D hydrodynamic equations include the Navier-Stokes equations with turbulent flows near the structures and solving them is very complex and difficult. Turbulence is a fluid motion in which velocity, pressure and other flow quantities fluctuate irregularly in time and space. Turbulence is an issue that requires interdisciplinary work. The equations are nonlinear and aren’t enough equation versus unknowns. This problem is called "closure problem". Also the modeling of turbulence in multiphase flows is extremely complex versus single phase modeling. There are various mathematical models used in flow modeling to understand turbulence. In this study, modified *k*-*ε* model is used for predicting of turbulence fluctuations for the fluid phase. ANSYS FLUENT uses Tchen theory (Tchen, 1947) correlations for the second phases. The eddy viscosity model is used to calculate average fluctuating quantities.

6.2.2.1 Turbulence in the Fluid Phase

The Reynolds stress tensor for the fluid phase *f* can be expressed as (ANSYS FLUENT 14.0 Theory Guide, 2011);

$$\overline{\overline{\tau_f}} = -\frac{2}{3}\left(\rho_f k_f + \rho_f \mu_{t,f} \nabla \overrightarrow{U_f}\right)\overline{\overline{I}} + \rho_f \mu_{t,f}\left(\nabla \overrightarrow{U_f} + \nabla \overrightarrow{U_f^T}\right) \tag{6.20}$$

where;

$\overrightarrow{U_f}$ = the phase weighted velocity

$\mu_{t,f}$ = the turbulent viscosity can be expresses as;

$$\mu_{t,f} = \rho_f C_\mu \frac{k_f^2}{\varepsilon_f} \tag{6.21}$$

where;

C_μ = 0.0848 for RNG *k*-*ε* turbulence model

k_f = turbulent kinetic energy

ε_f = dissipation rate

The turbulent energy k_f and dissipation rate ε_f can be obtained from the RNG *k*-*ε* turbulence model:

$$\frac{\partial}{\partial t}\left(\alpha_f \rho_f k_f\right)+\nabla\left(\alpha_f \rho_f \overrightarrow{U_f} k_f\right)=\nabla\left(\alpha_f \frac{\mu_{t,f}}{\sigma_k}\nabla k_f\right)+\alpha_f G_{k,f}-\alpha_f \rho_f \varepsilon_f + \alpha_f \rho_f \Pi_{k_f} \tag{6.22}$$

$$\frac{\partial}{\partial t}\left(\alpha_f \rho_f \varepsilon_f\right)+\nabla\left(\alpha_f \rho_f \overrightarrow{U_f} \varepsilon_f\right)=\nabla\left(\alpha_f \frac{\mu_{t,f}}{\sigma_k}\nabla \varepsilon_f\right)+ \alpha_f \frac{\varepsilon_f}{k_f}\left(C_{1\varepsilon} G_{k,f}-C_{2\varepsilon}\rho_f \varepsilon_f\right)+\alpha_f \rho_f \Pi_{\varepsilon_f} \tag{6.23}$$

where;

$G_{k,f}$ = the production of turbulent kinetic energy

Π_{ε_f} and Π_{k_f} = influences of the solid phase on the fluid phase

The production of turbulent kinetic energy $G_{k,f}$ is modeled identically for the standard, RNG and modified *k*-*ε* turbulence models. From the each equation for the transport of *k*, this term may be defined as:

$$G_{k,f} = -\rho\overline{u_i^{'} u_j^{'}}\frac{\partial u_j}{\partial x_i} \tag{6.24}$$

Π_{k_f} is derived from the instantaneous equation of the fluid phase. Π_{k_f} and Π_{ε_f} can be defined as below:

$$\Pi_{k_f} = \frac{K_{sf}}{\alpha_f \rho_f}\left(k_{sf} - 2k_f + \overrightarrow{v_{sf}}\,\overrightarrow{v_{dr}}\right) \tag{6.25}$$

$$\Pi_{\varepsilon_f} = C_{3_\varepsilon}\frac{\varepsilon_f}{k_f}\Pi_{k_f} \tag{6.26}$$

where;

k_{sf} = the covariance of the velocities of the fluid phase *f* and the solid phase *s*

$\overrightarrow{v_{sf}}$ = the relative velocity between fluid and solid phase

$\overrightarrow{v_{dr}}$ = the drift velocity resulted from turbulent fluctuations in the volume fraction

The RNG *k*-*ε* turbulence model for the water phase with supplement of extra terms which take into account the interphase turbulent momentum transfer was used. ε equation rederived using the renormalizes group (RNG) theory by Yakhot et. al. (1992). One new was introduced to take into account the highly anisotropic features of turbulence, usually associated with regions of large shear, and to modify the viscosity accordingly. This term was claimed to improve the simulation accuracy of the RNG *k*-*ε* turbulence model for highly strained flows (Wu, 2002). The Reynolds stress tensor and coefficient $C_{\varepsilon 1}$ and $C_{\varepsilon 2}$ constants determined from benchmark experiments. Yakhot et. al. (1992) expressed the constants $C_{\varepsilon 1} = 1.42 - \eta(1-\eta/\eta 0)/(1+\beta\eta^3)$. Here, $\beta=0.015$, $\eta=0.012$ and $\eta_0=4.38$, because of the term of the right side of the equation is small, $C_{\varepsilon 1}$=1.42. The other coefficients are $C_{\varepsilon 2}=1.68$, $C_\mu=0.0848$, $\sigma_k=0.7179$ and $\sigma_\varepsilon=0.7179$.

The drift velocity can be computed by:

$$\overrightarrow{v_{dr}} = -D_{t,sf}\left(\frac{1}{\sigma_{sf}\alpha_s}\nabla\alpha_s - \frac{1}{\sigma_{sf}\alpha_f}\nabla\alpha_f\right) \tag{6.27}$$

where;

$D_{t,sf}$ =the binary turbulent diffusion coefficient, D_s and D_f are diffusivities. When using Tchen theory in multiphase flows, ANSYS FLUENT assumes $D_s=D_f=D_{t,sf}$ and = 0.75 (default value).

σ_{sf} = dispersion Prandtl number that default value is 0.75

6.2.2.2 Turbulence in the Solid Phase

Tchen theory correlations are used for the dispersed phases which based on the particle turbulent kinetic energy and the turbulent energy due to interphase interaction are expressed as algebraic function of the continuous phase kinetic energy in ANSYS FLUENT. Time and length scales that characterize the motion are used to evaluate dispersion coefficients, correlation functions and the turbulent kinetic energy of each dispersed phase. There are two characteristic times. The first time scale is the characteristic particle relaxation time connected with internal effects acting on the particle and defined as (ANSYS FLUENT 14.0 Theory Guide, 2011);

$$\tau_{F,sf} = \alpha_s \rho_f K_{sf}^{-1} \left(\frac{\rho_s}{\rho_f} + C_v \right) \tag{6.28}$$

where;

C_v = the added mass coefficient and = 0.5 (default value)

The second time scale is the characteristic time of correlated turbulent motions or eddy particle interaction time which is defined as:

$$\tau_{t,sf} = \tau_{t,f} \left(1 + C_\beta \xi^2\right)^{-1/2} \tag{6.29}$$

where;

$\tau_{t,f}$ = the characteristic time of energetic turbulent eddies, and

$$\xi = \frac{\left|\vec{V_r}\right|}{\sqrt{\frac{2}{3} k_f}} \tag{6.30}$$

where;

$\vec{V}_r$ = the averaged value of the local relative velocity between a particle and surrounding fluid.

The characteristic time of energetic turbulent eddies can be defined as:

$$\tau_{t,f} = \frac{3}{2} C_\mu \frac{k_f}{\varepsilon_f} \tag{6.31}$$

$$C_\beta = 1.8 - 1.35\cos^2\theta \tag{6.32}$$

where;

θ = the angle between the mean particle velocity and the mean relative velocity

The ratio between these two characteristic times is defined as:

$$\eta_{sf} = \frac{\tau_{t,sf}}{\tau_{F,sf}} \tag{6.33}$$

The turbulence quantities for solid phase follow as (Simonin and Viollet (1990)):

$$k_s = k_f\left(\frac{b^2 + \eta_{sf}}{1+\eta_{sf}}\right) \tag{6.34}$$

The eddy viscosity for the solid phase is:

$$D_s = D_{t,sf} + \left(\frac{2}{3}k_s - b\frac{1}{3}k_{sf}\right)\tau_{F,sf} \tag{6.35}$$

The binary turbulent diffusion coefficient $D_{t,sf}$ and covariance of the velocities of the fluid phase and the solid phase k_{sf} can be defined as follows:

$$D_{t,sf} = \frac{1}{3}k_{sf}\tau_{t,sf} \tag{6.36}$$

$$k_{sf} = 2k_f\left(\frac{b+\eta_{sf}}{1+\eta_{sf}}\right) \tag{6.37}$$

where;

$$b = (1 + C_v)\left(\frac{\rho_s}{\rho_f} + C_v\right)^{-1} \tag{6.38}$$

6.2.3 Volume Fractions

Each phase behaves as an interpenetrating continuum in the Eulerian approach. The continua includes phasic volume fractions that denoted here by α_q. Volume fractions represent the space occupied by each phase, and the laws of conservation of mass and momentum are satisfied by each phase individually. The volume fraction is denoted as $0 \leq \alpha_q \leq 1$ for each phase and assumed to be continuous functions of space and time and their sum is equal to one. The volume of phase q and V_q are defined as;

$$V_q = \int_V \alpha_q dV \tag{6.39}$$

where; $\sum_{q=1}^{n} \alpha_q = 1$

6.3 Numerical Simulation of Scouring Using Eulerian Two Phase Model

The experiments described in Chapter 4 and corresponding to the piers P1 and P2 with the generation of the hydrograph Hid 2 are simulated by using ANSYS FLUENT software. The relevant experimental findings given in Chapter 5 are compared with those obtained from these numerical solutions.

The geometry configuration of the flume is shown in Figure 6.1. The grids statics were controlled by the ANSYS for good meshing. The computational domain is first meshed using a quad/tri cell size of 50 mm and then finer meshes were described in the vicinity of the pier to define the appropriate cell dimension for application of turbulent wall functions. Therefore, the cell size of 5 mm was used near the pier wall and increased up to 50 mm. Three dimensional grid system had 98.560 nodes and

86.073 cells with according to ANSYS meshing generator. Then the sediment layer of 26 cm was defined while initial and boundary conditions were given. The meshing grids for the simulation of P1 and P2 pier are shown in Figure 6.2a and 6.2b, respectively.

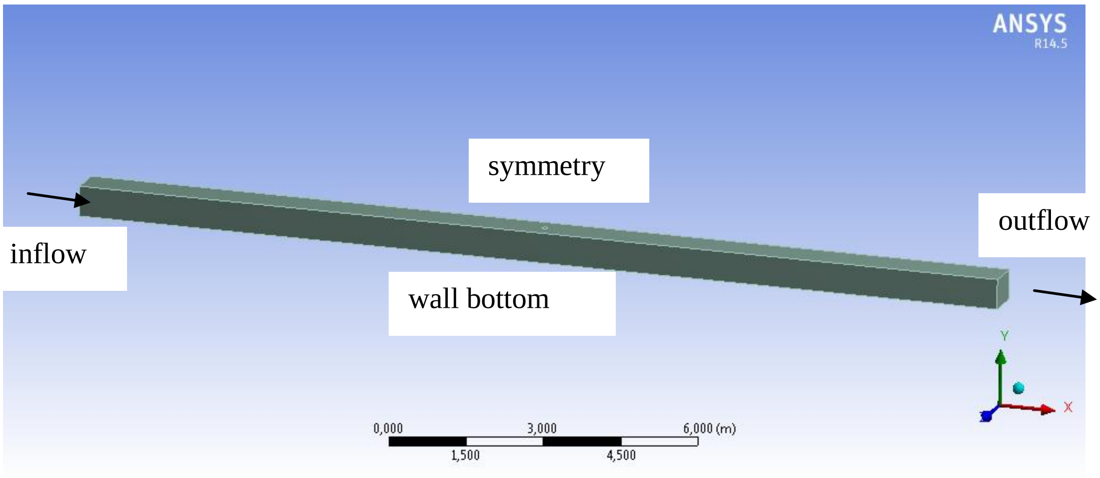

Figure 6.1 Geometry configuration of flume. X is the flow direction. The gravity was set to –Y direction. The sediment layer thickness is 26 cm. The figure has no scale

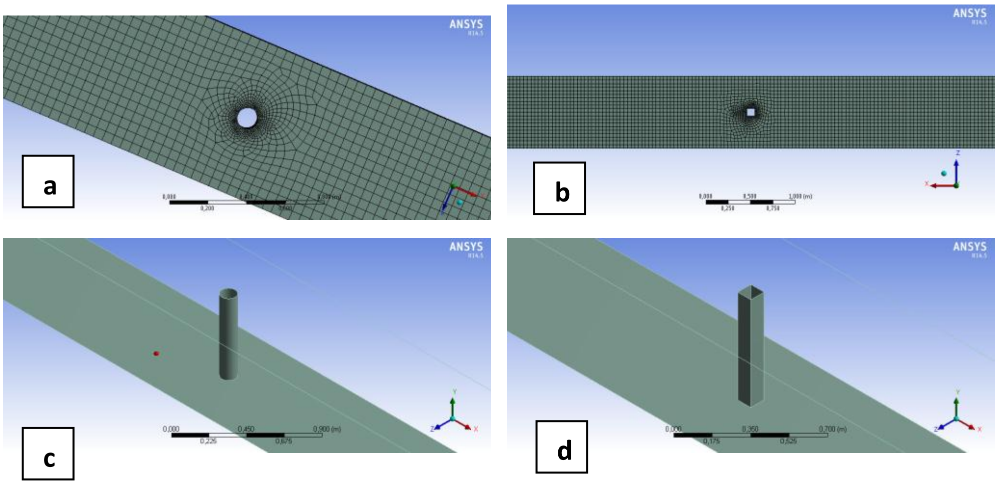

Figure 6.2 Meshing grid system used in FLUENT simulations a) and c) for pier P1 b) and d) for pier P2

At the wall boundaries no slip boundary condition was set; it means that all velocity components were zero. The side walls and pier wall were assumed to be smooth. On the other hand the roughness height of the bottom wall was specified according to D_{50} of the sediment. In the flume domain all velocity components were zero as initial conditions. At the inlet, the input hydrograph constitute the upstream boundary condition. The velocity was set to x direction by using user defined function UDF macro. A logarithmic velocity profile selected at the end of the inflow section while the hydrograph was passing. At the downstream outlet, the outflow boundary condition was set. It means that the normal gradients of all dependent variables were set zero for exit. The water surface of the flume was modelled as a symmetry plane where a zero-gradient condition is used for the velocity components parallel to the free surface, while the gradients of k, ε and velocity components perpendicular to the free surface are set to zero. The symmetry plan assumption is consistent since all Froude numbers are smaller than 0.4. Standard wall functions were used for near wall treatment. The Gidaspow model was used to determine the water sediment exchange drag coefficient, as made by Zhao (2005). The binary turbulent diffusion coefficient was set 0.75 as default value and particle collision coefficient was set 0.9 as suggested for sand material.

The volume fraction of the sediment was patched to adapted region before the calculation started. Density and viscosity of the water were taken as default values for 20 ^{0}C; 998.2 kg/m^3 and 0.001003 kg/ms respectively. The properties of the second fluid phase sediment was defined by kinetic theory. The gravitational acceleration is taken as 9.81 m/s^2 in – y direction. The atmosphere pressure was taken as 101325 Pa for open channel flow.

While defining boundary conditions, various turbulence parameters are required. In this study turbulence intensity and hydraulic diameter were selected for computing the values of k and ε. Turbulence intensity, I is defined as the ratio of the root mean square of the velocity fluctuations. An empirical formula is used to calculate the turbulence intensity (ANSYS Inc. 2001);

$$I \equiv \frac{u'}{u_{avg}} = 0.16(R_e)^{-\frac{1}{8}} \tag{6.40}$$

where;

u' = the velocity fluctuations

u_{avg} = the mean flow velocity

The solution conditions and methods were summarized in Table 6.1 below. In the simulations, the computation duration was 960 hours by using a computer with 8 core processors. The unsteady and implicit scheme was selected for simulations. For providing the stability conditions the Courant – Friedrichs – Lewy (CFL) condition was used. Since the water waves travel at a much higher velocity than the bed transients this condition is given by:

$$C_n = \frac{\left(u + \sqrt{gh}\right)\Delta t}{\Delta x} \leq 0.25 \tag{6.41}$$

where; C_n = Courant number

Table 6.1 Summary of the solution conditions and methods

Space :	3D
Time :	Unsteady
Turbulence Model :	RNG k-ε Model
	Standart Wall Functions
	Tchen Theory
Drag Coefficient :	Gidaspow
Viscosity Model :	Kinetic Theory for Sediment Phase
Pressure Velocity Coupling :	Phase Coupled SIMPLE
Momentum :	First order upwind
Volume Fraction :	First order upwind
Turbulence Kinetic Energy :	First order upwind
Turbulence Dissipation Rate :	First order upwind

6.4 Comparison of Experimental and Numerical Results

The interfaces between water and sediment was taken as profile which corresponded to the sediment volume fraction $\alpha_s = 0.5$. The simulated and measured scour holes configurations for P1 and P2 are given in Figure 6.3 and Figure 6.4, respectively.

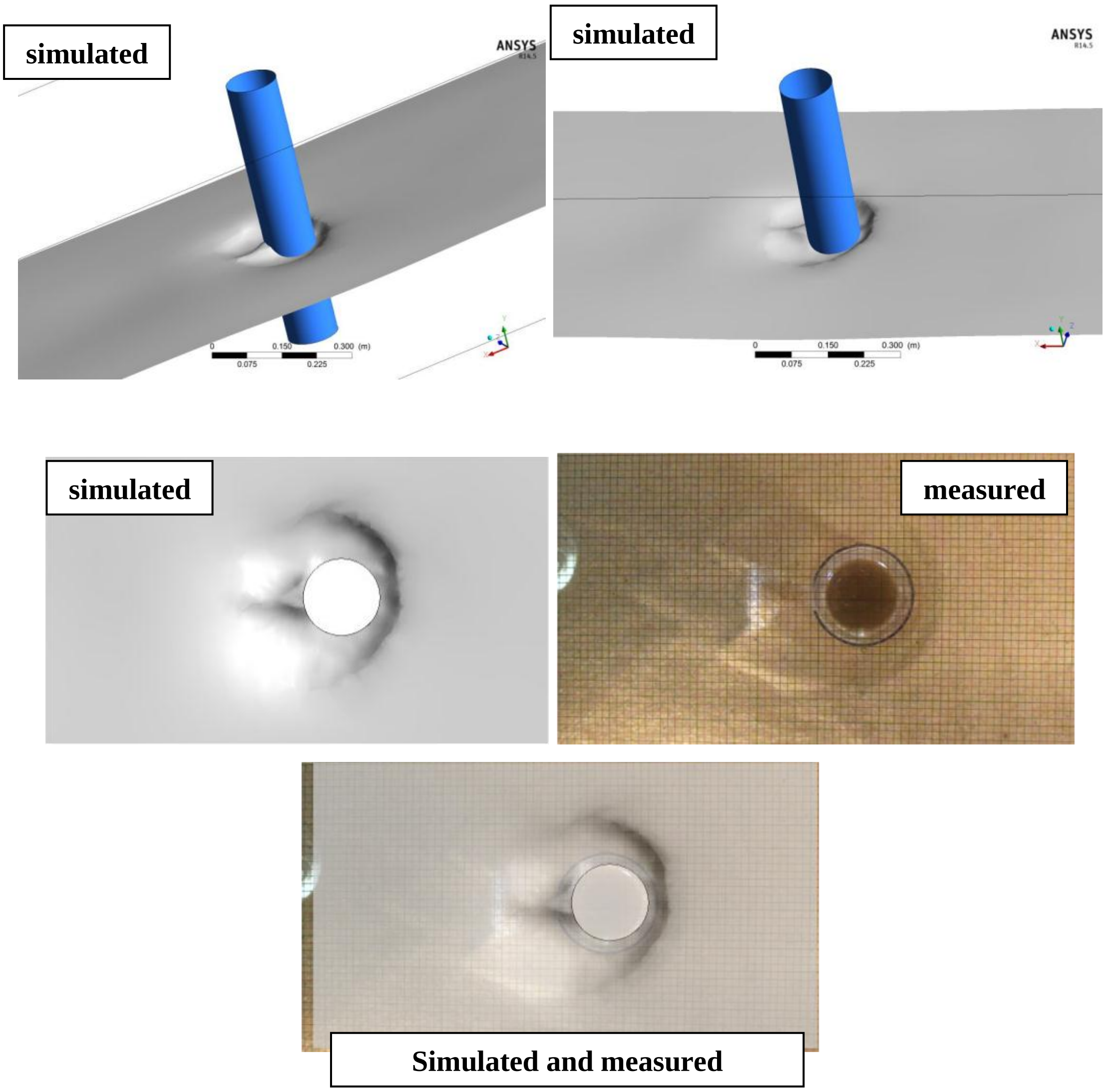

Figure 6.3 Final Scour hole configurations for P1 with Hid 2

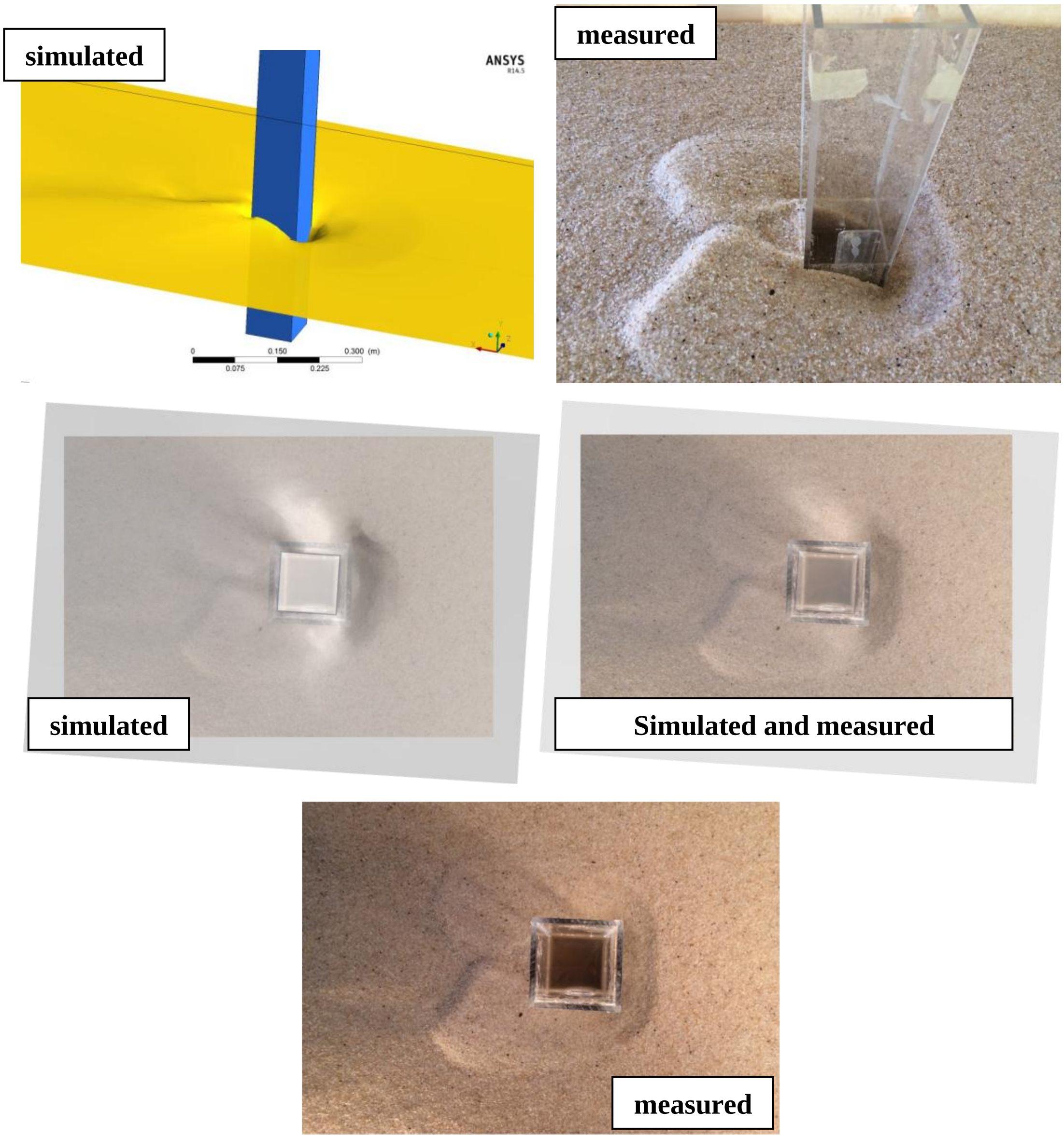

Figure 6.4 Final Scour hole configurations for P2 with Hid 2

Figures 6.5 and 6.6 represent the variations of bed elevations for P1 and P2 piers along the channel from the beginning of the experiment until the end of the hydrograph, involving both steady and unsteady cases. The final experimental and numerical elevations corresponding to t= 15 min are depicted in Figures 6.7 and 6.8 for piers P1 and P2, respectively. The values of RMSE, MAE errors and the determination coefficient R^2 are also given in related figures.

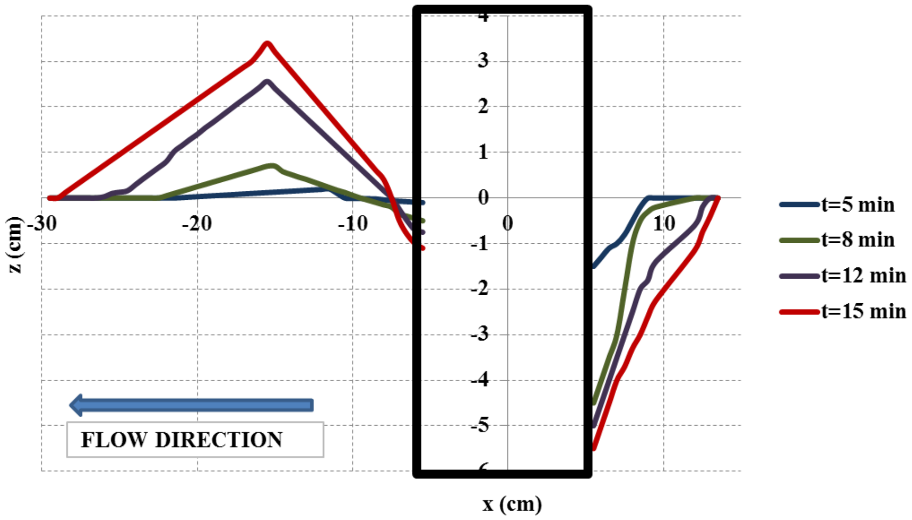

Figure 6.5 Bed elevations along the channel at the region near P1

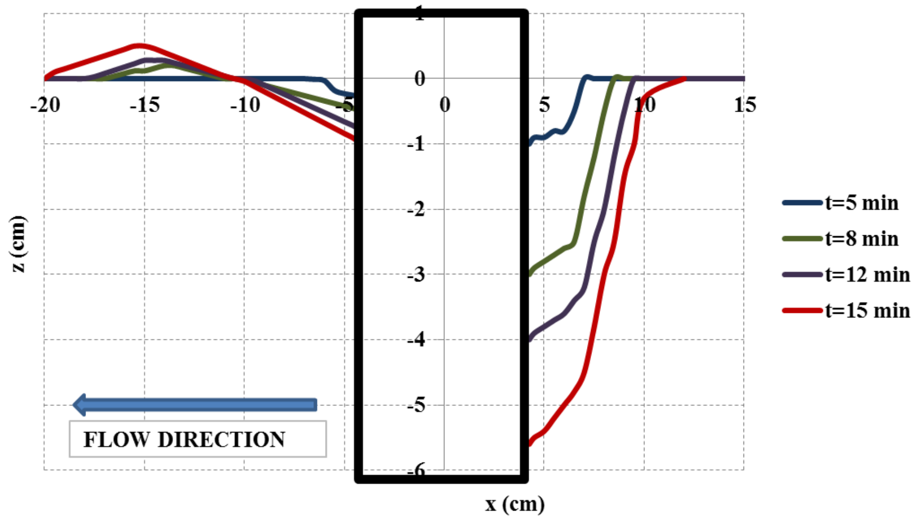

Figure 6.6 Bed elevations along the channel at the region near P2

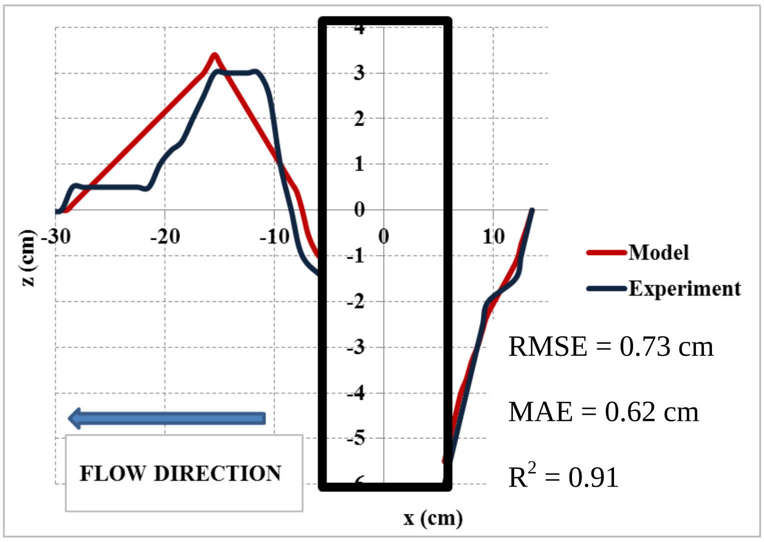

Figure 6.7 Bed elevations along the channel at the region near P1 at the t = 15 min

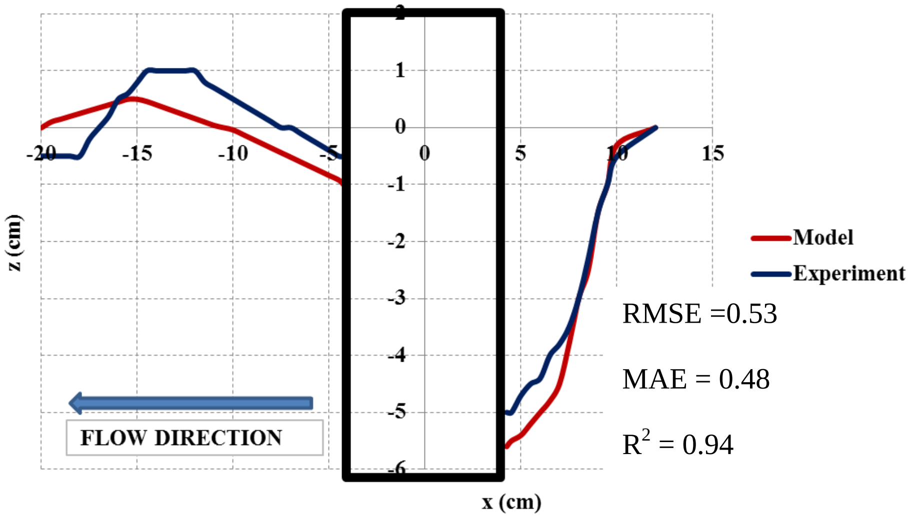

Figure 6.8 Bed elevations along the channel at the region near P2 at the t = 15 min

The experimental and numerical temporal variations of the scour depths at point A are provided in Figures 6.9 and 6.10 for P1 and P2, respectively.

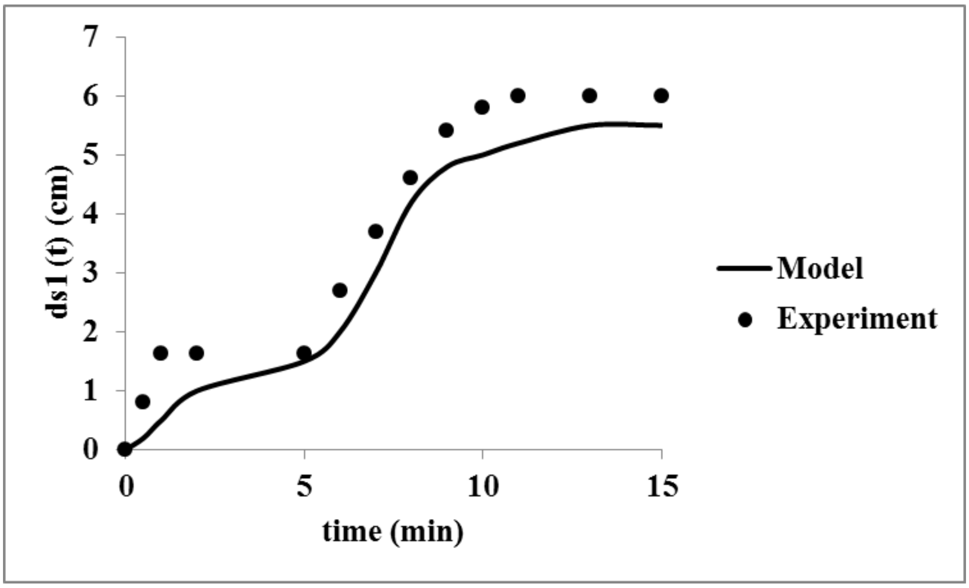

Figure 6.9 Measured and simulated $d_{s1}(t)$ values at point A for P1

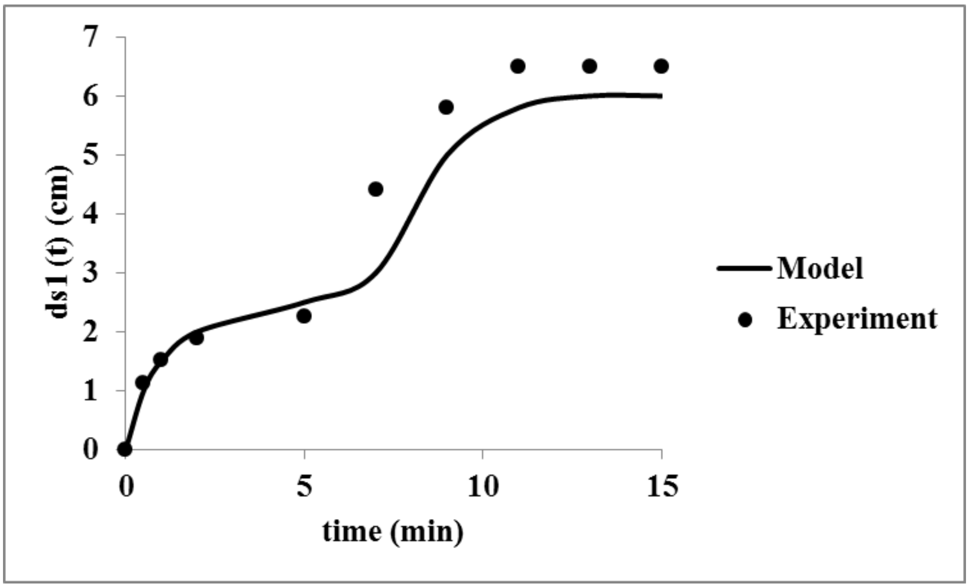

Figure 6.10 Measured and simulated $d_{s1}(t)$ values at point A for P2

The theoretical time dependent scour depths obtained from the software ANSYS FLUENT at points B and C are plotted in Figures 6.11 and 6.12 for P1 and P2, respectively. In these figures, only one experimental values appears since the final value (at the end of the experiment) was measured.

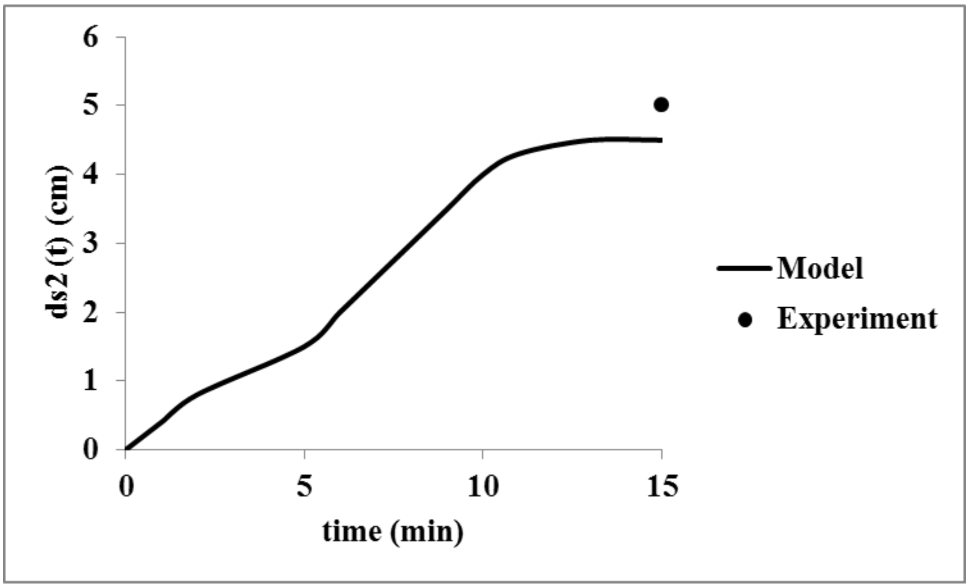

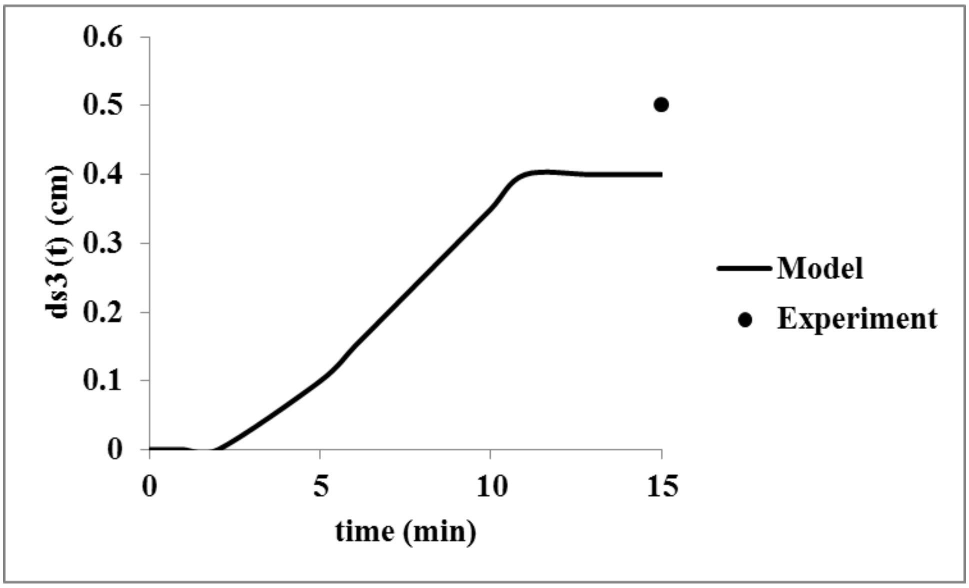

Figure 6.11 Measured and simulated $d_{s2}(t)$ and $d_{s3}(t)$ values at point B and C for P1

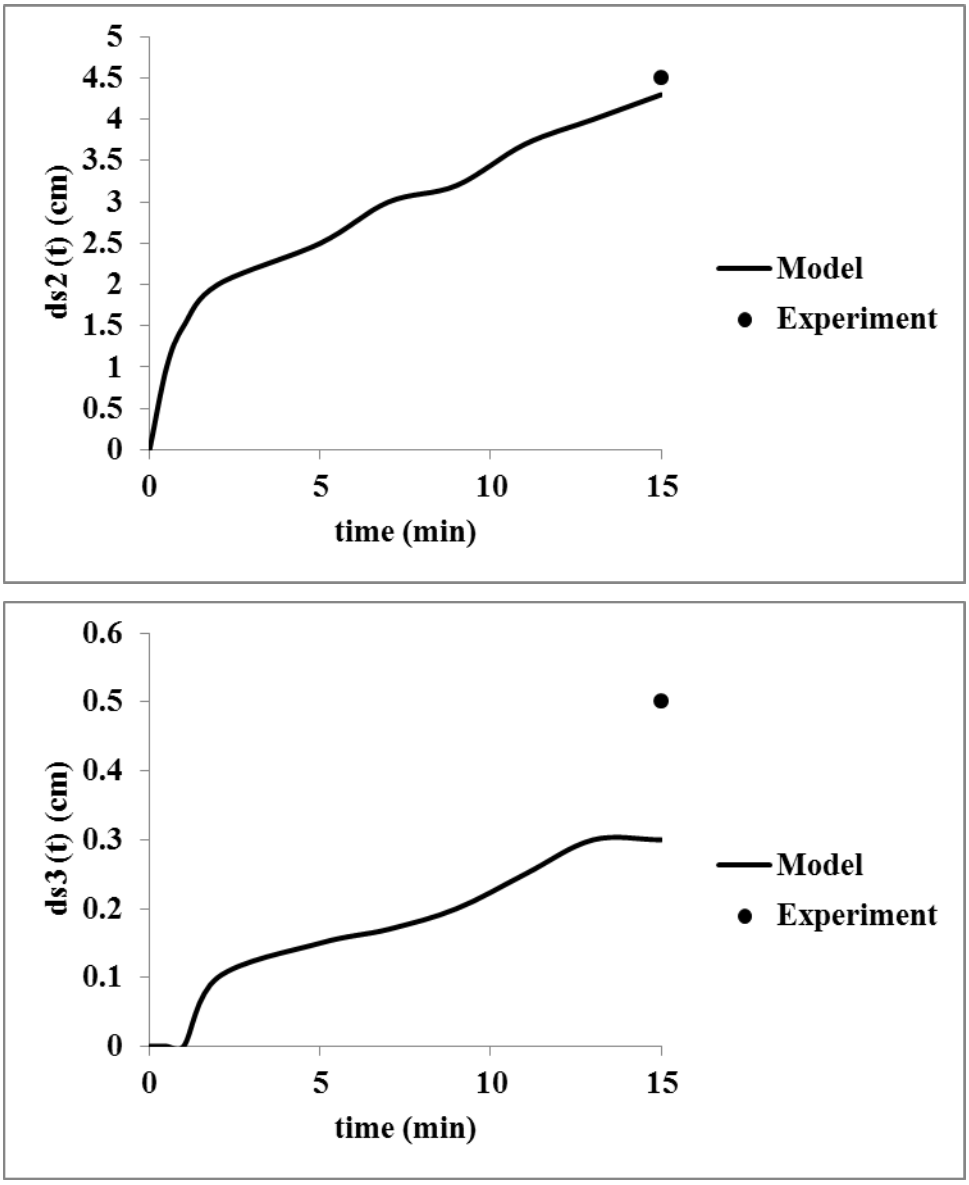

Figure 6.12 Measured and simulated $d_{s2}(t)$ and $d_{s3}(t)$ values at point B and C for P2

The velocity vectors around P1 at water surface calculated at t = 5, 7, 8 and 10 min are given in Figure 6.13a,b,c,d.

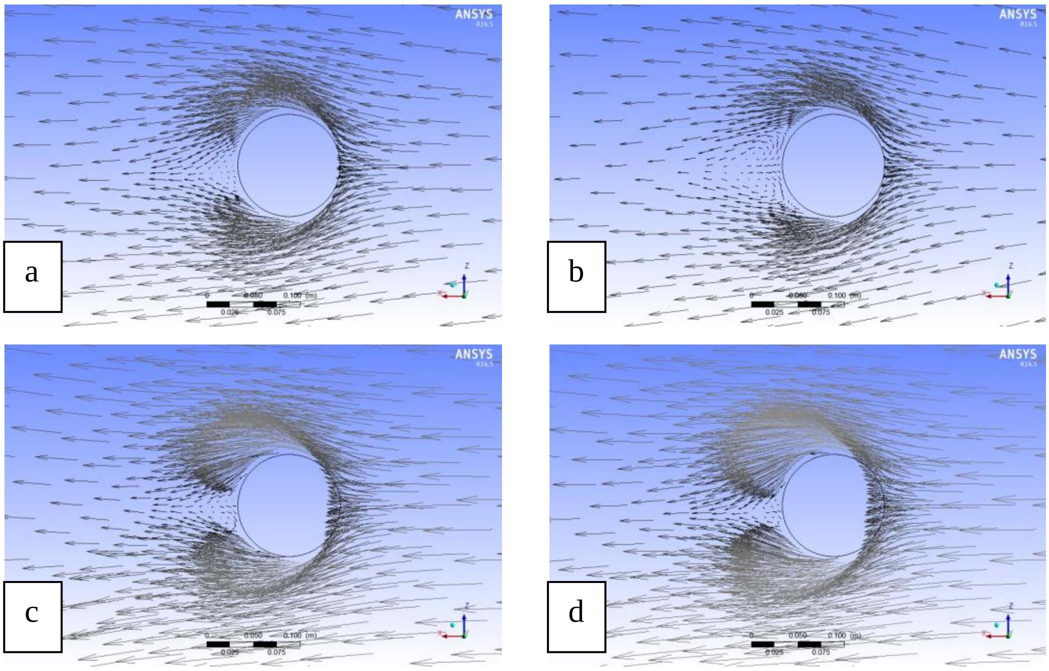

Figure 6.13 Velocity vectors around P1 at a) t = 5 min, b) t = 7 min c) t = 10 min

The velocity vectors around P2 at water surface calculated at t = 5, 7, 8 and 10 min are given in Figure 6.14a,b,c,d.

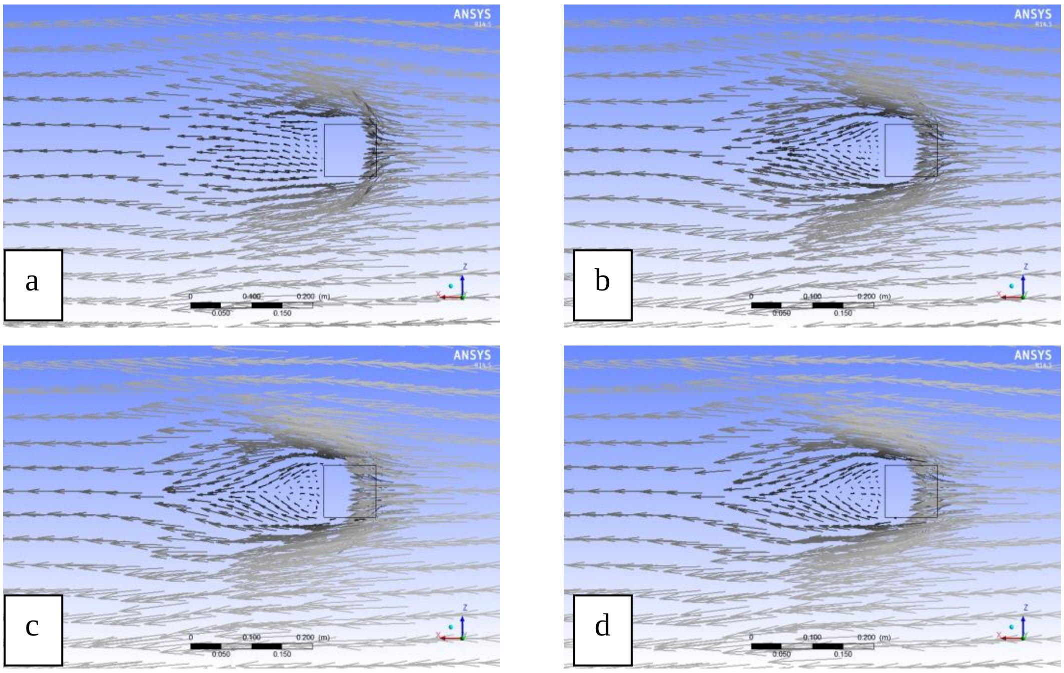

Figure 6.14 Velocity vectors around P2 at a) t = 5 min, b) t = 7 min c) t = 10 min

The Figure 6.13 and 6.14 show the simulated flow field at the water surface around the pier obtained by RNG k-ε model. The figure clearly displays circulation and reversed flow in the immediate vicinity of the pier.

Figure 6.15 indicates velocity vectors for F_r = 0.23 in longitudinal section. Downward flow occurs in front of the pier, with an increase in velocity magnitude and sharper angles when the bottom was approached. Wake vortices occur in the downstream of the pier which cause deposition.

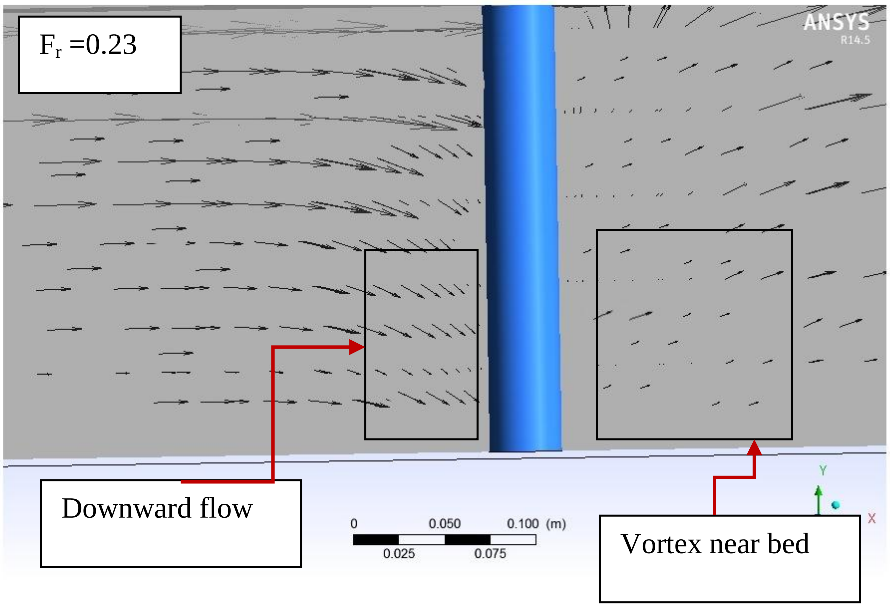

Figure 6.15 Velocity vectors in longitudinal section

The measured and calculated values of the scour hole length (L) and width (W) are given in Table 6.2 for P1. The R^2values are 0.98 and 0.99 for of the scour hole length (L) and width (W), respectively.

Table 6.2 Measured and calculated scour length *L* and scour width *W* values for P1

time	L calculated	L measured	W calculated	W measured
min	**cm**	**cm**	**cm**	**cm**
5	17.14	18.35	18.67	19.08
10	20.05	19.88	22.16	20.52
15	21.15	20.94	24.11	21.05

The measured and calculated values of the scour hole length (L) and width (W) are given in Table 6.3 for P2. The R^2values are 0.98 and 0.95 for of the scour hole length (L) and width (W), respectively.

Table 6.3 Measured and calculated scour length *L* and scour width *W* values for P2

time	L calculated	L measured	W calculated	W measured
min	**cm**	**cm**	**cm**	**cm**
5	9.68	10.44	15.95	16.36
10	10.9	10.66	17.05	16.36
15	15.25	13.24	20.66	21.58

CHAPTER SEVEN
CONCLUSION

In the scope of this thesis, the time dependent scour depths, the equilibrium scour depths and the temporal evolutions of the scour hole were investigated for five different pier shapes. Circular, square, rectangular, rectangular with circular nose and rectangular with trapezoidal nose piers were tested. All the experiments were performed under clear water conditions and by using uniform bed material.

The peak flow rates were found much more effective compared to hydrograph durations.

Equilibrium scour depths were calculated by applying the approach proposed by Shapperds. The measured and calculated equilibrium scour depth values were close to each other in the case of P1, P2 and P5. The calculated equilibrium depths were higher for P3 and P4 in steady flow case.

The observed equilibrium scour depths increased in the following order: P5 - P4 - P1- P2 and P3. According to this result, rectangle with trapezoidal noses shaped piers and rectangle with circular noses shaped bridge piers seem to be more advantageous in order to reduce the magnitude of the scour depth. When the experiments were considered as a whole, it was observed that the measured final scour depths increased in the same order.

The final and equilibrium scour depths were found closer to each other in the case of circular, square and rectangular with trapezoidal nose pier.

The discrepancy between the measured dimensionless scour depths and those calculated from the relation suggested by Oliveto and Hager (2002) seems to result from the fact that steady and unsteady flows are combined in this study.

The calculated shape factor was closer to that proposed by Oliveto and Hager (2002) for P2. The calculated shape factor was closer to that proposed by Tison (1940) for P3. The calculated shape factor was slightly less than the smallest value existing in literature for P4. It was not possible the compare the calculated shape factor for P5 since a similar study was not available.

The determination coefficients for the obtained empirical relations were in order of magnitude ranging from 0.85 to 1.00. This fact implies that these relations are significant statistically.

The smallest scour hole was observed for the rectangular with circular noses pier. The dimensions of the scour hole become greater in the following order: the rectangular with trapezoidal noses, circular, square and rectangular piers.

An acceptable compatibility was observed between experimental findings and numerical results obtained from the software ANSYS FLUENT used with RNG k-ε turbulence model, for circular and square piers.

The calculated lengths and widths of the scour hole were found close to the measured ones.

Recommendations for the future studies can be outlined as follows:

Circular, square, rectangular, rectangular with circular nose and rectangular with trapezoidal nose pier shapes with different dimensions can be tested to observe the effect of dimension for a given shape and also to perform much more advanced study related to the variation of the shape factor.

Sediment with different sizes could be tasted to reveal the influence of the sediment dimension.

Trapezoidal hydrographs may also be generated in order to study the shape of hydrographs.

Similar investigations can be carried out for abutments.

Similar studies can be carried out with protected piers in order to determine the efficiency of the countermeasures such as riprap, collar, slot,… etc.

Experiments with sediment feeding could be interesting since this situation reflects what happens in nature.

Scour phenomena can be studied in the case of pier groups and also piled piers.

The ANSYS FLUENT software can be used with various turbulence models.

REFERENCES

Alabi, P. D. (2006). *Time development of local scour at a bridge pier fitted with a collar.* Msc Thesis, University of Saskatchewan, Saskatchewan.

Ali, K. H., & Karim, O. (2002). Simulation of flow around piers. *Journal of Hydraulic Research , 40*, 161-174.

Ali, K. H., & Lim, S. Y. (1986). Local scour caused by submerged wall jets. *Proceedings of the Institution of Civil Engineers* , 607-645.

Ali, K. H., Karim, O., & O'Connor, B. A. (1997). Flow patterns around bridge piers and offshore structures . *Proceedings, Congress of the International Association of Hydraulic Research.* San Francisco: IAHR.

Ansari, S. A., & Qadar, A. (1994). Ultimate depth of scour around bridge piers. *1994 National Conference on Hydraulic Engineering,* 51-55. New York: ASCE.

Asano, T. (1990). Two-phase flow model on oscillatory sheet-flow. *Proceedings of 22nd Conference on Coastal Engineering*, 2372-2384.

Azhari, A., Saghravani, S. F., & Mohammadnezhad, B. A. 3D Numerical modeling of local scour around the cylindrical bridge piers . *XVIII International Conference on Water Resources CMWR 2010* . Barcelona: CIMNE.

Ballio, F., & Orsi, E. (2001). Time evolution of scour around bridge abutments. *Water Engineering Research , 2*, 243-259.

Beg, M. (2013). Predictive competence of existing bridge pier scour depth predictors. *European International Journal of Science and Technology , 2*, 161-178.

Bor Turkben, A., Elci, S., & Caliskan, A. (2008). Prediction of sedimentation in reservoirs by acoustic methods. *River Flow International Conference on Fluvial Hydraulic.* River Flow.

Breusers, H., & Raudkivi, A. J. (1991). *Scouring* (Vol. 2). Rotterdam: A.A. Balkema.

Breusers, H., Nicollet, G., & Shen, H. W. (1977). Local scour around cylindrical piers. *Journal of Hydraulic Research , 15*, 211-252.

Chabert, J., & Engeldinger, P. (1956). *Etude des affouillements autour des piles de ponts (Study of scouring around bridge piers).* Chatou, France: Laboratoire National d'Hydraulique.

Chang, W. Y., Lai, J. S., & Yen, C. L. (2004). Evolution of scour depth at circular bridge piers. *Journal of Hydraulic Engineering , 130*, 905-913.

Chatterjee, S., Ghosh, S., & Chatterjee, M. (1994). Local scour due to submerged horizontal jet. *Journal of Hydraulic Engineering,120*, 973-992.

Chiew, Y. M., & Melville, B. W. (1996). Temporal development of local scour depth at bridge piers. *North American Water and Environment Congress.* California: ASCE.

Coleman, S. E., & Melville, B. W. (2001). Case study:New Zeland bridge scour experiences. *Journal of Hydraulic Engineering , 127*, 535-546.

Coleman, S. E., Lauchian, C. S., & Melville, B. W. (2003). Clear-water scour development at bridge abutments. *Journal of Hydraulic Engineering, 41*, 521-531.

Constantinescu, G., & Squires, K. D. (2004). Numerical investigation of the flow over a sphere in the subcritical and supercritical regimes. *Physics of Fluids, 16*, 1449-1467.

Cunha, L. V. (1975). Time evaluation of local scour. *International Association for Hydraulic Research, Eleventh International Congress.* Sao Paulo: IAHR.

Dey, S., & Barbhuiya, A. K. (2005). Flow field at a vertical-wall abutment. *Journal of Hydraulic Engineering, 131*, 1126-1135.

Das, S., Das, R., & Mazumdar, A. (2014). Variations in clear water scour geometry at piers of different effective widths. *Turkish Journal of Engineering & Environmental Sciences , 38*, 97-111.

Diab, R. (2011). *Experimental investigation on scouring around piers of different shape and alignement in gravel.* Phd Thesis, Darmstadt University of Technology, Darmstadt.

Dou, X. (1997). *Numerical simulation of three-dimensional flow field and local scour at bridge crossings.* Phd Thesis, University of Mississippi, USA.

Elsebaie, I. H. (2013). An experimental study of local scour around circular bridge pier in sand soil. *International of Civil & Environmental Engineering, 13* (1), 23-28.

Escauriaza, C., & Sotiropoulos, F. (2011b). Lagrangian model of bed-load transport in turbulent junction flows. *Journal of Fluid Mechanics, 666*, 36-76.

Esmaeili, T. (2009). *Hydraulic and geometric numerical simulation of scouring around concrete bridge piers (case study).* MSc. Thesis, Islamic Azad University-South Tehran Branch, Tehran.

Etterna, R., Melville, B. W., & Barkdoll, B. (1998). Scale effect in pier-scour experiments. *Journal of Hydraulic Engineering, 124*, 639-642.

Etterna, R. (1980). *Scour at bridge piers.* Phd Thesis, University of Auckland, Auckland.

Etterna, R., Mostafa, E., Melville, B., & Yassin, A. (1998). Local scour at skewed piers. *Journal of Hydraulic Engineering* , 756-459.

Froehlich, D. C. (1989). Local scour at bridge abutments. *Proceedings National Conference on Hydraulic Engineering* (13-18). New York: ASCE.

Gao, D., Posada, G. L., & Nordin, C. F. (1993). Pier scour equations used in the people's Republic of China. *FHWA-SA-93-076* , Washington, D.C.

Ghorbani, B. (2008). A field study of scour at bridge piers in flood plain rivers. *Turkish Journal of Engineering & Environmental Sciences , 32*, 189-199.

Graf, W. H., & Istiarto, I. (2002). Flow pattern in the scour hole around a cylinder. *Journal of Hydraulic Research , 40* (1), 13-20.

Gulbahar, N. (2009). Case study: Comparing performance of pier scour equations using field data for the Gediz Bridge, Manisa, Turkey. *Canadian Journal of Civil Engineering , 36*, 801-812.

Gümgüm, F. (2012). *Dairesel kesitli köprü orta ayakları etrafında meydana gelen temiz su oyulmalarının deneysel ve nümerik olarak incelenmesi.* Msc Thesis, Dokuz Eylül University, Izmir.

Guney, M. S., Aksoy, A. O., & Bombar, G. (2011). Experimental study of local scour versus time around circular bridge pier. *6th International Advanced Technologies Symposium.* Elazig.

Günyaktı, A. (1988). Köprü ayakları etrafında oyulma derinliğinin grafik yöntemle tahmini. *TÜBİTAK Doğa Dergisi* , 96-108.

Hager, W. H., & Unger, J. (2010). Bridge pier scour under flood waves. *Journal of Hydraulic Engineering , 136*, 842-847.

Hancu, S. (1971). Sur le calcul des affouillements locaux dans la zone des piles de ponts. *14th International Association of Hydraulic Engineering & Research Congress. 3*, 299-313. Paris: IAHR.

Harlow, F. H., & Welch, J. E. (1965). Numerical calculation of time-dependent viscous incompressible flow of fluid with free surface. *The Physics of Fluids , 8*, 2182-2189.

Hirt, C., & Cook, J. (1972). Calculating three-dimensional flows around structures and over rough terrain. *Journal of Computational Physics , 10*, 324-340.

Hoffmans, G., & Verheij, H. J. (1997). *Scour manual.* Rotterdam: A.A. Balkema.

Jia, Y., Kitamura, T., & Wang, S. Y. (2001). Simulation of scour process in plunging pool of loose bed material. *Journal of Hydraulic Engineering , 127*, 219-229.

Karim, O., & Ali, K. H. (2000). Prediction of flow patterns in local scour holes caused by turbulent water jets. *Journal of Hydraulic Research , 38*, 279-287.

Kayser, M., & Gabr, M. (2013). Scour Assessment of bridge foundation using In situ erosion evaluation probe (ISEEP). *Journal of the Transportation Research Record, 2335*, 72-78.

Khassaf, S. I., & Shakir, S. S. (2013). Evaluation of the local scour around group piers (Babil Bridge as a case study). *International Journal of Innovative Research in Science, Engineering and Technology, 2*, 7409-7420.

Kirkil, G., Constantinescu, G., & Etterna, R. (2009). Detached eddy simulation investigation of turbulence at a circular pier with a scour hole. *Journal of Hydraulic Engineering, 135*, 888-901.

Koken, M., & Constantinescu, G. (2011). Flow and turbulence structure around a spur dike in a channel with a large scour hole. *Water Resources Research, 47* (W12511).

Koken, M., & Göğüş, M. (2010). Effect of abutment length on the bed shear stress and the horseshoe vortex system. *International Conference on Fluvial Hydraulics.*

Kose, O. (2007). *Experimental and analytical investigation of temporal variation of local scour at bridge abutments.* Phd Thesis, Middle East Technical University, Ankara.

Kothyari, U. C., & Ranga Raju, K. G. (2001). Scour around spur dikes and bridge abutments. *Journal of Hydraulic Research, 39*, 367-374.

Kothyari, U. C., Garde, R. C., & Raju, K. (1992). Temporal variation of scour around circular bridge piers. *Journal of Hydraulic Engineering, 118*, 1091-1106.

Kothyari, U. C., Hager, W. H., & Oliveto, G. (2007). Generalized approach for clear-water scour at bridge foundation elements. *Journal of Hydraulic Engineering, 133*, 1229-1240.

Lai, J. S., Chang, W. Y., & Yen, C. L. (2009). Maximum local scour depth at bridge piers under unsteady flow. *Journal of Hydraulic Engineering , 135*, 609-614.

Lanca, R. M., Fael, C. S., Maia, R. J., Pego, J. P., & Cardoso, A. H. (2013). Clear-water scour at comparatively large cylindrical piers. *Journal of Hydraulic Engineering, 139*, 1117-1125.

Laursen, E. M. (1963). An analysis of relief bridge scour. *American Society of Civil Engineers, Journal of the Hydraulics Division, 89* (HY3), 93-118.

Li, L., & Sawamoto, M. (1995). Multi-phase model on sediment transport in sheet flow regime under oscillatory flow. *Coastal Engineering Journal, 38*, 157-178.

Lu, J., Hong, J. H., Lee, J. J., & Raikar, R. V. (2011). Temporal variation of scour depth at non-uniform cylindrical piers. *Journal of Hydraulic Engineering, 137*, 45-46.

Lun, C., Savage, S., Jeffrey, D., & Chepumiy, N. (1984). Kinetic theories of granular flow: inelastic particles in coquette flow and slightly inelastic particles in a general flow field. *Journal of Fluid Mechanics , 140*, 223-256.

Link, O. (2006). An investigation on scouring around a single cylindrical pier in sand (in german). *Mitteilungen des Institutes für Wasserbau und Wasserwirtschaft der Technischen Universität Darmstadt, 136*, 117.

Liu, C., & Shen, Y. M. (2010). A three dimensional k-ε-Ap model for water-sediment movement. *International Journal of Sediment Research, 25*, 17-27.

Lopez, G., Teixeira, L., Sanchez, M. O., & Simarro, G. (2014). Estimating final scour depth under clear-water flood waves. *Journal of Hydraulic Engineering, 140*, 328-332.

Melville, B. W., & Coleman , S. E. (2002). *Birdge scour.* Colorado: Water Resources Publications.

Melville, B. W., & Sutherland, A. J. (1988). Design method for local scour at bridge piers. *Journal of Hydraulic Engineering, 114*, 1210-1226.

Melville, B. W. (1975). *Local scour at bridge sites.* Auckland: University of Auckland, School of Engineering.

Melville, B. W., & Chiew, Y. M. (1999). Time scale for local scour at bridge piers. *Journal of Hydraulic Engineering, 125*, 59-65.

Melville, B. W., & Raudkivi, A. J. (1996). Effects of foundation geometry on bridge pier scour. *Journal of Hydraulic Engineering, 122*, 203-209.

Mia, M., & Nago, H. (2003). Design method of time-dependent local scour at circular bridge pier. *Journal of Hydraulic Engineering, 129*, 420-427.

Nagata, N., Hosoda, T., Nakato, T., & Muramoto, Y. (2005). Three-dimensional numerical model for flow and bed deformation around river hydraulic structures. *Journal of Hydraulic Engineering , 131*, 1074-1087.

Neill, C. R. (1973). *Guide to bridge hydraulics.* Toronto: Roads and Transportation Association of Canada.

Nekoufar, K., & Kouhpari, H. (2013). Control and decrease the scouring of bridge pier by method of non-submerged plates using SSIIM software. *Acta Technica Corvininesis - Bulletin of Engineering , 6* (4), 35.

Nicollet, G., & Ramette, M. (1971). Afouillements au voisinage de piles des ponts cylindriques circulaires. *14th International Association of Hydraulic Engineering & Research (IAHR) Congress.* Paris: IAHR.

Odhiambo, B. K., & Boss, S. K. (2004). Integrated echo sounder, GPS and GIS for reservoir sedimentation studies: examples from two Arkansas lakes. *Journal of the American Water Resources Association, 40*, 981-997.

Oliveto, G., & Hager, W. H. (2005). Further results to time-dependent local scour at bridge elements. *Journal Of Hydraulic Engineering, 131*, 97-105.

Oliveto, G., & Hager, W. H. (2002). Temporal evaluation of clear-water pier and abutment scour. *Journal of Hydraulic Engineering, 128*, 811-820.

Olsen, N., & Melaaen, M. C. (1993). Three-dimensional calculation of scour around cylinders. *Journal of Hydraulic Engineering, 119*, 1048-1054.

Olsen, N. B., & Kjellesvig, H. M. (1998). Three-dimensional numerical flow modelling for estimation of maximum local scour depth. *Journal of Hydraulic Research , 4*.

Olsen, N. B. (2003). 3D CFD modelling of a self-forming meandering channel. *Journal of Hydraulic Engineering* .

Pasiok, R., & Stilger-Szydlo, E. (2010). Sediment particles and turbulent flow simulation around bridge piers. *Archives of Civil and Mechanical Engineering, X* (2).

Raudkivi, A. J., & Etterna, R. (1983). Clear water scour at cylindrical piers. *Journal of Hydraulic Engineering, 109*, 338-350.

Raudkivi, A. J., & Sutherland, A. J. (1981). Scour at Bridge crossings. *National Roads Board Road Research Unit Bulletin 54* , Wellington.

Richardson, E. V., & Davis, S. R. (1995). Evaluating scour at bridges - Third edition. *Hydraulic Engineering Circular No. 18, Federal Highway Administration Publication No. FHWA HI 96-031* , Washington, D.C.

Richardson, E. V., & Davis, S. R. (2001). Evaluating scour at bridges. *Federal Highway Administration Report Number FHWA NHI 01-001* , Washington, D.C.

Richardson, J., & Panchang, V. G. (1998). Three-dimensional simulation of scour-inducing flow at bridge piers. *Journal of Hydraulic Engineering, 124*, 530-540.

Salaheldin, T. M., Imran, J., & Chaudhry, M. H. (2004). Numerical modeling of three-dimensional flow field around circular piers. *Journal of Hydraulic Engineering, 130*, 91-100.

Shen, H. W., Agawa, Y., & Karaki, S. K. (1965). Time variation of bed deformation near the bridge piers. *International Association for Hydraulic Research, Eleventh International Congress.* Leningrad: IAHR.

Shen, H. W., Schneider, V. R., & Karaki, S. S. (1969). Local scour around bridge piers. *American Society of Civil Engineers, Journal of the Hydraulics Division , 95* (HY6).

Shen, H. W., Schneider, V. R., & Karaki, S. S. (1966). *Mechanics of local scour.* Colorado: Colorado State University, Civil Engineering Department.

Sheppard, D. M., Odeh, M., & Glasser, T. (2004). Large scale clear-water local pier scour experiments. *Journal of Hydraulic Engineering , 130*, 957-963.

Sumer, B. M., & Chua, L. H. (2003). Influence of turbulence on bed load sediment transport. *Journal of Hydraulic Engineering, 129*, 585-596.

Syamlal, M., & O'Brien, T. J. (1989). Computer simulation of bubbles in a fluidized bed. *AIChE Symposium Series 85*, (pp. 22-31).

Totapally, H., Kulne, R. A., & Alonso, C. V. (1999). Temporal variation of local scour at abutments under steady flow conditions and stepped hydrographs. *1999 International Water Resources Engineering Conference.*

Tseng, M., Yen, C. L., & Song, C. (2000). Computation of three-dimensional flow around square and circular piers. *International Journal for Numerical Methods in Fluids, 34*, 207-227.

Urick, R. J. (1983). *Principles of underwater sound.* California: McGraw-Hill.

Wang, S. Y., & Jia, Y. (1999). Computational simulations of local scour at bridge crossings - capabilities and limitations. *1999 International Water Resources Engineering Conference.* Highlands Ranch, Co: Water Resources Publications.

Wardhana, K., & Hadipriono, F. C. (2003). Analysis of recent bridge failures in the United States. *Journal of Performance of Constructed Facilities, 17*, 144-150.

Wu, W., & Wang, S. Y. (1999). Movable bed roughness in alluvial rivers. *Journal of Hydraulic Engineering, 125*, 1309-1312.

Wu, S., & Rajaratnam, N. (1995). Free jumps, submerged jumps and wall jets. *Journal of Hydraulic Research, 33*, 197-211.

Wu, W. (2002). *Computational river dynamics.* 2002: Taylor & Francis/Balkema.

Yalin, M. S. (1977). *Mechanics of sediment transport.* Pergamon.

Yakhot, V., Orszag, S. A., Thangam, S., Gatski, T. B., & Speziale, C. G. (1992). Development of turbulence models for shear flows by a double expansion technique. *Physics of Fluids , 4* (7).

Yanmaz, A. M. (2002). *Köprü hidroliği.* Ankara: Metu Press.

Yanmaz, A. M. (2006). Temporal variation of clear water scour at cylindrical bridge piers. *Canadian Journal of Civil Engineering, 33*, 1098-1102.

Yanmaz, A. M., & Altinbilek, H. D. (1991). Study of time-dependent local scour around bridge piers. *Journal of Hydraulic Engineering, 117*, 1247-1268.

Yarnell, D. L., & Nagler, F. A. (1931). Effect of turbulance on the registration of current meters. *Transactions of The American Society of Civil Engineers, 95*, 766-860.

Yeganeh-Bakhtiaary, A., Kazeminezhad, M. H., Etemad-Shahidi, A., Baas, J. H., & Cheng, L. (2011). Euler–Euler two-phase flow simulation of tunnel erosion beneath marine pipelines. *Applied Ocean Research, 33*, 137-146.

Zhao, Z. (2006). *Numerical simulation of scour around fixed and sagging pipelines using a two-phase model.* Phd Thesis: Arizona State University, Arizona.

Zhao, Z., & Fernando, H. J. (2007). Numerical simulation of scour around pipelines using an Euler–Euler coupled two-phase model. *Environmental Fluid Mechanics, 7*, 121-142.